

QUARTERLY PROGRESS REPORT

No. 81

APRIL 15, 1966

GPO PRICE \$ _____

CFSTI PRICE(S) \$ _____

Hard copy (HC) 3.75

Microfiche (MF) 1.50

ff 653 July 65

MASSACHUSETTS INSTITUTE OF TECHNOLOGY
RESEARCH LABORATORY OF ELECTRONICS
CAMBRIDGE, MASSACHUSETTS

FACILITY FORM 802

N66 31903
(ACCESSION NUMBER)

287
(PAGES)

CR-76504
(NASA CR OR TMX OR AD NUMBER)

(THRU)

(CODE)

(CATEGORY)

The Research Laboratory of Electronics is an interdepartmental laboratory in which faculty members and graduate students from numerous academic departments conduct research.

The research reported in this document was made possible by support extended the Massachusetts Institute of Technology, Research Laboratory of Electronics, by the following agencies.

Joint Services Electronics Programs (U.S. Army, U.S. Navy, and U.S. Air Force)

Contract DA 36-039-AMC-03200(E)

U.S. Air Force—Electronic Systems Division

Contract AF 19(628)-2487

U.S. Air Force—Office of Scientific Research

Grant AF-AFOSR-880-65

U.S. Air Force—Research and Technology Division

Contract AF 33(615)-1747

Contract AF 33(615)-3489

U.S. Navy—Office of Naval Research

Contract Nonr-1841-(42)

National Aeronautics and Space Administration

Grant NsG-496

Grant NGR-22-009-(114)

Grant NGR-22-009-131

Grant NsG-334

Grant NsG-419

Contract NSR-22-009-120

National Institutes of Health

Grant MH-04737-05

Grant 5 R01 NB-04985-03

Grant NB-06251-01

Grant 5 R01 NB-04897-03

Grant NB-04332-03

National Science Foundation

Grant GP-2495

Grant GK-57

Grant GK-614

U.S. Atomic Energy Commission

Contract AT (30-1)-3581

Contract AT (30-1)-3285

Contract AT (30-1)-1842

Bell Telephone Laboratories, Inc. Grant

The Teagle Foundation, Inc. Grant

Support of projects is acknowledged in footnotes to the appropriate sections.

Reproduction in whole or in part is permitted for any purpose of the United States Government.

MASSACHUSETTS INSTITUTE OF TECHNOLOGY
RESEARCH LABORATORY OF ELECTRONICS

QUARTERLY PROGRESS REPORT No. 81

April 15, 1966

Submitted by: H. J. Zimmermann
G. G. Harvey

TABLE OF CONTENTS

Personnel	vii
Publications and Reports	xv
Introduction	xx

GENERAL PHYSICS

I.	Microwave Spectroscopy	1
	Minimum Detectable Power in Superconducting Bolometers	1
	Fermi Surfaces of Gallium from Size Effect	8
II.	Radio Astronomy	11
	Temperature Dependence of the Microwave Emissivity of NaCl Solutions	11
	Microwave Absorption Measurements of the Terrestrial Atmosphere	12
	Measurements of Continuum Radiation from Cosmic Radio Sources at the Haystack Research Facility	13
	Observations of the Moon	21
III.	Optical and Infrared Spectroscopy	27
	Far Infrared Spectra of Tetrahalo, Tetraammine, and Dihalodiammine Complexes of Palladium	27
	Far Infrared Spectra of Metal Cluster Compounds	33
IV.	Geophysical Research	35
	High Magnetic Fields	35
	Perturbation of Electron Energy Distribution by a Probe	35
	Upper Atmosphere Physics	36
	Studies of Stratospheric Aerosols and Their Correlation with Ozone	36
V.	X-ray Diffraction Studies	39
	Multiple Scattering of X-rays by Amorphous Samples	39
VI.	Physical Acoustics	41
	Intensity Distribution of Light Scattered by Thermal Surface Waves on a Liquid Surface	41
	Acoustic Wave Amplification	43
	Lateral Acoustic Instability	44
	Conservation Equations for a Plasma	46

CONTENTS

VII.	Electrodynamics of Moving Media	49
	Special Relativity and Asymmetric Energy Momentum Tensors	49
PLASMA DYNAMICS		
VIII.	Plasma Physics	55
	Approximate Solution of the Collisionless Plasma-Sheath Equation for Beam-Generated Plasma in a Plane Geometry	55
	Laser Breakdown	58
IX.	Gaseous Electronics	63
	Electron-Atom Collision Frequency in the Cesium Afterglow	63
X.	Plasmas and Controlled Nuclear Fusion	69
	Active Plasma Systems	69
	Beam-Plasma Discharge: System D	69
	Beam-Plasma Discharge: System C	72
	Electron Beam Excitation of Ion Oscillations in an ECRD Plasma	75
	Instabilities in Hot-Electron Beam-Plasma Systems	81
	Theory of VHF Oscillations and Possible Interactions with Ions in the Beam-Plasma Discharge	85
	Quasi-Linear Theory of Narrow-Bandwidth Convective Instabilities	94
	Wave-Mirror Heating	101
	Theory of Plasma Excitation by a Line-Charge Source	102
	Experimental Investigation of Instabilities in an Electron Beam with Transverse Energy	104
	High-Frequency Electron-Phonon Interactions in a Magnetic Field	106
	Applied Plasma Physics Related to Controlled Nuclear Fusion	113
	Thermonuclear Reactor: Introductory System Analysis	113
	Analysis of the Operation of a Long Arc Column	115
	Transverse Diffusion of a Long Plasma Column	121
XI.	Energy Conversion Research	125
	Power Systems with Liquid Generators	125
	Experimental Results for Condensing Ejector M-1	125
	Alkali-Metal Magnetohydrodynamic Generators	129
	Performance Potential of Superheated Rankine Cycle Space Power Systems Employing Magnetohydrodynamic Generators	129

CONTENTS

XII.	Spontaneous Radiofrequency Emission from Hot-Electron Plasmas	133
	Instabilities in the Extraordinary Waves across the Magnetic Field	133
XIII.	Interaction of Laser Radiation with Plasmas and Nonadiabatic Motion of Particles in Magnetic Fields	139
	Incoherent Scattering of Light from a Plasma III	139
	Nonadiabatic Trapping in Toroidal Geometry	141
	Nonadiabatic Scattering in Magnetic Fields	147

COMMUNICATION SCIENCES AND ENGINEERING

XIV.	Statistical Communication Theory	161
	Work Completed	161
	A Class of Nonlinear Filters	161
	An Efficient Transversal Equalizer for Two-Path Channels	161
XV.	Processing and Transmission of Information	169
	Coding for Source-Channel Pairs	169
	An Upper Bound on the Distribution of Computation for Sequential with Rate above R_{comp}	174
XVI.	Linguistics	181
	Playing with Distinctive Features in the Babbling of Infants	181
	Syllable Finals in Chinese Phonology	186
	Transitive Softening in Russian	190
XVII.	Cognitive Information Processing	193
	Cognitive Processes	193
	Confusion Errors for Spatially Transformed Letters	193
	Picture Processing	194
	Reduction of the Output Noise Power on a Very Noisy PCM Channel	194
	Considerations on the Generation and Processing of Holograms by Digital Computers	199
XVIII.	Communications Biophysics	207
	Waveforms Recorded Extracellularly from Neurons in the Anteroventral Cochlear Nucleus of the Cat	207
	The Fluctuation of Excitability of a Node of Ranvier	213
	Bioelectric Potentials in an Inhomogeneous Volume Conductor	218

CONTENTS

XIX.	Neurophysiology	227
	Modelling the Group 2 Ganglion Cell of the Frog's Retina	227
	Experiment Dealing with the Development of Logical and Abstract Thought in Young Children	236
	Stereomicroscopy with One Objective	238
	Special Function Theory	240
	Receptor Potentials in Retinular Cells in Limulus	242
	Direct Photoelectric Effect in Photoreceptor Cell Membranes	249
XX.	Computation Research	253
	Further Computations Using Newton's Method for Finding Complex Roots of a Transcendental Equation	253
	Author Index	255

PERSONNEL

Administration

Prof. H.J. Zimmermann, Director
Prof. G. G. Harvey, Associate Director
Mr. R. A. Sayers, Assistant Director

Advisory Committee

Dean G. S. Brown
Prof. W. W. Buechner
Prof. W. B. Davenport, Jr.
Prof. P. Elias
Prof. G. G. Harvey
Prof. A. G. Hill
Prof. I. W. Sizer
Dean J. B. Wiesner
Prof. H. J. Zimmermann
(Chairman)

Research Committee

Dean S. C. Brown
Prof. L. J. Chu
Prof. M. Halle
Prof. G. G. Harvey
Prof. W. A. Rosenblith
Mr. R. A. Sayers
Prof. W. M. Siebert
Prof. L. D. Smullin
Prof. M. W. P. Strandberg
Prof. P. D. Wall
Prof. J. R. Zacharias
Prof. H. J. Zimmermann
(Chairman)

Professors

Allis, W. P.
Barrett, A. H.
Bitter, F.
Brown, S. C.
Burke, B. F.
Chomsky, N. A.
Chu, L. J. (Absent)
Eden, M.
Edgerton, H. E.
Elias, P.
Gold, B. (Visiting)
Gyftopoulos, E. P.
Halle, M.

Harvey, G. G.
Haus, H. A.
Hill, A. G.
Huffman, D. A.
Jakobson, R.
Kerrebrock, J. L.
King, J. G.
Kurylowicz, J. (Visiting)
Lee, Y. W.
Mason, S. J.
Minsky, M. L.
Rose, D. J.
Rosenblith, W. A.

Shannon, C. E.
Shapiro, A. H.
Siebert, W. M.
Smullin, L. D. (Absent)
Stevens, K. N.
Strandberg, M. W. P.
Wall, P. D.
Warren, B. E.
Waugh, J. S.
Wozencraft, J. M. (Absent)
Yilmaz, H. (Visiting)
Zacharias, J. R.
Zimmermann, H. J.

Associate Professors

Bekefi, G.
Bers, A.
Bose, A. G.
Brown, G. A.
Dennis, J. B.
Fodor, J. A.
Gallager, R. G.
Garland, C. W.

Geselowitz, D. B. (Visiting)
Hoffman, M. A.
Ingard, K. U.
Jackson, W. D.
Jacobs, I. M.
Katz, J. J.
Klima, E. S.
Kyhle, R. L.

Loewenthal, M.
Matthews, G. H.
McCune, J. E.
Oates, G. C.
Peake, W. T.
Penfield, P. L., Jr.
Pomorska, Krystyna
Rafuse, R. P.

PERSONNEL

Associate Professors (continued)

Schreiber, W. F. (Absent)
Searle, C. L.

Taillet, J. (Visiting)
Taylor, E. F. (Visiting)

Teager, H. M.
Van Trees, H. L.

Assistant Professors

Andersen, J. (1)
Bernard, G. D. (1)
Billman, K. W.
Black, W. L. (1)
Blum, M.
Bobrow, D. G.
Brown, J. E.
Bruce, J. D.
Carabateas, E. N. (Absent)
Cheng, H.
Dean, L. W., III
Dupree, T. H.
Fiocco, G.
Getty, W. D.
Goutmann, M. M. (1)

Gray, P. R. (1)
Heiser, W. H.
Hennie, F. C., III
Hoversten, E. V. (1)
Huang, T. S.
Ingraham, J. C.
Kahn, R. E. (1)
Katona, P. G. (1)
Kennedy, R. S.
Kiparsky, R. P. V.
Klatt, D. H. (1)
Lee, H. B.
Lenoir, W. B. (1)
Lidsky, L. M.

Oppenheim, A. V. (1)
Perry, C. H.
Pierson, E. S. (1)
Prasada, B.
Siambia, J. G. (1)
Staelin, D. H. (1)
Stickney, R. E.
Stockham, T. G., Jr.
Suzuki, R. (Visiting)
Tretiak, O. J.
Troxel, D. E.
Weiss, R.
Weiss, T. F.
Yip, S.
Zare, R. N.

Lecturers

Cohen, D. (Visiting)
Ferretti, E.

Graham, J. W.
Whitehouse, D. R.

Instructors

Bauer, R. F.
Burns, S. K.
Crystal, T. H.
Gentle, K. W.
Henke, W. L.

Kuroda, S-Y.
Landsman, E. E.
Nelsen, D. E.
Parker, R. R.
Prabhu, V. K.
Sachs, M. B.

Schafer, R. W.
Schindall, J. E.
Schneider, H. M.
Snyder, D. L.
Spann, R. N.

Research Associates

Barnett, G. O.
Bromberger, S.
Durlach, N. I.
Garrett, M. F.
Hall, R. D.

Herzberger, H. G.
Kolers, P. A.
K. Kornacker
Lee, F. F.
Lettvin, J. Y.

Newmark, R. A.
Papert, S. A.
Pfeiffer, R. R.
Smith, T. G., Jr.
Zisk, S. H.

Guests

Beddoes, M. P.
Bullowa, Margaret
Fraser, J. B.

Gragg, G. B.
Kessler, A. R.
Nevo, E.
Peterson, P. L.

Schell, A. C.
Sezaki, N.
Walker, D. E.

(1) Engineering Postdoctoral Fellow

PERSONNEL

Visiting Scientists

Moreno-Diaz, Roberto

Research Affiliates

Barlow, J. S.
Brodey, W. M.
Brown, R. M.

Crist, A. H.
Cunningham, J. E.
Fohl, T.

Howland, B.
Langbein, D.
McLardy, T.

Postdoctoral Fellows

Charney, Elinor K. (3)
Hartman, H. (1)
Lampis, G. (2)
Natapoff, A. (1)

Pickard, Barbara C. G. (1)
Pickard, W. F. (1)
Sachs, Jacqueline (1)

Schwartz, A. (1)
Slawson, A. W. (3)
Songster, G. F. (1)
Taub, A. (1)

R. L. E. Research Staff

Andrews, J. M.
Barrett, J. W.
Benhaim, N.
Bergman, J. G.
Brooks, T. H.
Burgess, R. G.
Chung, S-H
Crowther, Patricia P.
Cunningham, A. W. B.
Edwards, D. J.
Fischler, H.
Fontaine, C. L.
Fratar, Gail M.
Ingersoll, J. G.

Ingham, K. R.
Jensen, E. R.
Johnston, W. D., Jr.
Kiang, N. Y. S.
Kierstead, J. D.
Levy, Rachel J.
Mattison, E. M.
McCarthy, J. J.
McCulloch, W. S.
McCloud, Veronica E.
Menyuk, Paula
Mulligan, W. J.
Nacamuli, R. M.

O'Brien, F. J.
Pauwels, H. J.
Pennell, Martha M.
Pitts, W. H.
River, Eleanor C.
Rojas Carona, R. R.
Rosebury, F.
Ryan, L. W. (Absent)
Shaw, M. L.
Tse, F. Y-F
Vidale, Eda Berger
Viertel, J. J.
Wawzonek, J. J.
Wickelgren, G. L.

Research Assistants

Austin, M. E. (4)
Bartsch, R. R.
Bhushan, A. K.
Brown, T. S.
Catto, P. J.
Chan, S. W-C
Chandra, A. N.
Chang, R. P. H.
Chapin, P. G.
Chase, D.
Ching, H.

Citron, A.
Dean, Janet P.
DeRijk, R. P. G.
DeWolf, J. B.
Engelmaier, W.
Evers, W. H., Jr.
Ezekiel, S.
Flynn, R. W.
Fraim, F. W.
Gabrielian, A.

Gadzuk, J. W.
Good, W. E., Jr.
Graham, D. N.
Grams, G. W.
Gustafson, K. T.
Harvey, R. N.
Hebel, W. T., Jr.
Herba, F.
Hill, R. A.
Hofmann, T. R.
Hougen, M. L.

(1) National Institutes of Health Fellow
(2) Senior Fellow

(3) R. L. E. Fellow
(4) Lincoln Laboratory Staff Associate

PERSONNEL

Research Assistants (continued)

Huang, T.	McNary, C. A.	Speck, C. E.
Khanna, M.	Mendelsohn, R. L.	Spiridon, A.
Kitrosser, D. F.	Milne, D. C.	Steinbrecher, D. H.
Klouman, P. H. B.	Moldon, J. C.	Stone, E. T.
Koons, H. C.	Moran, J. M.	Taylor, M. G.
Kusse, B. R.	Moses, J.	Thome, R. J.
Lavoie, G. A.	Nahvi, M.	Tomlinson, R. S.
Levy, E. K.	Offenberger, A. A.	Wagner, C. E.
Lieberman, M. A.	Papadopoulos, G. D.	Waller, M. H.
Liu, J-H	Poussart, D. J. M.	Weinberg, S.
Logan, R. M.	Pruslin, D. H.	Williams, J. A.
Lou, D. Y-S	Qualls, C. B.	Woo, J. C.
Mangano, J. A.	Ribbeck, C. S.	Yamamoto, S.
Makhoul, J. J.	Rogers, A. E. E.	Young, R. A.
Maul, M. K.	Scholl, M. M.	Zeiders, G. W., Jr.
	Snyder, D. L.	

Graduate Assistants

Andrews, M. L.	Kronquist, R. L.	Reifenstein, E. C., III
Brenner, J. F.	Kukolich, S. G.	Reznek, S. R.
Cohen, A. J.	Langdon, R. M., Jr.	Rogoff, G. L.
Fertel, Jeanne H.	Llewellyn-Jones, D. T.	Silk, J. K.
Garosi, G. A.	Macon, J. L.	Wilheit, T. T., Jr.
Golub, R.	Manheimer, W. M.	Wright, B. L.
Guttrich, G. L.	McClintock, J. E.	Young, E. F.
Geis, M. L.	McEnally, T. E., Jr.	Yung, B. N.
	Pleasant, L. D.	

Teaching Assistants

Anderson, G. B.	Fehrs, D. L.	Ng, L. C.
Anderson, W. M., Jr.	Freeman, J. A.	O'Leary, G. C.
Bice, P. K.	Glaser, J.	Peters, P. S., Jr.
Blessner, B.	Guttman, D. S.	Poulo, L. R.
Brown, T. R.	Harris, R. V., III	Portner, E. M., Jr.
Bruce, R. D.	Helman, H. L.	Plummer, W. W.
Colburn, H. S.	Kosowski, J. F.	Samis, M. A.
Crane, D. E.	Lazarus, M. B.	Schaefer, D. W.
Dum, C. T.	Levin, M. I.	Seitz, C. L.
Eisenberg, M.	Metz, P. J.	Singer, J. J.
Edwards, R. K.	Meyn, J. H.	Smith, T. B.
Fargo, F. M., Jr.	Moir, R. W.	Veneklasen, L. H.
	Moxon, E. C.	

Graduate Students

Allen, R. J. (1)	Bedell, G. D., IV (4)	Browne, E. W. (4)
Anderson, J. A. (2)	Bever, T. G. (5)	Bruek, S. R. J. (3)
Arnstein, D. S.	Bigham, T. D., Jr. (6)	Bucher, E. A. (3)
Baggeroer, A. B. (3)	Blum, G. D. (3)	Caldwell, D. (3)
Barnwell, T. P., III (3)	Braida, L. D. (3)	Callen, J. D. (7)
	Bridwell, J. D. (6)	

(1) RCA Fellow

(2) National Institutes of Health Fellow

(3) National Science Foundation Fellow

(4) National Defense Education Act Fellow

(5) Harvard Fellow

(6) Bell Telephone Laboratories Fellow

(7) Atomic Energy Commission Fellow

PERSONNEL

Graduate Students (continued)

Carter, R. J. (1)	Huntington, T. A.	Rizk, H. M. (24)
Cattellani, V. (26)	Jackendoff, R. S. (10)	Roberson, J. E. (6)
Chapin, P. G. (13)	Jameson, P. W.	Ross, A. H. M. (4)
Clark, N. F. (4)	Jeanes, R. R., Jr. (14)	Ross, J. A. (4)
Clarke, J. F. (2)	Jenkins, L. (4)	Ross, J. R. (1)
Collins, L. D. (4)	Katyl, R. H. (4)	Schulz, H. M., III (4)
Cornew, R. W. (5)	Kawanami, M.	Shoap, S. C. (14)
Davis, A. M. (6)	Kayne, R. S. (10)	Shupe, D. S. (4)
Davis, J. A. (4)	Kimball, J. P. (1)	Simpson, J. I. (4)
Decher, R. (7)	Krakauer, L. J. (4)	Smith, M. G.
Doane, J. L. (8)	Leonardi, Cattolica, A. M. (17)	Snow, M. S. (4)
Dougherty, R. C. (1)	Lubin, M. D.	Spielman, C. A. (10)
Emonds, J. E. (1)	Mark, R. G.	Stafford, J. C. (6)
Evans, J. E. (4)	Max, J.	Stanley, R. J. (4)
Falconer, D. D. (9)	McDowell, G. Q. (4)	Stephenson, R. S.
Feldman, D. A.	Mendell, L. M. (1)	Strong, R. M. (8)
Fetz, E. E. (4)	Merrill, E. G. (19)	Swain, D. W. (25)
Fidelholtz, J. L. (10)	Mildonian, A. A., Jr. (6)	Tate, R. H. (6)
Flannery, D. L. (4)	Mozzi, R. L. (18)	Thomae, I. H. (4)
Free, J. Y., Jr.	Mueller, P. E. (20)	Thomas, R. H. (7)
Fukumoto, A. (11)	Murakami, M. (21)	Thompson, K. D. (6)
Gaut, N. E. (7)	Myers, Amy E. (10)	Thornburg, C. O., Jr.
George, E. V. (12)	Naro, A. J. (10)	Tremain, R. E., Jr. (14)
Goldberg, A. J. (14)	Nelson, G. P. (3)	von Bismarck, G.
Golden, B. P. (3)	Newell, J. E. (6)	Vugrinec, Z. (27)
Goldfield, R. (10)	Nolan, J. J., Jr.	Waletzko, J. A.
Greenspan, R. L.	Owolo, D. (16)	Wallace, R. N. (4)
Gruber, J. S. (10)	Parrish, J. H. (4)	Wang, C. H. (28)
Guinan, J. J., Jr. (4)	Perlmutter, D. M. (10)	Weinstein, C. J. (14)
Guldi, R. L. (14)	Perozek, D. M. (14)	Westerfeld, E. C.
Haccoun, D.	Pilc, R. (6)	Wickelgren, Barbara G. (4)
Harris, J. W. (3)	Pinkston, J. T., III (4)	Wiederhold, M. L. (3)
Hartline, D. K. (3)	Pittenger, L. C. (2)	Wilson, T. L. (4)
Hartmann, P. H. (15)	Portinari, J. C. (22)	Wolaver, D. H. (4)
Hebel, W. T., Jr.	Rabiner, L. R. (4)	Wolf, J. J.
Heggstad, H. M.	Rack, H. J.	Woo, Nancy H. (1)
Heller, J. A. (16)	Reeves, J. P. (1)	Wright, D. A. (29)
Hofmann, T. R. (1)	Reilly, R. D. (4)	Wright, W. A.
Houtsma, A. J. M.	Richters, J. S. (4)	Wu, W.
Hsiao, H. S.	Riehl, J. W. (23)	Yusek, R. (6)

- | | |
|---|--|
| (1) National Institutes of Health Trainee | (16) Xerox Fellow |
| (2) Atomic Energy Commission Fellow | (17) Whitney Predoctoral Fellow |
| (3) National Institutes of Health Fellow | (18) Raytheon Fellow |
| (4) National Science Foundation Fellow | (19) Public Health Service Trainee |
| (5) Sperry-Rand Fellow | (20) American Can Company Fellow |
| (6) Bell Telephone Laboratories Fellow | (21) Hyogo Prefecture-Japan Scholarship |
| (7) NASA Fellow | (22) National Research Council Fellow |
| (8) Hertz Foundation Fellow | (23) Proctor and Gamble Fellow |
| (9) Hughes Aircraft Fellow | (24) International Atomic Energy Commission Fellow |
| (10) National Defense Education Act | (25) NASA Trainee |
| (11) Kennicott Copper Corporation Fellow | (26) Fulbright Fellow |
| (12) RCA Fellow | (27) United Nations Fellow |
| (13) Danforth Fellow | (28) Woodrow Wilson Fellow |
| (14) National Science Foundation Trainee | (29) Royal Canadian Air Force |
| (15) Grass Fund Fellow | |

PERSONNEL

Undergraduates (Thesis or Special Problems)

Adler, A. P.	Hess, R. A.	Pearlman, J.
Assael, D.	Hildebrand, S. J.	Plice, W. A.
Babitch, D.	Holdaway, C. R.	Post, A. E.
Bourrie, G. H., Jr.	Jones, D. H.	Reintjes, J. F.
Brown, J., III	Juvkam-Wold, H. C.	Rhyne, T. L.
Byrd, G. C., III	King, A. P.	Sawchuk, A. A.
Casperson, L.	Koralek, R. W.	Schlitt, L. G.
Casseday, M. W.	Kosinar, W. J.	Schwartz, P. R.
Chase, D. L.	Leary, A. R.	Seddon, T. E.
Chow, S.	Lehr, J. J.	Small, J. G.
Costa, R. A.	Lewenstein, H.	Smith, D. P.
Cowan, M. J.	Lipsey, S. D.	Solin, J. R.
Davidow, J. E.	Lowman, C.	Stamm, P. L.
DeAngelis, D. L.	Madan, J. K.	Steele, J. M.
Eckstein, P. F.	Mallary, M. L.	Strand, T. F.
Eggers, T. W.	Mannos, J. L.	Tippett, W. R.
Forbes, B. E.	Masters, J. M.	Torode, J.
Funderberg, J. C.	Matison, G. G.	Vahey, D. W.
Furtek, F.	McGinnis, W. J.	Ward, M. J.
Goodman, J. M.	McNelly, T. F.	Warshaw, A. S.
Greenberg, S.	McQueen, D. H.	Weidner, M. Y.
Hahn, J. M.	Memishian, J., Jr.	Wertz, R. P.
Hall, T. E.	Milligan, D. D.	Williams, F. K.
Haney, D. L.	Morgan, H. D.	Wolfe, P. D.
Harris, J. W.	Nedzelitsky, V.	Zimmerman, R. R.
Hayashi, S. J.	Novenski, A. F.	Zucker, R. S.
	Patterson, J.	

Student Employees

Ackerman, W. B.	Lackner, J. R.	Ray, J. N.
Bozler, H. M.	Laird, P. D., III	Rosen, M. A.
Davis, D. M.	Michel, A.	Sahagen, Judith A.
Dunn, R. D.	Morton, R. M.	Solarz, R. W.
Emery, R. H.	Naqvir, A. A.	Spalding, J. W.
Granek, H.	O'Lague, P. H.	Sturges, R. H., Jr.
Jastrem, R. L., Jr.	Partridge, L. D.	Tuttle, Susan D.
Khan, A.	Perkell, J. S.	Tweed, D. G.
Kohler, R. F., Jr.		Wrigley, J. D., Jr.

R. L. E. Administrative Staff

Duffy, D. F.	Sayers, R. A.
Hewitt, J. H.	Smith, P. L.
Keyes, R. V., Jr.	Thomas, Helen L.

Administrative Assistant

Bella, C. J.

Office Clerks

Barron, Gladys G.	Gregor, C. A.	Scalleri, Mary B.
Chase, Arbella P.	Ippolito, Dorothy A.	Stagliola, Eleanor E.
Engler, R. R.	Kent, Susan M.	Toebe, Rita K.
Greene, Yvonne E.	Peck, J. S.	Whitehead, Saffron A.
	Ruggere, P. A.	

PERSONNEL

Typists

Foley, Ruth E.
Murphy, Mary R.

Myers, Alberta L.
Napolitano, Joan V.

Williams, Victoria
Young, Nancy E.

Technical Typists

Barnes, R. A.
Capron, Evelyn L.

Jones, Elizabeth
Smee, P. E.

Secretaries

Bedrosian, Isabel
Blum, Elaine
Bullard, Ann B.
Carbone, Angelina
Chorba, Linda D.
Cohen, Phyllis J.
Conwicke, Vera
Cummings, Jane F.
DiPietro, Toni R.
Finer, Faith L.
Geller, Elaine J.
Hamilton, Martha C.

Holden, Meredith
Hurvitz, Rose S.
Imperato, Eleanor M.
Ingersoll, Nancy L. B.
Johnson, Barbara A.
Kaloyanides, Venetia
Lipchinsky, Cheryl A.
Loeb, Charlotte G.
Lynch, Kathy Ann
McCarthy, Barbara L.
McEntee, Doris C.
Murray, Maureen P.

O'Neil, Patricia A.
Owens, Mary E.
Parrella, Cynthia A.
Pierce, Marilyn A.
Reid, Gloria C.
Ricker, Barbara J.
Riddle, Roberta M.
Russell, Susan P.
Smith, Clare F.
Van Wezel, Ruth
Wanner, Patricia A.
Whertritt, Irene M.

Engineering Assistants

Berg, A. E.
Crist, F. X.

McKenzie, J. A.

Papa, D. C.
Thompson, J. B.

Technical Assistants

Byers, F. H.
Grande, Esther D.
Iverson, Alice I.
Lyons, Jayne

Major, Diane
Miller, Bonnie J.
Rabin, Sylvia G.

Rosenthal, Kathryn F.
Shipley, Jenot W.
Swenson, Judith E.
Yaffee, M. A.

Technicians

Aucella, Alice G.
Babcock, E. R.
Barrows, F. W.
Bauer, T. K.
Butler, R. E., Jr.
Connolly, J. T.
DiPietro, P. J.
Fitzgerald, E. W., Jr.

Gage, R. B., Jr.
Gay, H. D.
Iovine, M. A.
Kaufman, D. E.
Kelly, M. A.
Lewis, R. R.
Massey, L. N.
McLean, J. J.

Neal, R. W.
North, D. K.
Schwabe, W. J.
Sears, A. R.
Sholder, J. A.
Sprague, L. E.
Stevens, J. A.
Tortolano, A. J.

Technicians' Shop

Lorden, G. J., Foreman

Fownes, Marilyn R.
Hill, R. F.

PERSONNEL

Laboratory Assistants

Beaton, Catherine M.
Cardia, P. F.

MacDonald, K. B.

Miller, S. A.
Wood, H.

Drafting Room

Navedonsky, C. P., Foreman
Donahue, J. B.

Hillier, Anna M.

Porter, Jean M.
Rollins, I. E.

Photographic Shop

Aradi, M. G.
Cook, J. F.
Karas, P.

Machine Shop

Keefe, J. B., Foreman
Aalerud, R. W.
Bletzer, P. W.
Brennan, J.
Bunick, F. J.

Cabral, M., Jr.
Carter, C. E.
Harvey, A. O.
Liljeholm, F. H.
Muse, W. J.
Reiman, W.

Ridge, P. A.
Ryan, J. F.
Sanroma, J. B.
Shmid, E.
Wentworth, W. G., Jr.

Tube Laboratory

Rosebury, F.

Griffin, J. L.
Leach, G. H., Jr.
MacDonald, A. A.

Glass Shop

DiGiacomo, R. M.
Doucette, W. F.

Stock Clerks

Doherty, R. H.
Haggerty, R. H.

Legier, D. O.

Morris, P. L.
Sharib, G.

Utility and Maintenance

Doiron, E. J., Foreman
Audette, A. G.

Lucas, W. G.
McDermott, J. F.
Riley, J. F.

Sincuk, J., Jr.
Thibodeau, D. S.

PUBLICATIONS AND REPORTS

MEETING PAPERS PRESENTED

Symposium on Sonics and Ultrasonics, sponsored by IEEE (PGUE), Boston, Massachusetts

December 1-3, 1965

J. M. Andrews, Jr. and M. W. P. Strandberg, Acoustic Dispersion Effects in Heat Pulse Experiments

Plasma Physics Laboratory Seminar, Princeton University, Princeton, New Jersey

December 9, 1965

A. Bers, Absolute and Convective Instabilities in Plasmas (invited)

Colloquium, Yale University, New Haven, Connecticut

December 10, 1965

U. Ingard, Acoustic Wave Generation and Amplification in a Plasma (invited)

Seminar, National Bureau of Standards, Washington, D. C.

December 14, 1965

C. H. Perry, Study of Crystal Lattice Vibrations for Far Infrared Spectroscopy (invited)

120th Meeting, American Astronomical Society, University of California, Berkeley

December 27-30, 1965

S. H. Zisk, Brightness Distributions of Discrete Radio Sources at 2-cm Wavelength

American Musicological Society Annual Meeting, University of Michigan, Ann Arbor, Michigan

December 29, 1965

A. W. Slawson, The Computer as an Aid to the Composer

Symposium of "Philosophy and Linguistics," Sixty-second Annual Meeting, American Philosophical Association, Eastern Division, New York

December 29, 1965

J. J. Katz, The Relevance of Linguistics to Philosophy

Institute of Electrical and Electronics Engineers, Huntsville Section Meeting, Huntsville, Alabama

January 12, 1966

H. J. Zimmermann, The Vital Role of Electronics in Biological Research (invited)

IEEE Industrial Symposium on Information Theory, Los Angeles, California

January 31, 1966

R. G. Gallager, Channel Capacity and Coding for Additive Gaussian Noise Channels with Power and Frequency Constraints

MEETING PAPERS PRESENTED (continued)

IEEE Informal Conference on Active Microwave Effects in Bulk Semiconductors, New York City

February 4, 1966

A. Bers and S. R. J. Brueck, Stimulated Emission of Phonons at an Angle to the Applied Magnetic Field (invited)

International Solid-State Circuits Conference, University of Pennsylvania, Philadelphia, Pennsylvania

February 9-11, 1966

R. P. Rafuse and D. H. Steinbrecher, Harmonic Multiplication with Punch-through Varactors

International Symposium on Neutron Noise, Waves and Pulse Propagation, University of Florida, Gainesville, Florida

February 14-16, 1966

R. J. Hooper and E. P. Gyftopoulos, On the Measurement of the Characteristic Kernels of a Class of Nonlinear Systems

Biophysical Society Tenth Annual Meeting, Boston, Massachusetts

February 23-25, 1966

W. M. Siebert, Signals and Noise in Primary Auditory Neurons (invited)

JOURNAL PAPERS ACCEPTED FOR PUBLICATION

(Reprints, if available, may be obtained from the Document Room, 26-327, Research Laboratory of Electronics, Massachusetts Institute of Technology, Cambridge, Massachusetts 02139.)

V. R. Algazi, Useful Approximations to Optimum Quantization (IEEE Trans. (CT))

J. M. Andrews, Jr. and M. W. P. Strandberg, Thermal Microwave Phonons (Proc. IEEE)

J. E. Brown and Diane Major, Cat Ganglion Cell Dendritic Fluids (Exptl. Neurol.)

L. J. Chu, H. A. Haus, and P. Penfield, Jr., The Force Density in Polarizable and Magnetizable Fluids (Proc. IEEE)

R. Geick, C. H. Perry, and G. Rupprecht, Normal Modes in Hexagonal Boron Nitride (Phys. Rev.)

R. Geick, W. J. Hakel, and C. H. Perry, Temperature Dependence of the Far Infrared Reflectivity of Magnesium Stannide (Phys. Rev.)

C. W. Garland and C. F. Yarnell, Order-Disorder Phenomena IV. Ultrasonic Attenuation near the Lambda Point in Ammonium Chloride (J. Chem. Phys.)

G. G. Hammes and T. B. Lewis, Ultrasonic Absorption in Aqueous Polyethylene Glycol Solutions (J. Phys. Chem.)

JOURNAL PAPERS ACCEPTED FOR PUBLICATION (continued)

- W. D. Johnston, Jr. and J. H. King, Field Ionization Detectors for Molecular Beams (Rev. Sci. Instr.)
- P. Kolers, Reading and Talking Bilingually (Am. J. Psychol.)
- R. G. Little and J. F. Waymouth, Experimentally Determined Plasma Perturbation by a Probe (Phys. Fluids)
- R. M. Logan and R. E. Stickney, Simple Classical Model for the Scattering of Gas Atoms from a Solid Surface (J. Chem. Phys.)
- R. Melzack and P. D. Wall, Pain Mechanism - A New Theory (Science)
- J. W. Moore, N. Anderson, M. Blaustein, M. Takata, J. Y. Lettvin, W. F. Pickard, T. Bernstein, and J. Pooler, Alkali Cation Selectivity of a Squid Axon Membrane (Ann. N. Y. Acad. Sci.)
- B. J. Murawski and S. K. Burns, Daily Correlation of Adrenal Steroids and Alpha Frequency in the EEG: A Demonstration (J. Appl. Physiol.)
- R. R. Pfeiffer, Classification of Response Patterns of Spike Discharges for Units in the Cochlear Nucleus: Tone-Burst Stimulation (Exptl. Brain Res.)
- P. Penfield, Jr. and H. A. Haus, Hamilton's Principle for Electromagnetic Fluids (Phys. Fluids)
- Barbara G. Pickard and K. V. Thimann, Geotropic Response of Wheat Coleoptiles in the Absence of Amyloplast Starch (J. Gen. Physiol.)
- W. A. Rosenblith, Physics and Biology - Where Do They Meet? (Physics Today)
- A. W. Slawson, Review of "Meta (+) Hodos: A Phenomenology of Twentieth Century Musical Materials and an Approach to the Study of Form" by James Tenney (Inter-American Institute for Musical Research, New Orleans, 1964) (J. Music Theory)
- D. H. Staelin and A. H. Barrett, Spectral Observations of Venus near 1-Centimeter Wavelength (Astrophys. J.)
- D. H. Staelin, Measurements and Interpretation of the Microwave Spectrum of the Terrestrial Atmosphere near 1-Centimeter Wavelength (J. Geophys. Res.)
- R. E. Stickney, P. B. Sun, and M. L. Shaw, Effect of Thermal and Ultraviolet Radiation on Thermionic Emission from Tungsten (J. Appl. Phys.)
- D. S. Thompson, E. E. Hazen, and J. S. Waugh, Electron Paramagnetic Resonance Study of Solutions of Europium in Liquid Ammonia (J. Chem. Phys.)

LETTERS TO THE EDITOR ACCEPTED FOR PUBLICATION

- C. Freed and H. A. Haus, Photoelectron Statistics Produced by a Laser Operating below the Threshold of Oscillation (Phys. Rev. Letters)
- H. B. Lee and R. W. Daniels, A Non-reciprocity Figure of Merit for Passive Resistance Devices (IEEE Trans. (CT))
- P. Penfield, Jr., Electromagnetic Force Density (Proc. IEEE)
- V. Prabhu, Noise Performance of Abrupt-Junction Varactor Frequency Multipliers (Proc. IEEE)
- D. L. Snyder, Optimum Linear Filtering of an Integrated Signal in White Noise (Trans. IEEE (AES))

TECHNICAL REPORTS PUBLISHED

(These and previously published technical reports, if available, may be obtained from the Document Room, 26-327, Research Laboratory of Electronics, Massachusetts Institute of Technology, Cambridge, Massachusetts 02139.)

- 441 Aubrey M. Bush, Some Techniques for the Synthesis of Nonlinear Systems

SPECIAL TECHNICAL REPORTS PUBLISHED

(These monographs are available from The M.I. T. Press, E19-741, Massachusetts Institute of Technology, Cambridge, Massachusetts 02142.)

- Number 13 Nelson Yuan-sheng Kiang with the assistance of Takeshi Watanabe, Eleanor C. Thomas, and Louise F. Clark, Discharge Patterns of Single Fibers in the Cat's Auditory Nerve (M.I. T. Monograph No. 35)

SPECIAL PUBLICATIONS

- J. S. Barlow, Some Possibilities of the Study of Visual-Oculomotor Processes with the Aid of Oriental Ideograms (invited discussion) (Proc. International Colloquium on Mechanisms of Orienting Reaction in Man, Smolenice and Bratislava, Czechoslovakia, September 11-15, 1965)
- J. G. Bergman and R. E. Stickney, Effect of Fluorine and Oxygen on Thermionic Emission from Polycrystalline Tungsten (Report on Twenty-sixth Annual Conference on Physical Electronics, Massachusetts Institute of Technology, March 21-23, 1966)

SPECIAL PUBLICATIONS (continued)

- M. Eden, Taxonomies of Disease (The Diagnostic Process, edited by John A. Jacquez, Proceedings of a Conference Sponsored by the Biomedical Data Processing Training Program, University of Michigan, Ann Arbor, Michigan, April, 1964)
- W. Engelmaier and R. E. Stickney, Thermionic and Adsorption Characteristics of a Single-Crystal Tungsten Filament Exposed to Oxygen (Report on Twenty-sixth Annual Conference on Physical Electronics, Massachusetts Institute of Technology, March 21-23, 1966)
- D. L. Fehrs and R. E. Stickney, Retarding Potential Measurements of the Work Function of Tantalum as a Function of Cesium Coverage (Report on Twenty-sixth Annual Conference on Physical Electronics, Massachusetts Institute of Technology, March 21-23, 1966)
- H. A. Haus, Model for Force Density in Moving Magnetized Material (1966 IEEE International Convention Record)
- J. J. Katz, The Philosophy of Language (Harper and Row, New York, 1966)
- P. Penfield, Jr., and H. A. Haus, "Energy-Momentum Tensor for Electromagnetic Fluids," in Recent Advances in Engineering Science, pp. 441-492 (Gordon and Breach Science Publishers, Inc., New York, 1966)
- D. E. Nelsen, Statistics of Switching-Time Jitter for a Tunnel Diode Threshold-Crossing Detector (1966 IEEE International Convention Record)
- P. Penfield, Jr., Thermodynamics and Force of Electromagnetic Origin (1966 IEEE International Convention Record)

INTRODUCTION

This report, the eighty-first in a series of quarterly progress reports issued by the Research Laboratory of Electronics, contains a review of the research activities of the Laboratory for the three-month period ending February 28, 1966. Since this is a report on work in progress, some of the results may not be final.

GENERAL PHYSICS

I. MICROWAVE SPECTROSCOPY*

Academic and Research Staff

Prof. M. W. P. Strandberg
Prof. R. L. Kyhl

Dr. J. M. Andrews

J. G. Ingersoll
J. D. Kierstead

Graduate Students

V. Castellani
J. U. Free, Jr.
A. Fukumoto

R. M. Langdon, Jr.
M. K. Maul

T. E. McEnally
S. R. Reznik
B. N. Yung

A. MINIMUM DETECTABLE POWER IN SUPERCONDUCTING BOLOMETERS

There is considerable interest in the development of sensitive, high-speed detectors for the far infrared portion of the electromagnetic spectrum. This is a particularly awkward energy range for the usual types of quantum detector (photomultiplier, photoconductor, etc.) because at these frequencies individual quantum events are completely masked by the statistical fluctuations associated with thermal equilibrium at ordinary temperatures. At cryogenic temperatures, on the other hand, the ultimate sensitivity of both quantum and thermal detectors is increased by several orders of magnitude. Thermal detectors have the added advantage that their response is not characterized by an absorption edge. The successful use of superconducting bolometers for the detection of far infrared lattice vibrations^{1,2} has stimulated an interest in examining their theoretical capabilities as sensitive, high-speed, far infrared detectors.

1. Sources of Noise in Radiation Bolometers

The ultimate sensitivity of a radiation bolometer is set by three noise processes: temperature noise, Johnson noise, and current noise. The first two can be easily derived from fundamental considerations. Temperature noise is determined by the statistical nature of thermal equilibrium within the sensing element of a thermal detector. Johnson or Nyquist noise is the manifestation of voltage fluctuations at the terminals of a conductor arising from the random motion of charged carriers. Current noise, on the other hand, is much more complex. Since it is produced by processes that cannot be adequately observed, it is usually determined empirically. Each of these noise processes has been treated in considerable detail by Smith, Jones, and Chasmar.³

The mean-square values of statistically independent fluctuations are additive, and the rms noise power arising from the three processes is given by

*This work was supported by the Joint Services Electronics Programs (U.S. Army, U.S. Navy, and U.S. Air Force) under Contract DA 36-039-AMC-03200(E).

(I. MICROWAVE SPECTROSCOPY)

$$\sqrt{\frac{W_m^2}{\epsilon}} = \epsilon^{-1} \left[4kT^2G + \frac{4kTR}{r^2} + \frac{SR^2i^2}{r^2f} \right]^{1/2} (\Delta f)^{1/2} \text{ watts.} \quad (1)$$

The first term in the bracket on the right is the contribution of thermal noise; the second, Johnson noise; and the third, current noise.

Let us now define the symbols appearing in Eq. 1: ϵ is the emissivity of the receiving area of the bolometer; k (joules/°K) is Boltzmann's constant; T (°K) is the absolute temperature; G (watts/°K) is the thermal conductance of the receiving area of the bolometer to its surroundings; R (ohms) is the electrical resistance of the bolometer; i (amps) is the current flowing through it; f (sec⁻¹) is the noise frequency; and Δf (sec⁻¹) is the bandwidth over which the noise is observed. The quantity S is an intrinsic structure parameter related to the geometry, material, crystal structure, purity and strain state of the conducting element. This is a complex factor that is usually determined empirically.

The quantity r is the responsivity of the bolometer. It is given by

$$r = \frac{F\epsilon R i \alpha}{G_e (1 + \omega^2 \tau^2)^{1/2}} \text{ volts/watt,} \quad (2)$$

where F is the "bridge factor" given by

$$F = \frac{R_\ell}{R + R_\ell}, \quad (3)$$

and R_ℓ (ohms) is the load resistance connected to the bolometer. The temperature coefficient of resistivity α is defined as

$$\alpha = \frac{1}{R} \frac{dR}{dT} \text{ } ^\circ\text{K}^{-1}. \quad (4)$$

The effect of Joule heating within the bolometer produced by the biasing current i is to alter the thermal conductance to an effective value given by

$$G_e = G - \alpha R i^2 \left(\frac{R_\ell - R}{R_\ell + R} \right) \text{ watts/}^\circ\text{K.} \quad (5)$$

It should be clear from Eqs. 2 and 5 that the stability of the bolometer is closely allied to its operating conditions. If, for example, $R_\ell > R$ and the biasing current i is increased to the point where G_e vanishes, Eq. 2 becomes singular and a thermal runaway condition develops. Within the stable portion of its operating range, the responsivity of a bolometer can be easily adjusted by varying the biasing current i and the load resistance R_ℓ .

Referring to Eq. 2, the quantity $\omega = 2\pi f$ (sec⁻¹) is the angular frequency of the signal,

and the quantity τ (sec) is the thermal time constant of the bolometric element.

$$\tau = C/G \text{ sec} \quad (6)$$

The thermal capacity of the bolometric element is

$$C = \rho C_v A d \text{ joules/}^\circ\text{K}, \quad (7)$$

where ρ (gms/cm³) is the density of the conducting element, C_v (joules/gm[°]K) is its specific heat, A (cm²) is its area, and d (cm) is its thickness.

Referring to Eq. 1, we wish to point out that the current noise spectrum is the only one that is a function of frequency. This f^{-1} law was found experimentally to hold over a wide range of frequencies in carbon resistors³:

$$10^{-3} < f < 10^4. \quad (8)$$

But clearly an integration over this noise spectrum would yield a logarithmic singularity at the origin, so it must be conceded that the f^{-1} behavior does not apply at all frequencies. Nevertheless, over the region of practical interest it is likely that current noise could be reduced to a tolerable level by chopping.

Both Johnson and current noises are inversely proportional to the responsivity r . Since the responsivity is directly proportional to the thermal coefficient of resistance α (see Eq. 2), materials with sufficiently high coefficients α can be utilized to effectively eliminate all noise contributions other than thermal noise. Since thermal noise is proportional to the absolute temperature T , the motivation for working at cryogenic temperatures is clear.

It may be argued that fluctuations in signal or background radiation introduce problems that transcend considerations of the ultimate sensitivity of a detector. We readily concede that there may be situations in which the ultimate detector sensitivity may be an irrelevant issue. Nevertheless, we maintain that an accurate knowledge of the Wiener spectra of the radiation of interest should suggest signal-processing techniques (such as chopping or filtering) that substantially reduce such fluctuations to the point where the ultimate detector sensitivity remains a relevant issue. These considerations are considerably more specialized and are outside the scope of the present discussion.

2. Superconducting Bolometer

In normal metals the necessary conditions of high α and low operating temperature T are mutually exclusive. But the superconducting transition exhibits enormous values for α at transition temperatures that can be driven arbitrarily close to absolute zero by means of an external magnetic field. Suppose, for example, we were to approximate the superconducting transition by the following function:

(I. MICROWAVE SPECTROSCOPY)

$$\rho(T) = \rho_0 \left\{ 1 + \exp \left[\frac{2(T_c - T)}{\Delta T_c} \right] \right\}^{-1} \text{ ohm cm.} \quad (9)$$

This function is sketched in Fig. I-1. The transition temperature T_c ($^{\circ}\text{K}$) is defined by

$$\rho(T_c) = \rho_0/2, \quad (10)$$

where ρ_0 is the limiting resistivity at absolute zero in the corresponding normal state.

The width of the superconducting transition ΔT_c ($^{\circ}\text{K}$) is so defined that

$$\rho(T_c - \Delta T_c/2) = \frac{\rho_0}{1 + e} = 0.27\rho_0 \quad (11)$$

and

$$\rho(T_c + \Delta T_c/2) = \frac{\rho_0}{1 + e^{-1}} = 0.73\rho_0. \quad (12)$$

In this approximation, evaluation of $\alpha(T_c)$ from Eq. 4 yields

$$\alpha(T_c) = (\Delta T_c)^{-1} \text{ } (^{\circ}\text{K})^{-1}. \quad (13)$$

The transition width ΔT_c is a complex function of metallic purity, perfection of crystal structure, mechanical strain, bias current density, and applied magnetic field. In alloys

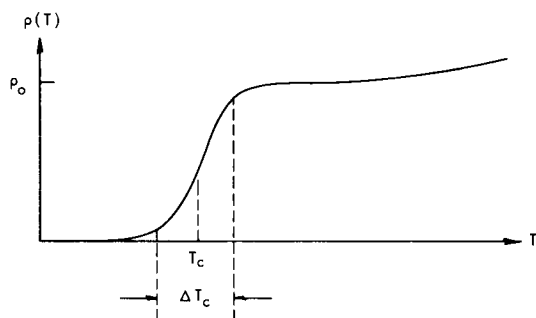


Fig. I-1. Temperature dependence of the resistivity of a superconductor. The quantity ρ_0 (ohm cm) is the limiting resistivity at absolute zero in the corresponding normal state.

ΔT_c may amount to several degrees Kelvin. On the other hand, ΔT_c has been measured in extremely pure, unstrained single crystals of tin at very low current densities.⁴ Values as low as 5×10^{-4} have been observed, and the authors remarked that even these finite widths may have been caused by small, mechanical strains existing in their samples.

In the approximation of Eq. 9, the corresponding coefficient of resistivity for the tin samples of de Haas and Voogd would amount to

$$\alpha(T_c) = 2 \times 10^3 \text{ } ^{\circ}\text{K}^{-1}. \quad (14)$$

But the values of α that have actually been observed in superconducting bolometers^{3, 5} are in the range $2\text{--}100^\circ\text{K}^{-1}$.

The effective suppression of Johnson noise in a superconducting bolometer by the enormous value for α inherent in the superconducting transition has been experimentally demonstrated by Andrews.⁶ With an observed $\alpha = 50^\circ\text{K}^{-1}$, the ratio of Johnson to thermal noise was found to be 0.12.

Probably the most sensitive superconducting bolometer that has been demonstrated is that of Martin and Bloor.⁵ The observed minimum detectable power was somewhat less than 10^{-12} watt in the far infrared within a bandpass of 10^{-1} sec^{-1} . The observed signal was one hundred times larger than that observed by means of a Golay cell. Martin and Bloor remark that their noise level was actually set by their amplifier and, in fact, their calculated value for the bolometer was 3.5×10^{-14} watt with a bandpass of 10^{-1} sec^{-1} . The extremely long thermal time constant (1.25 sec) of this bolometer, however, precludes its utility in many practical applications.

3. Thermal Boundary Resistance

Recent experiments on the propagation of heat between dissimilar solids⁷ at low temperatures have revealed that a temperature discontinuity develops at the interface which is proportional to the normal component of the thermal flux. The magnitude of the temperature discontinuity is proportional to the so-called "thermal boundary resistance" R^* ($^\circ\text{K cm}^2\text{ watts}^{-1}$) which is defined by

$$\dot{Q} = \frac{A\Delta T}{R^*} \text{ watts,} \quad (15)$$

where \dot{Q} is the rate of flow of thermal energy, A (cm^2) is the area of the interface, and ΔT ($^\circ\text{K}$) is the magnitude of the discontinuity developed at the interface.

Experiments on the thermal boundary resistance have resulted in an empirical relationship describing the temperature dependence of R^* .

$$R^* = \eta T^{-n} \text{ } ^\circ\text{K cm}^2\text{ watts}^{-1}. \quad (16)$$

The exponent n is dependent upon the nature of the interface, but it is usually very close to 3. The numerical factor η ($\text{cm}^2 \text{ } ^\circ\text{K}^{n+1}\text{ watts}^{-1}$) is also related to the nature of the interface and to the particular materials in contact. Typical values range between 0.3 and 30. The lower values are for intermetallic interfaces; the higher values are usually associated with metal-insulator interfaces.

Since the defining equation for thermal conductance G is

$$\dot{Q} = G\Delta T \text{ watts,} \quad (17)$$

(I. MICROWAVE SPECTROSCOPY)

upon comparing Eqs. 15 and 16, we have

$$G = A\eta^{-1}T^n \text{ watts } ^\circ\text{K}^{-1}. \quad (18)$$

4. Recent Experimental Developments

The thermal boundary resistance phenomenon has suggested a novel approach to the design of high-speed thermal detectors. A thin film ($\sim 1000 \text{ \AA}$) of a superconducting metal such as indium is evaporated directly upon a single-crystal substrate such as sapphire, which exhibits unusually high thermal conductivity at cryogenic temperatures. The thermal conductance between the film and substrate is sufficiently high to provide an extremely fast thermal response time. On the other hand, the sensitivity of the device in narrow-band applications is competitive with the best radiation detectors available,⁸ and is not limited to any particular portion of the electromagnetic spectrum.

Returning to the expression for the minimum detectable power (Eq. 1), let us assume that the thermal coefficient of resistance α is sufficiently high so that the thermal noise contribution dominates. Substitution of Eq. 18 in Eq. 1 yields

$$\sqrt{W_m^2} = \frac{2}{\epsilon} \left(\frac{AkT^{n+2}}{\eta} \right)^{1/2} (\Delta f)^{1/2}. \quad (19)$$

The thermal boundary resistance of an indium-sapphire interface has been measured by Neepner and Dillinger.⁷ Their experimental value is given by

$$R^* = 26T^{-2.8} \text{ } ^\circ\text{K cm}^2 \text{ watt}^{-1}. \quad (20)$$

The transition temperature⁹ of indium is 3.4°K . Assuming a perfectly absorbing surface (suitably blackened with $\epsilon = 1$), we evaluate the minimum detectable power of an indium-film bolometer with an effective area of $(0.25 \text{ mm})^2$, deposited upon a sapphire substrate, and connected to an amplifier with an effective bandwidth of 1 cps. Equation 19 yields

$$\sqrt{W_m^2} = 7 \times 10^{-13} \text{ watts (indium)}. \quad (21)$$

This value is approximately equal to that measured by Martin and Bloor⁵ for their tin bolometer.

Equation 19 indicates that considerable advantage is secured by low-temperature operation. Consider a zinc-film bolometer⁹ with a transition temperature of 0.92°K . Since no experimental thermal boundary resistance data are available for zinc-sapphire interfaces, we shall approximate the value with Eq. 20. The minimum detectable power for a zinc-film bolometer, evaluated under the same conditions as those for indium (Eq. 21), is

$$\sqrt{W_m^2} = 1.2 \times 10^{-14} \text{ watts (zinc).} \quad (22)$$

Thus, by lowering the temperature 2.5°K, nearly two orders of magnitude are gained in theoretical sensitivity.

The theoretical thermal time constants of these bolometers can be evaluated from Eqs. 6, 7, and 18. The low-temperature specific heat of a metal can be represented by

$$C_v = \beta T^3 + \frac{\gamma T}{W} \text{ joules gm}^{-1} \text{ } ^\circ\text{K}^{-1} \quad (23)$$

$$\beta = \frac{1941}{W\theta^3} \text{ joules gm}^{-1} \text{ } ^\circ\text{K}^{-4}, \quad (24)$$

where γ (joules mole⁻¹ °K⁻²) is the coefficient of the electronic specific heat, β represents the lattice contribution, W (gms mole⁻¹) is the molecular weight, and θ (°K) is the Debye temperature. Experimentally determined values of the constants β and γ have been tabulated in Rosenberg.¹⁰ The resulting expression for the thermal time constant of a superconducting film bolometer deposited upon an insulating crystal is given by

$$\tau = \rho \left(\beta T_c^3 + \frac{\gamma T_c}{W} \right) \eta d T_c^{-n} \text{ sec.} \quad (25)$$

Equation 25, evaluated for indium and zinc films, 1000 Å thick, deposited upon a sapphire substrate, yields

$$\begin{array}{ll} \tau = 35 \text{ n sec} & \tau = 22 \text{ n sec.} \\ \text{(indium)} & \text{(zinc)} \end{array} \quad (26)$$

These time constants indicate a degree of performance that greatly exceeds that of the more conventional thermal detectors.

J. M. Andrews, Jr.

References

1. R. J. von Gutfeld and A. H. Nethercot, Jr., Phys. Rev. Letters 12, 641 (1964).
2. J. M. Andrews, Jr. and M. W. P. Strandberg, Proc. IEEE (to be published April 1966).
3. R. A. Smith, F. E. Jones, and R. P. Chasmar, The Detection and Measurement of Infrared Radiation (Oxford University Press, 1957).
4. W. J. de Haas and J. Voogd, Commun. Phys. Lab. Univ. Leiden, No. 214c, 1931.
5. D. H. Martin and D. Bloor, Cryogenics 1, 1 (1961).
6. D. H. Andrews, Report of the International Conference on Low Temperatures, Cambridge, 1946; see also R. A. Smith, F. E. Jones, and R. P. Chasmar, op. cit., p. 275.
7. D. A. Neeper and J. R. Dillinger, Phys. Rev. 135, A1028 (1964).

(I. MICROWAVE SPECTROSCOPY)

8. J. A. Jamieson, R. H. McFee, G. N. Plass, R. H. Grube, and R. G. Richards, Infrared Physics and Engineering (McGraw-Hill Book Company, New York, 1963), p. 186.
9. E. A. Lynton, Superconductivity (Methuen, London, 2d edition, 1964), p. 5.
10. H. M. Rosenberg, Low Temperature Solid State Physics (Oxford University Press, 1963), p. 16.

B. FERMI SURFACES OF GALLIUM FROM SIZE EFFECT

The wave vectors corresponding to the cross section of the Fermi surfaces have been found for gallium single crystals whose normals are along the b and c axes (see Figs. I-2 and I-3). The experimental techniques used for these measurements were similar to those reported previously.¹

The signal obtained in these experiments has a complete line shape. The magnetic

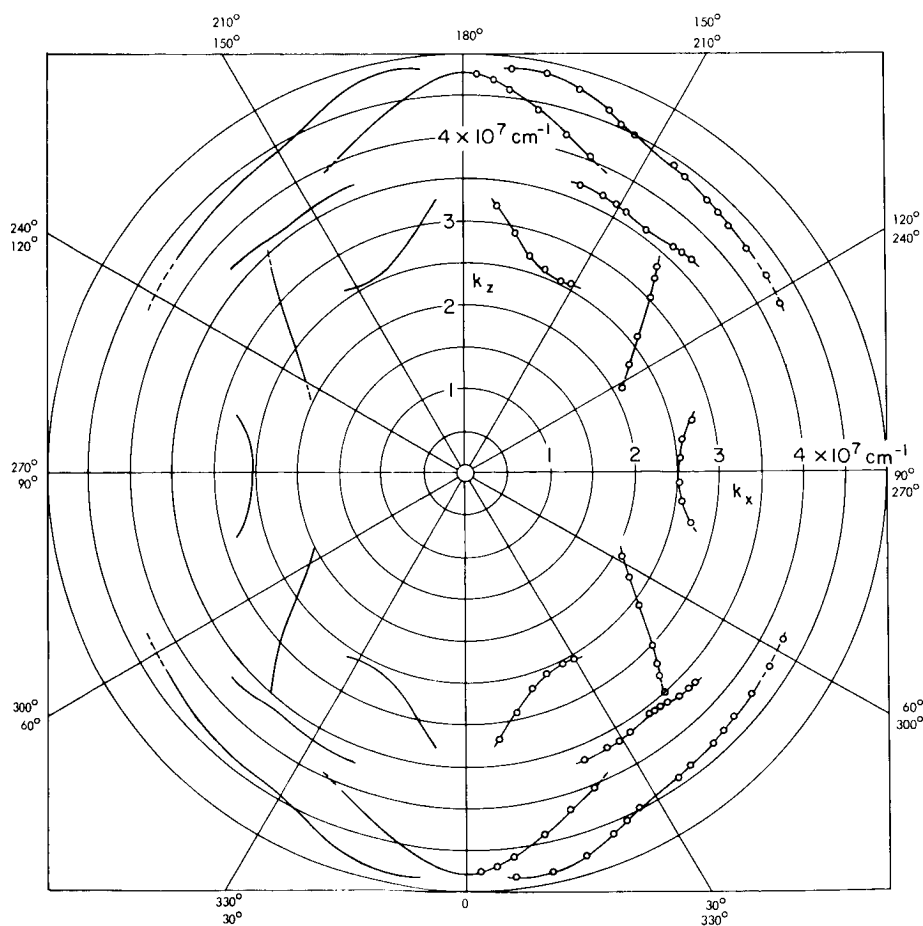


Fig. I-2. Wave vectors for b crystal.

(I. MICROWAVE SPECTROSCOPY)

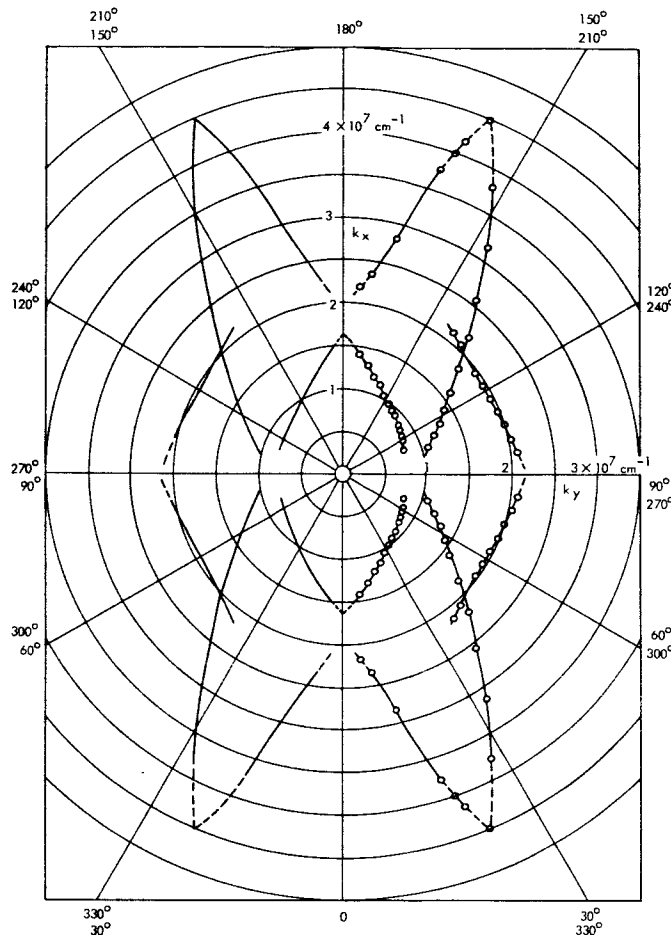


Fig. I-3. Wave vectors for c crystal.

field dependence of the signal as the radiofrequency changes was used to ascertain the portion of the curve for determining the external Fermi surface wave vector in terms of the magnetic field and the thickness of the sample. The portion of the line shape which had the smallest shift of magnetic field with frequency is identified in these curves as the orbit corresponding to the thickness of the sample. Although the line shape is not well understood, these data may be used with some confidence.

A. Fukumoto

References

1. A. Fukumoto, "Fermi Surfaces of Gallium Single Crystals by the Size Effect," Quarterly Progress Report No. 79, Research Laboratory of Electronics, October 15, 1965, pp. 14-16.

II. RADIO ASTRONOMY*

Academic and Research Staff

Prof. A. H. Barrett
Prof. B. F. Burke
Prof. M. Loewenthal

Prof. L. B. Lenoir
Prof. R. P. Rafuse
Prof. D. H. Staelin

Dr. S. H. Zisk
Patricia P. Crowther
E. R. Jensen

Graduate Students

R. J. Allen
N. E. Gaut
J. M. Moran, Jr.
G. D. Papadopolous

E. C. Reifenstein III
A. E. E. Rogers
D. H. Steinbrecker

K. D. Thompspn
A. Vander Vorst
Z. Vugrinec
T. L. Wilson

A. TEMPERATURE DEPENDENCE OF THE MICROWAVE EMISSIVITY OF NaCl SOLUTIONS

Satellite-borne microwave sensors designed to probe the atmosphere will have sea water as a background over two-thirds of the earth's surface. It is therefore important to know its microwave properties.

The emissivity of sea water depends upon a number of factors, notably wavelength, temperature, viewing angle, and salinity. Based on measurements of the complex dielectric constant of NaCl solutions by Collie, Hasted, and Ritson^{1,2} the temperature

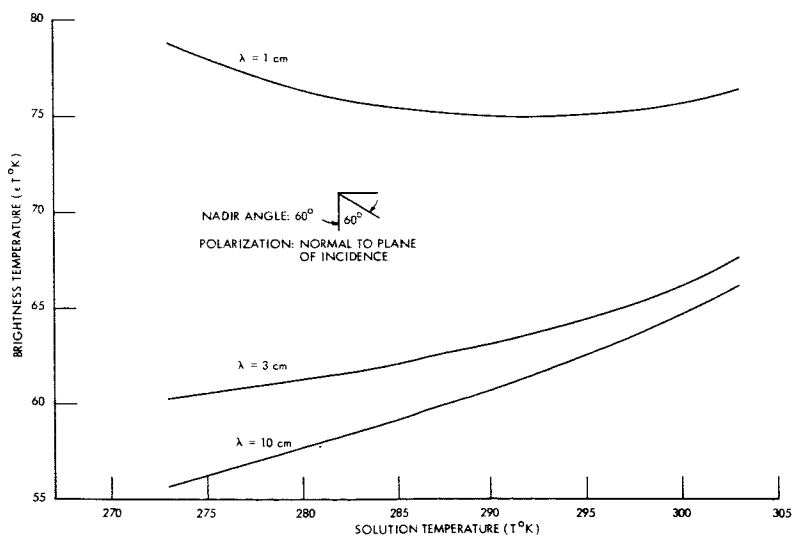


Fig. II-1. Microwave brightness temperature of salt water (0.66 m/l) as a function of thermometric temperature, viewed 60° from the surface normal with the observed \vec{E} parallel to the surface.

*This work was supported principally by the National Aeronautics and Space Administration (Grant NSG-419 and Contract NSR-22-009-120); and in part by Lincoln Laboratory Purchase Order No. 748.

(II. RADIO ASTRONOMY)

dependence of a 0.66 m/l NaCl solution has been calculated. A sample is shown in Fig. II-1 for 1-, 3-, and 10-cm wavelengths, with a viewing angle of 60° , and polarization normal to the plane of incidence. The important feature at smaller wavelengths is the partial compensation of increasing thermometric temperature by decreasing emissivity. This result will be helpful in reducing the uncertainty of determining the sea surface brightness temperature at these wavelengths.

N. E. Gaut

References

1. C. H. Collie, J. B. Hasted, and D. M. Ritson, Proc. Phys. Soc. (London) 60, 145-160 (1948).
2. J. B. Hasted, D. M. Ritson, and C. H. Collie, J. Chem. Phys. 16, 1 (1948).

B. MICROWAVE ABSORPTION MEASUREMENTS OF THE TERRESTRIAL ATMOSPHERE

Observations of sunlight extinction by the atmosphere at five frequencies around the 1.35-cm water-vapor spectral line are now in progress. The present data are being collected to provide information during winter meteorological conditions to supplement

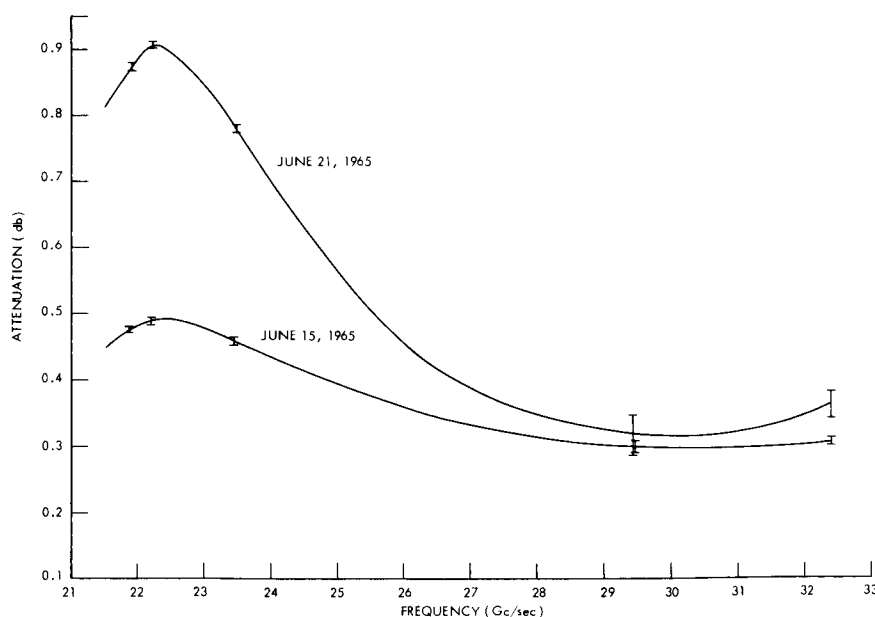


Fig. II-2. Zenith atmospheric attenuation near the water-vapor resonance at 22.235 Gc/sec (1.35-cm wavelength) observed on two days with quite different water-vapor distributions.

the data taken last summer. The ultimate goal of the program is to develop inversion techniques that will relate the microwave extinction spectrum to the total water vapor and its vertical distribution.

Thus far, 36 sunsets have been monitored from the 28-ft radio telescope at Lincoln Laboratory, M.I.T. Thirty-three of these observations have accompanying radiosonde information. The radiosondes have been launched either at the Reservoir Hill Launch Facility at Hanscom Field, or at M.I.T in Cambridge, for the most part within the periods of the sun observations.

Figure II-2 shows two extremes for the water-vapor spectral line obtained on the dates noted.

N. E. Gaut, D. H. Staelin

C. MEASUREMENTS OF CONTINUUM RADIATION FROM COSMIC RADIO SOURCES AT THE HAYSTACK RESEARCH FACILITY

The Haystack Research Facility has been described by H. G. Weiss, in Lincoln Laboratory Technical Report 365. A cursory description of the radiometric system was given in Quarterly Progress Report No. 78 (pages 27-35).

1. Absolute Flux Measurements

The antenna temperature $T_M(\theta', \phi')$ measured with an antenna of effective aperture $A(\theta-\theta', \phi-\phi')$, directed toward θ', ϕ' , is expressed by

$$T_M(\theta', \phi') = \frac{1}{\lambda^2} \int_{4\pi} A(\theta-\theta', \phi-\phi') T(\theta, \phi) d\Omega, \quad (1)$$

where λ is the wavelength of observation, and $T(\theta, \phi)$ expresses the brightness of the surroundings in direction θ, ϕ . If there is a source of radio emission contained within the solid angle Ω_S , one may write

$$T(\theta, \phi) = T_B(\theta, \phi) + T_S(\theta, \phi),$$

where $T_B(\theta, \phi)$ contains the "background" radiation, from the atmosphere, the ground, and so forth, and $T_S(\theta, \phi)$ represents the source. T_B extends over 4π steradians, while T_S is presumed to be zero outside of Ω_S . Rearranging (1), we have

$$\begin{aligned} T_A(\theta', \phi') &= T_M(\theta', \phi') - \frac{1}{\lambda^2} \int_{4\pi} A(\theta-\theta', \phi-\phi') T_B(\theta, \phi) d\Omega \\ &= \frac{1}{\lambda^2} \int_{\text{source } \Omega_S} T_S(\theta, \phi) A(\theta-\theta', \phi-\phi') d\Omega. \end{aligned} \quad (2)$$

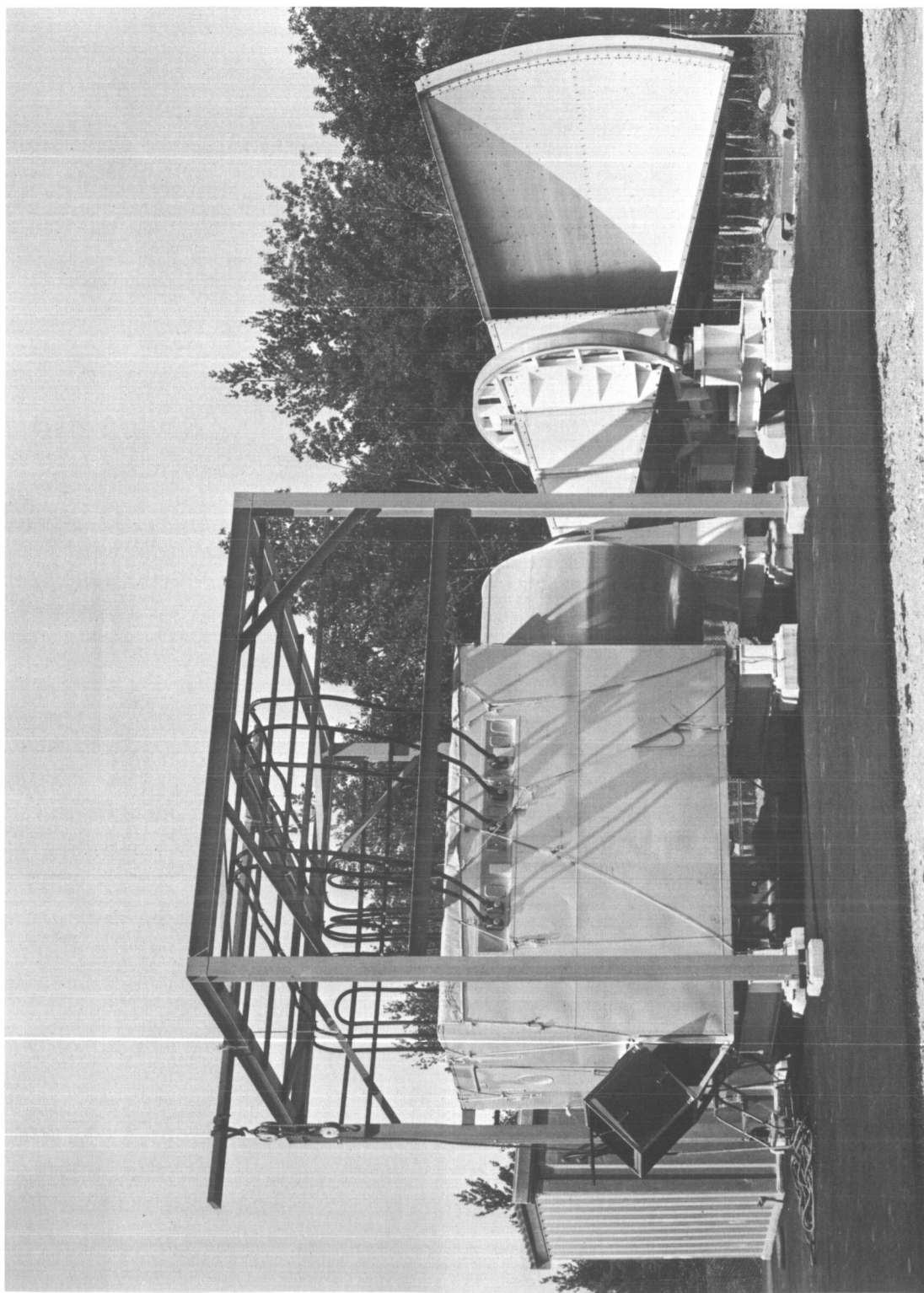


Fig. II-3. Radiometer instrument box connected to the cornucopia horn antenna.

(II. RADIO ASTRONOMY)

$T_A(\theta', \phi')$ is the measured antenna temperature after base-line subtraction. It is usual to express $A(\Omega) = \eta A_g f(\Omega)$, where η is the antenna efficiency, A_g is the geometric area of the aperture, $f(\Omega)$ is the antenna polar diagram, and $f(0) = 1$.

If the source distribution is contained within a solid angle much smaller than the antenna half-power beamwidth and the antenna is pointed directly at the source, then (2) evidently reduces to

$$T_A = \frac{1}{\lambda^2} \eta A_g \int_{\Omega_S} T_B(\Omega) d\Omega. \quad (3)$$

The total flux of a cosmic radio source received at the Earth's surface is given by

$$S_\nu = \frac{2k}{\lambda^2} \int_{\Omega_S} T_B(\Omega) d\Omega; \quad (4)$$

consequently,

$$S_\nu = \frac{2kT_A}{\eta A_g}. \quad (5)$$

A standard cornucopia horn antenna,¹ manufactured by Bell Telephone Laboratories, Inc., was procured for flux measurements at the Haystack facility. The

effective aperture area ηA_g has been measured on the antenna test range at Lincoln Laboratory, and the results agree well with the theoretical calculations.² The horn antenna is mounted as a transit instrument (movable in elevation along the local meridian) and may be directly connected to the radio-metric instrument box when it is removed from the 120-ft antenna. Figure II-3 shows the installation. This antenna was used for transit drift-scan observations of the strong radio sources in Cassiopeia and Taurus at 8.25 GHz during January 1966. Data from a single drift scan were recorded on punched paper tape, along with appropriate noise-tube calibrations, and subsequently were analyzed by

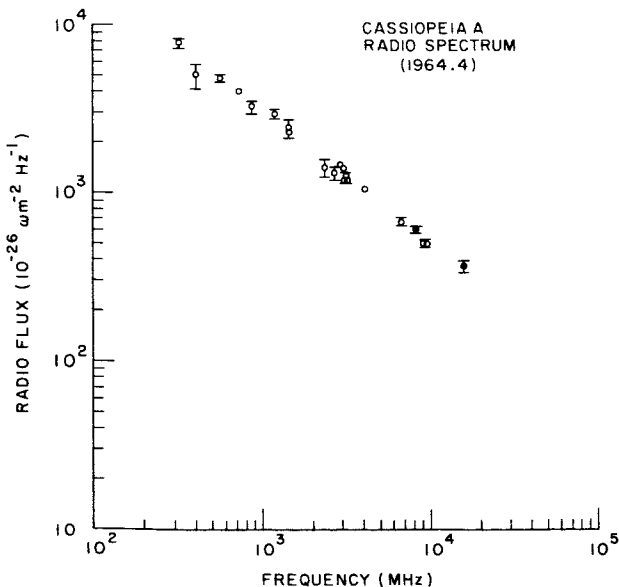


Fig. II-4. The radio spectrum of the strong source in Cassiopeia. ○ = other measurements. ● = present measurements.

(II. RADIO ASTRONOMY)

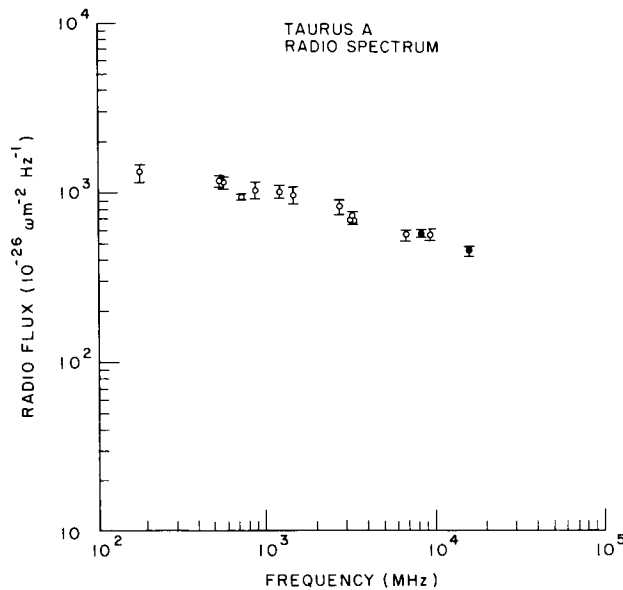


Fig. II-5. The radio spectrum of the strong source in Taurus. \circ = other measurements. \bullet = present measurements.

computers. Drift scans were taken at slightly different elevations on successive evenings, and the final antenna temperature was determined from the peak point of all observations. This was corrected for atmospheric extinction, equipment losses, and nonlinearity, and converted to a flux value by using Eq. 5. A complete description of the observational technique, the method of data reduction, and the measurement of the equipment effects will be given in a future progress report, together with the final numerical results. The result for the observations of Cas A is compared with the measurements of other observers in Fig. II-4. The antenna temperature measured on

Taurus must also be corrected for the linear polarization of the radiation. This quantity was measured with the 120-ft antenna by using a technique that is described below. The results for Taurus are compared with other work in Fig. II-5.

2. Observations with the 120-ft Paraboloid

In order to correctly interpret measurements of antenna temperature with the 120-ft antenna, it is, of course, necessary to know the characteristics of the antenna. The instrumental effects of radio-astronomical interest are the antenna efficiency and the instrumental polarization, and possible elevation dependences of these quantities.

a. Antenna Efficiency

When the cosmic radio source has an angular size of the same order of magnitude as the angular size of the antenna beam, Eq. 5 is not valid. One of two things may be done: The source may be modelled and a correction factor to the antenna temperature T_A may then be calculated or a contour map of $T_A(\theta', \phi')$ may be integrated. The former technique proceeds as follows: from Eq. 2, when the antenna is pointing directly at the source,

$$T_A = \frac{A_g}{\lambda^2} \int_{\Omega_S} f(\Omega) T_S(\Omega) d\Omega.$$

(II. RADIO ASTRONOMY)

One then models the source: $T_S(\Omega) = T_O g(\Omega)$, where $g(\Omega)$ is some function such that $g(0) = 1$. Hence, from Eq. 4,

$$S_\nu = \frac{2kT_O}{\lambda^2} \int_{\Omega_S} g(\Omega) d\Omega.$$

But,

$$2kT_A = \frac{\eta A_g}{\lambda^2} 2kT_O \int_{\Omega_S} f(\Omega) g(\Omega) d\Omega.$$

Consequently,

$$\eta = \frac{2kT_A}{S_\nu A_g} \frac{\int_{\Omega_S} g(\Omega) d\Omega}{\int_{\Omega_S} f(\Omega) g(\Omega) d\Omega}. \quad (6)$$

For future reference, we define

$$S = \int_{\Omega_S} g(\Omega) d\Omega$$

and

$$M = \int_{\Omega_S} f(\Omega) g(\Omega) d\Omega.$$

If the antenna pattern is known, then η is defined when the source model is specified.

On the other hand, the second method, or integration technique, proceeds as follows: From Eq. 2, if $T_A(\theta', \phi')$ is known over some region $\Omega_m > \Omega_S$, then upon integrating $T_A(\theta', \phi')$ over this region, we have

$$\int_{\Omega_m} T_A(\Omega') d\Omega' = \frac{1}{\lambda^2} \int_{\Omega_m} \int_{\Omega_S} A(\Omega - \Omega') T_B(\Omega) d\Omega d\Omega'. \quad (7)$$

But

$$\int_{\Omega_m} A(\Omega) d\Omega = \eta A_g \int_{\Omega_m} f(\Omega) d\Omega.$$

Let us define $\Omega_B = \int_{\Omega_m} f(\Omega) d\Omega$. Equation 7 then reduces to

(II. RADIO ASTRONOMY)

$$2k \int_{\Omega_m} T_A(\Omega') d\Omega' = \frac{2k}{\lambda^2} \int_{\Omega_S} T_B(\Omega) d\Omega \eta_A \Omega_B = S_\nu \eta_A \Omega_B;$$

consequently,

$$\eta = \frac{2k \int_{\Omega_S} T_A(\Omega') d\Omega'}{S_\nu \Omega_B} . \quad (8)$$

The advantages of the second technique are that it is independent of models of the radio source, and only the integral over part of the antenna polar diagram is required.

The first technique has been applied to calculate the antenna efficiency of the 120-ft paraboloid by using the values of radio flux measured with the cornucopia horn at 8.25 GHz.

Results from Cas A

The following model is suggested by high-resolution interferometer studies³: A ring of emission of diameter $W = 4.0$ ft and thickness $d \ll W$. The antenna beam is modelled as a circularly symmetric Gaussian with full width at half-power of 4.2 ft. The last assumption is supported by observations of the weak point source 3C273. These assumptions yield $S/M = 1.82$, and antenna efficiency $\eta = 0.31 \pm 0.02$ at 40° elevation.

Results from Tau A

The Taurus model⁴ is a two-dimensional Gaussian, 4.2 ft \times 2.6 ft; the flux is polarized 8% at 147° as will be described subsequently. This yields $S/M = 1.63$, and antenna efficiency $\eta = 0.29 \pm 0.02$ at 40° elevation.

The close agreement is probably deceptive; the results are very dependent on the source model parameters. Besides the fact that few observers agree on a satisfactory model, it is known that the structure of a source generally depends somewhat on frequency, so that models based on low-frequency observations are hazardous. Plans have been made to apply the second method for a more reliable estimation of η .

Measurements of 2% precision have been made of the elevation dependence of the antenna efficiency. Results of observations of peak antenna temperature made on a number of strong sources are compiled in Fig. II-6. No azimuth dependence of the antenna efficiency $>0.01\%$ has been noticed. The measurements on each source are corrected for atmospheric extinction and normalized to 40° elevation. The ordinate of Fig. II-6 may be identified with the antenna efficiency relative to 40° elevation. The general shape of the curve is understandable as sag of the subreflector at the prime focus, and a slight movement of the instrument box as the antenna is raised in elevation, both effects tending to alter the focal length of the antenna.

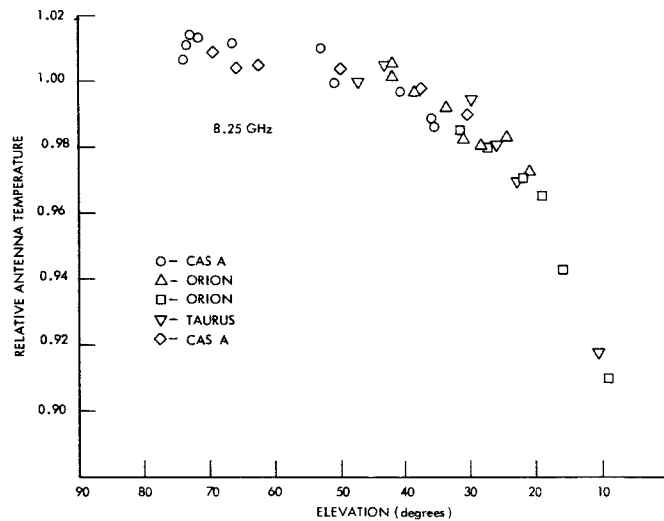


Fig. II-6. Relative antenna temperature versus elevation for a number of sources normalized to 1 at 40° elevation.

b. Instrumental Polarization

Measurements of the linear polarization of the radiation from cosmic sources is usually made by rotating a linearly polarized feed horn of the antenna, and determining the constants in the equation

$$T(A) = T_A (1 + p \cos 2(A - \phi)), \quad (9)$$

where

T_A = average antenna temperature

p = fractional linear polarization of the source

A = parallactic angle of feed (position angle of E on the celestial sphere)

ϕ = parallactic position angle of the polarized component of the radiation from the source.

Unfortunately, such measurements are usually contaminated by two effects: baseline shift caused by rotating antenna sidelobes picking up the partially polarized radiation from the earth, and an apparent dependence of the antenna efficiency with feed angle. The first problem can be overcome by suitable choice of observing techniques; the second can be measured by observations on a cosmic source of unpolarized radio emission. After many attempts, we conclude that the following observing technique allows unambiguous separation of these two effects; it consists essentially of always using the 120-ft antenna as if it were polar mounted. Although such a technique is hardly new in

(II. RADIO ASTRONOMY)

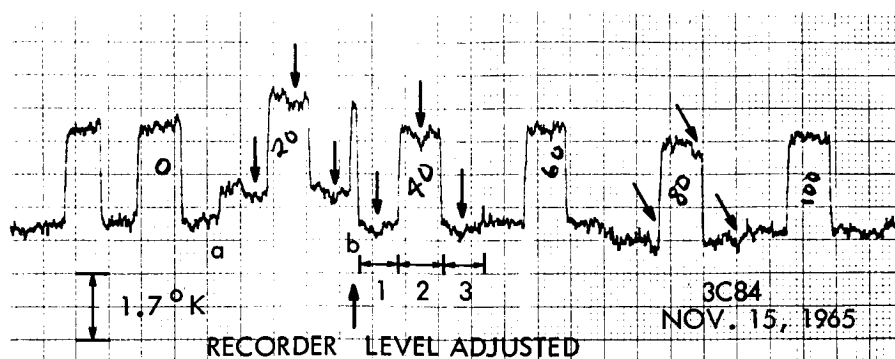


Fig. II-7. Example of the effects of varying radome space frame aperture blockage on the measurements of a weak source.

radio astronomy, it seems especially useful for antennas in radomes. Data taken when the antenna is tracking a source is corrected by subtracting data taken while the antenna is tracking the sky over exactly the same place on the radome. The usefulness of the technique is quite clear from Fig. II-7. In region 1, the sky is tracked at the sidereal rate a few half-power beamwidths ahead of the source. One then waits until the position of the earth brings the source into the same place on the radome, and then the source is tracked. In region 3, a measurement (again over exactly the same range of azimuth and elevation) is taken after the source has moved away. All three observations are made at the same feed angle, designated "40" on the chart. The arrows indicate features about 4 times the r.m.s. noise that seems to appear at the same azimuth and elevation each time, thereby suggesting a varying amount of aperture blockage attributable to the radome struts. Figure II-7 also shows the base-line change as the feed is rotated. As point a, the feed was rotated from "0" (0°) to "20" (36°). Note the change in base line. At b, the rotation from "20" to "40" (72°) would have put the observation off the chart, and the recorder level was readjusted.

The apparent dependence of antenna efficiency with feed angle was investigated by making observations of the type just described as a series of different feed angles on the strong unpolarized sources Cas A and Orion A: A compendium of data indicates that the parameters of Eq. 9 (where A is now the feed angle in "az-el" coordinates) are $100p = 1.05 \pm 0.2$, $\phi = 146 \pm 3^\circ$ measured eastward from north on the celestial sphere. There is some indication of a very small variation of these quantities with elevation and, perhaps, azimuth, the origin of which is not yet fully understood. Further observations are planned.

c. Observations of Other Cosmic Sources

Now that we are beginning to understand the instrumental effects, the original task of observing the flux and polarization properties of radio sources is being taken

(II. RADIO ASTRONOMY)

up again. The strong radio source in Taurus and a weak source in Perseus were the first candidates, and the results at 8.25 GHz are tabulated in Table II-1. Angular size

Table II-1. Results of observations.

	Peak Antenna Temperature	Polarization (%)	Position Angle	Angular Size (α)	δ	Radio Flux
Taurus A (3C144)	$37.65 \pm 0.03^\circ\text{K}$	8.0 ± 0.4	$147 \pm 4^\circ$	2.8'	2.5'	567 ± 50
Perseus A (3C84)	$2.51 \pm 0.01^\circ\text{K}$	<0.3	—	$<30''$	1.3'	18 ± 3

is measured in minutes of arc. The units of radio flux are 10^{-26} watt m^{-2} Hz^{-1} .

The results for Taurus are in good agreement with the work of other observers, especially the observations of Gardner⁵ at 6 cm, using an antenna having nearly the same half-power beamwidth as the Haystack antenna.

The radio source Perseus A has been identified with the peculiar galaxy⁶ NGC 1275, and is observed to have a curious spectrum of positive spectral index⁷ above 3 GHz. The present measurement confirms this, and we may add, first, that the radiation is essentially unpolarized, second, the source is less than 30 seconds of arc in right ascension and has a width of approximately 1.3' in declination. The last results have not been reported before, and are important to the models of the physical processes responsible for the radiation.

R. J. Allen, A. H. Barrett

References

1. R. W. Friis and A. S. May, AIEEE Trans. Part 1, Vol. 77, p. 97, 1958.
2. A. Sotiropoulos and J. Ruze, "Haystack Calibration Antenna," Technical Report 367, Lincoln Laboratory, M.I.T., December 1964.
3. M. Ryle, B. Elsmore, and A. Neville, Nature 205, 1259 (1965).
4. J. W. Baars, P. G. Mezger, and H. Wendker, Astrophys. J. 142, 122 (1965).
5. F. F. Gardner, Australian J. Phys. 18, 385 (1965).
6. W. A. Dent and F. T. Haddock, Quasi-Stellar Sources and Gravitational Collapse (University of Chicago Press, Chicago, Ill., 1965), chapter 29.
7. W. A. Dent and F. T. Haddock, Nature 205, 487 (1965).

D. OBSERVATIONS OF THE MOON

Radiometric observations¹ of the moon were made during the summer of 1964 with the 28-ft paraboloid antenna at Lincoln Laboratory. The first series of observations

(II. RADIO ASTRONOMY)

was conducted between June 15th and August 15th, 1964, using a five-channel Dicke radiometer.² The channels were centered at 32.4, 29.5, 25.5, 23.5, and 21.9 GHz. A total of 340 drift scans of the moon was taken on 15 different days. Typical shift scans through the center of the moon are shown in Fig. II-8.

Because of the moon's rotation, the temperature of every point on its surface can be expressed as a Fourier series with a fundamental period of 29.53 days. The brightness temperature is usually modelled as

$$T_B(\theta, \ell, f, t) = T_{B_0} + \cos^{1/4} \ell \sum_n T_{B_n}(f) \cos(n\omega t - n\theta - \psi_n(f)),$$

where θ and ℓ are the selenographic longitude and latitude, and f is the frequency of observation. The quantity measured by the antenna is the antenna temperature, which is the convolution of the antenna pattern with the source brightness temperature. The antenna smoothing was not severe, since the half-power beamwidth is 5.0 minutes of arc at 32.4 GHz, while the diameter of the moon is approximately 30 minutes of arc.

The Fourier components T_{B_n} and ψ_n were deduced from the shapes of the drift scans taken through the center of the moon over two lunar periods. This method is more

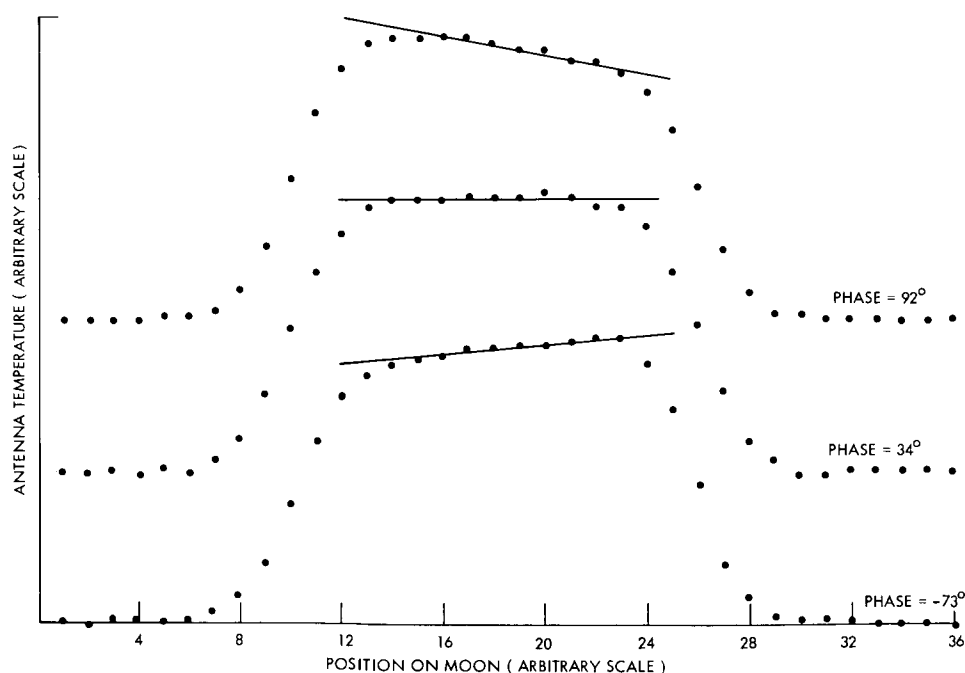


Fig. II-8. Average of three drift scans taken on three different days. Phase angle is measured from full moon. Amplitudes have been scaled to give center temperature of 217°K.

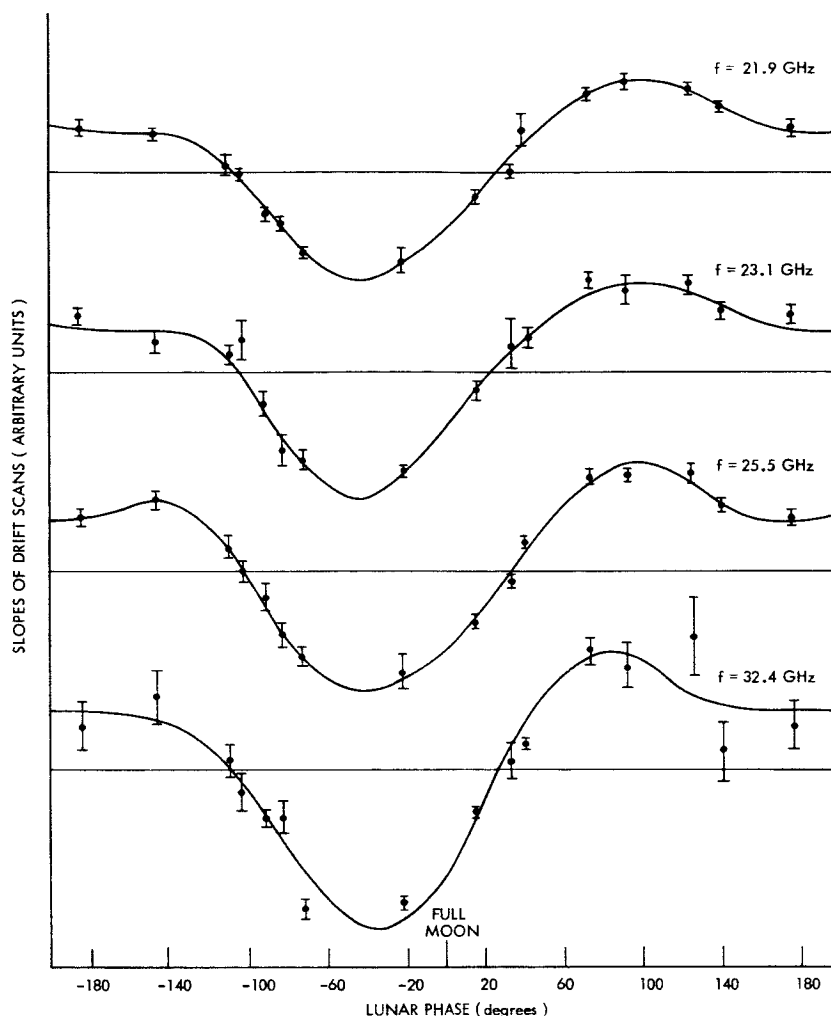


Fig. II-9. Slopes of central region of drift scans vs phase. Curves are two harmonic Fourier series. Notice that the second harmonic of the slope, which is proportional to the second harmonic of the brightness temperature, is necessary for a good fit of the data.

accurate than the customary technique of analyzing the magnitudes of the drift scans. The center temperatures of all scans were normalized to 217°K and the 9 central data points of each were fitted with a straight line using a minimum-square-error criterion as shown in Fig. II-8. Figure II-9 shows the slopes for 4 of the channels as functions of the lunar phase. These slope functions were Fourier analyzed. The Fourier coefficients obtained are proportional to the Fourier coefficients of the brightness distribution. The values obtained for T_{B1} , T_{B2} , ψ_1 , and ψ_2 are listed in Table II-2. These values are essentially independent of the lunar model used. This is the lowest frequency at which the second harmonic has been measured.

(II. RADIO ASTRONOMY)

The first-harmonic amplitude yields the value

$$\sqrt{\frac{ps}{K}} \frac{\epsilon}{\sigma} = 6900$$

at 32.4 GHz. Here, p, s, and K are the density, specific heat, and thermal conductivity in cgs units, ϵ is the dielectric constant and σ is the conductivity in mhos per meter.

Table II-2. Measured values of Fourier coefficients of the Moon's brightness temperature.

Frequency (GHz)	T_{B_0} (°K) (assumed)	T_{B_1} (°K)	ψ_1 (°)	T_{B_2} (°K)	ψ_2 (°)	T_{B_3} (°K)
21.9	217	21 ± 2	41 ± 5	5 ± 1	38 ± 5	<1
23.5	217	22	48	6	31	<1
25.5	217	25	42	6	40	<1
32.4	217	29	41	8	38	<1

This assumes a homogeneous surface with parameters independent of temperature. The thermal inertia, $(Kps)^{1/2}$, has been found from lunar infrared observations to be 0.001 (CGS) which is characteristic of material having very low density and thermal conductivity. Taking $p = .2$ grams/cm³, $K = 2.5 \times 10^{-6}$ cal sec⁻¹ cm⁻¹ °K⁻¹, $s = .2$, and $\epsilon = 1.5$ it follows that $\sigma = .05$ mhoes/meter. This is consistent with very dry sand. The second harmonic data does not give a clear distinction between the homogeneous and stratified surface models.

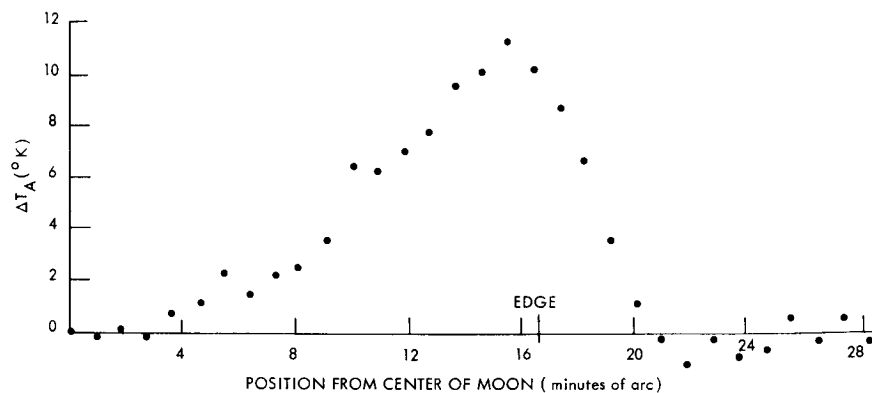


Fig. II-10. Horizontal minus vertical polarization antenna temperature obtained August 4, 1964. Central temperatures have been scaled to 217°K.

(II. RADIO ASTRONOMY)

The other set of observations was conducted at 35 GHz using the Lincoln Laboratory radiometer on the same 28-foot antenna. Drift scans were taken through the center of the moon near transit with polarization alternately parallel and perpendicular to the plane of incidence on successive scans. The antenna temperatures recorded with orthogonal polarizations differ because the emissivity of the surface depends on the polarization of the radiation as well as the angle of incidence. Figure II-10 shows the average difference between three pairs of scans.

Models for the lunar surface were generated on the computer by assuming that it

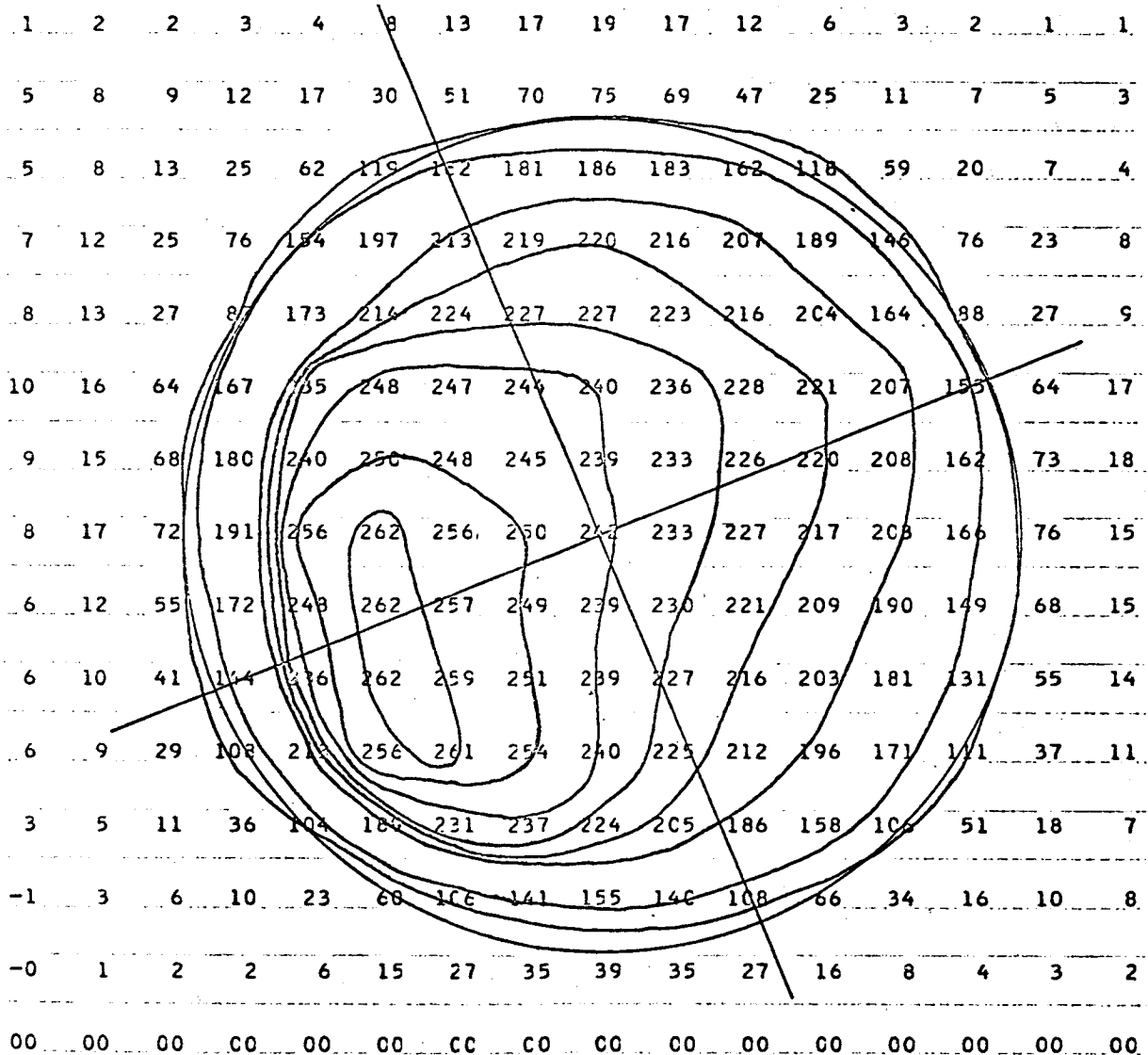


Fig. II-11. Antenna temperature distribution obtained on November 27, 1964. Grid spacing, 2.69 minutes of arc; lunar phase, 100°; frequency, 35.0 GHz; antenna beamwidth, 4.4 minutes of arc.

(II. RADIO ASTRONOMY)

consists of randomly oriented smooth facets whose normals are gaussianly distributed about the local normal. The expectation of the Fresnel reflection coefficients for each point on the moon were computed. If σ is the angular deviation of the facets and ϵ is the dielectric constant, then the data in Fig. II-10 are consistent with the following parameters:

σ	ϵ
0°	$1.5 \pm .1$
15°	1.7
30°	2.3

These results do not conflict with the value of 2.8 for the dielectric constant obtained from the radar experiments at 68-cm wavelength since the radar reflection may come largely from the denser substratum.

Many drift scans were taken over the entire lunar disk with both radiometer systems in order to map the temperature distribution at various phases. Figure II-11 shows a map made from 10 scans at 35.0 Kmc/s spaced at 3 minutes of arc intervals. It was made eight days after full moon while the left half of the disk was still sunlit.

We are indebted to Mr. J. Freedman and Dr. J. Cogdell for making available the facilities at Lincoln Laboratory.

J. M. Moran, A. H. Barrett, D. H. Staelin

References

1. J. M. Moran, "Radiometric Observations of the Moon near One-Centimeter Wavelength," S.M. Thesis, Department of Electrical Engineering, M.I.T., 1965.
2. D. H. Staelin, "Microwave Spectrum of Venus," Sc.D. Thesis, Department of Electrical Engineering, M.I.T., 1965.

III. OPTICAL AND INFRARED SPECTROSCOPY*

Academic and Research Staff

Prof. C. H. Perry

Graduate Students

Jeanne H. Fertel

J. F. Parrish

E. F. Young

A. FAR INFRARED SPECTRA OF TETRAHALO, TETRAAMMINE, AND DIHALODIAMMINE COMPLEXES OF PALLADIUM

1. Introduction

Recently, a number of far infrared studies of platinum halide complexes have been reported.¹⁻⁵ The majority of the compounds studied were alkali salts of the halide complexes of platinum (II). Thus far, the infrared investigation of the corresponding palladium complexes has covered only the spectral range $4000\text{-}250\text{ cm}^{-1}$.⁶⁻⁸ In this region the only skeletal vibrations observed are the Pd-N and Pd-Cl antisymmetric and symmetric stretching vibrations.

2. Discussion

The infrared spectra of a number of square planar palladium (II) complexes of the type M_2PdX_4 , PdL_4X_2 , and trans and cis isomers of PdL_2X_2 (where $M = NH_4^+$, K^+ , Rb^+ or Cs^+ ; $L = NH_3$; $X = Cl^-$, Br^- or I^-) have been recorded from 4000 to 40 cm^{-1} with the use of instrumentation described previously.⁹ The compounds were examined both at room temperature and at liquid-nitrogen temperature.

The investigation of four tetrachloropalladium (II) complexes gave Pd-Cl stretching vibrations in the range $327\text{-}336\text{ cm}^{-1}$, Pd-Cl in-plane bending vibrations in the range $183\text{-}205\text{ cm}^{-1}$, and Pd-Cl out-of-plane bending vibrations from 160 to 175 cm^{-1} . Four similar bromo complexes gave the corresponding Pd-Br vibrations in the ranges $249\text{-}260\text{ cm}^{-1}$, $130\text{-}169\text{ cm}^{-1}$, and $114\text{-}140\text{ cm}^{-1}$, respectively. The Pd-N in- and out-of-phase bending vibrations of the tetraammine complexes were found in the ranges $245\text{-}273\text{ cm}^{-1}$ and $160\text{-}190\text{ cm}^{-1}$, respectively. In the M_2PdCl_4 and M_2PdBr_4 compounds, the two bands of lowest frequency correspond to the lattice vibrations, and these assignments are confirmed by the decrease in these frequencies for the compounds in the order $NH_4^+ > K^+ > Rb^+ > Cs^+$ which is expected as the atomic (or molecular) weight of the cation increases.

*This work was supported by the Joint Services Electronics Programs (U. S. Army, U. S. Navy, and U. S. Air Force) under Contract DA 36-039-AMC-03200(E).

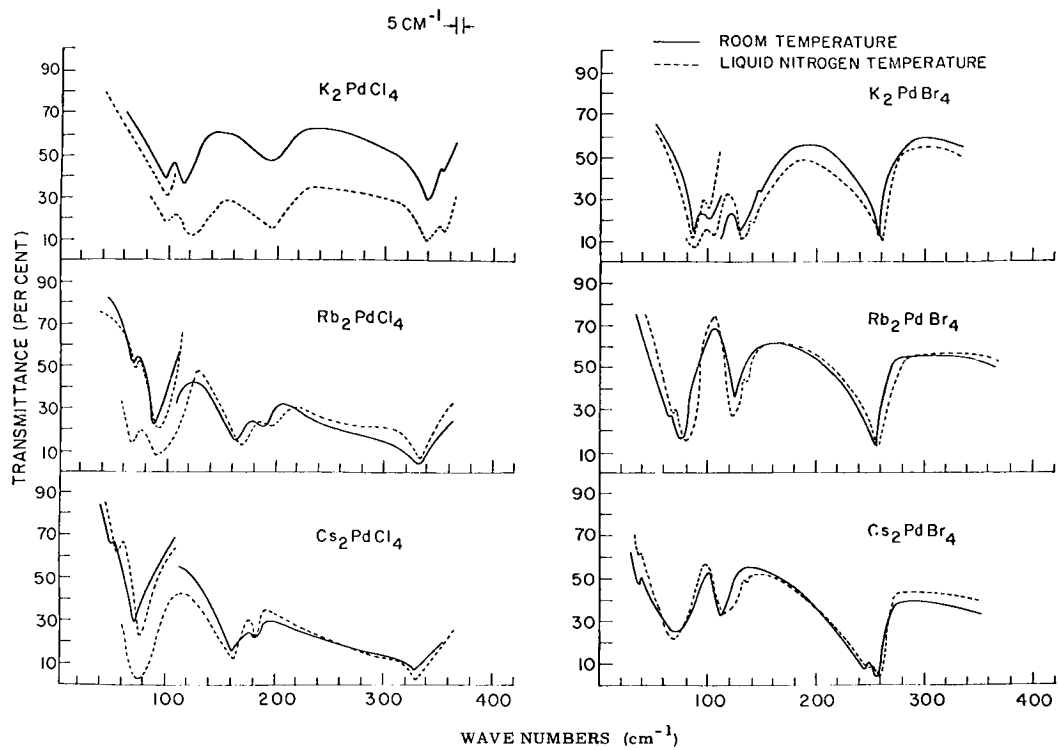


Fig. III-1. Far infrared spectra of some Tetrahalopalladium (II) Salts.

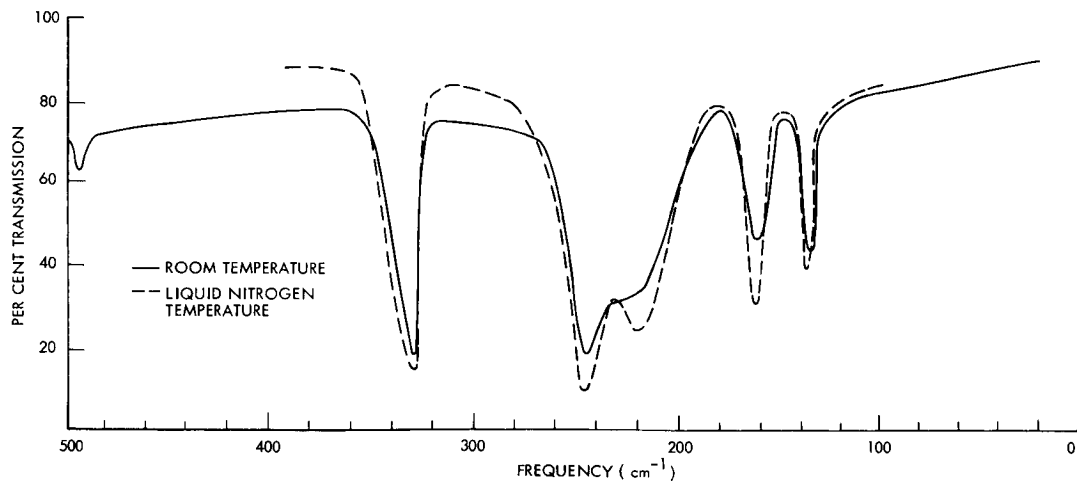


Fig. III-2. Far infrared spectrum of Trans $\text{Pd}(\text{NH}_3)_2\text{Cl}_2$. Solid line: room temperature; dotted line, liquid-nitrogen temperature.

Table III-1. Internal and lattice vibrations of M_2PdX_4 complexes.

$(NH_4)_2PdCl_4$	K_2PdCl_4	Rb_2PdCl_4	Cs_2PdCl_4	$(NH_4)_2PdBr_4$	K_2PdBr_4	Rb_2PdBr_4	Cs_2PdBr_4	Assignment
3182s				3170s				NH_4^+ stretching
3038s				3020s				NH_4^+ stretching
2812w				2796w				$2 \times 1398 = 2796$
1649m				1624m				NH_4^+ antisymmetric deformation
1398s				1398s				NH_4^+ symmetric deformation
340sh	356sh			363m				combination
							255sh	
327s	336s	331s	328s	254s	260s	258s	249s	ν_6 Pd-X stretching
205sbroad	193m	188m	183m	169sbroad	140sh	135sh	130sh	ν_7 in-plane bending
175s	n. o.	166m	160m	140sh	130s	125m	114m	ν_2 out-of-plane bending
120s	110s	88s	75s	n. o.	100s	76s	67m	A_{2u} lattice mode
n. o.	95s	70sh	50sh	97s	85s	65sh	38sh	E_u lattice mode

Abbreviations: m = medium, s = strong, w = weak, sh = shoulder, n. o. = not observed.

Table III-2. Infrared frequencies of $\text{Pd}(\text{NH}_3)_4\text{X}_2$ complexes.

$\text{Pd}(\text{NH}_3)_4\text{Cl}_2$	$\text{Pd}(\text{NH}_3)_4\text{Br}_2$	Assignment
3230s	3240s	NH_3 stretching
3140s	3147s	NH_3 stretching
2618w		$2 \times 1301 = 2602?$
2365w	2373w	?
2130w	2130w	$1301 + 830 = 2131$
2065w	2064w	?
1608s	1618s	NH_3 antisymmetric deformation
1320sh	1319sh	NH_3 rocking + Pd-N stretching
1301s	1301s	NH_3 symmetric deformation
1285sh	1284sh	?
1278sh	1277sh	?
830s	825s	NH_3 rocking
	515	?
505sh	501sh	?
500sh	495sh	?
494m	490m	Pd-N stretching
476w	471w	$2 \times 245 = 490$
330vw		?
245m	273m	in-plane bending
160w	190w	out-of-plane bending
115m	n. o.	lattice modes

Abbreviations: m = medium, s = strong, w = weak, sh = shoulder, n. o. = not observed.

Table III-3. Infrared frequencies of trans and cis isomers of $\text{Pd}(\text{NH}_3)_2\text{X}_2$.

<u>trans</u> $\text{Pd}(\text{NH}_3)_2\text{Cl}_2$	<u>trans</u> $\text{Pd}(\text{ND}_3)_2\text{Cl}_2$	<u>cis</u> $\text{Pd}(\text{NH}_3)_2\text{Cl}_2$	<u>trans</u> $\text{Pd}(\text{NH}_3)_2\text{Br}_2$	<u>cis</u> $\text{Pd}(\text{NH}_3)_2\text{Br}_2$	<u>trans</u> $\text{Pd}(\text{NH}_3)_2\text{I}_2$	Assignments
3320s	2479s	3314s	3307s	3307s	3296m	NH_3 stretching
3240m	2352m	3237s	3233m	3234s	3223m	NH_3 stretching
3181sh	2328m	3177sh	3171sh	3169sh	3152sh	NH_3 stretching
1605m	1183m	1610m	1598m	1601m	1594m	NH_3 antisymmetric deformation
	1148sh					$2 \times 579 = 1158$
	1116sh					?
1255sh	1051m	1269sh	1251sh	1263m	1256sh	NH_3 rocking + Pd-N antisymmetric stretching
1247s	974s	1248s	1245s	1245m	1242s	NH_3 symmetric deformation
				774sh		?
753m	579m	752s	753m	741m	n. o.	NH_3 rocking
496w	461w	495w	490w	480w	480w	Pd-N antisymmetric stretching
		476w		460w		Pd-N symmetric stretching
333s	329s	327s	n. o.	258w	191s	Pd-X antisymmetric stretching
		306s		n. o.		Pd-X symmetric stretching
245s	218vs	245s	220s	225s	263w	Pd-N bending
222s	194vs	218s	220s	225s	218s	Pd-N bending
				190m		?
				177m		?
162m	161m	160m	122m	120m	109m	Pd-X bending
137m	134m	135m	101m	100w	n. o.	Pd-X bending
	109vw	109w				lattice mode

Abbreviations used: m = medium, s = strong, w = weak, v = very, sh = shoulder, n. o. = not observed.

(III. OPTICAL AND INFRARED SPECTROSCOPY)

Weak shoulders are observed in some of the compounds and have been assigned as combinations of infrared and Raman active modes in the corresponding platinum complexes.¹ These bands in the palladium complexes cannot be uniquely assigned, however, as the Raman spectra have not been obtained, owing to their intense colors.

By using the assignments for the tetrahalo and tetraammine complexes, as well as the isotopic shift data, assignments for the fundamental modes for a series of *cis* and *trans* dihalodiammine complexes of palladium (II) are given. The results are summarized in Tables III-1, III-2, and III-3, and the far infrared spectra of some tetrahalopalladium (II) salts are shown in Fig. III-1. Figure III-2 shows the far infrared spectrum of *trans* Pd(NH₃)₂Cl₂. The interpretation of the data and discussion of the results in more detail are contained in a paper submitted to *Spectrochimica Acta* as Part III in a series on palladium complexes.^{6, 10}

We would like to express our thanks to Professor J. R. Durig and Mr. B. R. Mitchell, of the Chemistry Department, University of South Carolina, for some of the samples and cooperation in this research. All computation work connected with the Fourier transforms were performed on the IBM 7094 computer at the Computation Center, M. I. T. We would like to thank Dr. H. J. Sloane, Beckman Instruments, Fullerton, California, for the spectra of some of the alkali salts of palladium halide complexes taken on the Model IR-11 spectrophotometer and for checking our results at room temperature.

C. H. Perry, D. P. Athans, E. F. Young

[Mr. D. P. Athans is now in the Department of Mechanical Engineering, University of Southern California, Los Angeles, California.]

References

1. J. H. Fertel and C. H. Perry, *J. Phys. Chem. Solids* **26**, 1773 (1965).
2. D. M. Adams and H. A. Gebbie, *Spectrochim. Acta* **19**, 925 (1963).
3. H. Poulet, P. Delorme, and J. P. Mathieu, *Spectrochim. Acta* **20**, 1855 (1964).
4. A. Sabatini, L. Sacconi, and V. Scheltino, *Inorg. Chem.* **3**, 1775 (1964).
5. R. A. Walton, *Spectrochim. Acta* **21**, 1795 (1965).
6. J. R. Durig, R. Layton, D. W. Sink, and B. R. Mitchell, *Spectrochim. Acta* **21**, 1367 (1965).
7. S. Mizushima, I. Nakagawa, M. J. Schmely, C. Cuirraw, and J. V. Quagliano, *Spectrochim. Acta* **13**, 31 (1958).
8. D. M. Adams, J. Chatt, J. Gerratt, and A. D. Westland, *J. Chem. Soc.*, p. 734, 1964.
9. C. H. Perry, Quarterly Progress Report No. 70, Research Laboratory of Electronics, M. I. T., July 15, 1963, pp. 19-31; R. Geick, C. H. Perry, E. C. Reifenshtein III, H. D. Wactlar, and E. F. Young, Quarterly Progress Report No. 76, January 15, 1965, pp. 27-38.
10. J. R. Durig, B. R. Mitchell, D. W. Sink, and A. S. Wilson (to appear in *Spectrochim. Acta*, Vol. 22, 1966).

(III. OPTICAL AND INFRARED SPECTROSCOPY)

B. FAR INFRARED SPECTRA OF METAL CLUSTER COMPOUNDS

Recent crystallographic studies have revealed the existence of a surprisingly large number of inorganic compounds containing discrete, well-defined metal-metal bonds, and these compounds have recently been reviewed.¹ Great interest has been expressed by inorganic and theoretical chemists in the properties of these metal-metal bonds, but there is very little experimental data available. Since most of these compounds are intensely colored, Raman data will be scarce for some time, and any vibrational data must be obtained by far infrared spectroscopy.

The octahedral metal-atom cluster compounds were chosen for study mainly due to

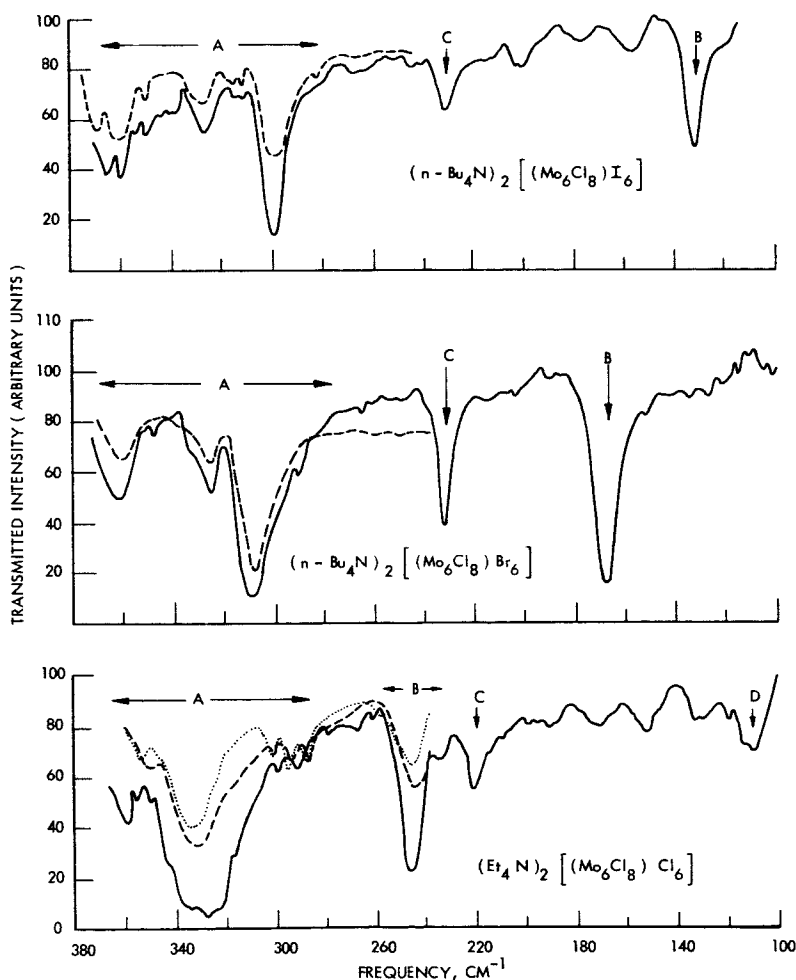


Fig. III-3. Far infrared spectra of $[(Mo_6X_8)Y_6]^{2-}$ compounds. Solid curves: spectra obtained on the interferometer; dashed curves, same sample run on the Perkin-Elmer 521; dotted curve, a nujol mull run on the Perkin-Elmer 521.

(III. OPTICAL AND INFRARED SPECTROSCOPY)

the completion of a molecular orbital calculation for these structures.² Spectra have been obtained over the region 350 to 100 cm^{-1} for the compounds $[\text{Mo}_6\text{Cl}_8(\text{X})_6]^{2-}$ ($\text{X} = \text{Cl}, \text{Br}, \text{I}$), $[\text{W}_6\text{Cl}_8\text{Cl}_6]^{2-}$, and $[\text{Nb}_6\text{Cl}_{12}(\text{X})_2]$ ($\text{X} = \text{Cl}, \text{Br}$). The only satisfactory results thus far, however, are for the $[\text{Mo}_6\text{Cl}_8(\text{X})_6]^{2-}$ compounds, and these spectra are shown in Fig. III-3. To make an assignment of the observed bands with assurance, we must wait for the spectra of the compounds $[\text{Mo}_6\text{X}_8(\text{Y})_6]^{2-}$ ($\text{X} = \text{Br}, \text{I}$) ($\text{Y} = \text{Cl}, \text{Br}, \text{I}$) which have been prepared and will be run soon. Several considerations, however, have led to the present tentative assignment of the bands as follows: Bands A, 2 degenerate vibrations of the triply-bridging Cl's; Band B, stretching of the terminal X_6 groups; Band C, stretching vibration of the metal-metal bonds in the M_6 octahedral frame.

All samples used were pressed polyethylene discs of the compound, and the spectra were run on the interferometer kindly made available by the Optical and Infrared Spectroscopy Group of the Research Laboratory of Electronics.

R. Zimmerman

[Mr. Ralph Zimmerman is a Research Assistant in the Department of Chemistry, M. I. T.]

References

1. F. A. Cotton (paper to be published in Quart. Rev.)
2. F. A. Cotton and T. E. Haas, Inorg, Chem. 3, 10 (1964).

IV. GEOPHYSICAL RESEARCH

A. High Magnetic Fields*

Academic and Research Staff

Prof. F. Bitter
Prof. G. Fiocco

Dr. T. Fohl
Dr. J. F. Waymouth

1. PERTURBATION OF ELECTRON ENERGY DISTRIBUTION BY A PROBE

[This report is an abstract of a paper that has been submitted for publication to the Journal of Applied Physics.]

In order to determine electron-energy distribution in a plasma, the electron current to a probe is measured as a function of potential on the probe. If the rate of removal of high-energy electrons by measurement is comparable with the rate of replenishment by the various plasma processes, serious perturbation of the electron-energy distribution will result as a consequence of the act of measurement. A criterion for deciding when this effect may be ignored is presented. It is based on the hypothesis that when the depletion time constant τ_d of electrons of a particular energy by a given probe in a given plasma is large compared with the "self-collision time" of electrons for coulomb collisions as given by Spitzer, perturbation of the electron-energy distribution is negligible. The depletion time constant is $\tau_d = 4V/A_p \cdot v$, where V is plasma volume, A_p is probe area, and v is electron velocity. The criterion for no perturbation of the electron-energy distribution then becomes $N \gg 2600 T^2 A_p$, in which N is the total number of electrons in the plasma, T is the temperature in degrees Kelvin, and A_p is the probe area in square centimeters. It is shown that even if the criterion is not satisfied, probe measurements of the electron-energy distribution may still be made by using a pulsed or transient system with pulses of length τ_p , provided $\frac{1}{\omega_p} \ll \tau_p \ll \tau_d$.

J. F. Waymouth

*This work is supported by the Joint Services Electronics Programs (U.S. Army, U.S. Navy, and U.S. Air Force) under Contract DA 36-039-AMC-03200(E).

IV. GEOPHYSICAL RESEARCH

B. Upper Atmosphere Physics*

Academic and Research Staff

Prof. G. Fiocco

Graduate Students

R. P. H. Chiang
J. B. DeWolf

G. W. Grams

D. F. Kitrosser
H. C. Koons

1. STUDIES OF STRATOSPHERIC AEROSOLS AND THEIR CORRELATION WITH OZONE

Observations of stratospheric aerosols were conducted for one hundred days in a two-year study with an optical radar at Lexington, Massachusetts. During the summer of 1964, some observations were also conducted at College, Alaska simultaneously with studies of mesospheric clouds. The optical radar system and the techniques used to record and analyze the data have been described previously.^{1,2} Observations conducted after the summer of 1964 were made with the improved apparatus used in Sweden

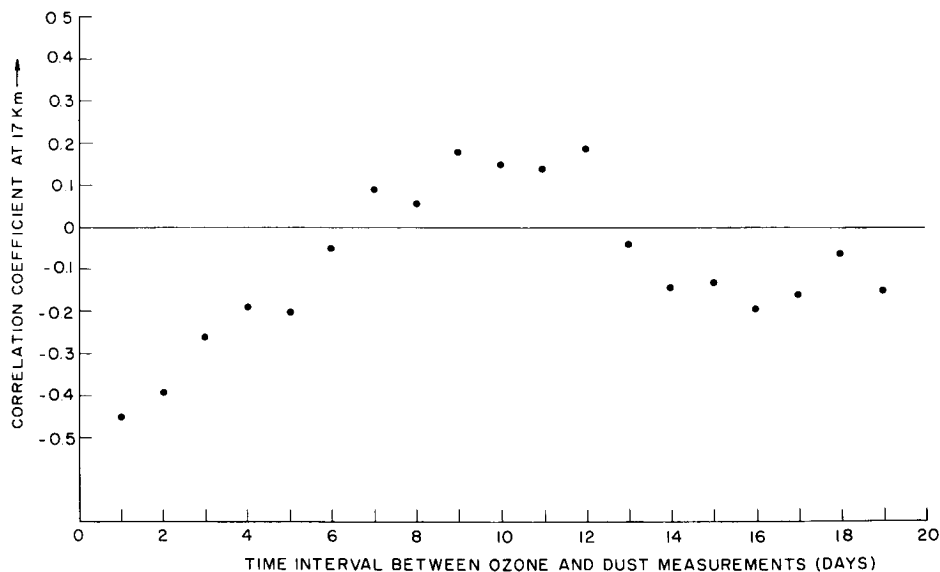


Fig. IV-1. Correlation coefficient for ozone and dust displayed as a function of time.

*This work is supported principally by the National Aeronautics and Space Administration (Grants NGR-22-009-131 and NGR-22-009-(114)), and in part by the Joint Services Electronics Programs (U.S. Army, U.S. Navy, and U.S. Air Force) under Contract DA 36-039-AMC-03200(E).

(IV. GEOPHYSICAL RESEARCH)

for the mesospheric cloud study.³

The data show that the aerosol layer at ~20 km exhibits little temporal variation. Profiles obtained on different nights may differ as much as 10-20%; smaller fluctuations are observed during a single night of observation.

The observed aerosol profiles have been correlated with ozone profiles obtained at Bedford, Massachusetts by the Air Force Cambridge Research Laboratories. Figure IV-1 shows the correlation between the amounts of dust and ozone at the altitude where a maximum in the aerosol mixing ratio is observed (17 km); correlation coefficients for 17-km altitude are displayed as a function of the time between the dust and ozone observations. The relatively large negative correlation observed for shorter time intervals seems to be a significant result.

Pitcock⁴ presents evidence suggesting that, at times, the presence of dust in the stratosphere may destroy ozone; Kroening⁵ has also suggested that stratospheric aerosols may be an important sink for ozone. The observed negative correlation between dust and ozone in the lower stratosphere substantiates these views.

Other explanations for the negative correlation are also being investigated, since in the lower stratosphere chemical destruction of ozone is usually assumed to be negligible.

G. Grams, G. Fiocco

References

1. G. Fiocco and L. D. Smullin, "Detection of Scattering Layers in the Upper Atmosphere (60-140 km) by Optical Radar," *Nature* 199, 1275-1276 (1963).
2. G. Fiocco and G. Grams, "Observations of the Aerosol Layer at 20 km by Optical Radar," *J. Atmos. Sci.* 21, 323-324 (1964).
3. G. Fiocco and G. Grams, "Observations of the Upper Atmosphere by Optical Radar in Alaska and Sweden during the Summer 1964," *Tellus* (to be published).
4. A. B. Pitcock, "Possible Destruction of Ozone by Volcanic Material at 50 mbar," *Nature* 207, 182 (1965).
5. J. L. Kroening, "Stratosphere and Troposphere: Transport of Material between Them," *Science* 147, 862-864 (1965).

V. X-RAY DIFFRACTION STUDIES*

Academic and Research Staff

Prof. B. E. Warren

Graduate Students

R. L. Mozzi

A. MULTIPLE SCATTERING OF X-RAYS BY AMORPHOUS SAMPLES

A rigorous treatment of the multiple scattering of x-rays in amorphous samples has been developed in connection with the x-ray studies of the structure of simple glasses. A paper concerning this research has been submitted for publication to Acta Crystallographica.

B. E. Warren, R. L. Mozzi

*This work is supported by the Joint Services Electronics Programs (U.S. Army, U.S. Navy, and U.S. Air Force) under Contract DA36-039-AMC-03200(E).

VI. PHYSICAL ACOUSTICS*

Academic and Research Staff

Prof. K. U. Ingard
Prof. L. W. Dean III
Prof. K. W. Gentle

Graduate Students

R. H. Katyl
J. L. Macon

W. M. Manheimer

J. A. Ross
H. M. Schulz III

A. INTENSITY DISTRIBUTION OF LIGHT SCATTERED BY THERMAL SURFACE WAVES ON A LIQUID SURFACE

The intensity distribution of light scattered by a thermal ensemble of surface waves on the plane surface of a metallic conductor was calculated with the use of a vector Kirchhoff integral formula. The calculation is similar to that of Gans¹ and will not be repeated here; the results are presented and expected intensities are shown for an experiment to be undertaken with liquid mercury.

The geometry of the problem is the following. The unperturbed liquid surface is taken to be the x-y plane, and the z-axis extends from the liquid. The direction of the incident plane wave of light is taken to be in the x-z plane, at an angle θ_0 to the z-axis, and the observer is at the angles θ, ϕ . This is shown in Fig. VI-1.

With this definition of angles, we find for the electric field at the peak of the diffraction maximum, for scattering off of one surface wave of peak surface displacement ζ_0

$$\begin{bmatrix} E_{S\phi} \\ E_{S\theta} \end{bmatrix} = 8a^2 k^2 \zeta_0 \frac{e^{ikr}}{4\pi r} \begin{bmatrix} \cos \theta_0 \cos \phi \cos \theta; -\cos \theta \sin \phi \\ \cos \theta_0 \sin \phi; (\cos \phi - \sin \theta_0 \sin \theta) \end{bmatrix} \begin{bmatrix} E_{\perp} \\ E_{\parallel} \end{bmatrix}$$

where the liquid surface has been taken to be a square of side a .

The choice of parameters λ , the light wavelength, and θ and ϕ , the observation direction angles, determines uniquely the surface wave wavelength, Λ , and surface wave direction, ψ , up to an additive constant of 180° . These relations are

$$\tan \psi = - \frac{x \sin \phi}{1 - x \cos \phi}; \quad x = \frac{\sin \theta}{\sin \theta_0}$$

$$\frac{\Lambda}{\lambda} = \{\sin^2 \theta_0 + \sin^2 \theta - 2 \sin \theta \sin \theta_0 \cos \phi\}^{-1/2}.$$

* This work was supported principally by the U. S. Navy (Office of Naval Research) under Contract Nonr-1841-(42); and in part by the Joint Services Electronics Programs (U. S. Army, U. S. Navy and U. S. Air Force) under Contract DA 36-039-AMC-03200(E).

(VI. PHYSICAL ACOUSTICS)

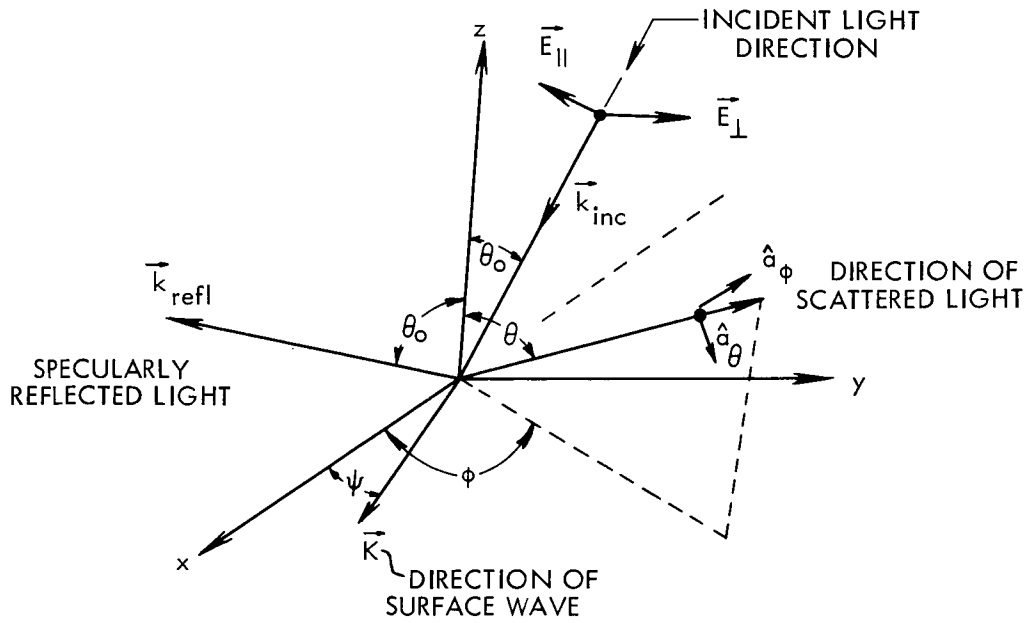


Fig. VI-1. Scattering Geometry

For scattering off of a thermal ensemble of surface waves, the number of waves scattering into solid angle $\Delta\Omega$ is

$$\Delta n = \left(\frac{L}{2\pi}\right)^2 K dK d\psi = \left(\frac{kL}{2\pi}\right)^2 (\cos \theta) (\Delta\Omega).$$

For surface tension waves, the rms surface displacement is

$$\zeta_{o\text{rms}} = \sqrt{\frac{4K_B T}{\sigma(KL)^2}},$$

where K_B is Boltzmann's constant, and σ is the surface tension.

Summing the scattered waves incoherently, we find for the total scattered intensity

$$\begin{bmatrix} I_\phi \\ I_\theta \end{bmatrix} = \frac{4K_B T \Delta\Omega}{\sigma \lambda^2} \frac{1}{\sin^2 \theta + \sin^2 \theta_o - 2 \sin \theta \sin \theta_o \cos \phi} \cdot \begin{bmatrix} (\cos \theta_o \cos \phi \cos \theta)^2 & (-\cos \theta \sin \phi)^2 \\ (\cos \theta_o \sin \phi)^2 & (\cos \phi - \sin \theta_o \sin \theta)^2 \end{bmatrix} \begin{bmatrix} I_\perp \\ I_\parallel \end{bmatrix}$$

For the case of mercury, $\sigma \approx 500 \text{ ergs/cm}^2$, and the multiplying constant at

room temperature is

$$I_{sc} \sim (8.26 \cdot 10^{-8}) \Delta \Omega I_{in} f(\theta_o, \theta, \phi),$$

and for a collecting solid angle of 0.1, 10% transmission through the optics, and an incident intensity of 100 μ watts, $I_{sc} \sim 10^{-13} f(\theta, \phi)$ watts. For backscattering at a grazing incident angle $f \approx 1$ for the proper polarization, and the expected signal current is of the order of the photomultiplier dark current.

R. H. Katyl

References

1. R. Gans, Ann. Physik 74, 231 (1924); 79, 204 (1926). See also A. Andronow and M. Leontowicz, Z. Physik 38, 485 (1926).

B. ACOUSTIC WAVE AMPLIFICATION

Theoretical studies have been carried out on the spontaneous amplification of an acoustic wave in a weakly ionized gas. The amplification mechanism is a coherent heating of the neutral gas by the electrons, which move in phase with the neutrals and ions in the acoustic mode. The linearized equations of motion for the three components of a plasma ionized to the extent of approximately 10^{-6} and with a pressure ≈ 1 torr lead to the acoustic dispersion relation

$$k^2 \approx (\omega/c_n)^2 \left[1 + i/\omega\tau_a + (i/\omega\tau_\beta)(1 - i/\omega\tau'_a)(1 + i/\omega\tau'_\beta)^{-1} \right]^{-1},$$

where

$$\tau_a = c_n^2/(\gamma_n - 1) a_n N_e \approx 1$$

$$\tau_\beta = c_n^2/(\gamma_n - 1)(\gamma_e - 1) \beta_n T_e \approx 1$$

$$\tau' = (\gamma_n - 1)m_e N_e c_e^2 \tau / \gamma_e m_n N_n c_n^2 \approx 10^{-4}.$$

The quantities in these expressions are defined by the following relations:

$$a_n = 2(m_e/m_n)^2 (KT_e/m_e)^{3/2} \sigma(2/\pi)^{1/2}$$

$$\beta_n = 2(m_e/m_n)^2 (KT_e/m_e)^{3/2} \sigma(N_e/T_e)(2/\pi)^{1/2} (3/2 + d \ln \sigma / d \ln T_e)$$

T = equilibrium temperature

(VI. PHYSICAL ACOUSTICS)

N = equilibrium particle number density

m = particle mass

γ = specific heat ratio

K = Boltzmann's constant

$c = (\gamma KT/m)^{1/2}$ = speed of sound

k = wave number

$\omega = (2\pi)$ times the frequency, ($10^2 < \omega < 10^5$)

σ = cross section for energy transfer,

with the subscripts n and e referring to the neutrals and electrons.

At high frequencies (for example, $\omega \gg 10^4 \text{ sec}^{-1}$) the process is almost adiabatic and the electron temperature is not significantly affected by the amplification mechanism. The dispersion relation becomes

$$k \approx (\omega/c_n) \left[1 - i(\tau_a^{-1} + \tau_\beta^{-1})/2\omega \right].$$

At low frequencies, however, the electron temperature is strongly affected by the process, and the degree of amplification depends on the energy dependence of the electron-neutral cross section. The dispersion relation becomes

$$k \approx (\omega/c_n) \left[1 + (\tau'_a + \tau'_\beta)/2\tau_\beta - i(\tau_a^{-1} - \tau_\beta^{-1})/2\omega - i\omega^2 \tau'_a \tau'^2_\beta / 2\tau_\beta \right],$$

and the degree of amplification depends on the energy-dependence of the electron-neutral cross section. For a hard-sphere gas with $\gamma_n = \gamma_e = 5/3$, it develops that $\tau_a = \tau_\beta$. Significant amplification is possible at low frequencies only if σ decreases with energy.

A similar calculation for ion-acoustic waves in a strongly ionized gas yields substantially the same results, but the electron-ion cross section always decreases with energy. The amplification mechanism, however, competes with the attenuation caused by ion-neutral momentum-transfer collisions.

H. M. Schulz III

C. LATERAL ACOUSTIC INSTABILITY

Strickler and Stewart¹ have reported a lateral acoustic instability which results in a pronounced modification of the path of a constricted argon discharge when the current is modulated at a lateral resonant frequency of the neutral gas in the discharge tube.

Further examination of this effect has recently revealed that the geometric shape of the discharge path depends on the longitudinal pressure wave, as well as on the radial and azimuthal one. Thus all three quantum numbers of the wave play a role in determining the discharge path. In a typical experiment situation the discharge tube has a

length much greater than its diameter, and the frequency is determined principally by the radial and azimuthal quantum numbers, that is, by the indices of the Bessel function $J_m(k_n r)$. The longitudinal wave function $\cos \ell\pi z/L$ contributes only a small increment to the frequency but is very important in establishing the path of the discharge. It has been possible to resolve the fine structure of the $m=1, n=1$ mode, that is, of the lowest mode of the tube, from $\ell=0$ up to approximately $\ell=15$.

Preliminary results are consistent with a model in which the discharge follows a path of maximum pressure variation. Both spiral and planar discharge paths have been observed. It would appear that spiral paths must be associated with modes having $m \geq 2$, while planar displacements are most logically associated with models having $m \leq 1$.

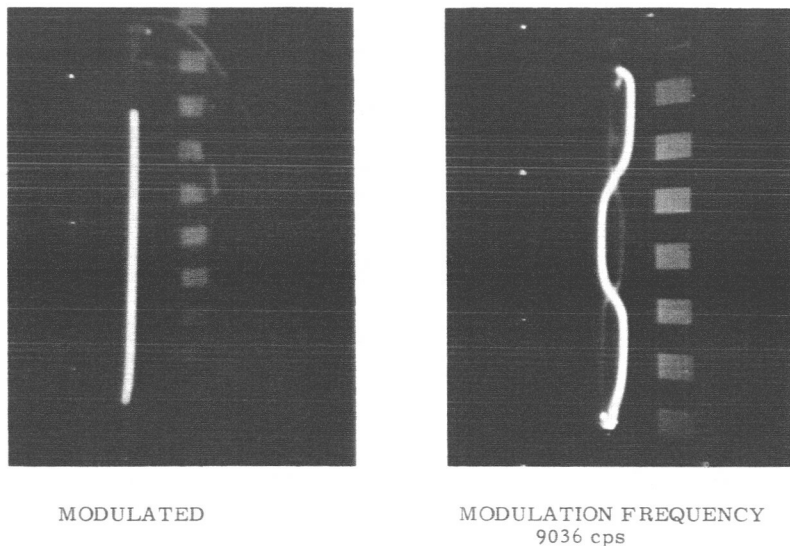


Fig. VI-2. Lateral displacement of an intensity-modulated plasma filament at modulation frequencies close to the acoustic lateral resonances in the tube. Each white rectangle and each black rectangle on the scale has a height of 2 cm, and the tube is 2.5 cm in diameter and 40 cm in length.

Figure VI-2. shows an unmodulated discharge and a discharge for which $m=1$, $n=0$, and $\ell \approx 4$ or 5. The less intense trace is a reflection of the discharge in the tube wall. The frequencies correspond to a gas temperature $\approx 350^\circ \text{ K}$.

H. M. Schulz III, K. W. Gentle

References

1. S. D. Strickler and A. B. Stewart, Phys. Rev. Letters 11, 527 (1963).

(VI. PHYSICAL ACOUSTICS)

D. CONSERVATION EQUATIONS FOR A PLASMA

The object of the present report is to derive for the general case the equations for conservation of particles, momentum, and energy for a plasma, and to examine the physical nature of the various terms in these equations. The treatment will include the relativistic and nonrelativistic cases, consider gravitational and electromagnetic (but not nuclear) forces, and allow for the existence of field sources external to the plasma.

The starting point for the discussion is the Boltzmann equation

$$\frac{\partial f_a}{\partial t} + \frac{\partial}{\partial \vec{x}} \cdot (\vec{v} f_a) + \frac{\partial}{\partial \vec{p}} \cdot \left\{ q_a \left(\vec{E} + \frac{\vec{v}}{c} \times \vec{B} \right) f_a + m_a \vec{g} f_a \right\} = \left(\frac{df_a}{dt} \right)_{\text{collisions}}. \quad (1)$$

Here the subscript a refers to the a^{th} species contained in the plasma ($a=1, 2, \dots, n$), and the gravitational force per unit mass is assumed to be $\vec{g}(\vec{x})$. Note that (1) is appropriate for both the relativistic and nonrelativistic cases. To obtain the equation for the conservation of particles, we merely integrate (1) over all momentum space. If there is no excitation, ionization, or recombination during collisions the result is

$$\frac{\partial n_a}{\partial t} + \frac{\partial}{\partial \vec{x}} \cdot \vec{J}_a = 0 \quad (2)$$

$$n_a = \int d^3 p f_a \quad \vec{J}_a = \int d^3 p \vec{v} f_a$$

Thus n_a is just the particle density of the a^{th} species, and \vec{J}_a is the particle current. Equation 2 is clearly a simple continuity equation; the mass and charge continuity equations for the a^{th} species may easily be obtained by multiplying (2) by m_a and q_a , respectively.

The momentum conservation equation is obtained by multiplying (1) by \vec{p} , integrating the result over all momentum space, and then summing over all a . The result, since momentum is conserved in any collision, is

$$\begin{aligned} \frac{\partial}{\partial t} \sum_a \int d^3 p \vec{p} f_a + \frac{\partial}{\partial \vec{x}} \cdot \sum_a \int d^3 p \vec{p} \vec{v} f_a = \\ \sum_a \int d^3 p f_a \left\{ q_a \left(\vec{E} + \frac{\vec{v}}{c} \times \vec{B} \right) + m_a \vec{g} \right\}. \end{aligned} \quad (3)$$

With the aid of Maxwell's equations

$$\begin{aligned} \frac{\partial}{\partial \vec{x}} \cdot \vec{E} &= 4\pi\rho & \frac{\partial}{\partial \vec{x}} \cdot \vec{B} &= 0 \\ \nabla \times \vec{E} &= -\frac{1}{c} \frac{\partial \vec{B}}{\partial t} & \nabla \times \vec{B} &= \frac{4\pi\vec{J}}{c} + \frac{1}{c} \frac{\partial \vec{E}}{\partial t}, \end{aligned} \quad (4)$$

and the analogous gravitational equations

$$\frac{\partial}{\partial \vec{x}} \cdot \vec{g} = -4\pi G \rho_m \quad \nabla \times \vec{g} = 0, \quad (5)$$

where ρ_m is the mass density, and G is Newton's gravitational constant, (3) becomes

$$\frac{\partial}{\partial t} \vec{P} + \frac{\partial}{\partial \vec{x}} \cdot \vec{T} = 0 \quad (6)$$

$$\vec{P} = \sum_a \int d^3p \, \vec{p} f_a + \frac{\vec{S}}{c^2}$$

$$\vec{T} = \sum_a \int d^3p \, \vec{p} \vec{v} f_a - \left\{ \frac{\vec{E}\vec{E}}{4\pi} - \frac{E^2}{8\pi} + \frac{\vec{B}\vec{B}}{4\pi} - \frac{B^2}{8\pi} \right\} - \left\{ -\frac{\vec{g}\vec{g}}{4\pi G} + \frac{g^2}{8\pi G} \right\}$$

$$\vec{S} = \frac{c}{4\pi} \vec{E} \times \vec{B} = \text{Poynting vector.}$$

Thus (6) is also a continuity equation, similar in form to (2), except that in (6) we have summed over all the various species. The vector \vec{P} is obviously the total momentum density of the entire system, while \vec{T} is an effective pressure tensor equal to the "particle" pressure tensor minus the electromagnetic (Maxwell) stress tensor minus the analogous gravitational stress tensor.

Finally, we obtain the energy conservation equation by multiplying (1) by $[m_a c^2 (1-v^2/c^2)^{-1/2} - m_a c^2]$, integrating the result over all momentum space, and then summing over all a . If we assume that all collisions are elastic, the result is

$$\frac{\partial U}{\partial t} + \frac{\partial}{\partial \vec{x}} \cdot \vec{Q} = \vec{g} \cdot \sum_a \int d^3p \, m_a f_a \vec{v} \quad (7)$$

$$U = \sum_a \int d^3p \, f_a m_a c^2 [(1-v^2/c^2)^{-1/2} - 1] + \frac{E^2}{8\pi} + \frac{B^2}{8\pi}$$

$$\vec{Q} = \sum_a \int d^3p \, f_a m_a c^2 [(1-v^2/c^2)^{-1/2} - 1] \vec{v} + \vec{S}.$$

(VI. PHYSICAL ACOUSTICS)

Equation 7 is almost an energy continuity equation; U is clearly the total energy density, while \vec{Q} is apparently the total energy flow. The term on the right-hand side seems to correspond to some kind of gravitational flow, although its form certainly does not fit in well with the other terms of (7). This difficulty would quickly disappear if we postulated the existence of a gravitational magnetic field \vec{h} which was coupled to \vec{g} by a set of "gravitational Maxwellian equations":

$$\begin{aligned} \frac{\partial}{\partial \vec{x}} \cdot \vec{g} &= -4\pi\rho_m & \frac{\partial}{\partial \vec{x}} \cdot \vec{h} &= 0 \\ \nabla \times \vec{g} &= \mp \frac{1}{c_g} \frac{\partial \vec{h}}{\partial t} & \nabla \times \vec{h} &= -\frac{4\pi}{c_g} \vec{j}_m \pm \frac{1}{c_g} \frac{\partial \vec{g}}{\partial t}. \end{aligned} \quad (8)$$

Equations 8 are written in units in which $G = 1$; and c_g , the speed of "gravitational waves" in vacuo is presumably c . The "gravitational Lorenz force" would be

$$\vec{F}_g = m \left(\vec{g} + \frac{\vec{v}}{c_g} \times \vec{h} \right), \quad (9)$$

and the "gravitational Poynting vector" is

$$\vec{S}_g = \frac{c_g}{4\pi} \vec{g} \times \vec{h}. \quad (10)$$

For this case, Eq. 7 would now have no term at all on the right-hand side, while \vec{Q} would contain the additional term \vec{S}_g , and U would contain the term $-g^2/8\pi$.

It seems quite possible that the set of equations (8) is actually valid. It would certainly be very difficult to measure the force attributable to \vec{h} directly in any experiment, since it would be greatly masked by the force resulting from \vec{g} . In electromagnetic theory, this problem can be circumvented by the use of currents having no net charge density; the (apparent) nonexistence of negative mass precludes this technique in gravitational experiments, however. The release of energy through radiation of gravitational waves is presumably negligible, except in stars. Since gravitational effects tend to completely dominate electromagnetic effects in such bodies, however, it seems likely that this is the chief source of energy loss from asteral systems.

J. A. Ross

VII. ELECTRODYNAMICS OF MOVING MEDIA*

Academic and Research Staff

Prof. H. A. Haus
Prof. P. Penfield, Jr.

A. SPECIAL RELATIVITY AND ASYMMETRIC ENERGY MOMENTUM TENSORS

The principle of virtual work applied to systems with intrinsic angular momentum leads to asymmetric stress tensors. In this report ways are shown for reconciling the relativistic law of angular momentum conservation with the asymmetry of the stress energy tensors.

1. Introduction

The stress tensor of a time dispersive polarizable or magnetizable medium obtained from the principle of virtual work (or principle of virtual power) is nonsymmetric.^{1, 2} This asymmetry is due in part to the terms $\mu_0 \overline{\mathbf{M}} \mathbf{H}$ and/or $\overline{\mathbf{P}} \mathbf{E}$, which are asymmetric, if the polarization and magnetization do not align with the electric and magnetic field intensities. From the nonrelativistic point of view, there are no difficulties with such an asymmetry of the stress tensor. Indeed, in a time-dispersive medium there is an intrinsic angular momentum associated with the rotation of the polarization or magnetization vectors. Such an angular momentum requires torques if it is to be changed, and these torques are provided by the antisymmetric part of the stress tensor. Certain difficulties do arise, however, in a relativistic formulation of such media if one tries to write the law of conservation of angular momentum in the conventional four-notation. It is customary to define a four-tensor of third rank describing the angular momentum

$$\theta_{\alpha\beta\gamma} = x_{\alpha} T_{\gamma\beta} - x_{\beta} T_{\gamma\alpha}, \quad (1)$$

where $T_{\alpha\beta}$ is the stress energy tensor of the entire system satisfying the equation of motion

$$\partial/\partial x_{\alpha} T_{\alpha\beta} = 0. \quad (2)$$

The conservation of angular momentum is then written in the form

$$\frac{\partial}{\partial x_{\gamma}} \theta_{\alpha\beta\gamma} = 0. \quad (3)$$

When (1) and (2) are introduced into (3), the result is

*This work was supported by the Joint Services Electronics Programs (U.S. Army, U.S. Navy, and U.S. Air Force) under Contract DA 36-039-AMC-03200(E).

(VII. ELECTRODYNAMICS OF MOVING MEDIA)

$$T_{a\beta} - T_{\beta a} = 0. \quad (4)$$

Hence, if one insists on conservation of angular momentum, as well as the specific expression (3), one must conclude that the system must possess a symmetric stress-energy four-tensor. Taking as an example a time dispersive polarizable fluid and constructing the stress energy tensor in the usual way, one arrives at an asymmetric four-tensor for the system.^{1,2}

This report will show how it is possible to preserve a law of conservation of angular momentum of the form (3) on the one hand, and the expression for the stress tensor as obtained from the principle of virtual power, on the other hand. At the same time, we shall construct a law of angular momentum conservation which approaches the proper nonrelativistic limit.

2. Fundamental Postulates

We shall require that our theory satisfy the following postulates.

Postulate 1: The angular momentum tensor in four-notation is to be given by

$$\theta_{a\beta\gamma} = x_a T_{\gamma\beta}^{(s)} - x_\beta T_{\gamma a}^{(s)} \quad (5)$$

and satisfies the conservation law

$$\frac{\partial}{\partial x_\gamma} \theta_{a\beta\gamma} = 0, \quad (6)$$

where $T_{a\beta}^{(s)}$ is a stress-energy four-tensor containing the mechanical translational equations of motion in the form

$$\frac{\partial}{\partial x_a} T_{a\beta}^{(s)} = 0. \quad (7)$$

A direct consequence of (6) and (7) is the symmetry of the stress energy tensor $T_{a\beta}^{(s)}$.

Postulate 2: The equations of motion of the entire system are also expressible in terms of the equation

$$\frac{\partial}{\partial x_a} T_{a\beta}^{(n)} = 0, \quad (8)$$

where $T_{a\beta}^{(n)}$ is a nonsymmetric tensor whose three-space part is obtained from the principle of virtual power.

The problem is thus the construction of a symmetric tensor $T_{a\beta}^{(s)}$ from the nonsymmetric tensor obtained from the principle of virtual power in a way that both (7) and (8) are satisfied and at the same time, the usual equation for the conservation of

(VII. ELECTRODYNAMICS OF MOVING MEDIA)

angular momentum is obeyed.

Postulate 3: The vector torque per unit volume, $\bar{\tau}$, constructed from the three-space part of the energy-momentum tensor, according to

$$\bar{T}_{\beta\alpha}^{(n)} - \bar{T}_{\alpha\beta}^{(n)} \longrightarrow \bar{\tau} \quad \alpha, \beta = 1, 2, 3 \quad (9)$$

gives the law of conservation of angular momentum $\bar{\sigma}$ per particle in the rest frame:

$$\bar{\tau} = n^0 \left[\frac{d}{dt} \bar{\sigma} \right]^0, \quad (10)$$

where the superscripts indicate evaluation in the rest frame.

Let us look briefly at the cause of the asymmetry of the three-space part of the stress-energy tensor. Consider an isotropic time-dispersive polarizable medium. In such a medium the only contribution to the asymmetric three-space part is the term $\bar{P} \times \bar{E}$.^{1,2} Suppose now that we construct the torque per unit volume from

$$T_{\beta\alpha}^{(n)} - T_{\alpha\beta}^{(n)} \quad (11)$$

and look at its one-two component. We obtain

$$T_{\beta\alpha}^{(n)} - T_{\alpha\beta}^{(n)} \Big|_{12} = P_1^0 E_2^0 - P_2^0 E_1^0 = (\bar{P}^0 \times \bar{E}^0)_3. \quad (12)$$

Apparently, the one-two component of this tensor is the three-component of the vector $\bar{P} \times \bar{E}$ in the rest frame. This is the torque acting on the dipoles of strength \bar{p} and number density n so that the dipole moment per unit volume results in $\bar{P} = n\bar{p}$. This torque, in turn, is equal to the time rate of change of the intrinsic angular momentum of the dipoles. Let us denote the angular momentum per particle by $\bar{\sigma}$. If the number density in the rest frame is n^0 , one must have

$$\bar{P}^0 \times \bar{E}^0 = n_0^0 \frac{d}{dt} (\bar{\sigma}). \quad (13)$$

This equation can be written in four-space notation, once we establish the correct transformation laws for the vector $\bar{\sigma}$. According to Landau and Lifshitz³ the angular momentum of a body is expressible as the four-tensor of second rank (we interchanged indices to conform to our definition of the force equation).

$$\sigma_{\alpha\beta} = -\frac{i}{c} \int x_\alpha T_{\gamma\beta} - x_\beta T_{\gamma\alpha} dS_\gamma. \quad (14)$$

In the rest frame, defined as the frame with no net momentum or energy flow, dS_γ is defined as having a time direction only.

If we apply this formula to a particle, we conclude that its angular momentum is represented by the four-tensor with the components in the rest frame:

(VII. ELECTRODYNAMICS OF MOVING MEDIA)

$$\sigma_{\alpha\beta} = \begin{bmatrix} 0 & \sigma_3^0 & -\sigma_2^0 & 0 \\ -\sigma_3^0 & 0 & \sigma_1^0 & 0 \\ \sigma_2^0 & -\sigma_1^0 & 0 & 0 \\ 0 & 0 & 0 & 0 \end{bmatrix}$$

We find a complete analogy between $\sigma_{\alpha\beta}$ and the tensor constructed from the magnetization four-vector

$$\frac{1}{ic} \epsilon_{\alpha\beta\gamma\delta} M_\gamma u_\delta \quad (15)$$

which assumes the above form in the rest frame, with σ_a replaced by M_a . Hence the four-vector angular momentum defined in the rest frame by

$$\sigma_a \equiv [\vec{\sigma}^0, 0] \quad (16)$$

transforms like a magnetization density four-vector.

It is worth considering briefly the implications of this analogy. A magnetization density can be represented by a density of loops of circulating charge currents. The angular momentum is the result of a circulating mass current. Charge-current densities, and mass-current densities do not transform relativistically in the same way. The difference in the transformation laws is compensated for by the fact that M_a contains, in addition, a particle density, whereas σ_a does not contain such a density.

We note that the vector equation (13) is contained in the three-space part of the tensor equation

$$T_{\beta\alpha}^{(n)} - T_{\alpha\beta}^{(n)} = n_0 u_\gamma \frac{\partial}{\partial x_\gamma} \sigma_{\alpha\beta}. \quad (17)$$

A problem arises with the four-components of (17). Take, for example, the four-component in the rest frame of (17) for $\beta = 1, 2, 3$. If one makes the identification (12) and uses the transformation laws for $\sigma_{\alpha\beta}$, one finds in the rest frame (in which usually $T_{\beta 4} = T_{4\beta}$, $\beta = 1, 2, 3$):

$$0 = -\frac{i}{c} \left[\frac{d\vec{v}}{dt} \right]_0 \times \vec{\sigma}^0. \quad (18)$$

This equation puts an inadmissible constraint upon the acceleration. Therefore, one cannot take directly the nonsymmetric tensor as obtained from the principle of virtual power with no modification and hope that it will lead to a consistent equation (17). Modifications

are necessary. Here we point out one simple modification that does not produce any additional changes in the principle of virtual power.

3. Modification of Stress-Energy Tensor

We assume that in the rest frame the space-time and time-space parts of the stress-energy four-tensor are symmetric. This has been found true in all examples treated by the authors. We postulate that the time-dispersive medium possesses an additional momentum per unit volume

$$\bar{\mathbf{G}}^0 = \frac{1}{c^2} \left[\frac{\partial \bar{\mathbf{v}}}{\partial t} \right]^0 \times \bar{\mathbf{v}}^0 n^0. \quad (19)$$

The principle of virtual power (of a closed system, with $\phi^0 = 0$),

$$\begin{aligned} [\nabla \cdot \bar{\mathbf{S}}^0]^0 + \left[\frac{\partial}{\partial t} W \right]^0 + W^0 [\nabla \cdot \bar{\mathbf{v}}]^0 + \frac{\bar{\mathbf{S}}^0}{c^2} \cdot \left(\frac{\partial \bar{\mathbf{v}}}{\partial t} \right)^0 \\ = -\bar{\mathbf{T}}^0 : [\nabla \bar{\mathbf{v}}]^0 - \bar{\mathbf{G}}_1^0 \cdot \left(\frac{\partial \bar{\mathbf{v}}}{\partial t} \right)^0, \end{aligned} \quad (20)$$

is not affected by such a term because the dot product of the acceleration with the momentum (19) is zero. Therefore, no additional changes have to be made in any of the expressions entering the principle of virtual power if the four-tensor is supplemented by such a momentum density. The addition of the momentum density (19) leaves the stress tensor, the power-flow density, and the energy density of the material system intact. It should be pointed out, however, that the force density on the kinetic system is changed by such a modification. Indeed, the time rate of change of the momentum density and its convective flow have to be subtracted when the kinetic force density is obtained. Hence, a relativistic correction to the force density results even in the rest frame.

We modify the nonsymmetric four-tensor $T_{\alpha\beta}$, obtained from the principle of virtual power (without consideration of intrinsic angular momentum) by the addition of such a momentum density and define the four-tensor

$$T_{\alpha\beta}^{(n)} = T_{\alpha\beta} + \frac{u_\alpha u_\beta}{c^2} \frac{\partial}{\partial x_\gamma} \left(\sigma_{\delta\beta} n^0 u_\gamma \right) \quad (21)$$

in which we have included the momentum density (19) by the last term. In terms of the modified nonsymmetric tensor, the conservation of angular momentum (17) is now valid for all values of β or α

$$T_{\beta\alpha}^{(n)} - T_{\alpha\beta}^{(n)} = n_0 u_\gamma \frac{\partial}{\partial x_\gamma} (\sigma_{\alpha\beta}). \quad (22)$$

(VII. ELECTRODYNAMICS OF MOVING MEDIA)

4. Symmetrization of the Stress-Energy Tensor

We shall now construct from the modified stress-energy tensor of (22) a symmetric stress-energy tensor that obeys the same equation of motion (8). This is accomplished by adding to $T_{\alpha\beta}^{(n)}$ the expression

$$\frac{\partial}{\partial x_\gamma} \psi_{\alpha\beta\gamma} = \frac{1}{2} \frac{\partial}{\partial x_\gamma} \left[\sigma_{\alpha\beta} n_\gamma^0 u_\gamma + \sigma_{\beta\gamma} n_\alpha^0 u_\alpha - \sigma_{\gamma\alpha} n_\beta^0 u_\beta \right], \quad (23)$$

where $\psi_{\alpha\beta\gamma}$ is antisymmetric in $\gamma\alpha$. Because of this antisymmetry, the symmetrized tensor $T_{\alpha\beta}^{(s)} = T_{\alpha\beta}^{(n)} + \frac{\partial}{\partial x_\gamma} \psi_{\alpha\beta\gamma}$ obeys the equation of motion

$$\frac{\partial T_{\alpha\beta}^{(s)}}{\partial x_\alpha} = 0. \quad (24)$$

Next we test that the law of conservation of angular momentum (22) is contained in (6). One obtains

$$T_{\beta\alpha}^{(s)} - T_{\alpha\beta}^{(s)} = T_{\beta\alpha}^{(n)} - T_{\alpha\beta}^{(n)} + \frac{\partial}{\partial x_\gamma} (\sigma_{\beta\alpha} n_\gamma^0 u_\gamma) = 0. \quad (25)$$

We see that the law of conservation of angular momentum is indeed contained in (6).

The present discussion has led to results different from those obtained by Meixner.⁴ Since the terms in our theory and in Meixner's theory are relativistic, experimental verification of either theory seems out of the question and simplicity of the result is one legitimate criterion to decide between the two.

P. Penfield, Jr., H. A. Haus

References

1. L. J. Chu, H. A. Haus, and P. Penfield, Jr., "The Force Density in Polarizable and Magnetizable Fluids," Technical Report 433, Research Laboratory of Electronics, M.I.T., June 1, 1965.
2. P. Penfield, Jr. and H. A. Haus, "Electrodynamics of Moving Media," Class Notes for 6.583, "Advanced Topics in Continuum Electrodynamics," Massachusetts Institute of Technology, Cambridge, Mass., Fall 1965.
3. L. D. Landau and E. M. Lifshitz, The Classical Theory of Fields (Pergamon Press, London, and Addison-Wesley Publishing Co., Inc., Reading, Mass., 2d edition, 1962).
4. J. Meixner, "Relativistic Thermodynamics of Irreversible Processes in a One-Component Fluid in the Presence of Electromagnetic Fields," Radiation Laboratory, Department of Electrical Engineering, University of Michigan (unpublished report RL-184, April 1961).

PLASMA DYNAMICS

VIII. PLASMA PHYSICS*

Academic and Research Staff

Prof. S. C. Brown
Prof. W. P. Allis

Prof. G. Bekefi
Prof. J. C. Ingraham
Dr. G. Lampis

J. J. McCarthy
W. J. Mulligan

Graduate Students

M. L. Andrews
D. L. Flannery
E. V. George

W. H. Glenn, Jr.
P. W. Jameson
R. L. Kronquist
D. T. Llewellyn-Jones

G. L. Rogoff
D. W. Swain
F. Y-F. Tse

A. APPROXIMATE SOLUTION OF THE COLLISIONLESS PLASMA-SHEATH EQUATION FOR BEAM-GENERATED PLASMA IN A PLANE GEOMETRY

The collisionless plasma-sheath equation for beam-generated plasma in a plane geometry has the form¹

$$\frac{a^2}{2} [S''(x)]^{-1} + \beta + e^{-x} = \int_0^x [x-\xi]^{-1/2} S'(\xi) d\xi, \quad (1)$$

where

$$a \equiv \frac{(M/m)^{1/2} v}{\omega_p} \quad (2)$$

is a small parameter with typical values between 10^{-3} and 10^{-1} , and $\beta \equiv n_b/n_{e0}$ is the ratio of the beam electron density to the plasma electron at the center. With the boundary condition $\left[\frac{ds}{dx} \right]_{x=0}^{-1} = 0$, Eq. 1 can be integrated analytically with respect to x to give

$$\frac{a^2}{4} [S'(x)]^{-2} + H_0(x) = 2 \int_0^x [x-\xi]^{1/2} S'(\xi) d\xi, \quad (3)$$

where $H_0(x) = \beta x + 1 - e^{-x}$.

Integrating the right-hand side of Eq. 3 by parts and denoting S by S_a for $a \neq 0$ yields the plasma-sheath equation in the form

$$\frac{a^2}{4} [S'_a(x)]^{-2} + H_0(x) = \int_0^x [x-\xi]^{-1/2} S_a(\xi) d\xi. \quad (4)$$

For $a = 0$, and since $H(0) = 0$, Eq. 4 is an Abel's integral equation with the solution

*This work is supported by the United States Atomic Energy Commission (Contract AT (30-1)-1842).

(VIII. PLASMA PHYSICS)

$$S_0(x) = \frac{1}{\pi} \frac{d}{dx} \int_0^x (x-\xi)^{-1/2} H_0(\xi) d\xi. \quad (5)$$

By changing $\xi \rightarrow \xi - x$, Eq. 5 gives

$$S_0(x) = \frac{1}{\pi} \int_0^x (x-\xi)^{-1/2} H'_0(\xi) d\xi. \quad (6)$$

For $H_0(x) = \beta x + (1-e^{-x})$, Eq. 6 reduces to the solution derived previously by Harrison and Thompson² ($\beta=0$):

$$S_0(x) = \frac{2}{\pi} x^{1/2} [\beta + B(x)], \quad (7)$$

where

$$B(x) \equiv \int_0^1 \exp[x^2(\xi^2-1)] d\xi$$

$$\longrightarrow \begin{cases} 0 & \text{as } x \rightarrow 0 \\ \frac{1}{2x} & \text{as } x \rightarrow \infty \end{cases} \quad (8)$$

We found it convenient to use the function $B(x)$ rather than the Dawson function that Harrison and Thompson used. The function $B(x)$ is related to Dawson function by the relation

$$x^{1/2} B(x) \equiv e^{-x} D(x^{1/2}). \quad (9)$$

For $a \neq 0$ we shall separate solution into two regions. For the inner solution we define

$$R_a(x) \equiv S_a(x) - S_0(x) \quad \text{for } 0 \leq x \leq x_c - \delta,$$

where $x_c = 0.3444$ with $S'_0(x_c) = 0$, and δ is a positive number such that $R_a(x) \ll S_0(x)$ in this region.

Then the integro-differential equation satisfied by $R_a(x)$ has the form

$$\frac{a^2}{4} [S'_0(x) + R'_a(x)]^{-2} = \int_0^x (x-\xi)^{-1/2} R_a(\xi) d\xi. \quad (10)$$

Equation 10 also has the form of the Abel's equation with the solution

$$R_a(x) = \frac{a^2}{4\pi} \int_0^x (x-\xi)^{-1/2} \frac{d}{d\xi} \left\{ [S'_0(\xi) + R'_a(\xi)]^{-2} \right\} d\xi. \quad (11)$$

Since $R'_a(\xi) \ll S'_0(\xi)$ in this region, Eq. 11 can be written

$$R_a(x) \approx \frac{a^2}{2\pi} \int_0^x \frac{(x-\xi)^{-1/2} |S''_0(\xi)|}{[S'_0(\xi)]^3} d\xi. \quad (12)$$

Equation 12 thus gives $R_a(x)$ in terms of known functions. Note that Eq. 12 is good only for $x \leq x_c - \delta$ because at $x = x_c$ S'_0 is zero. For the outer solution we define

$$S_a(x) \equiv S_a(x_c - \delta) + af_a(x) \quad \text{for } x > x_c - \delta, \quad (13)$$

where $S_a(x_c - \delta)$ is given by the inner solution. With $H_0(x) = \int_0^x (x-\xi)^{-1/2} S_0(\xi) d\xi$ as required by Eq. 4, and if we neglect $R_a(x)$ for the inner region $0 \leq x \leq x_c - \delta$, Eq. 4 becomes

$$\begin{aligned} \frac{1}{4} [f'_a(x)]^{-2} &\approx \int_0^{x_c - \delta} (x-\xi)^{-1/2} S_0(\xi) d\xi \\ &+ \int_{x_c - \delta}^x (x-\xi)^{-1/2} [S_a(x_c - \delta) + af_a(\xi)] d\xi \\ &- \int_0^x (x-\xi)^{-1/2} S_0(\xi) d\xi \\ &= \int_{x_c - \delta}^x (x-\xi)^{-1/2} [S_a(x_c - \delta) + af_a(\xi) - S_0(\xi)] d\xi. \end{aligned} \quad (14)$$

Assume that $af_a(\xi) \ll S_a(x_c - \delta) - S_0(\xi)$ for small a . Then Eq. 14 gives

$$f_a(x) = \frac{1}{2} \int_{x_c - \delta}^x \frac{d\xi}{\sqrt{\int_{x_c - \delta}^{\xi} (\xi - \eta)^{-1/2} [S_a(x_c - \delta) - S_0(\eta)] d\eta}}. \quad (15)$$

Equation 15 gives $f_a(x)$ in terms of known functions. In this particular form, however, it is not very useful for computational purpose and more work is being done along this line.

It should be stated that the assumption $af_a(\xi) \ll S_a(x_c - \delta) - S_0(\xi)$ is rigorously justifiable but is omitted here for the sake of brevity.

F. Y-F. Tse

References

1. D. A. Dunn and S. A. Self, J. Appl Phys. 35, 113 (1964).
2. E. R. Harrison and W. B. Thompson, Proc. Phys. Soc. (London) 72, 2145 (1959).

B. LASER BREAKDOWN

VERTICAL : gv/div
HORIZONTAL : $20 \text{ nsec}/\text{div}$

The plasma spark produced in the focus of the lens is cylindrically shaped with the axis in the direction of the ruby beam. The plasma is being studied by crossing it with

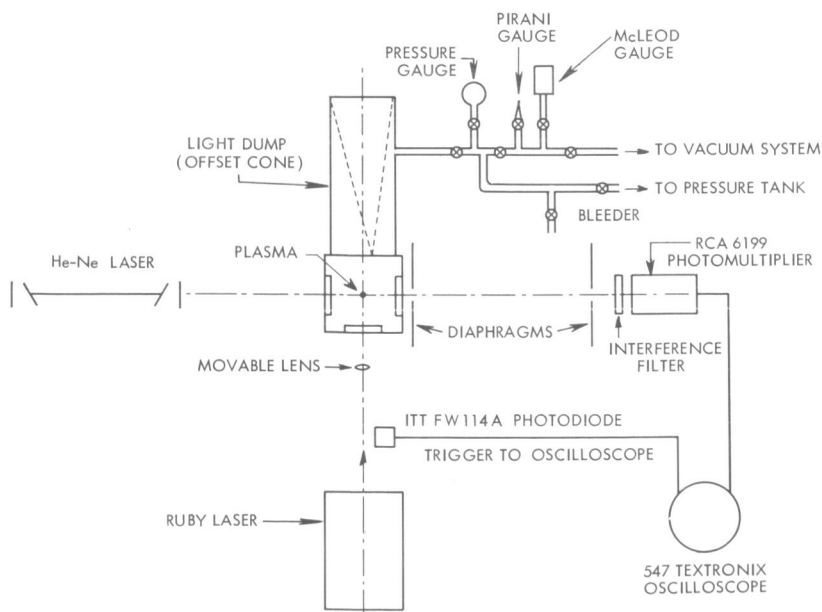


Fig. VIII-2. Experimental arrangement.

the light of a Helium-Neon laser, whose beam is at an angle of 90° with the ruby beam. See Fig. VIII-2.

The gas laser light emerging from the spark is detected together with the emission from the plasma by a photomultiplier tube (RCA 6199) in front of which a diaphragm system and a sharp interferential filter (7 \AA half-width centered at 6328 \AA) have been introduced. The 547 Textronix oscilloscope is triggered by an ITT FW114A photodiode looking at the side of the ruby beam and collecting the Rayleigh scattered signal. Figure VIII-3 shows the combination of the signals caused by the emission from the plasma and the light from the gas laser, which has crossed the spark. On the left is shown the level of the steady-state value of the power P_ℓ from the gas laser. When the breakdown happens, the pulse presents a fast rise time $\approx 30 \text{ nsec}$ resulting from the strong emission from the plasma. The emission then decays (see Fig. VIII-4) and meanwhile the He-Ne laser light is being absorbed. This causes the pulse amplitude to decrease back to the initial value P_ℓ and beyond. When the signal equals the initial steady-state value of the He-Ne laser (before the breakdown) the following equality is verified:

$$P_\ell \cdot e^{-2aR} + P_{\text{plasma}}(R, T) = P_\ell, \quad (1)$$

where P_ℓ is the power of the He-Ne laser which reaches the photomultiplier tube when there is no plasma in the geometry of the experiment; a is the absorption coefficient of the plasma for the laser frequency; R is the radius of the cylindrically shaped bubble of plasma; $P_\ell e^{-aL}$ is then the power from the gas laser attenuated by the plasma; $P(R, T)$ is the power emitted by the plasma, reaching the photomultiplier tube in the band of the filter and in the geometry of the experiment; and T is the temperature of the plasma, which is supposed to be homogeneous.

Figure VIII-4 shows the shape of the emission from the plasma in the band of the interferential filter. This picture was obtained by blinding the gas laser beam while the breakdown was being produced. By subtracting from the combination of the emission and absorption signals (Fig. VIII-3) the signal of the emission alone (Fig. VIII-4), both being detected in the same geometry, the optical thickness, aL , of the plasma is thus determined at every time of the plasma's life.

This subtraction of data taken during different sparks, is allowed by the fairly good reproducibility of the emission and absorption. By calculating theoretically, as a function of the radius and of the temperature of the plasma, the value $P_{\text{plasma}}(T, R)$ of the emitted power impinging on the photomultiplier tube, and knowing R through measurements of the velocity of the radial expulsion of the bubble, the temperature T can be calculated at the instant t^* in which relation (1) is true, as a function of P_ℓ . P_ℓ is measured by substituting for the photomultiplier a colorimetric cell (401 spectra physics power meter), which calibrates the whole geometry. By using different values of the

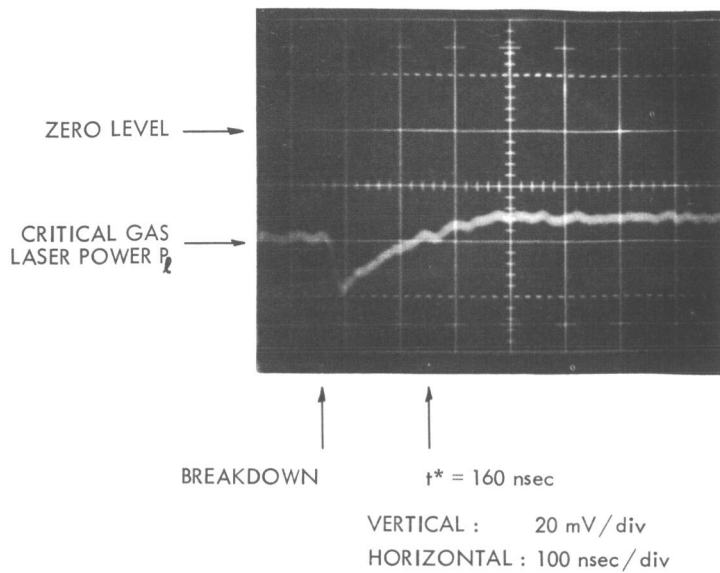


Fig. VIII-3.
Typical emission curve from the plasma.

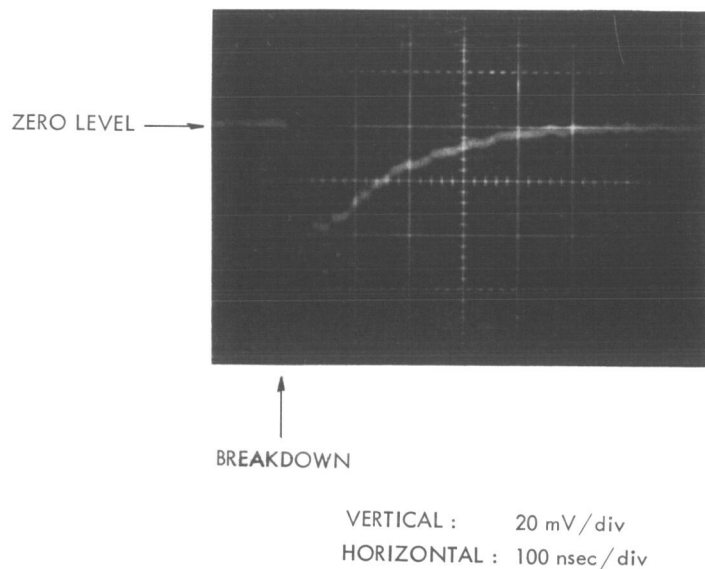


Fig. VIII-4. Typical absorption curve.

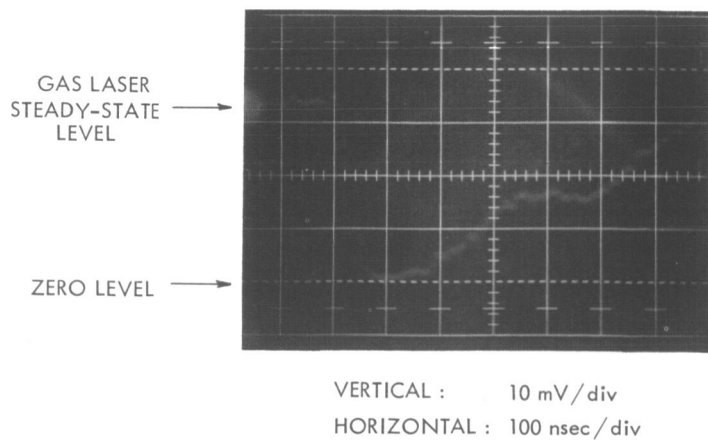


Fig. VIII-5.
Signal combination of the power signals from the plasma and from the gas laser.

power of the gas laser, the instant t^* can be shifted and a sampling of the temperature of the plasma can be made. Thus far, samplings between 100 nsec and 1.2 μ sec have been obtained. By using very small-diameter diaphragms for limiting the light reaching the photomultiplier tube, it is possible to eliminate completely the contribution from the plasma emission and allow only the detection of the gas laser beam. In this situation, clear pictures of the absorption of the He-Ne laser have been obtained (Fig. VIII-5), which show that the total absorption takes place in the early stages of the life of the plasma.

Measurements of the radial expansion velocity are being made by offsetting by a known distance the helium-neon beam in a plane normal to the ruby beam and measuring the delay in the absorption effect.

By moving in known amounts the position of the lens, focussing the ruby laser, and measuring the delay in the absorption on the helium beam, measurements of the expansion velocity along the cylindrical axis of the plasma are being made; previous measurements give values of 2.5×10^5 cm/sec at 11.5 atm pressure. Theoretical work is under way on the calculation of $P_{\text{plasma}}(R, T)$.

Further experimental work will be related to the study of the dependence of T on the pressure of the gas and on improving the geometry of the detection.

When the diameter of the plasma is large with respect to the acceptance of the diaphragms, a simplification made by averaging on the solid angle through which the beams from the plasma spark are received by the photomultiplier gives

$$P_{\ell} e^{-aL} + \xi B(T) (1 - e^{-aL}) = P_{\ell}, \quad (2)$$

where ξ is a constant depending on the geometry and on the interference filter characteristics, and $B(T)$ is the Planck function.

The factor $(1 - e^{-aL})$ drops out and the quantity $B(T)$ is proportional to the measured P_{ℓ} .

$$B(T) = \frac{P_{\ell}}{\xi}.$$

At 110 nsec after breakdown, a temperature of 4 ev has been calculated in this way.

G. Lampis

References

1. S. L. Mandel'shtam et al., Soviet Phys. - JETP 22, No. 1 (January 1966).
2. Ya. Zel'dovich and Yu. Raizer, Soviet Phys. - JETP 20, No. 3 (March 1965).
3. Yu. Raizer, Soviet Phys. - JETP 21, No. 5 (November 1965).
4. G. Akor'yan and M. S. Rabinovich, Soviet Phys. - JETP 21, No. 1 (July 1965).
5. D. Ryutov, Soviet Phys. - JETP 20, No. 6 (July 1965).
6. R. G. Meyerand, Jr. and A. F. Haught, Phys. Rev. Letters 1, 9 (November 1, 1963).
7. R. G. Meyerand, Jr. and A. F. Haught, Phys. Rev. Letters 13, 1 (July 6, 1964).

IX. GASEOUS ELECTRONICS*

Academic and Research Staff

Prof. S. C. Brown
Prof. W. P. Allis

Prof. G. Bekefi
Prof. J. C. Ingraham

J. J. McCarthy
W. J. Mulligan

Graduate Students

J. C. de Almeida Azevedo
A. J. Cohen

G. A. Garosi
J. E. McCintock

T. T. Wilheit, Jr.
B. L. Wright

A. ELECTRON-ATOM COLLISION FREQUENCY IN THE CESIUM AFTERGLOW

In a previous Quarterly Progress Report¹ experimental measurements of the electron cyclotron absorption line shape were reported. These measurements were used to deduce the approximate variation of the electron-atom collision frequency as a function of electron velocity and the result was found not to agree, except over limited ranges of electron velocity, with the collision frequency measurements of others. This was not necessarily unexpected, since the other experiments do not agree very well among themselves.

Subsequently, measurements made with the use of the same technique have yielded collision frequencies in agreement with the originally reported values. A computer analysis has been developed in which the collision frequency as a function of velocity, $\nu_c(v)$, is determined from the temperature dependence of the half-width at half maximum, $\Delta(T)$, of the electron cyclotron absorption coefficient. Previous to the development of the computer program, an approximate collision frequency had been determined by setting it equal to $\Delta(T)$. This gives the exact answer only for cases in which $\Delta(T)$ is independent of temperature.

1. Computer Analysis

The electron cyclotron absorption coefficient¹ is

$$a(\omega - \omega_b, T) = \text{const} \left(\int_0^\infty \frac{v^4 \nu_c e^{-mv^2/2kT} dv}{\nu_c^2 + (\omega - \omega_b)^2} \right), \quad (1)$$

where ν_c , m , v , T , and ω_b are the electron collision frequency, mass, velocity, temperature, and radian cyclotron frequency, ω is the radian frequency of the probing signal, and k is Boltzmann's constant. The ratio

* This work was supported by the Joint Services Electronics Programs (U.S. Army, U.S. Navy, and U.S. Air Force) under Contract DA 36-039-AMC-03200(E).

(IX. GASEOUS ELECTRONICS)

$$\left[r = \frac{a(\Delta, T)}{a(0, T)} = \frac{1}{2} = \frac{\int_0^\infty \frac{v^4 \nu_c e^{-mv^2/2kT} dv}{v_c^2 + \Delta^2}}{\int_0^\infty \frac{v^4 e^{-mv^2/2kT} dv}{v_c}} \right] \quad (2)$$

defines the half-width, $\Delta(T)$, at the half-maximum of a .

The computer analysis developed initially used $\Delta(T)$ as input data and determined the polynomial form for $\nu_c(v)$ best satisfying Eq. 2. This method was found to be extremely sensitive to small variations in the input data $\Delta(T)$ and therefore unworkable.

A second approach that employs a computer program to calculate $\Delta(T)$, given a trial form for $\nu_c(v)$, has been found to be much more workable. The best form of $\nu_c(v)$ is then found by trial and error. This computer program also evaluates the averages of $\nu_c(v)$,

$$\overline{(\nu_c(v))} = \frac{\int_0^\infty \nu_c(v) v^4 e^{-mv^2/2kT} dv}{\int_0^\infty v^4 e^{-mv^2/2kT} dv} \quad (3)$$

and

$$\left(\frac{1}{\overline{\nu_c(v)}} \right)^{-1} = \left(\frac{\int_0^\infty \frac{1}{\nu_c(v)} v^4 e^{-mv^2/2kT} dv}{\int_0^\infty v^4 e^{-mv^2/2kT} dv} \right)^{-1}. \quad (4)$$

For purposes of evaluation of the program and comparison of the variation with temperature of these various averages of $\nu_c(v)$, the electron-atom collision frequency in argon as determined by Frost and Phelps² has been used as the "trial" $\nu_c(v)$ in the above-mentioned computer analysis. (The argon $\nu_c(v)$ was chosen because an experiment is now under way in which $\Delta(T)$ for argon is being measured and will be compared with the values calculated above as a check on the experimental method.)

In Fig. IX-1 are plotted $\overline{(\nu_c(v))}$, $\left(\frac{1}{\overline{\nu_c(v)}} \right)^{-1}$, and $\Delta(T)$, with the $\nu_c(v)$ values given by Frost and Phelps used in the computer program. Also plotted for comparison is the actual $\nu_c(v)$, but evaluated with $v = \left(\frac{3kT}{m} \right)^{1/2}$.

The various averages of $\nu_c(v)$ are seen to smear-out the sharper velocity dependence of the actual $\nu_c(v)$. Also, $\overline{(\nu_c(v))}$ is always greater than $\left(\frac{1}{\overline{\nu_c(v)}} \right)^{-1}$. This will always be true because, as can be seen, the integral for $\overline{(\nu_c(v))}$, Eq. 3, emphasizes the values of

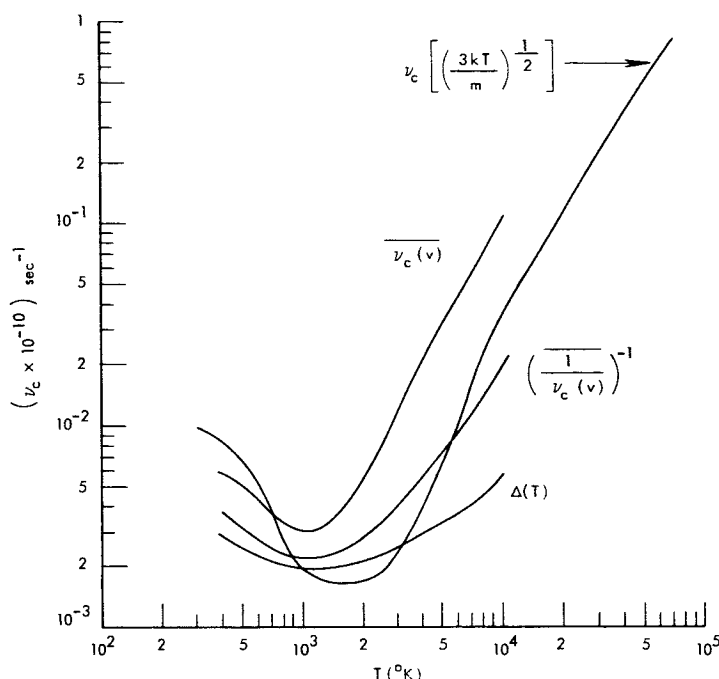


Fig. IX-1. Plotted as a function of temperature for electron-atom collisions in argon, three thermal averages of $\nu_c(v)$, $\overline{\nu_c(v)}$, $\left(\frac{1}{\nu_c(v)}\right)^{-1}$, and $\Delta(T)$ (the half-width at half-maximum of the electron cyclotron absorption curve). Shown for comparison is $\nu_c(v)$ plotted with $v = \left(\frac{3kT}{m}\right)^{1/2}$.

$\nu_c(v)$ where $\nu_c(v)$ is largest, and the integral for $\left(\frac{1}{\nu_c(v)}\right)^{-1}$, Eq. 4, emphasizes the values of $\nu_c(v)$ where $\nu_c(v)$ is smallest. It also appears to be generally true that $\Delta(T)$ is less than either of the two other averages, $\overline{\nu_c(v)}$ and $\left(\frac{1}{\nu_c(v)}\right)^{-1}$. This has also been demonstrated with several other trial forms for $\nu_c(v)$. As is seen from Fig. IX-1 these averages at a given temperature may differ by more than an order of magnitude! Experimentally, the average $\overline{\nu_c(v)}$ is measured whenever an absorption coefficient is measured with $|\omega - \omega_b| \gg \nu_c$ (see Eq. 1), as in the wings of the cyclotron absorption curve or in an absorption experiment with $\omega_b = 0$ and $\omega \gg \nu_c$. The average $\left(\frac{1}{\nu_c(v)}\right)^{-1}$ is measured at the peak of the cyclotron absorption curve (Eq. 4), or in an experimental measurement of the DC mobility of the electrons. From Eq. 1 and Fig. IX-1, it can be seen that the ratio

$$\frac{\overline{\nu_c(v)} \left(\frac{1}{\nu_c(v)}\right)^{-1}}{\Delta^2(T)} \approx \frac{(\omega - \omega_b)^2 a[(\omega - \omega_b), T]}{a(0, T) \Delta^2(T)}, \quad (5)$$

(IX. GASEOUS ELECTRONICS)

where $|\omega - \omega_b| \gg \nu_c$, will deviate from one only when $\nu_c(v)$ has a velocity dependence, being equal to one when ν_c is constant.

2. Computer Fitting of $\nu_c(v)$ to Cesium Data

Figure IX-2 shows the experimentally measured half-width of the electron cyclotron resonance in cesium plotted as a function of $(4kT/m)^{1/2}$. Also plotted is a half-width, Δ_{trial} , which was calculated by using an assumed form for ν_c . This assumed form for

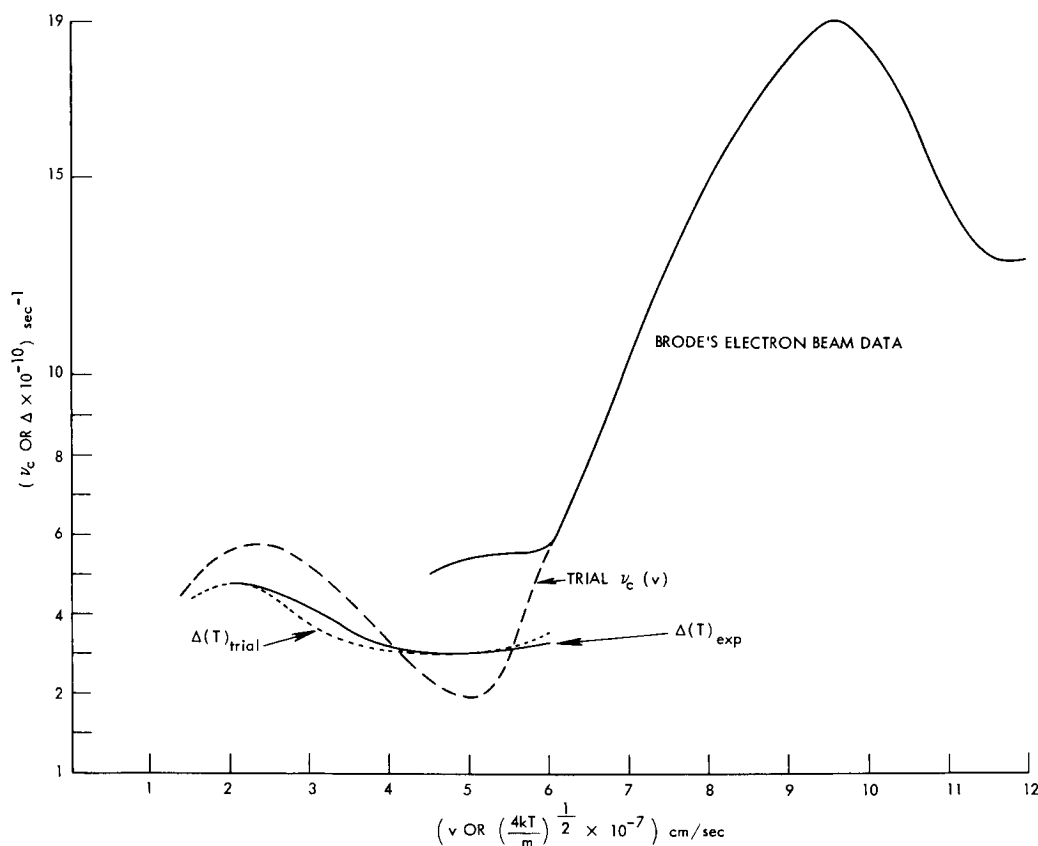


Fig. IX-2. ν_c versus velocity and Δ versus $(4kT/m)^{1/2}$, showing a comparison between the experimental and trial Δ and the form of the trial ν_c .

ν_c gave the best fit to the experimental data out of four trials and will be improved upon. This trial ν_c is also plotted on Fig. IX-2 versus velocity. For large values of v the form of ν_c was assumed to be given by Brode's electron beam data. To obtain a reasonable fitting, it was found necessary to ignore the values of ν_c obtained by Brode at low

(IX. GASEOUS ELECTRONICS)

electron velocities, as is indicated on the graph. This computer-determined form of $v_c(v)$ is still in strong disagreement with other experimental measurements and work continues in order to resolve this.

J. C. Ingraham

References

1. J. C. Ingraham, Quarterly Progress Report No. 77, Research Laboratory of Electronics, M.I.T., April 15, 1965, p. 112.
2. L. S. Frost and A. V. Phelps, Scientific Paper 64-928-113-P6, Westinghouse Research Laboratories, Pittsburgh, Pennsylvania, June 18, 1964.

X. PLASMAS AND CONTROLLED NUCLEAR FUSION

A. Active Plasma Systems*

Academic and Research Staff

Prof. A. Bers
Prof. G. D. Bernard

Prof. G. Bolz
Prof. W. D. Getty

Prof. J. G. Siambis
Prof. J. Taillet

Graduate Students

R. R. Bartsch
S. R. J. Brueck
J. A. Davis
F. N. Herba

B. R. Kusse
M. A. Lieberman
J. A. Mangano

R. R. Parker
R. D. Reilly
H. M. Schneider
R. N. Wallace

1. BEAM-PLASMA DISCHARGE: SYSTEM D

Microwave mode-shift electron density measurements have been made on System D for a beam-plasma discharge occurring in a side-injected gas pulse.¹ Two mode-shift techniques have been used: the shift of the TM_{010} mode of the discharge cavity at 740 Mc, and the higher order mode-shift technique of Fessenden.²³ Representative

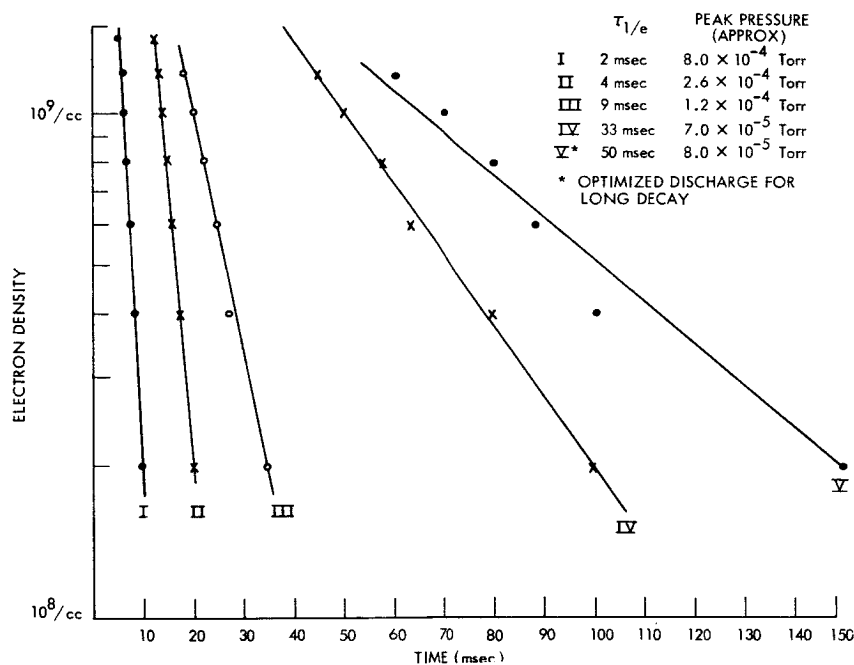


Fig. X-1. Fundamental mode-shift density decay measurement.

* This work was supported by the National Science Foundation (Grants GK-57 and GK-614).

(X. PLASMAS AND CONTROLLED NUCLEAR FUSION)

density decays of the afterglow as measured by the shift of the fundamental mode are shown in Fig. X-1 for various peak pressures. The frequency shift of the TM_{010} mode is related to the electron density by the following expression, if we assume that the plasma density is $n = n_0 \cos \pi \hat{x}/l J_0(2.405 r/R_p)$ with cavity walls at $x = \pm L/2$ and the plasma radius, R_p , equal to half the discharge-tube radius (discharge tube radius = 13 cm).

$$n_0 \text{ (in particles/cc)} = 10^2 \Delta f.$$

A typical electron density decay as measured by the higher order mode-shift technique is shown in Fig. X-2. The number of modes, l , shifted past a given frequency

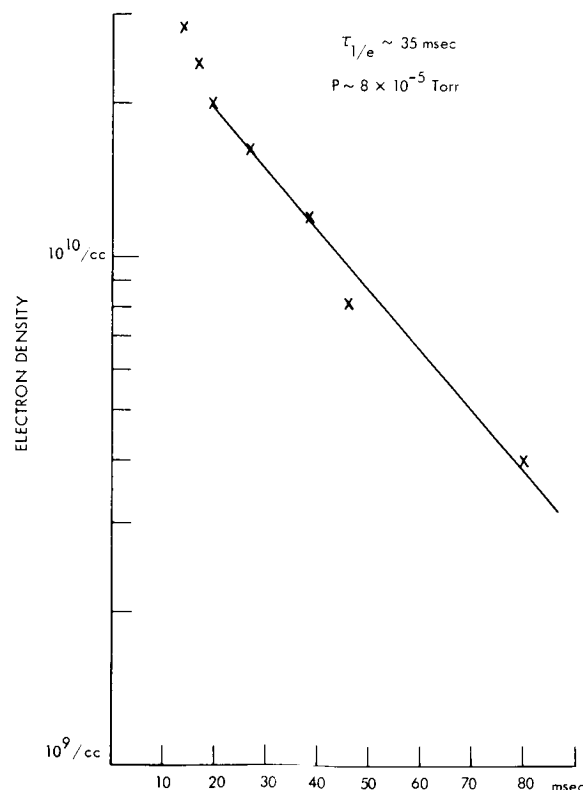


Fig. X-2. Higher order mode-shift electron density decay measurement.

is related to the mode spacing, δf , and the density as follows: n (in particles/cc) = $1300 l \delta f$, where the frequency of operation is 10 kMc/sec. We expect the mode spacing at 10 kMc to be ≈ 200 kcps; however, the experimentally observed mode shift is 3 Mc/sec. The difference is due to the overlap of adjacent modes of the cavity. Only the modes that are strongly excited are detected as distinct modes.

No explanation has been found for the factor of 5 difference between the two density

(X. PLASMAS AND CONTROLLED NUCLEAR FUSION)

measurements. Data for each were taken on different runs, and the discharge with side injection is not always reproducible from pulse to pulse.

If we assume that the decay rate is governed by electron-neutral mirror scattering losses, then we may infer an electron energy for the hot-electron component of the plasma of approximately 5 keV, using the relations given in Quarterly Progress

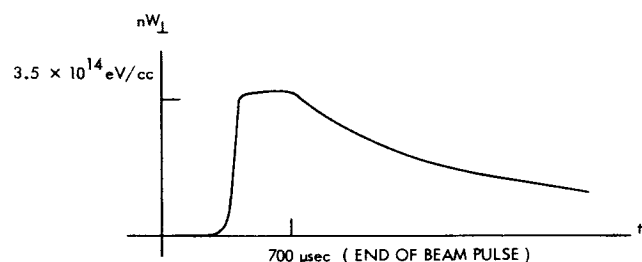


Fig. X-3. Transverse energy density from the diamagnetic signal.

Report No. 80 (pages 128-132). Since the plasma diamagnetism (Fig. X-3) does not show an immediate drop after the electron beam pulse, we assume that the diamagnetism is caused by the hot electrons (the low-energy electrons will be lost from the system within a millisecond and we would expect the diamagnetism to fall just after the beam pulse to the level resulting only from the high-energy electrons).

The initial density of hot electrons is found to be $\approx 7 \times 10^{10}/\text{cc}$ by dividing the initial diamagnetism by the energy per particle.

We can estimate the total electron density by assuming that cold electrons are produced and lost as follows: Ionizing collisions produce cold electrons at a rate given by

$$\nu_i = n_o \sigma_i v_e,$$

where n_o is the neutral (hydrogen) density, σ_i is the ionization cross section ($\sim 10^{-16} \text{ cm}^2 / (E/1 \text{ keV})^{1/2}$), and v_e is the hot-electron velocity.⁴ Cold electrons are lost from the system in the time that it takes a room-temperature ion to move half the length of the system ($\sim 1 \text{ msec}$). We have the following equation for the production and loss of cold electrons.

$$\frac{dn_c}{dt} + 10^3 n_c = 6 \times 10^{-8} n_o n_h(t),$$

where n_c is the density of cold electrons, n_h the density of hot electrons, and n_o the density of neutrals. If we assume that $n_o \approx 3 \times 10^{11}/\text{cc}$ and the hot-electron decay is $7 \times 10^{10} e^{-at}$, where $a^{-1} \gg 1 \text{ msec}$, we have the following (neglecting the initial build-up transient) result:

$$n_c(t) = 1.3 \times 10^{12} e^{-at} \text{ cm}^{-3}.$$

This analysis indicates that the density of cold electrons is approximately 20 times the density of hot electrons.

(X. PLASMAS AND CONTROLLED NUCLEAR FUSION)

Further density measurements will be made with a Fabry-Perot interferometer and with a phase-shift interferometer to determine the density during the initial, high-density portion of the decay.⁵ A Marshall valve is being constructed to give a faster, more reproducible gas pulse.⁶

The use of the facilities of the National Magnet Laboratory for this experiment is gratefully acknowledged.

R. R. Bartsch

References

1. L. D. Smullin, W. D. Getty, T. Musha, and R. R. Bartsch, Quarterly Progress Report No. 78, Research Laboratory of Electronics, M. I. T., July 15, 1965, pp. 102-105.
2. S. C. Brown and D. J. Rose et al., Technical Reports No. 66, 140, 222, 223, 230, Research Laboratory of Electronics, M. I. T.
3. T. J. Fessenden, Sc.D. Thesis, Department of Electrical Engineering, M. I. T., June 1965.
4. D. J. Rose and M. Clark, Jr., Plasmas and Controlled Fusion (The M. I. T. Press Cambridge, Mass., 1961), p. 39.
5. M. A. Lieberman, Quarterly Progress Report No. 76, Research Laboratory of Electronics, M. I. T., January 15, 1965, pp. 109-111.
6. H. Forsen, "Fast Acting Valve Which Operates at Temperatures up to 400°C," Rev. Sci. Instr. 35, 1362 (1964).

2. BEAM-PLASMA DISCHARGE: SYSTEM C

a. Digital Data System

In the course of experiments concerned with ion-cyclotron wave generation in System C, a need arose for a means of obtaining time-resolved averages of signals having relatively large variance. Standard methods of obtaining such averages (for example, sample-and-hold circuits followed by electronic integration) proved to be of little use, on account of the low repetition rate (1/sec). The difficulty was that the signal-to-noise ratio of a collection of samples ("signal" defined as mean, and "noise" as variance) improves as \sqrt{N} , where N is the number of samples. To obtain a reliable estimate of the mean, a large number of samples, say, 100, was required. Because of the low repetition rate, this involved a long real-time interval, and the long-term stability of existing circuitry was not sufficient to produce reliable results.

The problem was solved by using the digital system shown in Fig. X-4. The input signal is sampled at a given time with respect to the firing of the beam pulse. The sample is then converted to digital form by the analog-to-digital converter (ADC) and the digital form is counted and stored in a preselected channel of a 400-channel counter. The process is repeated once per beam pulse and each subsequent count is added to the count existing in the selected channel. When enough samples have been taken to insure

(X. PLASMAS AND CONTROLLED NUCLEAR FUSION)

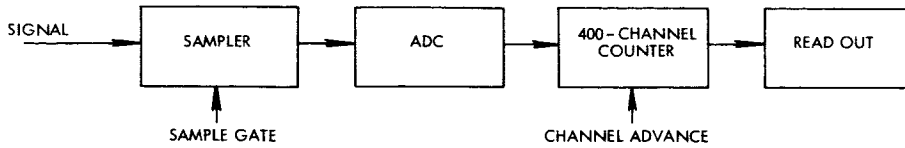


Fig. X-4. Digital data system.

reliability, the count is read out on a cathode-ray tube presentation or x-y recorder.

In the usual application, we want to obtain a plot of the sampled signal as a function of some variable such as magnetic field, distance into the discharge, and so forth. When this is the case, the variable is slowly changed by mechanical means and the counting channel is simultaneously advanced, again, only after a sufficient number of samples have been accumulated. If the variable is time relative to the initiation of the beam pulse, the time of the sampling gate may be slowly varied in the manner just described or, more efficiently, the "sample gate" may be a burst of 400 sampling gates uniformly distributed over the time of interest. In this mode it is necessary that each gate also serve as a channel advance, so that each sample is stored in a different channel, and that the whole system be reset before the occurrence of each beam pulse.

An example of the use of the system in the ion-cyclotron wave experiment¹ is shown in Fig. X-5. Here we have plotted the axial dependence of the azimuthal component of wave magnetic field as a function of distance from the collector for two frequencies.

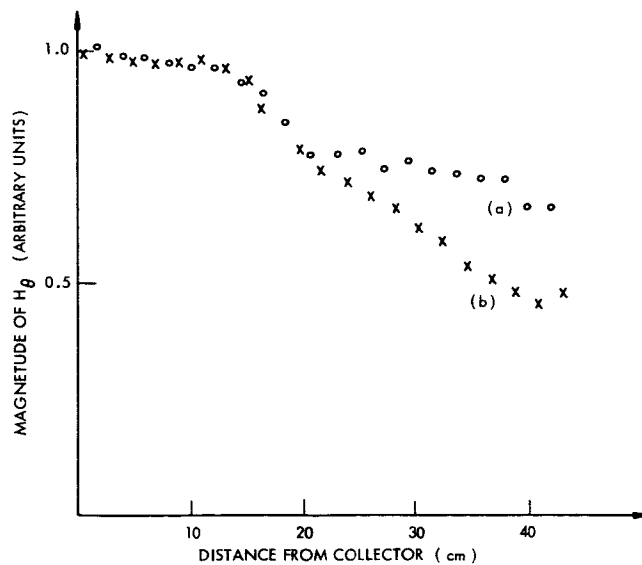


Fig. X-5. Plots of H_θ vs distance from collector: (a) $f = 1.1$ Mc;
(b) $f = 1.3$ Mc with $f_{ci} = 1.4$ Mc.

(X. PLASMAS AND CONTROLLED NUCLEAR FUSION)

Each point represents the average of approximately 50 pulses. Curves such as these are found to be very reproducible and are yielding valuable information on the propagation of waves near the ion-cyclotron frequency.

b. Ion-Cyclotron Wave Generation

We have previously reported effects associated with wave propagation in the plasma near ω_{ci} .¹ Further wave-field measurements, as well as measurement of the electrode impedance, have failed to reveal the expected rapid shortening of the wavelength for $\omega < \omega_{ci}$. This negative result must be a consequence of either damping processes that

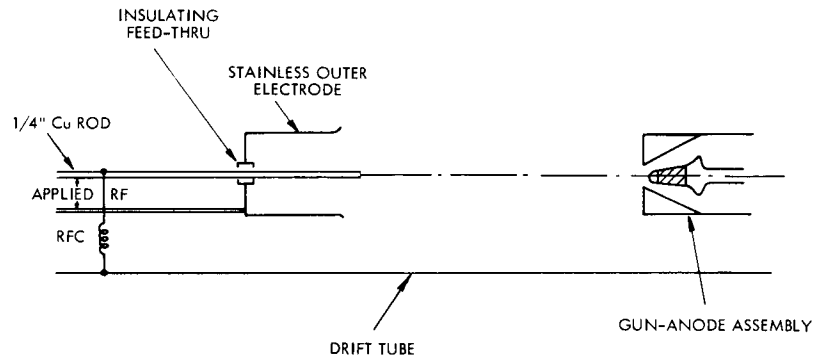


Fig. X-6. New wave-launching system.

are not contained within a theory based on cold plasma plus resistivity² or a larger resistivity than our experimental conditions predict.

To eliminate possible effects at the boundary of the plasma, we have installed the wave-launching system shown in Fig. X-6. The purpose of this system is to better confine the waves within the body of the plasma and thus minimize any effects associated with the plasma boundary. The first experiment was to measure the radial dependence of the azimuthal magnetic field at a point 45 cm from the beam collector and at a frequency of 1.06 Mc, well below the ion-cyclotron frequency of 1.4 Mc. The result is shown in Fig. X-7; thus our expectation that the wave fields are well contained within the plasma column is confirmed.

The curve shown in Fig. X-7 has an implication that may be important. From the cold-plasma plus resistivity theory one obtains a dispersion equation which, for the branch of interest, yields an axial wave number which, for $\omega < \omega_{ci}$, is essentially real and independent of radial wave number. (The last feature is a consequence of the small impedance presented to electron current flow along the field lines.) The implication, as far as the system of Fig. X-5 is concerned, is that the RF fields should be confined to an annular region defined by those field lines intersecting the outer surface of the inner electrode and the inner

(X. PLASMAS AND CONTROLLED NUCLEAR FUSION)

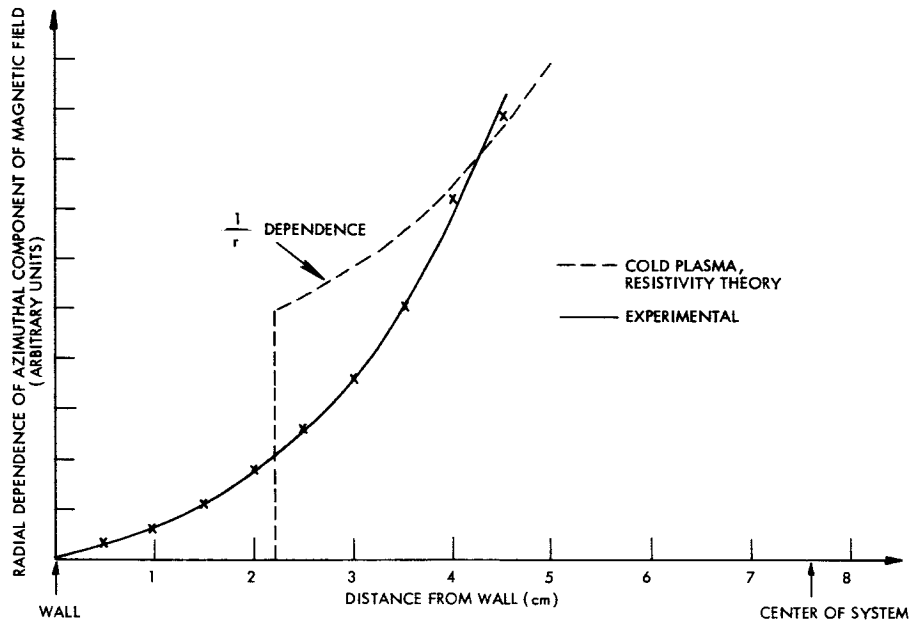


Fig. X-7. Radial dependence of wave field 45 cm from the collector, $f = 1.06$ Mc.

surface of the outer electrode. Hence, this theory predicts the radial dependence shown (dashed) on Fig. X-6. As this is not the case experimentally, we conclude that the cold-plasma plus resistivity theory does not adequately explain our results.

We are now considering the effects of viscosity on the cold-plasma theory, as well as the possibility of an enhanced resistivity resulting from the unstable nature of our beam-generated plasma. The last effect has apparently been observed in a hollow-cathode arc by Boulassier and co-workers, and many of our results could be explained simply as a result of an anomalously high resistivity.

R. R. Parker

References

1. R. R. Parker, "Beam-Plasma Discharge: System C," Quarterly Progress Report No. 80, Research Laboratory of Electronics, M.I.T., January 15, 1965, pp. 115-117.
2. F. I. Boley, J. M. Wilcox, A. W. DeSilva, P. R. Forman, G. W. Hamilton, C. N. Watson-Munro, "Hydromagnetic Wave Propagation near Ion Cyclotron Resonance," *Phys. Fluids* 6, 925 (1963).
3. J. C. Boulassier et al., *Proc. VI Conference on Ionization Phenomena in Gases*, Paris, 1963, Vol. I, p. 359.

3. ELECTRON BEAM EXCITATION OF ION OSCILLATIONS IN AN ECRD PLASMA

a. Beam-Excited Low-Frequency Oscillations

Strong electron beam-excited low-frequency oscillations (6-25 Mc) have been observed

(X. PLASMAS AND CONTROLLED NUCLEAR FUSION)

in the electron-cyclotron resonance discharge (ECRD). These oscillations appear over a wide range of discharge pressures, magnetic fields, and beam voltages. Typically, a 50-300 volt electron beam, of perveance 1×10^{-6} , is injected into a stainless-steel discharge tube, 7 inches in diameter and 3 ft long. Hydrogen gas is continuously admitted to the discharge tube so as to maintain a gas pressure of $1-10 \times 10^{-5}$ torr. A static magnetic field with a central value of 350-550 gauss and a mirror ratio of approximately 3 is maintained along the axis of the discharge tube. The ECRD is excited by a 2450-Mc "cooking" magnetron driven by an unfiltered, 3-phase power supply. RF power pulses approximately 2 msec long are generated every 8.3 msec, as shown in Fig. X-8. The average power incident on the ECRD plasma is 180 watts, while the absorbed power varies from 70 watts to 100 watts, over the range of pressures and magnetic fields encountered in this experiment.

When both the electron beam and the ECRD are simultaneously activated, strong low-frequency oscillations appear in the beam-collector current. These oscillations appear primarily in the afterglow region of the ECRD, as shown in the middle column of Fig. X-9. The oscillations disappear or are greatly reduced if either the beam or the plasma is turned off. Therefore they must arise from a beam-plasma interaction.

To study the axial variation of the beam-excited oscillations, a 4-ft section of 8-mm Pyrex glass tubing was sealed at one end and mounted against the discharge tube inner wall, with its length parallel to the axis of the discharge tube. A coaxial \bar{E} probe, 4 ft

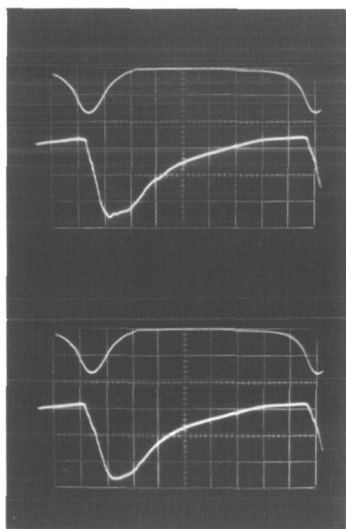


Fig. X-8.

RF power pulse and diamagnetic signal vs time. Upper trace: RF power pulse. Lower trace: diamagnetic signal. Time scale, 1.0 msec/cm.

long and 1/8 inch in diameter, was slid into the glass tube to study the variation of the axial electric field as a function of axial distance. Preliminary measurements indicate that the probe and glass tube do not disturb the beam or plasma, and that the

(X. PLASMAS AND CONTROLLED NUCLEAR FUSION)

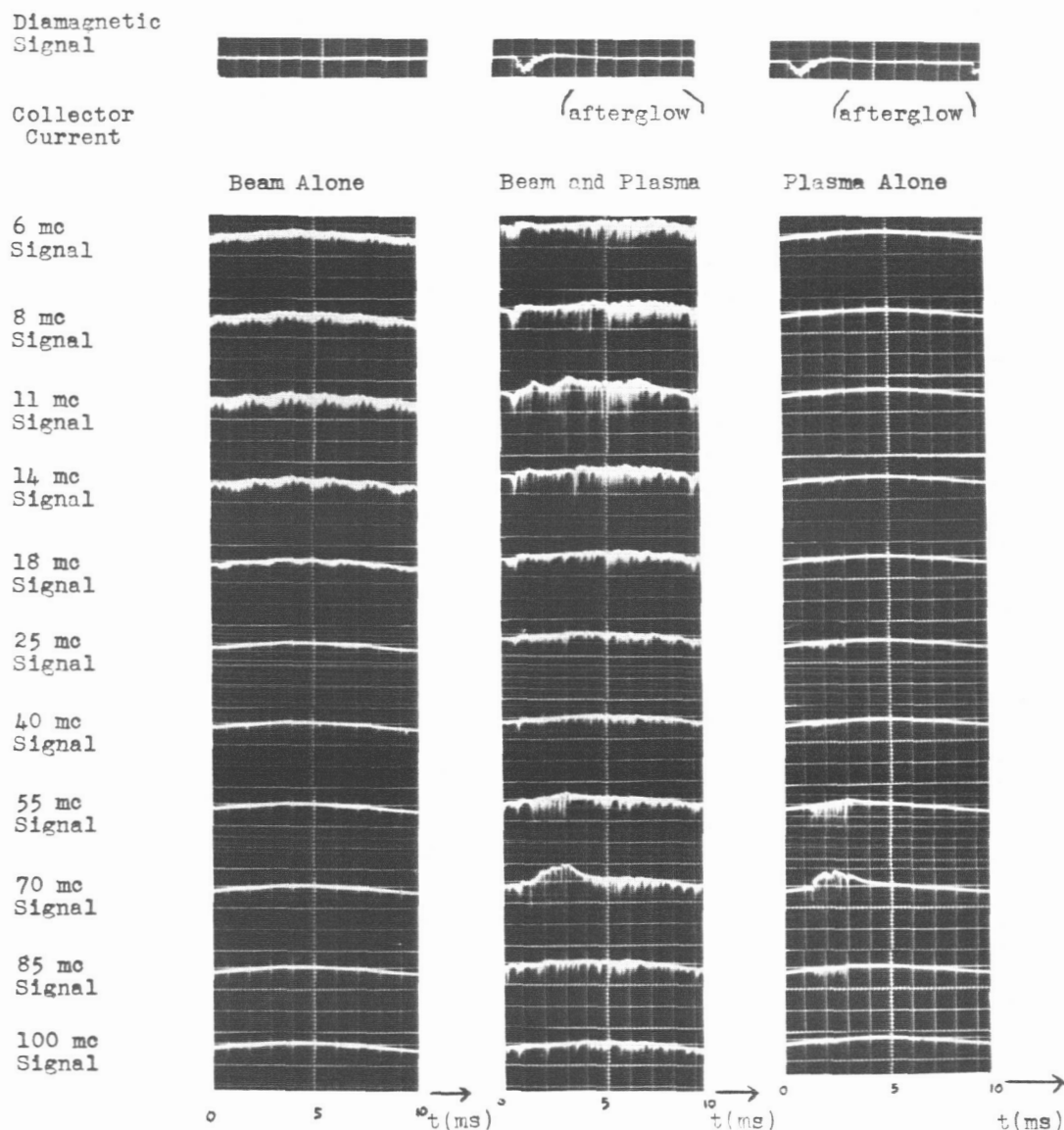


Fig. X-9. Time characteristics of the beam-excited RF oscillations. Pressure: 10^{-4} torr H_2 gas. Central magnetic field: 420 gauss. Average incident power: 180 watts. Average absorbed power: 80 watts. Beam voltage: 300 volts. Beam perveance: 1.0 microperv. Time scale: 1.0 msec/cm.

beam-excited oscillations observed in the collector current also appear on the axial probe. A rough sketch of the "strength" of the beam-excited oscillations as a function of axial distance is shown in Fig. X-10. This sketch shows that the oscillations are well confined to the center of the magnetic mirror. Since the E probe is against the inner discharge tube wall, the oscillations are not confined to the beam region in the center of the plasma, but extend outward radially to the discharge tube wall.

(X. PLASMAS AND CONTROLLED NUCLEAR FUSION)

Previous attempts¹⁻⁴ with the same apparatus to observe a low-frequency beam-plasma interaction were unsuccessful. The electron beam was velocity-modulated at

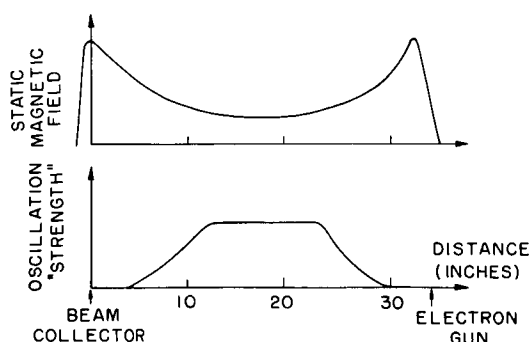


Fig. X-10.

Strength of the beam-excited RF oscillations as a function of axial distance.

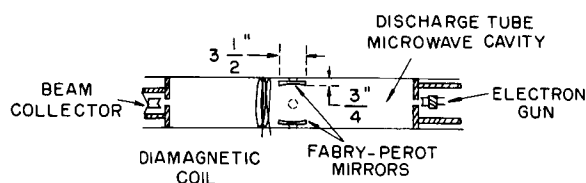


Fig. X-11.

Diagram of the discharge tube showing the Fabry-Perot mirrors and the diamagnetic coil. The RF power pulses are fed into the discharge tube through a circular port in the center of the tube.

low frequencies (20-200 Mc) in an effort to detect even a weak beam-plasma interaction, but no interaction was observed. The negative result of these experiments was traced to a pair of Fabry-Perot microwave interferometer mirrors which were placed inside the discharge tube to measure the plasma density. Each mirror was $3\frac{1}{2}$ inches in diameter and $\frac{1}{2}$ inch thick, and protruded approximately $\frac{3}{4}$ inch into the discharge tube, as shown in Fig. X-11. In the course of these experiments, a diamagnetic probe consisting of 40 turns of wire was wound around the discharge tube. With the Fabry-Perot mirrors in place, no diamagnetic signal could be observed. (Typical plasma densities of 10^9 - 10^{10} electrons/cm³ were measured with the Fabry-Perot interferometer.) The mirrors were then removed, and a strong diamagnetic signal was detected. Simultaneously, the beam-excited low-frequency oscillations of Fig. X-9 made their appearance. If, with the mirrors absent, a glass or grounded metal rod is inserted in the radial direction more than $\frac{3}{4}$ inch into the discharge tube, then the diamagnetic signal is extinguished. It is unlikely that much plasma is present so close to the discharge tube wall. Wall sensors show that the plasma is well confined in the radial direction. More probably, the effect of the mirrors and radial rods is to modify the electric field in the discharge, so that the hot electrons are not contained by the mirror magnetic field. In any case, the Fabry-Perot mirrors were permanently removed from the system.

b. X-ray Bremsstrahlung Spectra

The ECRD generates a flux of x rays exceeding 5 roentgens/hr, for some values of the pressure and magnetic field. The Bremsstrahlung spectra of these x rays were

measured by using a 400-channel pulse-height analyzer with a scintillating crystal of sodium iodide. The x-ray detector was collimated so that x rays generated at the walls of the discharge tube could not be detected by the scintillating crystal. Only x rays generated in the center of the magnetic mirror could pass through the collimator and reach the detector.

Time-resolved measurements of the x-ray spectra were made by gating the analyzer on for synchronized periods after each microwave power pulse. In this way, the time dependence of the spectra could be studied. A typical time-resolved x-ray spectrum is shown in Fig. X-12. From the exponential falls of spectra such as these, the

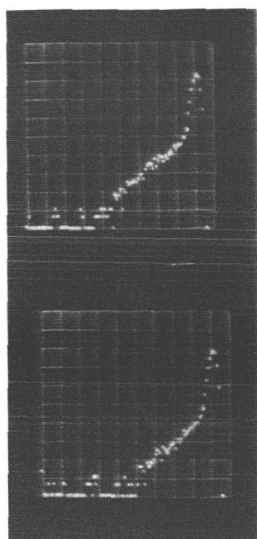


Fig. X-12. X-ray Bremsstrahlung spectrum. Ordinate: relative photon intensity on a logarithmic scale, 10^5 counts full scale. Abscissa: 75 keV full scale, reading from right to left. Central magnetic field: 420 gauss. Average incident power: 180 watts. Average absorbed power: 80 watts. Pressure: 2.7×10^{-4} torr H_2 gas. Analyzer gated on for 1.0 msec, beginning 2.0 msec after the initial rise of the diamagnetic signal.

"temperature" of the hot electrons was determined. If the electron distribution is Maxwellian, then the Bremsstrahlung spectrum should fall⁵ as $\exp(-E/T)$, where T is the temperature of the electrons (in energy units) and E is the photon energy.

Experimental studies of the x-ray spectra for various magnetic fields and pressures have yielded the following results:

- (i) The "tail" of the electron distribution function is Maxwellian, corresponding to a "temperature" of 5-9 keV.
- (ii) The "temperature" as a function of time is roughly constant. The only effect of looking at longer times after each power pulse is a decrease in the photon intensity; thus a decay of the plasma density is indicated. The exponential fall of the x-ray spectrum remains constant.

It is possible to calculate a decay time τ_s for the hot-electron component of the plasma. The hot-electron density decays because the hot electrons are scattered into the loss cone of the magnetic mirror and lost. The dominant scattering process in the

(X. PLASMAS AND CONTROLLED NUCLEAR FUSION)

ECRD is electron-neutral collisions. For scattering of fast electrons by neutrals, the scattering frequency⁶ is

$$\frac{1}{\tau_s} = \frac{p}{T^{3/2}} 3.1 \times 10^7 (1 + .275 \ln T), \quad (1)$$

where p is the neutral gas pressure in torr, and T is the electron energy in kilovolts.

The decay time τ_s calculated from (1) can be compared with the decay of the diamagnetic signal. Figure X-8 shows a typical diamagnetic signal during one power

Table X-1. Scattering times τ_s and τ_d for various pressures. Average magnetic field: 420 gauss. Average incident power: 180 watts. Average absorbed power: 80 watts.

Pressure (torr)	τ_s (msec)	τ_D (msec)
1.9×10^{-4}	1.4	1.8
2.6×10^{-4}	1.9	1.9
5.2×10^{-4}	0.8	1.0

pulse of the ECRD. This signal is obtained by integrating the voltage developed across a 40-turn coil wrapped around the outside of the discharge tube. After the RF power pulse has ended, the diamagnetic signal decays exponentially with a time constant τ_D . In Table X-1, τ_D and τ_s are compared for various pressures.

In calculating τ_s , the neutral-gas pressure was measured with a Bayard-Alpert gauge, which was calibrated against a McLeod gauge to give a measurement of absolute pressure. The hot-electron "temperature" was determined by the x-ray Bremsstrahlung measurements.

M. A. Lieberman, A. Bers

References

1. Quarterly Progress Report No. 73, Research Laboratory of Electronics, M. I. T., April 15, 1964, pp. 81-85.
2. Quarterly Progress Report No. 75, Research Laboratory of Electronics, M. I. T., October 15, 1964, pp. 120-121.
3. Quarterly Progress Report No. 76, Research Laboratory of Electronics, M. I. T., January 15, 1965, pp. 109-111.
4. Quarterly Progress Report No. 77, Research Laboratory of Electronics, M. I. T., April 15, 1965, pp. 137-140.
5. T. J. Fessenden, Sc.D. Thesis, Department of Electrical Engineering, M. I. T., June 1965, p. 117.
6. Ibid., p. 105.

4. INSTABILITIES IN HOT-ELECTRON BEAM-PLASMA SYSTEMS

In a hot-electron, Maxwellian plasma, the dispersion function $D(\omega, k, \dots)$ is transcendental, and no analytical method for obtaining its roots exists. Therefore, computer solutions are often necessary. A computer program to find the roots of D has been written. This program uses the Newton-Raphson method to follow a root of D as some parameter of the dispersion function D is varied. The user must provide an initial guess that is "close" to the root he wishes to follow. Using this program, the dispersion diagrams of several beam-plasma systems have been studied.

a. Longitudinal Waves in a Cold-Ion Hot-Electron Plasma

In Quarterly Progress Report No. 79 (pages 126-130) the dispersion equation for longitudinal waves in a cold-ion, hot-electron plasma was considered:

$$1 - \frac{\omega_{pi}^2}{\omega^2} - \frac{\omega_{pb}^2}{(\omega - \beta V_o)^2} + \frac{1}{\beta^2 \lambda_D^2} \left[1 + \frac{1}{\sqrt{2} \beta \lambda_D} \frac{\omega}{\omega_{pe}} Z \left(\frac{1}{\sqrt{2} \beta \lambda_D} \frac{\omega}{\omega_{pe}} \right) \right] = 0. \quad (1)$$

The discussion of this dispersion equation given there must be corrected. The caption on p. 129 of Q.P.R. No. 79 should read: (a) $\eta = \frac{1}{4}$ (b) $\eta = 1$ where $\eta = \frac{n_b}{n_p} \frac{V_T^2}{V_o^2}$. Thus Briggs' condition¹ $\eta > 1$ for a strong ion interaction is not met for either of the dispersion diagrams in Quarterly Progress Report No. 79 (page 129). In fact, as Briggs has pointed out,² the condition $\eta > 1$ leads to an ion interaction in a Maxwellian plasma in which the gain is infinite for frequencies just below ω_{pi} . Thus, one always has a solution of Eq. 1 with $|\beta| \rightarrow \infty$ as $\omega \rightarrow \omega_{pi}$. A stability analysis shows that this solution is evanescent for $\eta < 1$ and convectively unstable for $\eta > 1$.

Figure X-13a shows the dispersion diagram of the convectively unstable solution of Eq. 1 for $\eta < 1$. The stability analysis for this solution is presented in Fig. X-13b. The gain is finite and is peaked at a frequency slightly below ω_{pi} . For $\omega < \omega_{pi}$, the gain is large and represents reactive medium amplification of the slow beam wave by the "inductive" plasma ions. For $\omega > \omega_{pi}$, the gain is very small and represents resistive medium amplification of the slow beam wave by the Landau damped plasma electrons.

Figure X-13c shows the transition occurring when $\eta > 1$. The convectively unstable solution of Eq. 1 now has an infinite growth rate for ω slightly below ω_{pi} . The stability analysis for this solution is shown in Fig. X-13d.

The gain mechanism is a reactive medium amplification for $\omega < \omega_{pi}$ and resistive (Landau damping) medium amplification for $\omega > \omega_{pi}$, as before. Note that in the weak-beam limit $n_b \ll n_p$, the condition $\eta = 1$ requires $V_T \gg V_o$. Landau damping is small in

(X. PLASMAS AND CONTROLLED NUCLEAR FUSION)

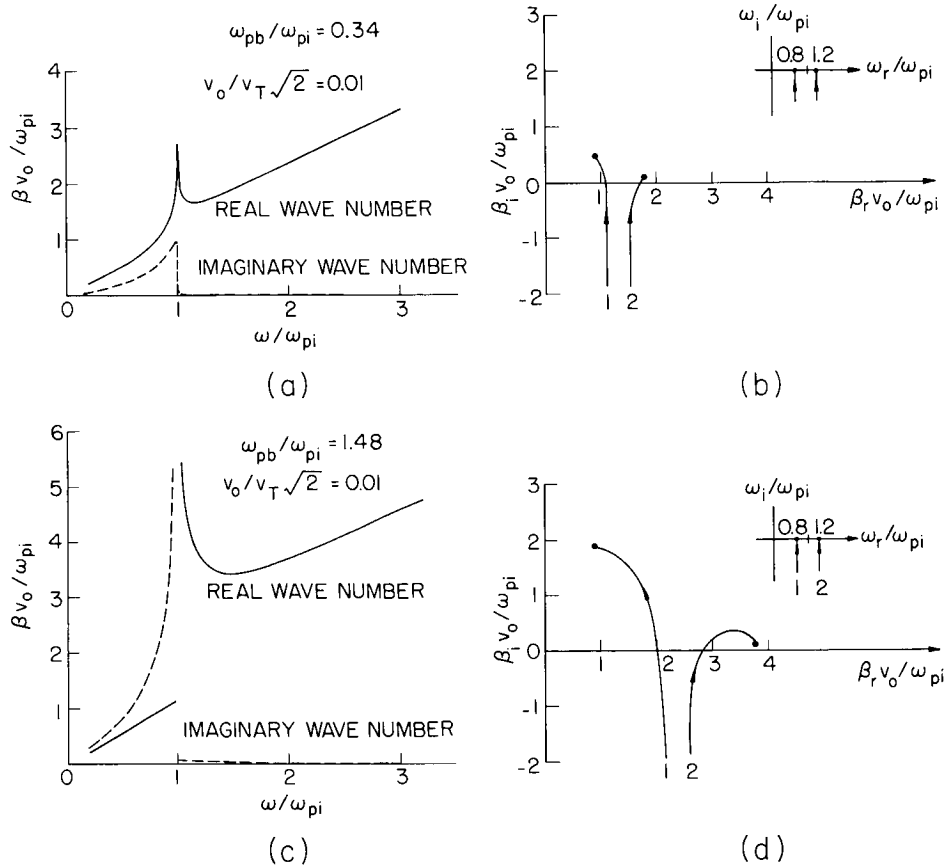


Fig. X-13. Beam-plasma dispersion equation for longitudinal waves (Landau damping and ion motions included). (a) $\eta = 0.32$. (b) Stability criteria for $\eta = 0.32$. (c) $\eta = 6.0$. (d) Stability criteria for $\eta = 6.0$.

this limit, so the resistive medium amplification rates are very small.

It is clear from Eq. 1 that a finite ion temperature would lead to a finite growth rate at ω_{pi} in all cases.

b. Onset of the Absolute Ion Instability in a Hot-Electron, Beam-Plasma Waveguide

Consider a waveguide of radius a whose axis is parallel to the static magnetic field \vec{B}_0 . The waveguide is uniformly filled with a plasma consisting of cold ions and Maxwellian electrons of thermal velocity V_T . An electron beam uniformly filling the waveguide drifts along the magnetic field with a constant velocity V_o .

Under the assumption that as a boundary condition the tangential electric field vanishes at the walls, the quasi-static dispersion equation is

$$K_e + K_i + K_b - 2 = 0, \quad (2)$$

where

$$K_i = 1 - \frac{k_{\parallel}^2 \omega_{pi}^2}{k^2 \omega^2} - \frac{k_{\perp}^2 \omega_{pi}^2}{k^2 \omega^2 - \omega_{ci}^2} \quad (3)$$

$$K_b = 1 - \frac{k_{\parallel}^2 \omega_{pb}^2}{k^2 (\omega - k_{\parallel} V_o)^2} - \frac{k_{\perp}^2 \omega_{pb}^2}{k^2 (\omega - k_{\parallel} V_o)^2 - \omega_{ce}^2} \quad (4)$$

$$K_e = 1 + \frac{\omega_{pe}^2}{k^2 V_T^2} \left[1 + \sum_{n=-\infty}^{\infty} I_n(\lambda) e^{-\lambda} \zeta_o Z(\zeta_n) \right] \quad (5)$$

$$\lambda = \frac{k_{\perp}^2 V_T^2}{\omega_{ce}^2} = \left(\frac{\text{Larmor radius}}{\text{Waveguide radius}} \right)^2 \quad (6)$$

$$\zeta_n = \frac{\omega - n\omega_{ce}}{k_{\parallel} V_T \sqrt{2}} \quad (7)$$

and the linearized potential is assumed to vary as

$$\exp[-j(\omega t - k_{\parallel} z)] J_m(k_{\perp} r) e^{jm\phi}. \quad (8)$$

The boundary condition at the waveguide wall requires that

$$k_{\perp} = \frac{\epsilon_{m\ell}}{a}, \quad (9)$$

where $\epsilon_{m\ell}$ is the ℓ^{th} zero of J_m . Consider the limit of large magnetic fields, for which $\lambda \ll 1$ and $\omega_{pb} \ll \omega_{ce}$, but $\omega_{pi} \gg \omega_{ci}$. For many beam-plasma systems of interest, these assumptions are well satisfied. Physically, they state that the beam and plasma electrons are constrained to move only along the field lines. The transverse motion of the ions is allowed, however, because of their larger mass. Excluding cyclotron harmonic frequencies $n\omega_{ce}$ and wave numbers for which $k \approx \omega_{ce}/V_o$, the dispersion equation (2) can be written

$$k_{\parallel}^2 \left[1 - \frac{\omega_{pi}^2}{\omega^2} - \frac{\omega_{pb}^2}{(\omega - k_{\parallel} V_o)^2} - \frac{\omega_{pe}^2}{2k_{\parallel}^2 V_T^2} Z' \left(\frac{\omega}{k_{\parallel} V_T \sqrt{2}} \right) \right] + k_{\perp}^2 \left[1 - \frac{\omega_{pi}^2}{\omega^2 - \omega_{ci}^2} \right] = 0, \quad (10)$$

where Z' is the derivative of the plasma dispersion function, tabulated by Fried and Conte.³

(X. PLASMAS AND CONTROLLED NUCLEAR FUSION)

Several authors have studied Eq. 10 under one approximation or another. Briggs¹ considered the limit $\omega/k_{\parallel} V_T \sqrt{2} \ll 1$ and showed that an absolute instability could exist near the ion plasma frequency ω_{pi} , even when the plasma in the absence of the beam supports only a forward travelling wave. This result cannot be predicted by weak coupling theory. Briggs' condition for the absolute ion instability can be written

$$\omega_{pb} \gtrsim \omega_{pi}, \quad \text{provided } V_T/V_o \gg 1. \quad (11)$$

Puri⁴ and Wallace⁵ both considered a dispersion equation similar to (10), in which the hot electrons were represented by a rectangular velocity distribution function instead of a Maxwellian. Their condition for the absolute ion instability can be written

$$\omega_{pb} \gtrsim \omega_{pi}, \quad V_T \gtrsim V_o. \quad (12)$$

Both Puri and Wallace realized that their condition (12), obtained for a rectangular distribution of electrons, could not be applied to a Maxwellian distribution in the region of heavy Landau damping $V_T \sim V_o$. Therefore, their condition (12) does not correctly describe the onset of the absolute ion instability in a Maxwellian plasma. This condition can be obtained only by properly accounting for the Landau damping.

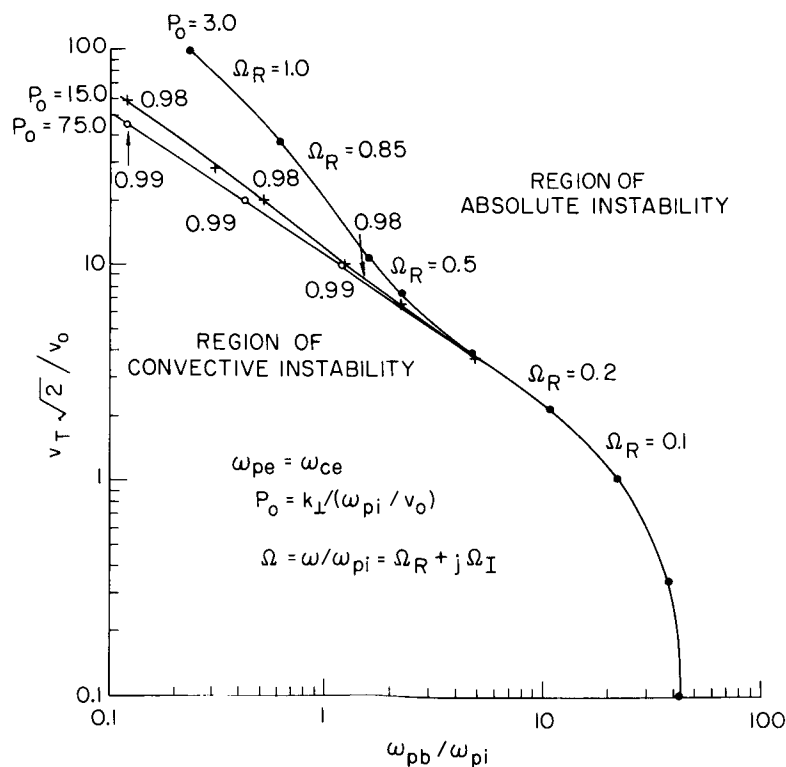


Fig. X-14. Onset of absolute ion instability in a hot-electron beam-plasma waveguide.

(X. PLASMAS AND CONTROLLED NUCLEAR FUSION)

In this report the condition for the onset of the absolute ion instability in a Maxwellian plasma has been determined by numerically setting the lhs of (10) and its derivative with respect to k_{\parallel} equal to zero. For a given set of system parameters, the frequency ω and wave number k_{\parallel} are determined from these two equations. The additional constraint $\text{Im } \omega = 0$ then imposes a relation among the system parameters, which is the onset condition. This condition is shown in Fig. X-14. The quantity $V_T \sqrt{2}/V_0$ is plotted along the ordinate, and the quantity ω_{pb}/ω_{pi} is plotted along the abscissa. For a given value of $P_0 = k_{\perp} V_0/\omega_{pi}$, the onset condition $\text{Im } \omega = 0$ divides the graph into two regions. In the upper right-hand region, the absolute ion instability is obtained. In the lower left-hand region, only a convective instability exists. Alongside the line $\text{Im } \omega = 0$, and for each value of P_0 , the real part of the normalized frequency ω/ω_{pi} is specified. This frequency is the oscillation frequency of the beam-plasma system at the onset of absolute instability.

The onset condition has been computed for $\omega_{ce} = \omega_{pe}$ as pertinent to our beam-plasma experiment in an ECRD plasma. The magnetic field \bar{B}_0 enters into the problem only through the ion cyclotron frequency ω_{ci} , so, for $|\omega| \gg \omega_{ci}$, the onset condition $\text{Im } \omega = 0$ is essentially independent of the magnetic field.

M. A. Lieberman, A. Bers

References

1. R. J. Briggs, Electron Stream Interaction with Plasmas (The M.I.T. Press, Cambridge, Mass., 1964), Chapter 5.
2. R. J. Briggs, Private communication (1966).
3. B. Fried and S. Conte, The Plasma Dispersion Function (Academic Press, New York, 1961).
4. S. Puri, "Electron Beam Interaction with Ions in a Warm Electron Plasma," S.M. Thesis, Department of Electrical Engineering, M.I.T., June 1964. See also Quarterly Progress Report No. 74, pp. 121-128.
5. R. N. Wallace, "An Investigation of Complex Waves in Electron Beam-Plasma Systems," S.M. Thesis, Department of Electrical Engineering, M.I.T., September 1964. See also Quarterly Progress Report No. 76, pp. 111-117.

5. THEORY OF VHF OSCILLATIONS AND POSSIBLE INTERACTIONS WITH IONS IN THE BEAM-PLASMA DISCHARGE

In the beam-plasma discharge, a pulsed electron beam of moderate perveance when injected into a low-pressure gas produces a plasma to which it gives up a considerable portion of its DC kinetic energy. In his study of the beam-plasma discharge, Getty¹ observed strong RF oscillations and scattering of beam electrons across confining magnetic fields of several hundred gauss. Hsieh² studied the frequency spectrum and

(X. PLASMAS AND CONTROLLED NUCLEAR FUSION)

time dependence of the RF power radiated by the beam-plasma discharge in some detail. He observed RF radiation principally in two bands of frequencies, the kMc band (7 kMc to 27 kMc) and the VHF band (30 Mc to 600 Mc). Hsieh interpreted the kMc oscillations as electron plasma oscillations. This interpretation was verified by Getty, who actually measured the density of the plasma. In experiments with different gases, Hsieh attempted to interpret the VHF oscillations as ion plasma oscillations; however, the results of these experiments were inconclusive.

It is shown here that the gross features of the frequency spectrum of the VHF oscillations observed in the beam-plasma discharge may possibly be understood in terms of a model in which the VHF oscillations arise from the interaction of a filamentary electron beam with a uniformly filled cold-plasma waveguide immersed in a uniform, longitudinal magnetic field. This interaction causes a snaking or "firehose" motion of the beam, corresponding to an azimuthal wave number n equal to plus or minus one. Since the gain for this interaction is relatively small and the interaction is convective, an efficient feedback mechanism is a necessary part of this model.

In the model, the kMc oscillations are electron plasma oscillations; that is, the oscillations are characteristic of the electron plasma frequency ω_{pe} . The VHF oscillations are not "tied" to the ion plasma frequency ω_{pi} , but rather arise from the coupling between a propagating plasma wave and a slow-beam cyclotron wave. The frequency at which this coupling occurs may turn out to be in the vicinity of ω_{pi} .

a. Experimental Observations of the Beam-Plasma Discharge by Hsieh

Figure X-15 illustrates the time characteristics of the beam generated plasma studied by Hsieh, in which a 200- μ sec pulse of electron beam current is injected into a volume of gas at pressures of 10^{-3} - 10^{-4} torr in a magnetic mirror to produce a plasma. The idealized plasma geometry of the beam-plasma discharge is shown in Fig. X-16.

At some time T_B ($\approx 50 \mu$ sec) into the beam pulse, a burst of strong oscillations near ω_{ce} (≈ 800 Mc) appears. These oscillations are accompanied by scattering of beam electrons across the confining magnetic field and by a rapid rise in the plasma density. These oscillations near ω_{ce} usher in the regime of beam-plasma discharge proper. This regime is characterized by steady light and diamagnetic signals, by energetic plasma electrons (as evidenced by the X-ray signal) and by strong RF oscillations. The frequency spectra of these RF oscillations were measured by Hsieh for three different time intervals within the beam-plasma discharge and for three different gases. The behavior of these frequency spectra can be summarized as follows:

- (i) The RF radiation is concentrated in two bands of frequencies, the kMc band (7-27 kMc) and the VHF band (30-600 Mc).
- (ii) There is a missing band of frequencies, extending from 600 Mc to 7 kMc and

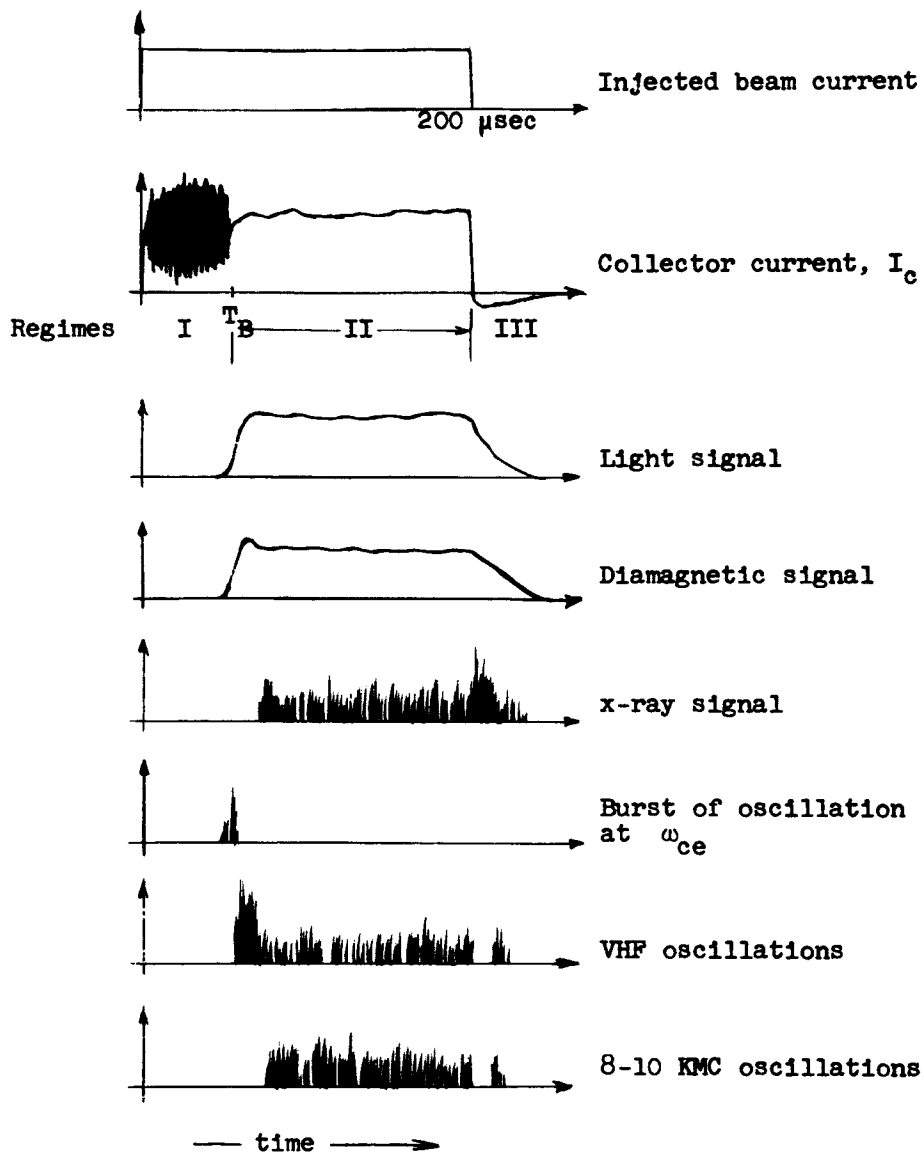


Fig. X-15. Time characteristics of the beam-plasma discharge (after H. Hsieh, Sc.D. Thesis, M.I.T., 1964, p. 37).

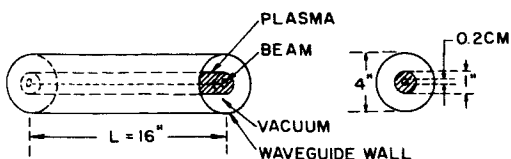


Fig. X-16. Idealized plasma geometry of the beam-plasma discharge (after H. Hsieh, Sc.D. Thesis, M.I.T., 1964).

(X. PLASMAS AND CONTROLLED NUCLEAR FUSION)

including the electron cyclotron frequency ω_{ce} (890 Mc), in which no RF oscillations are observed.

(iii) The kMc band shifts toward higher frequencies as the delay time, the beam voltage or the gas pressure is increased.

(iv) The frequency spectrum of the VHF oscillations is relatively independent of the delay time, type of gas, gas pressure, and (over a limited range) beam voltage.

b. Weak Coupling of a Filamentary Electron Beam with a Cold Plasma Waveguide

Physically, the VHF oscillations can be understood in terms of two dispersion diagrams, Figs. X-17 and X-18. These two dispersion diagrams show the coupling of beam and plasma waves for the circularly symmetric (azimuthal wave number $n = 0$, Fig. X-17) and noncircularly symmetric ($n = \pm 1, \pm 2$, etc., Fig. X-18) modes in the filamentary beam approximation.

The model is a plasma-filled waveguide of radius a . An electron beam of radius $b \ll a$ flows down the center of the waveguide. The electrons and ions of the plasma have zero temperature. Experimentally, the VHF oscillations are observed for frequencies roughly one-half to one-third of the electron cyclotron frequency ω_{ce} . For such frequencies, the filamentary beam approximation can be made and proved to be valid. This approximation stated that

$$\begin{aligned} pb &\ll 1 \\ qb &\ll 1, \end{aligned} \tag{1}$$

where p and q are the transverse wave numbers in the beam and plasma regions, respectively. In this approximation, only two beam waves appear for the $n = 0$ mode (n is the azimuthal wave number, $n = 0$ is the circularly symmetric mode). These waves are the "beam space-charge" waves. No "beam cyclotron" waves appear for the $n = 0$ mode. This is to be expected, since the electric field is purely longitudinal at the position of the beam ($r = 0$) for this mode.

A synchronism between the "slow beam-space-charge" wave and the propagating plasma wave can only occur if the beam velocity v_o is equal to the phase velocity v_{ph} of a plasma wave somewhere in the VHF region.

In Fig. X-17 we show the situation generally occurring in the beam-plasma discharge for the $n = 0$ mode. The phase velocity v_{ph} of the forward propagating plasma waves in the VHF region is less than or equal to $\frac{\omega_{ce}}{x_{nm}} a$, where x_{nm} is the n^{th} zero of the m^{th} -order Bessel function J_m . Since in the beam-plasma discharge

$$v_o > \frac{\omega_{ce} a}{x_{o0}} > \frac{\omega_{ce} a}{x_{no}} > v_{ph}, \tag{2}$$

(X. PLASMAS AND CONTROLLED NUCLEAR FUSION)

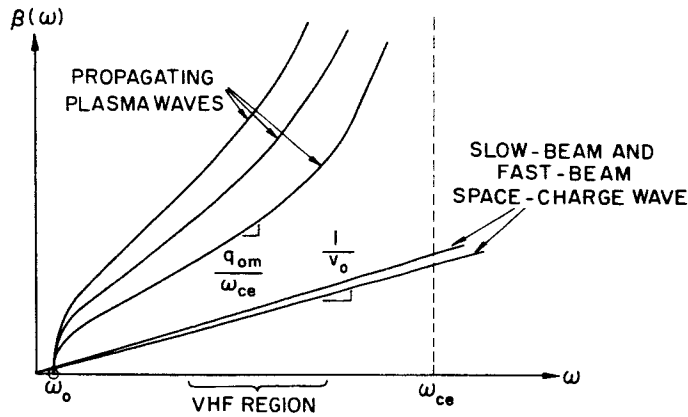


Fig. X-17. Beam waves and propagating plasma waves for the $n = 0$ (circularly symmetric) mode.

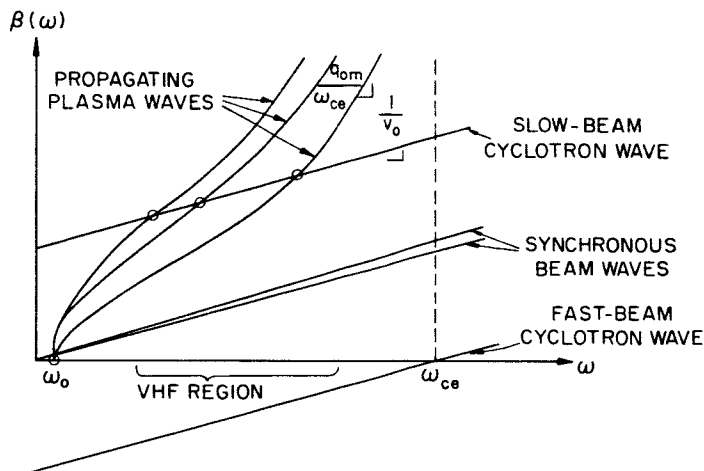


Fig. X-18. Beam waves and propagating plasma waves for the $n \neq 0$ (noncircularly symmetric) modes.

no intersection occurs in the VHF region. The intersection in Fig. X-17 near the lower hybrid frequency $\omega_0 = \frac{1}{43} \omega_{ce}$ is not within the VHF region.

In Fig. X-18, the situation generally occurring in the beam-plasma discharge is shown for all modes other than the $n = 0$ mode. The $n = \pm 1$ modes are the "fire-hose" modes, corresponding to a snaking motion of the beam. The $n = \pm 2$ modes have a double angular variation, and so on. For each pair ($\pm 1, \pm 2, \pm 3$, etc.) of noncircularly symmetric modes, four beam waves appear: two "synchronous" beam waves and two "cyclotron" beam waves. The slow cyclotron wave intersects the plasma waves in the VHF region, as shown by the circles in Fig. X-18. This intersection between a negative and positive energy wave must lead to a convective instability.

(X. PLASMAS AND CONTROLLED NUCLEAR FUSION)

The dispersion equation for the interaction of a filamentary beam with a cold plasma waveguide is^{3,4}

$$\frac{\omega_{pb}^2}{\omega_d(\omega_d + \omega_{ce})} = \frac{2K_{\perp}}{1 + \frac{\pi}{4} q^2 b^2 \frac{N_1(qa)}{J_1(qa)}} \quad (3)$$

Near synchronism between the slow-beam cyclotron wave and the propagating plasma waves of Fig. X-18, $J_1(qa) \approx 0$. Expanding J_1 in a Taylor series, one finds

$$J_1(qa) \approx -\frac{2}{\pi \beta_o N_1(q_{n1}a)} (\beta - \beta_o). \quad (4)$$

Using (4), one can cast (3) into the form

$$(\beta - \beta_o) \left(\beta - \frac{\omega}{v_o} - \frac{\omega_{ce}}{2v_o} - \frac{1}{v_o} \sqrt{\frac{\omega_{ce}^2}{4} + \frac{\omega_{pb}^2}{2K_{\perp}}} \right) = -c_o^2(\omega). \quad (5)$$

Here, $c_o(\omega)$ is to be evaluated at the synchronous frequency and is given by

$$c_o(\omega) = \frac{\pi \omega_{pb} q_{n1} b N_1}{4v_o} \left(\frac{\omega}{2K_{\perp}} \right)^{\frac{1}{2}} \left(\frac{\omega_{ce}^2}{4} + \frac{\omega_{pb}^2}{2K_{\perp}} \right)^{\frac{1}{4}}. \quad (6)$$

The maximum amplification rate occurs exactly at synchronism and is

$$(\beta_i)_{\max} = c_o(\omega). \quad (7)$$

c. Comparison Between Theory and Experiment

The theoretical growth rates have been calculated from Eq. 7. For the experimental parameters shown in tabular form below, the first few interaction frequencies and their growth rates are

$\omega_1 = 460 \text{ mc}$	$\beta_{i1} = .0048/\text{cm}$
$\omega_2 = 380 \text{ mc}$	$\beta_{i2} = .0054/\text{cm}$
$\omega_3 = 240 \text{ mc}$	$\beta_{i3} = .0052/\text{cm}$

These growth rates are quite small. The effect of a finite temperature or collision frequency on the magnitude of these gains has not been investigated.

(X. PLASMAS AND CONTROLLED NUCLEAR FUSION)

These amplification rates could not by themselves lead to the observed VHF oscillations. For a 40-cm system, these rates correspond to a power amplification of only 1.6 db over the length of the discharge. Unless the power is fed back to the entering beam, oscillations at these frequencies will not take place. Therefore, a feedback mechanism is a necessary part of this theory if it is to be relevant for explaining the observed VHF oscillations in the beam-plasma discharge. One possible feedback device is the plasma wave propagating in the negative z direction. This wave has a negative real β and a negative group velocity v_g . It is the mirror image (about the frequency axis) of the forward propagating plasma wave shown in Fig. X-18. This negative z -directed wave is only slightly perturbed by the filamentary beam. The feedback system then consists of the positive z -directed wave having a gain $\approx .005/\text{cm}$ and a group velocity v_o , coupled with the negative z -directed wave having a gain of unity and a group velocity v_g . Oscillations will build up in this feedback system at a rate ω_i given by

$$\omega_i = \beta_i \frac{v_o v_g}{v_o + v_g}. \quad (8)$$

For the parameters of Table X-1, the time constant $\tau = 2\pi/\omega_i$ for the buildup of VHF oscillations in the discharge is

$$\tau = 1 \text{ } \mu\text{sec.} \quad (9)$$

Thus this simple feedback mechanism might explain the observation of VHF oscillations in the beam-plasma discharge.

A detailed study of the predictions of the filamentary beam theory shows:

1. In the frequency range $460 \text{ Mc} < f < 2.7 \text{ kMc}$, which includes the cyclotron frequency $f_{ce} = 890 \text{ Mc}$, no RF oscillations should be present.
2. Below 460 Mc, VHF oscillations should be excited which display a mode structure; that is, the frequency spectrum of these oscillations should consist of a series of peaks which begin to blur together as the frequency f is decreased greatly below 460 Mc.
3. The RF intensity of the VHF oscillations should be greater near the beginning of the beam-plasma discharge since the amplification rate β_i given by (7) is a monotonically decreasing function of plasma density.
4. The VHF oscillation frequencies should be only a function of ω_{ce} , v_o , and a . That is, the frequencies at which VHF oscillations occur should be independent of the plasma density, type of gas, gas pressure, beam perveance, beam diameter, and beam density. On the other hand, the oscillation amplitudes should be functions of all these parameters.

These theoretical predictions are all borne out by Hsieh's data.

(X. PLASMAS AND CONTROLLED NUCLEAR FUSION)

Table X-1. Typical parameters for the beam-plasma discharge studied by Hsieh.

Beam pulse length = 170 μ sec
Beam breakup $T_B = 4$ to 6 μ sec
Beam voltage $V_b = 6$ kev
Beam velocity $v_o = 4.6 \times 10^9$ cm/sec
Beam perveance $K = 1.0 \times 10^{-6}$
Beam diameter $2b = 0.2$ cm
Beam density $n_b = 2.0 \times 10^{10}$ cm $^{-3}$
Beam-plasma frequency $\omega_{pb} = 1.3$ kMc = 8.0×10^9 /sec
Mirror ratio $R \approx 3$
Central magnetic field $B_o = 280$ gauss
Electron cyclotron frequency $\omega_{ce} = 0.89$ kMc = 5.6×10^9 /sec
Ion cyclotron frequency $\omega_{ci} = 0.48$ Mc = 3.0×10^6 /sec H_2
Hybrid frequency $\sqrt{\omega_{ce}\omega_{ci}} = 21.0$ Mc = 1.3×10^8 /sec H_2
Plasma diameter $2a = 2.5$ cm
Pressures: 1.1×10^{-3} torr H_2
2.8×10^{-3} torr He
2.5×10^{-4} torr A
Electron plasma frequency $\omega_{pe} = 15$ to 25 kMc (94 - 156×10^9 /sec)
Plasma density $n_p = 3.5$ to 4.5×10^{12} cm $^{-3}$

d. Small-Signal Ion and Electron Energies

One can calculate the small signal electron and ion oscillation energies for the VHF oscillations occurring in the beam-plasma discharge. This calculation is independent of the particular mechanism which drives the oscillations. One assumes only that VHF oscillations exist and that they are oscillations of a cold electron-ion plasma immersed in a static magnetic field \bar{B}_o .

Using the small-signal ion and electron force equations and assuming plane wave propagation at an angle to the magnetic field, one finds that the ratio of the ion-to-electron oscillation energy is given by

$$\frac{E_i}{E_e} = \frac{m}{M} \frac{1 + \omega^2 \left| \frac{K_{\parallel}}{K_{\perp}} \right| \frac{\omega^2 + \omega_{ci}^2}{(\omega^2 - \omega_{ci}^2)^2}}{1 + \omega^2 \left| \frac{K_{\parallel}}{K_{\perp}} \right| \frac{\omega^2 + \omega_{ce}^2}{(\omega^2 - \omega_{ce}^2)^2}}, \quad (10)$$

where K_{\parallel} and K_{\perp} are the parallel and perpendicular dielectric constants of the plasma. For VHF frequencies ($\omega \sim \frac{\omega_{ce}}{3}$), $E_i/E_e \approx 2\frac{m}{M}$. Therefore the VHF oscillations do not represent ion motions. No significant amount of ion oscillation energy exists at VHF frequencies.

e. Suggestions for Beam Interactions with Ions in a Cold Plasma

The ratio E_i/E_e is unity at the lower hybrid frequency $\omega_o = \sqrt{\omega_{ce}\omega_{ci}}$. The ratio E_i/E_e continues to rise as the frequency is decreased, and has a resonance at the ion cyclotron frequency ω_{ci} . The detection of RF oscillations in this frequency range in the beam-plasma discharge would indicate the presence of significant ion motions.

If energy is to be transferred from an electron beam directly to the ions of a plasma, two conditions must be satisfied.

1. There must be an interaction frequency ω for which unstable waves exist in the beam-plasma system.
2. The ratio E_i/E_e of ion-to-electron oscillation energies must be reasonably large at this interaction frequency.

There are two interaction frequencies that satisfy both of these conditions in a cold-plasma waveguide: the ion cyclotron frequency ω_{ci} and the lower hybrid frequency $\omega_o = \sqrt{\omega_{ce}\omega_{ci}}$. The growth rates for beam-plasma interactions near the ion cyclotron frequency ω_{ci} are usually quite small. One is thus led to consider whether a beam-plasma interaction at the lower hybrid frequency ω_o could significantly excite ion motions.

Convective instability at the lower hybrid frequency ω_o arises from two mechanisms:

1. reactive medium amplification for frequencies slightly below ω_o .
2. synchronous interaction between a slow beam space-charge wave and a propagating plasma wave, for frequencies slightly above ω_o .

The growth rates at the hybrid frequency ω_o can be quite large. For example, in the filamentary beam approximation, reactive medium amplification rates^{3,4} of 0.06/cm are obtained in the beam-plasma discharge. "Ion heating" might thus be accomplished by modulating the electron beam at the lower hybrid frequency ω_o .

M. A. Lieberman, A. Bers

References

1. W. D. Getty, Sc.D. Thesis, Department of Electrical Engineering, M.I.T., February, 1962.
2. H. Y. Hsieh, Sc.D. Thesis, Department of Electrical Engineering, M.I.T., June, 1964.
3. M. A. Lieberman, "Theory of VHF Oscillations in the Beam-Plasma Discharge," Internal Memorandum No. 1, December, 1965 (unpublished).
4. R. J. Briggs, Electron-Stream Interaction with Plasmas (The M.I.T. Press, Cambridge, Mass., 1960), Section 4.2.2. The notation is that of Briggs.

6. QUASI-LINEAR THEORY OF NARROW-BANDWIDTH CONVECTIVE INSTABILITIES

Consider an electron beam that is injected into a semi-infinite electron-ion plasma, plasma waveguide or other slow-wave structure. For many beam-plasma systems, linearized theory predicts that the interaction between beam and plasma gives rise to a narrow-bandwidth, convective instability.¹ By a convective instability, one means that the linearized fields vary as

$$\exp[j(\omega t - \bar{\beta} \cdot \bar{r})],$$

where the frequency ω is taken to be purely real, and $\bar{\beta}$ is complex. The imaginary part of $\bar{\beta}$ describes the growth or decay in space of the waves arising from the beam-plasma interaction. In many systems, these spatially growing waves are narrow-bandwidth; that is, the gain $\bar{\beta}_i(\omega)$ is sharply peaked within a small frequency region $\Delta\omega \ll \omega_0$ about the frequency of maximum gain ω_0 . The dispersion diagram for narrow-bandwidth, convective instability is shown in Fig. X-19.

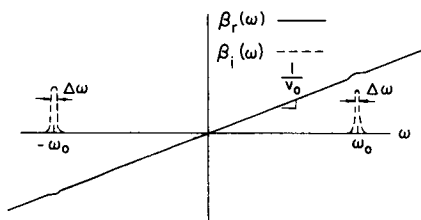


Fig. X-19. Dispersion of a narrow-bandwidth, convective instability.

In this report, we would like to investigate the onset of nonlinear effects and obtain a description of the slowing down of the electron beam. The theory and computations presented in a previous report² were found to be largely erroneous.

a. Formulation of the Quasi-Linear Theory

Each of the N species (beam electrons, plasma electrons, plasma ions, etc.) is described by the collisionless Vlasov equation

$$\left[\frac{\partial}{\partial t} + \bar{v} \cdot \frac{\partial}{\partial \bar{r}} + \frac{e}{m} (\bar{E} + \bar{v} \times \bar{B}) \cdot \frac{\partial}{\partial \bar{v}} \right] f_i = 0. \quad (1)$$

These N equations are coupled through a curl-free electric field \bar{E} (we make the electrostatic approximation):

$$\frac{\partial}{\partial \bar{r}} \times \bar{E} = 0 \quad (2)$$

$$\epsilon_0 \frac{\partial}{\partial \bar{r}} \cdot \bar{E} = \sum_i e_i n_i \int f_i d\bar{v}. \quad (3)$$

A time average $\langle \rangle$ can be defined:

$$\langle \rangle \equiv \frac{1}{T_0} \int_0^{T_0} dt, \quad (4)$$

where

$$\frac{2\pi}{\omega_0} \ll T_0 \ll \frac{2\pi}{\Delta\omega}. \quad (5)$$

Since the gain is narrow-bandwidth, the averaging time T_0 always exists.

Let us define two functions

$$f_0(\bar{r}, \bar{v}, t) \equiv \langle f(\bar{r}, \bar{v}, t) \rangle \quad (6)$$

$$f_1(\bar{r}, \bar{v}, t) \equiv f(\bar{r}, \bar{v}, t) - f_0(\bar{r}, \bar{v}, t). \quad (7)$$

It follows immediately that

$$\langle f_1 \rangle = 0. \quad (8)$$

Thus f has been decomposed into the sum of a slowly varying and a rapidly varying function of time.

We assume that no external electric field is applied, from which

$$\langle \mathbf{E} \rangle = 0. \quad (9)$$

We then write

$$\bar{\mathbf{E}}(\bar{r}, t) = 0 + \bar{\mathbf{E}}_1(\bar{r}, t). \quad (10)$$

Substituting (7) and (10) in the Vlasov equation (1) yields

$$\left[\frac{\partial}{\partial t} + \bar{\mathbf{v}} \cdot \frac{\partial}{\partial \bar{\mathbf{r}}} + \frac{e}{m} (\bar{\mathbf{E}}_1 + \bar{\mathbf{v}} \times \bar{\mathbf{B}}_0) \cdot \frac{\partial}{\partial \bar{\mathbf{v}}} \right] (f_0 + f_1) = 0. \quad (11)$$

Time averaging (11), we get

$$\left(\frac{\partial}{\partial t} + \bar{\mathbf{v}} \cdot \frac{\partial}{\partial \bar{\mathbf{r}}} + \frac{e}{m} \bar{\mathbf{v}} \times \bar{\mathbf{B}}_0 \cdot \frac{\partial}{\partial \bar{\mathbf{v}}} \right) f_0 = -\frac{e}{m} \frac{\partial}{\partial \bar{\mathbf{v}}} \cdot \langle \bar{\mathbf{E}}_1 f_1 \rangle. \quad (12)$$

Subtracting (12) from (11) yields

$$\left(\frac{\partial}{\partial t} + \bar{\mathbf{v}} \cdot \frac{\partial}{\partial \bar{\mathbf{r}}} + \frac{e}{m} \bar{\mathbf{v}} \times \bar{\mathbf{B}}_0 \cdot \frac{\partial}{\partial \bar{\mathbf{v}}} \right) f_1 + \frac{e}{m} \bar{\mathbf{E}}_1 \cdot \frac{\partial f_0}{\partial \bar{\mathbf{v}}} = -\frac{e}{m} \frac{\partial}{\partial \bar{\mathbf{v}}} \cdot \left\{ \bar{\mathbf{E}}_1 f_1 - \langle \bar{\mathbf{E}}_1 f_1 \rangle \right\}. \quad (13)$$

Note that if $\bar{\mathbf{E}}_1$ and f_1 are first-order quantities in some small parameter, then the right-hand sides of both (12) and (13) are second-order in this parameter. This suggests an iterative scheme for solving (12) and (13), in which the right-hand sides of both equations are initially set to zero. One then recovers the equations of linearized theory.

(X. PLASMAS AND CONTROLLED NUCLEAR FUSION)

In the procedure of quasi-linear theory,³ the right-hand side of (13) alone is set equal to zero. The solutions f_1 and E_1 of Eq. 13 are then explicitly obtained in terms of the unknown function f_0 . When these solutions are substituted in the right-hand side of (12), a nonlinear differential equation for f_0 is obtained. It is the fundamental equation of quasi-linear theory:

$$\left(\frac{\partial}{\partial t} + \bar{\mathbf{v}} \cdot \frac{\partial}{\partial \bar{\mathbf{r}}} + \frac{e}{m} \bar{\mathbf{v}} \times \bar{\mathbf{B}}_0 \cdot \frac{\partial}{\partial \bar{\mathbf{v}}} \right) f_0 = - \frac{e}{m} \frac{\partial}{\partial \bar{\mathbf{v}}} \cdot \langle \bar{\mathbf{E}}_1(f_0) f_1(f_0) \rangle. \quad (14a)$$

One can show that if the wave vector $\bar{\beta}$ is independent of f_0 , then the product $E_1 f_1$ appearing in (14a) would be a linear function of f_0 . In this case (14a) reduces to a diffusion equation:

$$\frac{\partial}{\partial t} + \bar{\mathbf{v}} \cdot \frac{\partial}{\partial \bar{\mathbf{r}}} + \frac{\partial}{\partial \bar{\mathbf{v}}} \cdot \left(\bar{\mathbf{D}}(\bar{\mathbf{r}}, \bar{\mathbf{v}}) \cdot \frac{\partial f_0}{\partial \bar{\mathbf{v}}} \right) = 0, \quad (14b)$$

where $\bar{\mathbf{D}}(\bar{\mathbf{r}}, \bar{\mathbf{v}})$ is the diffusion tensor.

In the interest of mathematical tractability, (14a) will be linearized by setting the wave vector $\bar{\beta}$ equal to its initial value when the beam first enters the interaction region. One expects this linearization to be valid, provided the diffusion of the beam does not significantly alter the value of the gain $\beta_1(\omega)$ from its initial value. Provided the gain is limited by other factors (finite transverse boundaries, finite plasma temperature, etc.), the effect of beam diffusion on the wave vector $\bar{\beta}(\omega)$ should be unimportant during the initial stage of the interaction.

b. Diffusion Coefficient in One Dimension

We consider a one-dimensional problem and derive the diffusion coefficient D . Let us assume that the electron beam can be described by the one-dimensional Vlasov equation

$$\left(\frac{\partial}{\partial t} + v \frac{\partial}{\partial z} + \frac{e}{m} \bar{\mathbf{E}} \cdot \frac{\partial}{\partial \mathbf{v}} \right) f(z, v, t) = 0. \quad (15)$$

The linearized solutions (E_1, f_1) are given by

$$\begin{aligned} \bar{\mathbf{E}}_1 &= - \frac{\partial \Phi_1}{\partial z} \bar{\mathbf{i}}_z \\ \Phi_1 &= \sum_n \int_{-\infty}^{\infty} d\omega \Phi_{\omega n} e^{j(\omega t - \beta_n(\omega)z)} \end{aligned} \quad (16)$$

$$f_1 = - \frac{e}{m} \frac{\partial f_0}{\partial v} \sum_n \int_{-\infty}^{\infty} d\omega \Phi_{\omega n} \frac{\beta_n(\omega)}{\omega - \beta_n(\omega)v} e^{j(\omega t - \beta_n(\omega)z)}. \quad (17)$$

(X. PLASMAS AND CONTROLLED NUCLEAR FUSION)

In Eqs. 16 and 17 we have written the linearized solutions (E_1, f_1) as a sum over elementary traveling waves. The sum over n is taken over the different branches of the dispersion function $\beta_n(\omega)$. Only one of these branches is taken to be convectively unstable. The quantity $\Phi_{\omega n}$ is the "Fourier coefficient" of the linearized solution at the real frequency ω . This coefficient describes the initial excitation of Φ_1 at $z = 0$, when the beam first enters the interaction region. Note that since Φ_1 must be a real function,

$$\Phi_{\omega n}^* = \Phi_{-\omega n}.$$

The diffusion coefficient D will now be evaluated. From (14a),

$$D = +\frac{e}{m} \langle E_1 f_1 \rangle \left(\frac{\partial f_0}{\partial v} \right)^{-1}. \quad (18)$$

Using (16) and (17), and doing the time average, we have

$$D = +\frac{e^2}{m^2} \sum_n \sum_{n'} \int d\omega \int d\omega' E_{n\omega} E_{n'\omega'} \frac{j}{\omega' - \beta_{n'}(\omega')v} e^{-j(\beta_n(\omega) + \beta_{n'}(\omega'))z} \frac{1}{j(\omega + \omega')T_0} \left(e^{j(\omega + \omega')T_0} - 1 \right) \quad (19)$$

or

$$D = \sum_{n, n'} D_{nn'}. \quad (20)$$

Here we have written

$$E_{n\omega} \equiv j\beta_n(\omega) \Phi_{\omega n}. \quad (21)$$

Physically, the double sum over n and n' represents a summation over all the waves present in the one-dimensional system. Only one of these waves, say $n = 1$, is assumed to be convectively unstable. Let the maximum gain $|\text{Im } \beta_1(\omega)|_{\text{max}}$ of this unstable wave be γ . For $\gamma z \lesssim 1$, the unstable wave has not greatly increased in amplitude over its initial value at $z = 0$. Therefore, physically, we expect each term in the sum (20) to be equally important; the contributions of the purely propagating or evanescent waves to D for $\gamma z \lesssim 1$ cannot be neglected. On the other hand, for $\gamma z \gg 1$, the amplitude of the unstable wave has increased greatly over its initial value at $z = 0$. This should manifest itself by an increase in the diffusion term D_{11} . For γz sufficiently large, we expect the term D_{11} to be much larger than any of the other terms $D_{nn'}$ in the sum (20).

Note that there is an upper limit L on the size of γz . If $\gamma z \gtrsim L$, then f_1 becomes comparable in magnitude to f_0 , and the whole procedure of quasi-linear theory, in which the right-hand sides of (12) and (13) are assumed small, is invalid. The upper limit L is set by the magnitude of the initial excitation $\Phi_{\omega n}$. If $\Phi_{\omega n}$ is "small enough," then $L \gg 1$. We then assert that

(X. PLASMAS AND CONTROLLED NUCLEAR FUSION)

$$D(z, v) \approx D_{11} \quad (22a)$$

within the range

$$1 \lesssim \gamma z \lesssim L. \quad (22b)$$

The diffusion term D_{11} is given by

$$D_{11} = \frac{e^2}{m^2} \int d\omega \int d\omega' E_{\omega} E_{\omega'} j \frac{1}{\omega' - \beta(\omega')v} e^{-j(\beta(\omega) + \beta(\omega'))z} \frac{1}{j(\omega + \omega')T_0} \left(e^{j(\omega + \omega')T_0} - 1 \right). \quad (23)$$

The gain $\text{Im } \beta(\omega)$ of the unstable wave has a positive peak γ at $\omega = \omega_0$ and $\omega = -\omega_0$, as shown in Fig. X-19. Let us expand the dispersion function $\beta(\omega)$ in a Taylor series around ω_0 and $-\omega_0$:

$$\begin{aligned} \beta(\omega_0 + s) &= q + \frac{1}{v_g} s + \dots + j \left(\gamma - \frac{1}{2} c_0 s^2 + \dots \right) \\ \beta(-\omega_0 - s) &= -q - \frac{1}{v_g} s - \dots + j \left(\gamma - \frac{1}{2} c_0 s^2 + \dots \right) \end{aligned} \quad (24)$$

in which by definition,

$$\frac{1}{v_g} \equiv \left. \frac{\partial(\text{Re } \beta)}{\partial \omega} \right|_{\omega_0} \quad (25)$$

$$c_0 \equiv - \left. \frac{\partial^2(\text{Im } \beta)}{\partial \omega^2} \right|_{\omega_0}. \quad (26)$$

The bandwidth $\Delta\omega$ thus appears in a natural manner from these expansions:

$$\Delta\omega \equiv \sqrt{\frac{2\gamma}{c_0}}. \quad (27)$$

For $\gamma z \gg 1$, the exponential space factor of the integrand in (23) is peaked near $\omega = \pm\omega_0$ and $\omega' = \pm\omega_0$. From the inequalities (5), one can thus write (23) in the form

$$D_{11} = \frac{e^2}{m^2} (I_1 + I_2), \quad (28)$$

where

$$I_1 = \int_{(\omega_0)} d\omega' \int_{(-\omega_0)} d\omega j E_{\omega} E_{\omega'} \frac{1}{\omega' - \beta(\omega')v} e^{-j(\beta(\omega) + \beta(\omega'))z} \quad (29)$$

and

$$I_2 = \int_{(-\omega_0)} d\omega' \int_{(\omega_0)} d\omega jE_\omega E_{\omega'} \frac{1}{\omega' - \beta(\omega')v} e^{-j(\beta(\omega) + \beta(\omega'))z}. \quad (30)$$

In (29) we let $\omega' = \omega_0 + s$ and $\omega = -\omega_0 - t$, use the expansions (24), and do the s and t integrations to obtain

$$I_1 = j\pi |E_{\omega_0}|^2 \sqrt{\frac{2}{c_0 z}} e^{\left(2\gamma - \frac{1}{c_0 v g^2}\right)z} Z\left(\sqrt{\frac{c_0 z}{2}} \left(qv - \omega_0 + j\gamma v + j\frac{1}{c_0 v g}\right)\right), \quad (31)$$

where $Z(y_0)$ is the plasma dispersion function, tabulated by Fried and Conte.⁴

Let us return to (30), the other half of D_{11} . Setting $\omega' = -\omega_0 - s$ and $\omega = \omega_0 + t$ in this integral and using the expansions (24), we obtain

$$I_2 = I_1^*. \quad (32)$$

Thus

$$D_{11}(\gamma z \gg 1) = -\frac{2\pi e^2}{m^2} \frac{\Delta\omega}{\sqrt{\gamma z}} |E_{\omega_0}|^2 e^{\left(2\gamma - \frac{(\Delta\omega)^2}{2\gamma v^2 g}\right)z} \text{Im} Z\left(\frac{\sqrt{\gamma z}}{\Delta\omega} \left(qv - \omega_0 + j\gamma v + j\frac{(\Delta\omega)^2}{2\gamma v g}\right)\right). \quad (33)$$

The terms in $(\Delta\omega)^2$ can usually be neglected, since $\Delta\omega$ is assumed small. Furthermore, for most systems, the argument of the Z function is much larger than unity, even at resonance $v = \omega_0/q$, unless the gain γ is very small. Expanding the Z function in an asymptotic series, one obtains a simplified form for the diffusion coefficient D :

$$D_{11}(\gamma z \gg 1) = -\frac{2\pi e^2}{m^2} |E_{\omega_0}|^2 (\Delta\omega)^2 \frac{e^{2\gamma z}}{\gamma z} \frac{\gamma v}{(\omega_0 - qv)^2 + \gamma^2 v^2}. \quad (34)$$

Note that (34) has a singularity in the limit as $\gamma z \rightarrow 0$; however, D_{11} is not correctly given by (34) in this limit. In fact, we shall neglect the diffusion of the beam in the region $\gamma z \lesssim 1$.

c. Beam Diffusion in the Steady State

Assume that at $t = 0$, an electron beam is injected into a semi-infinite interaction region. After the initial transients have died out, the beam will reach a steady state, in which the velocity diffusion of the beam will be a function of the distance z from the beam entrance plane $z = 0$. Accordingly, we set $\frac{\partial}{\partial t} \equiv 0$ in the diffusion equation to obtain

$$v \frac{\partial f_0}{\partial z} + \frac{\partial}{\partial v} \left(D(z, v) \frac{\partial f_0}{\partial v} \right) = 0, \quad (35)$$

(X. PLASMAS AND CONTROLLED NUCLEAR FUSION)

where $D(z, v)$ is given by (33) or (34). One can demonstrate the following properties concerning all distribution functions f_0 that satisfy (35):

1. The number of beam electrons is conserved. Proof: Integrate (35) over all velocity space.

2. The distribution function has a velocity derivative $(\partial f_0 / \partial v)_{v=0}$ which is zero for any z . Proof: Expand (35) and take the limit $v \rightarrow 0$, using (34) to evaluate the limiting form of the diffusion coefficient D .

3. Beam electrons are never reflected or "turned around" in velocity space. Proof: Integrate (35) over negative velocities and use 2.

4. Assume that the entering beam is monoenergetic at $\gamma z \approx 1$. Then initially, the beam loses power provided $v_0 > \omega/q$. Proof: The power flow $p(z)$ is given by

$$p(z) = \int_0^\infty dv v^3 f_0(v, z).$$

Multiply (35) by v^2 and integrate over positive velocities. The second term can be integrated by parts twice to yield

$$\left(\frac{\partial p}{\partial z} \right)_{\gamma z \lesssim 1} = - \frac{\partial}{\partial v} (v D(z, v))_{v=v_0}$$

From (34), it then follows that

$$\left(\frac{\partial p}{\partial z} \right)_{\gamma z \lesssim 1} < 0, \text{ provided } v_0 > (\omega_0/q) \text{ which is the condition for the existence of a}$$

convective instability. Q. E. D.

Computations on the diffusion of f_0 for a particular example are at present in progress.

M. A. Lieberman, A. Bers

References

1. R. J. Briggs, Electron-Stream Interaction with Plasmas (The M.I.T. Press, Cambridge, Mass., 1964). The interaction of a filamentary electron beam with a cold-plasma waveguide gives rise to a narrow-bandwidth convective instability for frequencies slightly below the upper hybrid. As another example, the interaction of an electron beam with a slow-wave structure, as in a traveling-wave tube, can give rise to a narrow-bandwidth, convective instability.
2. Quarterly Progress Report No. 79, Research Laboratory of Electronics, M.I.T., October 15, 1965, pp. 118-126.
3. W. E. Drummond and D. Pines, "Non-linear Stability of Plasma Oscillations," Nuc. Fusion 1962, Suppl. Part 3, pp. 1049-1057. In the usual technique of quasi-linear theory, $\bar{\beta}$ is considered to be purely real, and ω is complex. This technique is not suitable for the study of convective instability.
4. B. Fried and S. Conte, The Plasma Dispersion Function (Academic Press, New York, 1961).

(X. PLASMAS AND CONTROLLED NUCLEAR FUSION)

7. WAVE-MIRROR HEATING

In our last report,¹ we looked at the heating of electrons reflecting off hard walls (idealized magnetic mirrors) in the presence of a longitudinal traveling wave. We found that this heating could be considerable, if the walls were perfectly reflecting or if the electrons bounced back from the walls with a phase random to the entering phase.

Computer experiments were run to check the theory, since a number of approximations had been made. The heating arising from the hard walls and the random phase of the re-entry model was even greater than expected (Fig. X-20).

Computer experiments were also run with a more realistic model of the mirrors. For a wave varying as $\cos(\omega t - kz)$, distances were normalized to k^{-1} , times to ω^{-1} .

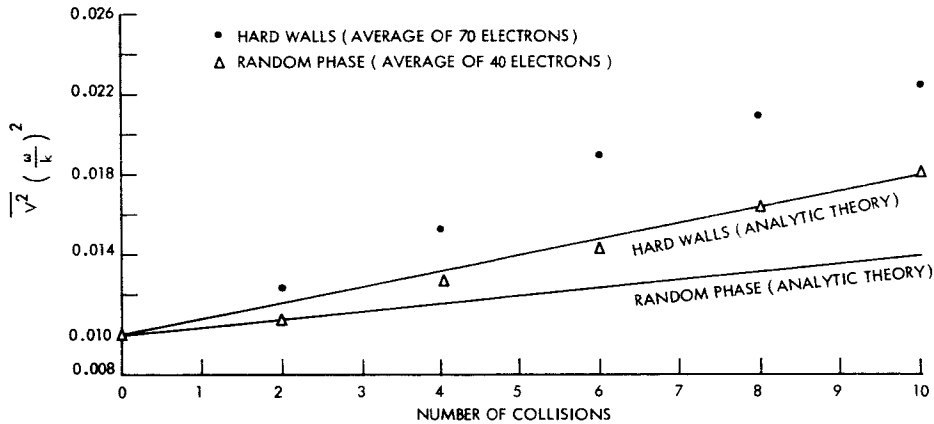


Fig. X-20. Average energy gain vs number of wall collisions.
(Hard walls and random phase of re-entry.)

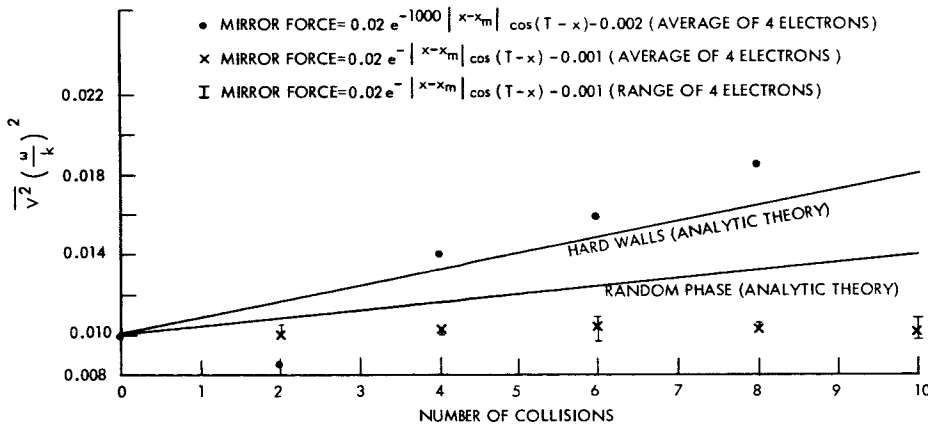


Fig. X-21. Average energy gain vs number of mirror collisions.
(Constant decelerating force in mirrors, with exponentially decaying waves.)

(X. PLASMAS AND CONTROLLED NUCLEAR FUSION)

The wave (normalized), varied as $0.02 \cos(t-x)$ between the mirrors, and as $0.02 e^{-a|x-x|_m} \cos(t-x) \pm .001$ in the mirrors. The initial velocity in all cases was $0.1 \omega/k$. The results for $a = 1000$ and $a = 1$ are shown in Fig. X-21. For $a = 1000$, the results are about the same as for the random phase theory. For $a = 1$, however, the heating is practically nonexistent. Similar results occur for $a = 0.1$ and $a = 0$. For the $a = 1$ case, the maximum point of penetration into the mirrors is $5k^{-1}$, less than a wavelength. The time involved in reflection was ≈ 30 oscillation periods.

The results are physically plausible. For hard walls or a random-phase model, an electron can be accelerated for a half-period, reflected, and accelerated for another half-period, since both the velocity and field have changed sign. For more realistic mirrors, the electron spends several periods in being reflected. Each half-period is then almost exactly cancelled by the next half-period.

Since the wavelength in a beam-plasma system is normally small compared with the mirror dimensions, it seems unlikely that this kind of heating is important.

J. A. Davis

References

1. J. A. Davis, Quarterly Progress Report No. 80, Research Laboratory of Electronics, M.I.T., January 15, 1966, pp. 120-124.

8. THEORY OF PLASMA EXCITATION BY A LINE-CHARGE SOURCE

As a first step in understanding the excitation of the beam-plasma discharge (BPD) by a modulated beam^{1,2} we consider the following theoretical model: Assume a linearized hydrodynamic representation of the fully ionized macroscopically neutral two-component plasma, with a longitudinal DC magnetic field, $B_0 \bar{i}_z$. The unbounded plasma is excited by a sinusoidally varying line charge oriented parallel to the DC magnetic field, $\rho = \rho_0 \delta(x) \delta(y)$, for $\exp(j\omega t)$ sinusoidal steady-state time dependence. The constant ρ_0 has units of coulombs per meter. We are interested in quasi-static solutions that have azimuthal symmetry and no longitudinal variation.

The linearized transport equations are

$$j\omega m_e N_0 \bar{v}_e = -N_0 e (\bar{E} + \bar{v}_e \times B_0 \bar{i}_z) - m_e u_e^2 \nabla n_e \quad (1)$$

$$j\omega m_i N_0 \bar{v}_i = N_0 e (\bar{E} + \bar{v}_i \times B_0 \bar{i}_z) - m_i u_i^2 \nabla n_i, \quad (2)$$

with the linearized equations of continuity

$$N_o \nabla \cdot \bar{v}_e = -j\omega n_e \quad (3)$$

$$N_o \nabla \cdot \bar{v}_i = -j\omega n_i \quad (4)$$

$$\nabla \cdot \bar{E} = \frac{\rho_o}{\epsilon_o} \delta(x)\delta(y) + \frac{e}{\epsilon_o} (n_i - n_e). \quad (5)$$

Introduce a scalar potential Φ , where

$$\bar{E} = -\nabla\Phi. \quad (6)$$

We are interested in solutions for which $E_z = 0$, and $v_{ez} = v_{iz} = 0$, leaving seven unknowns Φ , n_e , n_i , v_{ex} , v_{ey} , v_{ix} , and v_{iy} .

The set of seven equations is solved by using Fourier transform theory, and the following transform pair:

$$f(x, y) = \frac{1}{(2\pi)^2} \int_{-\infty}^{\infty} \int_{-\infty}^{\infty} f(k_x, k_y) e^{-jk_x x - jk_y y} dk_x dk_y \quad (7)$$

$$f(k_x, k_y) = \int_{-\infty}^{\infty} \int_{-\infty}^{\infty} f(x, y) e^{jk_x x + jk_y y} dx dy.$$

The solutions for the transformed equations are

$$n_e = \frac{\rho_o}{e} \omega_{pe}^2 \left[\frac{(k_T^2 u_i^2 - \omega^2 + \omega_{ci}^2)}{D(k_x, k_y)} \right] \quad (8)$$

$$n_i = \frac{-\rho_o}{e} \omega_{pi}^2 \left[\frac{(k_T^2 u_e^2 - \omega^2 + \omega_{ce}^2)}{D(k_x, k_y)} \right] \quad (9)$$

$$\Phi = \frac{\rho_o}{\epsilon_o} \left[\frac{(k_T^2 u_i^2 - \omega^2 + \omega_{ci}^2)(k_T^2 u_e^2 - \omega^2 + \omega_{ce}^2)}{k_T^2 D(k_x, k_y)} \right] \quad (10)$$

$$v_{ex} = -\frac{\rho_o e}{m_e \epsilon_o} \left[\frac{(\omega k_x + j\omega_{ce} k_y)(k_T^2 u_i^2 - \omega^2 + \omega_{ci}^2)}{k_T^2 D(k_x, k_y)} \right] \quad (11)$$

$$v_{ey} = -\frac{\rho_o e}{m_e \epsilon_o} \left[\frac{(\omega k_y - j\omega_{ce} k_x)(k_T^2 u_i^2 - \omega^2 + \omega_{ci}^2)}{k_T^2 D(k_x, k_y)} \right] \quad (12)$$

(X. PLASMAS AND CONTROLLED NUCLEAR FUSION)

$$v_{ix} = \frac{\rho_o e}{m_i \epsilon_o} \left[\frac{(\omega k_x - j\omega_{ci} k_y)(k_T^2 u_e^2 - \omega^2 + \omega_{ce}^2)}{k_T^2 D(k_x, k_y)} \right] \quad (13)$$

$$v_{iy} = \frac{\rho_o e}{m_i \epsilon_o} \left[\frac{(\omega k_y + j\omega_{ci} k_x)(k_T^2 u_e^2 - \omega^2 + \omega_{ce}^2)}{k_T^2 D(k_x, k_y)} \right] \quad (14)$$

Here, $D(k_x, k_y)$ is the dispersion relation³ given by

$$D(k_x, k_y) = (k_T^2 u_i^2 - \omega^2 + \omega_{ci}^2 + \omega_{pi}^2)(k_T^2 u_e^2 - \omega^2 + \omega_{ce}^2 + \omega_{pe}^2) - \omega_{pe}^2 \omega_{pi}^2 \quad (15)$$

where

$$k_T^2 = k_x^2 + k_y^2 \quad (16)$$

The quantities of Eqs. 8-14 are the spatial Fourier transforms of the first-order densities, potential, and velocities caused by the sinusoidally varying line charge. The responses as a function of x and y are obtained by taking the inverse Fourier transforms as given in Eq. 7. This work is at present in progress.

G. D. Bernard, A. Bers

References

1. L. D. Smullin, "Beam-Plasma Discharge: Excitation of Ions at the Ion Cyclotron Frequency (Theory)," Quarterly Progress Report No. 80, Research Laboratory of Electronics, M.I.T., January 15, 1966, pp. 111-113.
2. W. D. Getty and G. D. Bernard, "Beam-Plasma Discharge: Excitation of Ions at the Ion Cyclotron Frequency (Experiment)," Quarterly Progress Report No. 80, Research Laboratory of Electronics, M.I.T., January 15, 1966, pp. 113-115.
3. W. P. Allis, S. J. Buchsbaum, and A. Bers, Waves in Anisotropic Plasmas (The M.I.T. Press, Cambridge, Mass., 1963), p. 76, Eq. (5.44).

9. EXPERIMENTAL INVESTIGATION OF INSTABILITIES IN AN ELECTRON BEAM WITH TRANSVERSE ENERGY

Calculations of Bers and Gruber have predicted instabilities in an electron beam confined by a magnetic field if the electrons have enough transverse energy.¹ To find the optimum conditions for the instabilities, it was necessary to plot the dispersion relation for different values of the plasma frequency ω_p and of the parameter $k_{\perp} v_{0\perp} / \omega_c$ (k_{\perp} = propagation constant perpendicular to the magnetic field, $v_{0\perp}$ = transverse velocity of the electrons, ω_c = cyclotron frequency).² These resulting figures show that an instability can be expected in a plasma at $\omega = 0.6 \omega_c$ or in a beam at $\omega = 0.6 \omega_c + k_{\parallel} v_{0\parallel}$ (k_{\parallel} and $v_{0\parallel}$ are the propagation constant and electron velocity parallel to the magnetic

(X. PLASMAS AND CONTROLLED NUCLEAR FUSION)

field). The necessary condition for the plasma frequency is $\omega_p > 0.6 \omega_c$. If $\omega_p = 0.7 \omega_c$, the ratio of the propagation constants parallel and perpendicular to the beam will be $k_{||}/k_{\perp} \geq 2$. In a cylindrical beam surrounded by a metal cylinder the electric field of the wave should have a transverse dependence proportional to the Bessel function $J_0(k_{\perp}r)$. For a metal cylinder of radius 1.2 cm, it follows that $k_{\perp} = 2/\text{cm}$ and $k_{||} \geq 4/\text{cm}$. With a magnetic field of 70 gauss ($f_c = 200 \text{ Mc/sec}$) and a velocity of the electrons corresponding to 100 V, the instability should occur at a frequency of 600 Mc/sec or higher. This value is only an estimation because the theory assumes infinite transverse dimensions of the beam.

For the experiment two tubes were built (Fig. X-22). They are mounted inside a solenoid producing a constant magnetic field. A gap of 1 cm in the solenoid is located immediately before the phosphor-coated collector to allow the observation of the beam striking the collector and the detection of any RF signal. Two grids are mounted in front of the cathode so that the beam voltage and the beam current can be varied independently.

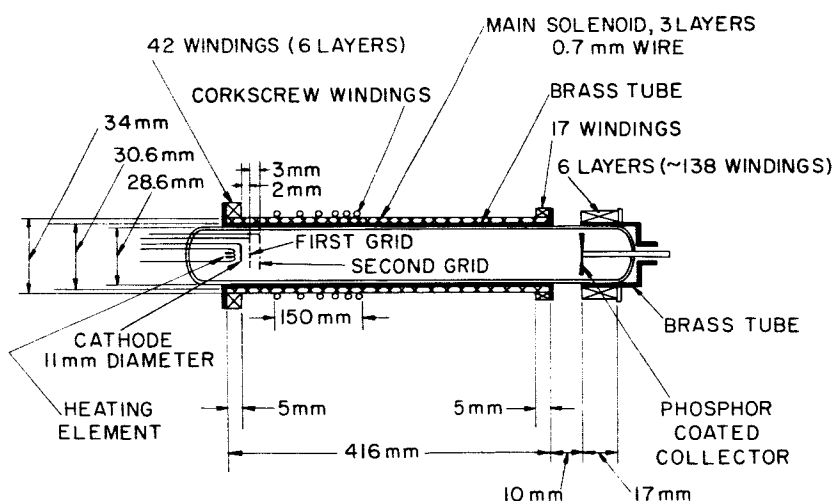


Fig. X-22. Schematic diagram of the experimental tube.

A fraction of the total kinetic energy of the electrons is converted into transverse energy by a corkscrew device.³ Two corkscrews were designed and built for a magnetic field of 70 gauss and 100 gauss. The corkscrews decelerate electrons starting at a beam voltage of 150 V, converting one-third of the electron energy into transverse energy. The electrons leaving the corkscrew spiral around in orbits of 7-mm diameter at 70 gauss and 5-mm diameter at 100 gauss.

The first tube was built to check the corkscrew device. In this tube the second grid

(X. PLASMAS AND CONTROLLED NUCLEAR FUSION)

is replaced by a plate with three small holes at different radial distances from the axis of symmetry. The three holes produce three thin beams and three points on the collector. The corkscrew transforms the three points into three circles with a diameter of 7 mm or 5 mm. The corkscrew device worked very well. Small deviations from the correct values of the magnetic field, beam voltage, and corkscrew current were admissible.

Under the assumption of a beam cross section equal to that of the cathode (1 cm^2), the necessary current at 70 gauss, 100 V, and $\omega_p = 0.7 \omega_c$ is 23 mA. Thus the perveance of the beam is $23 \cdot 10^{-6} \text{ I/V}^{3/2}$, which is close to the highest possible perveance. This value could not be reached with the tube, however, since the beam becomes unstable at 15 mA and spreads out. Operating at lower magnetic field should permit lower current density, but unfortunately the magnetic field is then too small for sufficient confinement of the beam.

No oscillation was found at the expected frequencies, but the tube showed strong oscillations at 250 Mc/sec when working without the corkscrew. In this case the tube acts as a double-stream amplifier. The rate of back-scattered electrons from the collector⁴ with sufficient energy is high enough to form a second beam confined by the magnetic field. This beam flows toward the cathode and is reflected again by the cathode (or grid) potential.

To find the predicted instabilities, it appears that higher beam densities are necessary. One possible way of achieving this is to use a neutralized beam. This work will continue either at M.I.T. or at the Technical University of Berlin.

G. Bolz

References

1. A. Bers and S. Gruber, Appl. Phys. Lett. 6, 27 (1965).
2. G. Bolz, Quarterly Progress Report No. 80, Research Laboratory of Electronics, M.I.T., January 15, 1966, pp. 135-136.
3. R. C. Wingerson, T. H. Dupree, and D. Rose, Phys. Fluids 7, 1475 (1964).
4. E. J. Sternglass, Phys. Rev. 95, 345 (1954).

10. HIGH-FREQUENCY ELECTRON-PHONON INTERACTIONS IN A MAGNETIC FIELD

Bers and Musha have previously reported¹ the classical dispersion relation for electrons interacting with acoustic waves in a solid. They considered parallel electric and magnetic fields in the quasi-static approximation. Taking the deformation potential as the coupling between the electron and phonon systems, they found the dispersion relation

$$K_p + K_e - 1 = 0, \quad (1)$$

where

$$K_p = \frac{\omega^2 - q^2 s^2}{\omega^2 - q^2 s^2 + \frac{c^2 \epsilon_L}{\rho e^2} q^4} \quad (2)$$

$$K_e = 1 - \frac{\omega_p^2}{q^2} \frac{\int_{-\infty}^{\infty} dw_{\parallel} \int_0^{\infty} dw_{\perp} w_{\perp} 2\pi \sum_n \frac{J_n^2(p) \left(\frac{n\omega_c}{w_{\perp}} \frac{\partial f_{01}}{\partial w_{\perp}} - q_{\parallel} \frac{\partial f_{01}}{\partial w_{\parallel}} \right)}{(\omega + i\nu - q_{\parallel} w_{\parallel} - n\omega_c)}}{1 + i\nu \int_{-\infty}^{\infty} dw_{\parallel} \int_0^{\infty} dw_{\perp} w_{\perp} 2\pi f_0 \sum_n \frac{J_n^2(p)}{(\omega + i\nu - q_{\parallel} w_{\parallel} - n\omega_c)}}. \quad (3)$$

Here, s is the sound velocity, ω_p is the electron plasma frequency, ω_c is the electron cyclotron frequency, q_{\parallel} is the wave-number component along B_0 , q_{\perp} is the wave-number component across B_0 , and $p = q_{\perp} w_{\perp} / \omega_c$; ν is the electron-lattice collision frequency, and phonon decay is ignored in Eq. 2.

We have been analyzing the instabilities predicted by these equations for parameters typical of InSb at 77°K with an effective deformation potential coupling constant taken to be 30 ev.² For these parameters Maxwell-Boltzmann statistics are appropriate and we assume:

$$f_0 = \frac{1}{(2\pi)^{3/2} v_T^3} \exp - \left(\frac{w_{\perp}^2 + w_{\parallel}^2}{2v_T^2} \right) \quad (4)$$

$$f_{01} = \frac{1}{(2\pi)^{3/2} v_T^3} \exp - \left(\frac{w_{\perp}^2 + (w_{\parallel} - v_D)^2}{2v_T^2} \right) \quad (5)$$

where v_T is the thermal velocity, and v_D is the drift velocity.

The imaginary part of the frequency, ω , for real wave vector, \bar{q} , has been computed as a function of the angle of propagation for various values of electric and magnetic fields with the aid of Project MAC CTSS. The results are shown in Fig. X-23.

Taking the appropriate values of the parameters, we find that ω may be considered to be purely real in Eq. 3, as $\omega_i \gg \nu$. The computations were carried out with this approximation.

Since the electron-phonon interaction has a relatively small effect on the unperturbed electron and phonon systems, $\omega_i \ll \omega_r \approx q_r s$ and $\text{Re } K_e \gg 1$. In this approximation the dispersion relation may be solved explicitly for the growth rate of phonons:

$$\omega_i \approx \frac{C^2 \epsilon_L q^3}{\rho e^2 s} \text{Im}(K_e). \quad (6)$$

The physics of the interaction and the results of our more exact computations may be readily interpreted from this approximate description. For the high frequencies that

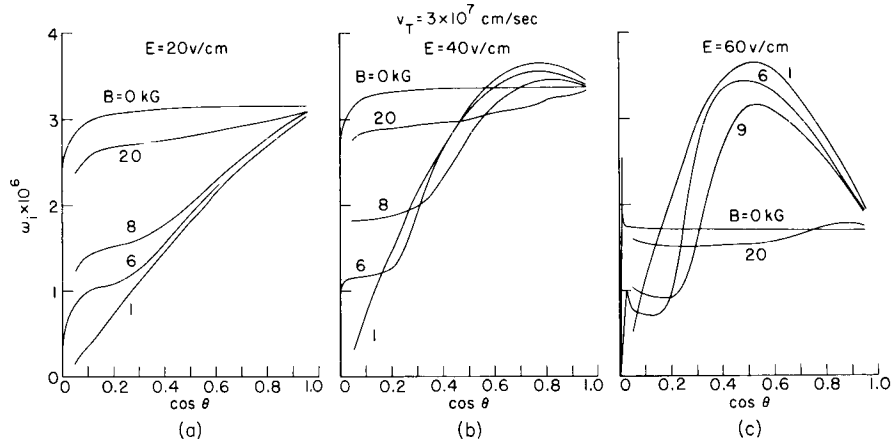


Fig. X-23. Variation of amplification with direction of propagation. The variation for very small $\cos \theta$ has been included only for $B = 0$ kg and $B = 6$ kg. (a) v_D much less than v_T . (b) v_D slightly greater than v_T . (c) v_D much greater than v_T .

we are considering, the mean-free path of the electrons is large compared with a phonon wavelength ($qv_T/v \gg 1$). Thus the major contribution to $\text{Im}(K_e)$ that gives rise to growth comes from anti-Landau damping, and the effect of collisions is usually small.

a. Zero Magnetic Field

In the limit of zero magnetic field, the expression for K_e reduces to

$$K_e = 1 + \frac{\frac{\omega_p^2}{q^2} \int_{-\infty}^{\infty} dw_{\parallel} \int_0^{\infty} dw_{\perp} \frac{w_{\perp} 2\pi q_{\parallel} \frac{\partial f_{01}}{\partial w_{\parallel}}}{(\omega + i\nu - q_{\parallel} w_{\parallel})}}{1 + i\nu \int_{-\infty}^{\infty} dw_{\parallel} \int_0^{\infty} dw_{\perp} \frac{w_{\perp} 2\pi f_0}{(\omega + i\nu - q_{\parallel} w_{\parallel})}} \quad (7)$$

and the general behavior of ω_i versus angle can be explained on the basis of anti-Landau damping. The most interesting feature of these curves is the sharp peak in the

(X. PLASMAS AND CONTROLLED NUCLEAR FUSION)

amplification that occurs for propagation almost across the field when $v_D > v_T$. This peak occurs at just that angle where one would expect the largest Landau damping effect, namely $\cos \theta = \frac{\omega}{qv_T}$, as can be seen from Fig. X-24.

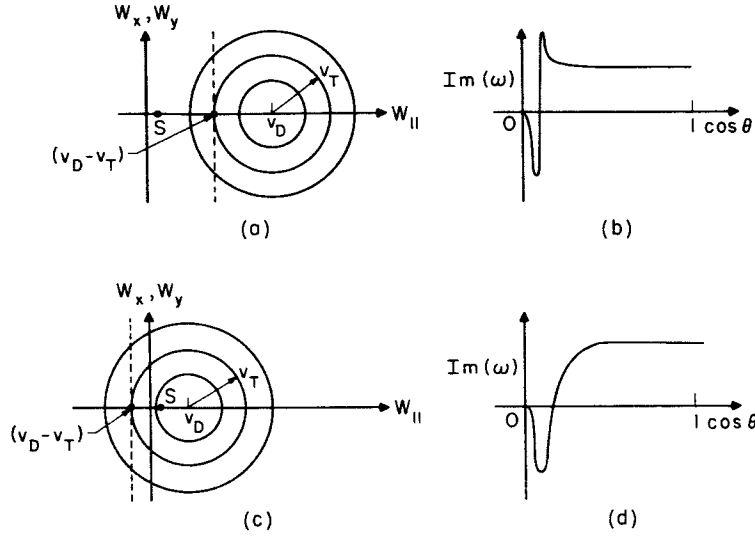


Fig. X-24. (a) Distribution function, f_{01} , for $v_D > (v_T + s)$. Circles represent loci of constant f_{01} . $\frac{\partial f_{01}}{\partial w_{||}}$ is maximum along the dotted line ($w_{||} = v_D - v_T$). (b) Expected variation of the amplification with angle of propagation for the case represented in (a). (c) Same as (a) except that $v_D < v_T$. (d) Expected variation in the amplification for the case represented in (c). Note that there is no peak in the amplification for propagation almost transverse to the field as was the case in (b).

The maximum Landau damping effect is expected when the electrons along the line $(v_D - v_T)$ (maximum slope of the distribution function) are moving in the direction of wave propagation with a velocity equal to the phase velocity of the wave. Also, damping is expected whenever there are more electrons moving infinitesimally slower than the wave than are moving infinitesimally faster than the wave; this condition is satisfied for $\cos \theta \leq \frac{\omega}{qv_D}$. Mathematically this is contained in the dispersion relation, in that $\frac{\partial f_{01}}{\partial w_{||}}$ must be evaluated at the pole of the denominator, i.e., $\cos \theta = \frac{\omega}{qv_{||}}$, neglecting collisions. Thus as $\cos \theta$ varies from 0 to 1, $w_{||}$ varies from ∞ to s and the general form of the growth as a function of $\cos \theta$ is shown in Fig. X-24.

(X. PLASMAS AND CONTROLLED NUCLEAR FUSION)

b. Finite Magnetic Field

When a magnetic field is applied the situation becomes more complicated. One physical process that can be identified in these curves (Figs. X-23b and c) is that of Doppler-shifted cyclotron resonance. This comes in through the resonant denominator in the integrals of Eq. 3. According to Eq. 6, the amplification will be maximum when the angle of propagation is such that

$$\sum_n J_n^2(p) \left(\frac{n\omega_c}{w_\perp} \frac{\partial f_{01}}{\partial w_\perp} - q_\parallel \frac{\partial f_{01}}{\partial w_\parallel} \right)$$

is maximum at the pole of the denominator. For low magnetic fields (≈ 1 kgauss) none of the terms of this expression dominate and hence a large number of terms in the series must be taken into account and the position of the peak cannot be given by any simple formula. For moderate magnetic fields (≈ 6 kgauss), the parameters are such that the Bessel functions decrease rapidly with increasing order and hence the major effect is given by the first term. Also, $\frac{\omega_c}{w_\perp} \frac{\partial f_{01}}{\partial w_\perp}$ is much larger than $q_\parallel \frac{\partial f_{01}}{\partial w_\parallel}$. Hence the maximum is given by $w_\parallel = v_D$ or $\cos \theta = \frac{\omega + \omega_c}{qv_D}$, with collisions neglected.

For $v_T > v_D$, the amplification does not rise over the zero magnetic field value for any magnetic field (Figs. X-23, X-25 and X-26). For high magnetic fields this can be explained by noting that the condition given above for Doppler-shifted cyclotron resonance cannot be met for $0 \leq \cos \theta \leq 1$. We do not yet fully understand the situation for lower

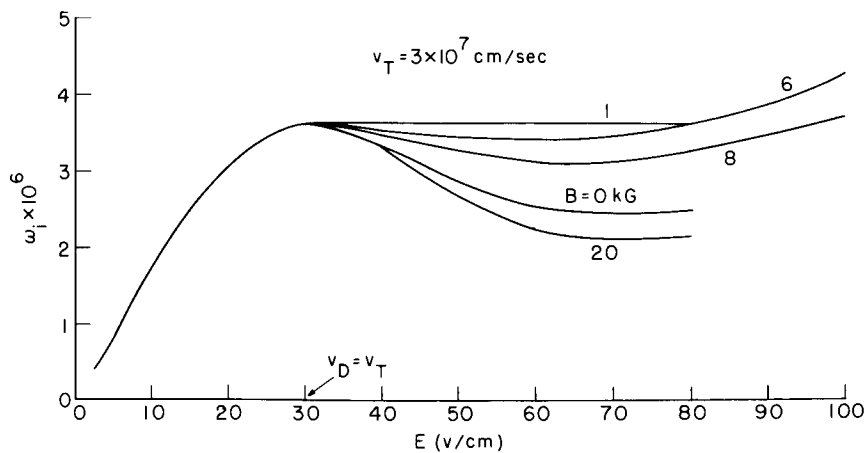


Fig. X-25. Maximum (with respect to angle) amplification vs electric field, with the magnetic field as a parameter.

(X. PLASMAS AND CONTROLLED NUCLEAR FUSION)

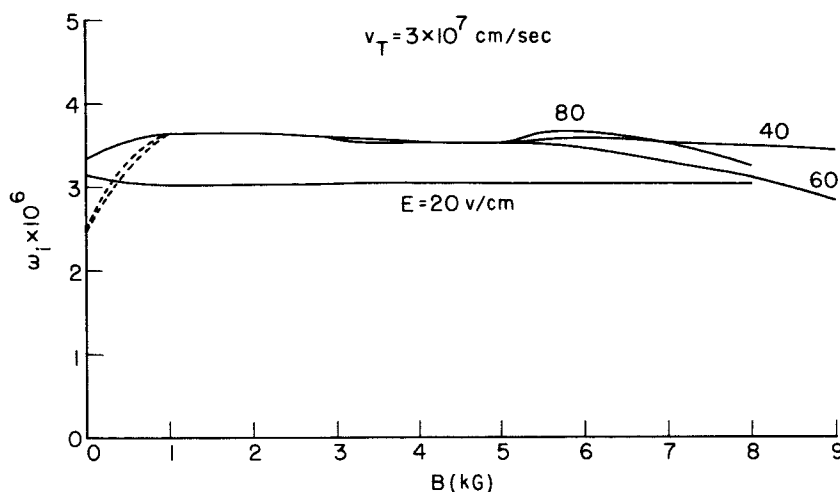


Fig. X-26. Maximum (with respect to angle) amplification vs magnetic field, with the electric field as a parameter.

magnetic fields. Note that $v_T > v_D$ is the usual situation in a solid; when the electric field is increased in order to increase v_D , v_T also increases because of the high collision rate. As can be seen from Fig. X-25, for $v_D < v_T$ the growth rate is independent of the applied magnetic field.

Work is now under way to determine the nature of these instabilities – whether they are absolute or convective. Also, the quantum-mechanical formulation of the dispersion relation, given by Bers and Musha,¹ is being examined to determine the specifically quantum-mechanical aspects of the interaction and when they may be important.

A. Bers, S. R. J. Brueck

References

1. A. Bers and T. Musha, Quarterly Progress Report No. 79, Research Laboratory of Electronics, M.I.T., October 15, 1965, p. 104.
2. Recent measurements at Lincoln Laboratory, M.I.T., indicate that the dominant electron-phonon coupling mechanism in InSb at 9 kMc is piezoelectric rather than deformation potential (Kenneth Hill, private communication).

X. PLASMAS AND CONTROLLED NUCLEAR FUSION*

B. Applied Plasma Physics Related to Controlled Nuclear Fusion

Research Staff

Prof. D. J. Rose
Prof. T. H. Dupree

Prof. L. M. Lidsky

Prof. E. P. Gyftopoulos
L. M. Lontai

Graduate Students

R. W. Flynn
R. A. Hill

C. S. Ribbeck
C. E. Wagner
D. R. Wilkins

J. C. Woo
N. D. Woodson

1. THERMONUCLEAR REACTOR: INTRODUCTORY SYSTEM ANALYSIS

Considerable work has been done on investigating various controlled thermonuclear power devices. Plasma physics problems are still to be solved before fusion power will be available, but it is evident already that the engineering aspects of the problem will be very challenging. The results of an engineering analysis may alter the direction and intensity of the controlled thermonuclear power program.

The present study concentrates first on general comparisons of steady-state and pulsed devices. Following this, specific introductory engineering analyses involving the magnitude of the leakage of the magnetic field into the coolant of a pulsed device, the temperature distribution in the vacuum wall of a pulsed device of small radius, and power-generating cost estimates are presented.

The study of the magnetic leakage was an extension of the work performed by Ribe and co-workers.¹ Ribe's device has a 10-cm vacuum wall radius and a maximum B field of 200 kgauss. Ribe presents data for a given magnetic pulse, $B_{\max} = 200$ kgauss, showing the diffusion of the magnetic field into a conductor as a function of time. With these data, an approximate value of the average magnetic field within the conductor as a function of time may be found. Thus, if the conductor is a liquid-metal coolant, we shall have the value of the magnetic field through which the coolant will be pumped. The results show that for a 50-cm coolant thickness, the average field is approximately 20% of the maximum field (200 kgauss) initially, and drops to approximately 10% of the maximum after a typical heat time (500 msec) has elapsed. The power required to pump the liquid-metal coolant through this field will be enormous. Thus, a fused salt still appears to be the best coolant available.

Our small-radius vacuum-wall study continues Dean's work,² to reach new conclusions. Dean proposed to examine the Bremsstrahlung radiation absorption with a model

*This work was supported principally by the National Science Foundation (Grant GK-614).

(X. PLASMAS AND CONTROLLED NUCLEAR FUSION)

that approximates the actual attenuation of the radiation. This model assumes that the Bremsstrahlung is not a surface heat flux, but is instead absorbed within a small volume just inside the wall.

By using this model and equations derived by Carslaw and Jaeger,³ temperature distributions can be obtained as functions of space and time. For a Copper inner wall of 1-cm thickness and 10-cm radius, we found that the temperature rise attributable to the Bremsstrahlung from a single 0.04-sec pulse is approximately 105°C. Similarly, the temperature rise caused by neutron heating is approximately 200°C at the inner face of the wall. Next, the energy dissipation during the dead time is examined. By calculating the temperature drop after the initial peak, we found that approximately 70% of the initial energy input remains in the wall at the end of the dead time. Thus the following pulses tend to build up on one another and approach a quasi-steady state. It is estimated that for the wall under consideration, this average steady state at the inner face will be approximately 1000°C above the initial level of 600°C, which melts Copper and seriously damages any other material considered. The temperature distribution for a single pulse will be superimposed over this average, as shown in Fig. X-28.

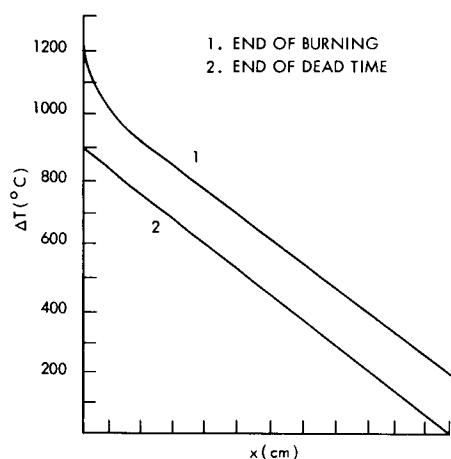


Fig. X-28. Vacuum-wall temperature distribution.

Returning to large-vacuum walls, of approximately 1-meter radius, the economic considerations of thermonuclear devices are developed. The costs presented represent the power plant up to the heat exchanger, but not beyond. Under the assumption that Tritium has no value and, therefore, no costs of separation accrue, injection is performed by 5-amp ion guns valued at \$40,000 per gun, burn-up in a steady-state device is 0.5, (while in a pulsed device burn-up is 0.1), the final cost will be approximately 0.5 M/kWe for either system. Steady-state device costs are approximately 25% lower, but at a value of 0.5 M/kWe the inaccuracies in the data may become significant.

What is important to see from this study is that a fusion-fission machine may be economically competitive with pure fission devices in the future. The results of this study may be stated as follows: 1) liquid-metal coolants will be supremely difficult to use, 2) prohibitive temperatures found in small-radius vacuum walls re-enforce our opinion that large vacuum systems must be used, and 3) steady-state or pulsed devices with large vacuum systems surrounded by a Uranium bearing salt will be competitive in the future if the assumptions are valid.

(X. PLASMAS AND CONTROLLED NUCLEAR FUSION)

Further studies of all energy losses and gains must be made. Especially important in large devices are the coolant pumping requirements. Schemes for efficiently utilizing the exhaust energy in pulsed devices must be brought to mind in the development of any pulsed systems. Finally, schemes to incorporate a fusion "core" with a "fission breeder blanket" must be advanced. Inclusion of solid-fuel elements in the blanket may be the next step in advancing the blanket design.

N. D. Woodson

References

1. F. Ribe, "Feasibility Study of a Pulsed Thermonuclear Reactor," LASL, LA-3294-MS.
2. S. O. Dean, "Heating of Vacuum Wall by Bremsstrahlung Radiation in a Pulsed Thermonuclear Reactor," USAEC Division of Research, 1965 (unpublished).
3. H. S. Carslaw and J. C. Jaeger, Conduction of Heat in Solids (Clarendon Press, Oxford, 1948).

2. ANALYSIS OF THE OPERATION OF A LONG ARC COLUMN

A long arc column generated by a hollow-cathode discharge has been operated over a broad range of parameters. In the study of various oscillation phenomena associated with the plasma having the arc as a source, it is important to have a quantitative understanding of the conditions in the arc. For the analysis, we consider the geometry shown in Fig. X-29. We shall be concerned with the arc in the region between the baffle and

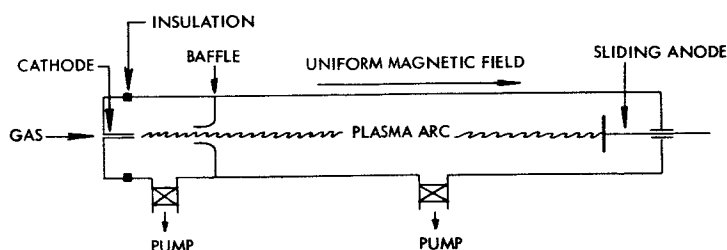


Fig. X-29. Geometry of the experiment.

the movable anode. Because of the differential pumping scheme, the plasma in this region is fully ionized, and a strong uniform magnetic field is applied along the axis of the column so that $\omega_i \tau_i > 1$ and $\omega_e \tau_e > 1$. In this case we need only be concerned with transport along the magnetic field lines. The transport equations for a steady-state fully ionized plasma may be written

$$\frac{d}{dz} \Gamma_e = 0 \quad (1)$$

(X. PLASMAS AND CONTROLLED NUCLEAR FUSION)

$$\frac{d}{dz} \Gamma_i = 0 \quad (2)$$

$$m \Gamma_e \frac{d}{dz} \frac{\Gamma_e}{n} + \frac{d}{dz} n T_e = -enE - .51 \frac{m_e}{\tau_e} (\Gamma_e - \Gamma_i) - .71 n \frac{dT_e}{dz} \quad (3)$$

$$m_i \Gamma_i \frac{d}{dz} \frac{\Gamma_i}{n} + \frac{d}{dz} n T_i = enE + .51 \frac{m_e}{\tau_e} (\Gamma_e - \Gamma_i) + .71 n \frac{dT_e}{dz} \quad (4)$$

$$\frac{3}{2} \Gamma_e \frac{d}{dz} T_e + n T_e \frac{d}{dz} \frac{\Gamma_e}{n} = .51 \frac{m_e}{n \tau_e} (\Gamma_e - \Gamma_i)^2 - 3 \frac{m_e}{m_i} \frac{n}{\tau_e} (T_e - T_i) \quad (5)$$

$$\frac{3}{2} \Gamma_i \frac{d}{dz} T_i + n T_i \frac{d}{dz} \frac{\Gamma_i}{n} = 3 \frac{m_e}{m_i} \frac{n}{\tau_e} (T_e - T_i), \quad (6)$$

where

$$\tau_e = \frac{(32)(2\pi)^{1/2} \epsilon_0^2 m_e^{1/2} T_e^{3/2}}{e^4 n \ln \Lambda} \quad (7)$$

is the electron collision time. We have ignored the thermal conductivity in Eqs. 5 and 6, since the temperature gradient is generally small.

It is convenient to discuss this set of equations with variables expressed in dimensionless form. Hence we define

$$\Gamma_e = \frac{\Gamma_e}{n_o} \left(\frac{m_e}{T_{eo}} \right)^{1/2}, \quad \Gamma_i = \frac{\Gamma_i}{n_o} \left(\frac{m_e}{T_{eo}} \right)^{1/2}, \quad T_e = \frac{T_e}{T_{eo}}, \quad T_i = \frac{T_i}{T_{eo}}$$

$$n = \frac{n}{n_o}, \quad m = \frac{m_i}{m_e}, \quad \theta = \frac{T_{eo}^2 \epsilon_0^2}{e^4 n_o L \ln \Lambda}, \quad z = \frac{z}{L},$$

where n_o and T_{eo} are the density and electron temperature at some convenient reference point in the system, and L is the length of the plasma column.

From the momentum equations we obtain

$$\left[T_e + T_i - \frac{\Gamma_e^2 + m \Gamma_i^2}{n^2} \right] \frac{dn}{dz} + n \left[\frac{dT_e}{dz} + \frac{dT_i}{dz} \right] = 0 \quad (8)$$

which integrates to express the conservation of energy of the system:

$$\frac{\Gamma_e^2 + m \Gamma_i^2}{n} + n(T_e + T_i) = P = \text{constant}. \quad (9)$$

Making use of the energy equations, we obtain

$$\frac{dn}{dz} = (.015) \frac{(\Gamma_e - \Gamma_i)n^4}{P\theta m \Gamma_e \Gamma_i T_e^{1/2}} \left[\frac{.51m(\Gamma_e - \Gamma_i) \Gamma_i}{3n^2 T_e} + 1 \right] \left[\frac{8(\Gamma_e^2 + m\Gamma_i^2)}{5Pn} - 1 \right] \quad (10)$$

$$\frac{dT_e}{dz} = \frac{2}{3} \frac{T_e}{n} \frac{dn}{dz} + \frac{.025}{\Gamma_e m \theta} \left[\frac{.51m(\Gamma_e - \Gamma_i)^2}{3n^2 T_e} - 1 \right] \frac{n^2}{T_e^{1/2}} \quad (11)$$

$$\frac{dT_i}{dz} = \frac{2}{3} \frac{T_i}{n} \frac{dn}{dz} + .025 \frac{n^2}{\Gamma_i m \theta T_e^{1/2}}. \quad (12)$$

Equations 10, 11, and 12 are the equations of interest. From these equations it is clear that the electron temperature may be adjusted by the balance of three processes: expansion cooling, Joule heating, and energy transfer caused by collision between electrons and ions. For the ions, since Joule heating from collision with electrons is of order $1/m$, only the first and third processes are effective. In the geometry under consideration, Γ_e is always positive. The sign of Γ_i is determined by whether or not an ion source is supplied at the anode, and this also determines the sense of the density gradient.

If we divide Eqs. 11 and 12 by (10), we obtain

$$\frac{dT_e}{dn} = \frac{2}{3} \frac{T_e}{n} + \frac{5P\Gamma_i \left[\frac{8(\Gamma_e^2 + m\Gamma_i^2)}{5Pn} - 1 \right] \left[\frac{.51m(\Gamma_e - \Gamma_i)^2}{3n^2 T_e} - 1 \right]}{3(\Gamma_e - \Gamma_i)n^2 \left[\frac{.51m(\Gamma_e - \Gamma_i) \Gamma_i}{3n^2 T_e} + 1 \right]}. \quad (13)$$

$$\frac{dT_i}{dn} = \frac{2}{3} \frac{T_i}{n} + \frac{5P\Gamma_e \left[\frac{8(\Gamma_e^2 + m\Gamma_i^2)}{5Pn} - 1 \right]}{3(\Gamma_e - \Gamma_i)n^2 \left[\frac{.51m(\Gamma_e - \Gamma_i) \Gamma_i}{3n^2 T_e} + 1 \right]}. \quad (14)$$

The behavior of Eqs. 13 and 14 can be grouped naturally into three regimes:

$$(I) \quad 6nT_e \gg \frac{m(\Gamma_e - \Gamma_i)^2}{n} \gtrsim \frac{m(\Gamma_e - \Gamma_i) \Gamma_i}{n} \quad (15)$$

(X. PLASMAS AND CONTROLLED NUCLEAR FUSION)

$$(II) \quad \frac{m(\Gamma_e - \Gamma_i)^2}{n} > 6nT_e > \frac{m(\Gamma_e - \Gamma_i) \Gamma_i}{n} \quad (16)$$

$$(III) \quad \frac{m(\Gamma_e - \Gamma_i)^2}{n} \gtrsim \frac{m(\Gamma_e - \Gamma_i) \Gamma_i}{n} \gg 6nT_e \quad (17)$$

which express the various possible partitions of energy of the system.

In each case, Eqs. 13 and 14 reduce to a form that can be integrated exactly.

Case I

For the condition expressed by inequality (15), we obtain

$$T_e = (1+a)n^{2/3} - \frac{a}{n}, \quad (18)$$

where

$$a = \frac{\Gamma_i}{\Gamma_e - \Gamma_i}.$$

The behavior of (18) is shown in Fig. X-30, with the lower bounds for which (15) is valid shown in dotted lines. Since, in general $|\Gamma_i| \leq |\Gamma_e|$, therefore $-1 \leq a \leq 0.5$ and for

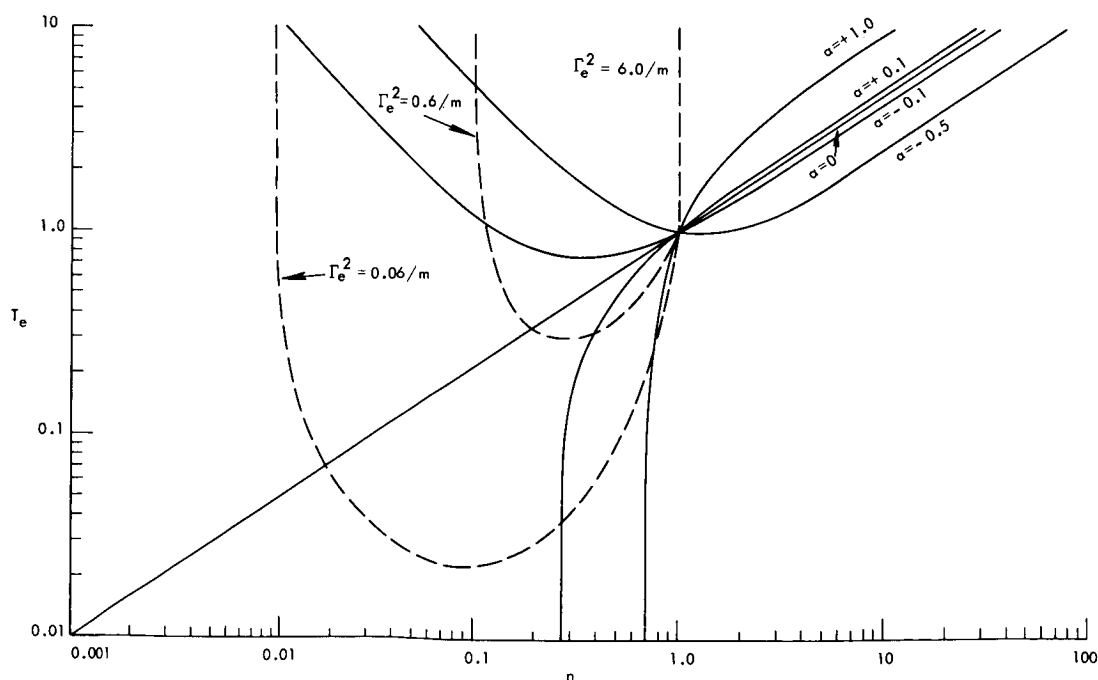


Fig. X-30. Regimes for Case I.

$n > 1$, we can express Eq. 18 by

$$T_e = n^\delta \quad (19)$$

$$1 \leq \delta \leq 0.$$

Case II

In case that inequality (16) is valid, we obtain from Eq. 13

$$T_e^2 = \left\{ 1 - .13m\Gamma_i(\Gamma_e - \Gamma_i) \left[1 - 1.3 \frac{(\Gamma_e^2 + m\Gamma_i)^2}{p} \right] \right\} n^{4/3} \\ + .13 \frac{m\Gamma_i(\Gamma_e - \Gamma_i)}{n} \left[\frac{1}{n^2} - 1.3 \frac{(\Gamma_e^2 + m\Gamma_i)^2}{pn^3} \right]. \quad (20)$$

For $n > 1$, the plasma behaves very closely to the ideal law

$$T_e = n^{2/3}. \quad (21)$$

Case III

When the drift energy is very large compared with the electron thermal energy, inequality (17) is valid, and the Joule heating effect is all-important. In this case

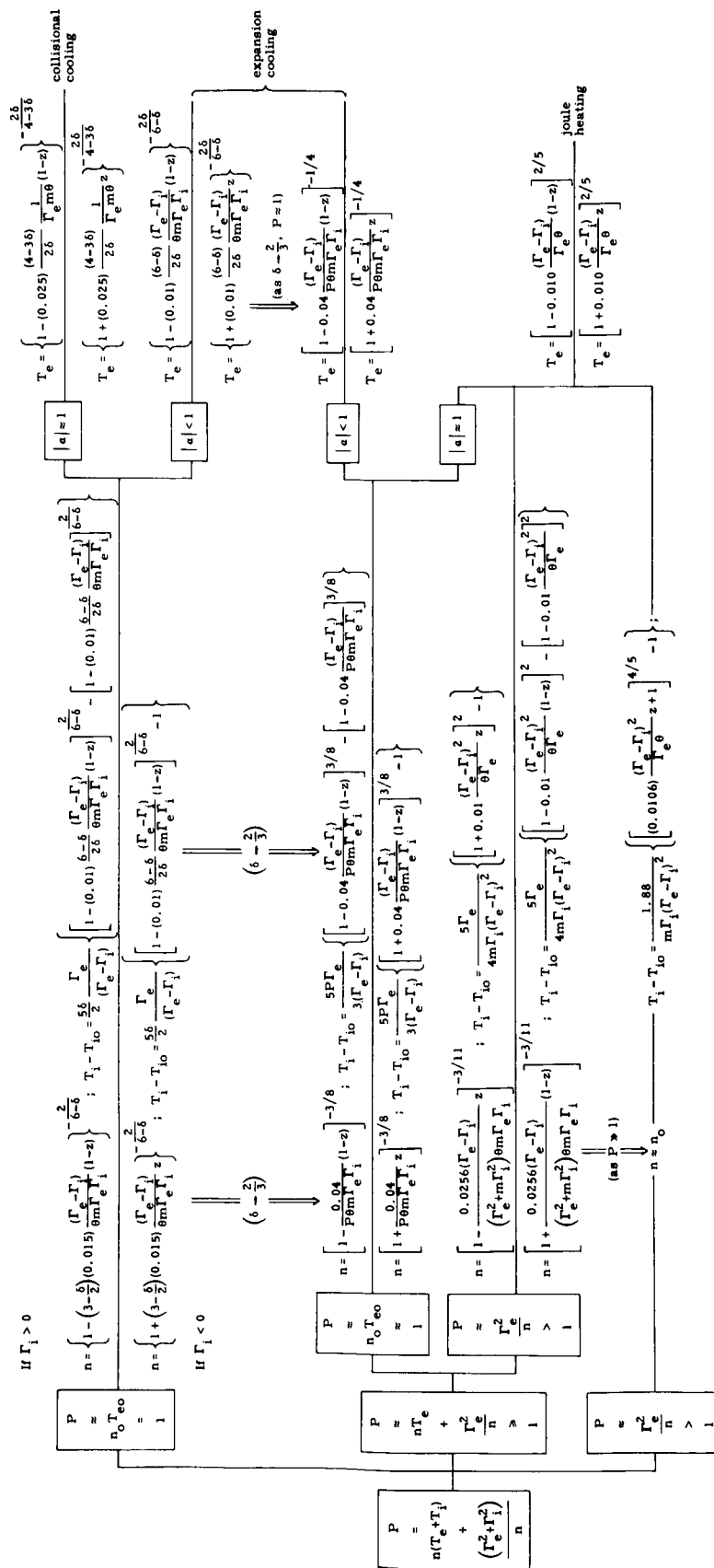
$$T_e = n^{2/3} + p \left[\frac{\Gamma_e^2 + m\Gamma_i^2}{Pn^2} - \frac{1}{n} \right]. \quad (22)$$

Here $P \gg 1$ and the second term is always dominant. If the temperature is not to rise rapidly down stream, the density must remain approximately constant for all practical purposes.

Having obtained the relationship between T_e and n , we can obtain the spatial variations of n , T_e , and T_i by integrating Eqs. 10, 11, and 12 in each case. The results are summarized in Table X-1.

From the results it is seen that the conditions of the arc are determined by the partition of the total energy that can be controlled by proper adjustment of the boundary conditions. In each case the behavior of the arc column along its length is characterized by the dimensionless parameter

Table X-1. Results of calculations.



$$\theta = \frac{T_{eo}^2 \epsilon_o^2}{e^4 n_o L \ln \Lambda}$$

which, together with the electron and ion fluxes Γ_e and Γ_i , completely specifies the system.

J. C. Woo

3. TRANSVERSE DIFFUSION OF A LONG PLASMA COLUMN

The diffusion of a magnetically confined plasma across the field lines has been considered by many authors. Simon¹ has pointed out that for an open system the transverse diffusion is coupled to the longitudinal electron mobility; consequently, the diffusion rate is considerably greater than the unidirectional ambipolar rate. In his analysis, Simon assumes that $E_R/E_L \approx L/R$, and for a stubby apparatus such as the experiment of Neidigh, to which Simon's analysis was directed, the radial electric field may be neglected. In a long plasma column, for example, in many recent arc experiments, $L/R \gtrsim 10$, and the radial electric field is significantly larger than the longitudinal field. The fact that a large radial electric field can exist suggests that the Simon short-circuiting effect is not fully effective. The longitudinal mobility is, however, much greater than any transverse loss mechanism for the electrons; consequently, the radial electric field will seek for itself a value that is consistent with the longitudinal mobility of the electrons and limits the transverse diffusion of the ions. The resulting loss rate will lie between the ambipolar and the Simon short-circuit process rates.

We shall evaluate the effect of the presence of a radial electric field, using a simple diffusion model. As is typical of arc plasmas, both the density and the electron temperature have approximately the same radial profile; consequently, the assumption that the diffusion and mobility coefficients are constant in space is not too bad an approximation.

Writing the continuity equation for the electrons and single charged ions, we have

$$\frac{\partial n_e}{\partial t} = D_e \frac{\partial^2 n_e}{\partial x^2} - b_e \frac{\partial}{\partial x} \left(n_e \frac{\partial \phi}{\partial x} \right) + D_e \frac{\partial^2 n_e}{\partial z^2} - b_e \frac{\partial}{\partial z} \left(n_e \frac{\partial \phi}{\partial z} \right) \quad (1)$$

$$\frac{\partial n_i}{\partial t} = D_i \frac{\partial^2 n_i}{\partial x^2} + b_i \frac{\partial}{\partial x} \left(n_i \frac{\partial \phi}{\partial x} \right) + D_i \frac{\partial^2 n_i}{\partial z^2} + b_i \frac{\partial}{\partial z} \left(n_i \frac{\partial \phi}{\partial z} \right). \quad (2)$$

Here we have used a rectangular coordinate system with the magnetic field in the z -direction. Even though we are specifically interested in the space charge that would exist across the field lines, the net imbalance between the electron and ion, nevertheless, is small, and we can still set $n_e = n_i = n$.

(X. PLASMAS AND CONTROLLED NUCLEAR FUSION)

Eliminating the transverse mobility between the two equations, we obtain

$$\frac{\partial n}{\partial t} = D_{\perp} \frac{\partial^2 n}{\partial x^2} + D \frac{\partial^2 n}{\partial z^2} - b \left(\frac{\partial n}{\partial z} \frac{\partial \phi}{\partial z} + n \frac{\partial^2 \phi}{\partial z^2} \right), \quad (3)$$

where

$$D_{\perp} = \frac{D_{e\perp} b_{i\perp} + D_{i\perp} b_{e\perp}}{b_{i\perp} + b_{e\perp}} \approx \frac{D_i}{b_i} b_{e\perp} + D_{e\perp} \quad (4)$$

$$D = \frac{D_e b_{i\perp} + D_i b_{e\perp}}{b_{i\perp} + b_{e\perp}} \approx D_e \quad (5)$$

$$b = \frac{b_e b_{i\perp} + b_i b_{e\perp}}{b_{i\perp} + b_{e\perp}} \approx b_e. \quad (6)$$

Since the longitudinal electron mobility is high, space charge cannot exist in the axial direction. For a long column, we can assume $\partial^2 \phi / \partial z^2 \approx 0$, and $\partial \phi / \partial z = -E_z = \text{constant}$.

Assuming that a plasma source exists only along the axis $x = 0$, away from the source, Eq. 3 is homogenous:

$$D_{\perp} \frac{\partial^2 n}{\partial x^2} + D \frac{\partial^2 n}{\partial z^2} + b E_z \frac{\partial n}{\partial z} = 0 \quad (7)$$

$$n = \frac{N_0}{\left[1 - \exp \left(-\frac{x_0}{p} \right) \right]} \left[\exp \left(-\frac{1}{2} \frac{x}{p} \right) - \exp \left(-\frac{1}{2} \frac{(2x_0 - x)}{p} \right) \right] \left[\exp \left(-\frac{z}{q} \right) \right] \cos \frac{\pi}{L} z, \quad (8)$$

where

$$p = \sqrt{\frac{D_{\perp}}{D}} \frac{1}{\left(\frac{b^2 E_z^2}{D^2} + \frac{\pi^2}{L^2} \right)^{1/2}} \quad (9)$$

$$q = \frac{D}{b E_z}. \quad (10)$$

The axial density distribution is plotted in Fig. X-31 for a range of values of q . Making use of the Einstein relation yields

$$q \approx \frac{T_e L}{q \phi_0}.$$

In the external plasma of the hollow cathode arc

$$\frac{L}{2} \gtrsim q \gtrsim \frac{L}{5},$$

and this profile is in good agreement with the experimental observation as shown in Fig. X-31. The slight disagreement at the ends is due to the existence of a sheath, and

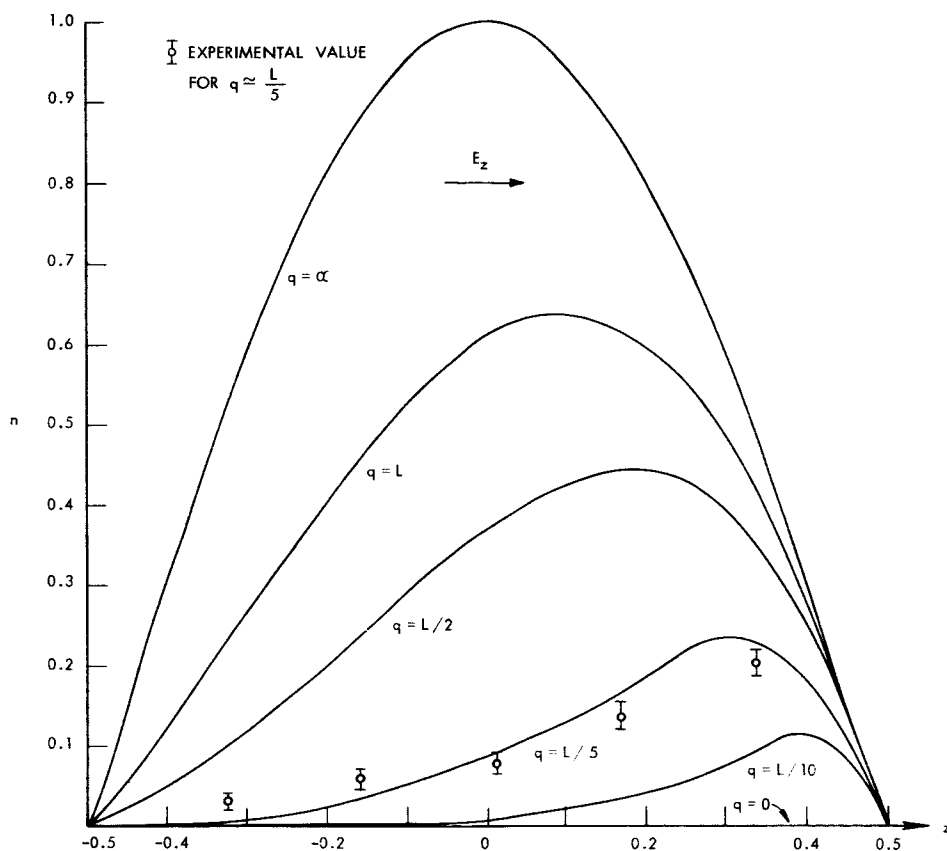


Fig. X-31. Axial density distribution for a range of values of q .

therefore the density of the interior plasma does not vanish at the boundary.

The radial e-folding distance is now given by

$$2p = 2\sqrt{\frac{D_{\perp}}{D}} \frac{1}{\left(\frac{b^2 E_z^2}{D^2} + \frac{\pi^2}{L^2}\right)^{1/2}} \approx 2\left(\frac{T_i}{T_e}\right)^{1/2} \frac{1}{a_e} \frac{L}{\pi},$$

where $a_e = \omega_e \tau_e$.

(X. PLASMAS AND CONTROLLED NUCLEAR FUSION)

This result differs from Simon's in that the e-folding distance is inversely proportional to α_e rather than α_i and, for the condition of the arc, leads to a value of the order of centimeters which is also consistent with observation (rather than a fraction of a meter as expected from the Simon result).

The question arises as to the effect of the large-scale fluctuations arising from drift-wave instabilities that could lead to turbulent diffusion. These oscillations generally appear in the kilocycle range. Since the electron mobility determines the over-all diffusion rate of the system, and the electrons traverse the system in microseconds, these oscillations cannot significantly affect the loss rate of the plasma in an open system of moderate length.

J. C. Woo

References

1. A. Simon, Report P/366, Second International Conference on the Peaceful Uses of Atomic Energy, Geneva, 1958.

XI. ENERGY CONVERSION RESEARCH*

A. Power Systems with Liquid Generators

Academic and Research Staff

Prof. W. D. Jackson
Prof. G. A. Brown

Prof. E. S. Pierson
R. P. Porter

Graduate Students

E. K. Levy
R. J. Thome

1. EXPERIMENTAL RESULTS FOR CONDENSING EJECTOR M-1

A detailed experimental program has been conducted on condensing ejector mixing section M-1 with steam and water used as the working fluids. The tests were made on the condensing ejector test facility which has been described in Quarterly Progress Reports No. 78 (pages 149-159) and No. 79 (pages 149-151).

Mixing section M-1 was machined from brass; the important details are shown in Fig. XI-1. The total length of the convergent mixing section, constant-area mixing section, and diffuser is 23.37 inches. The convergent section has an inlet diameter of 1.352 inches and is tapered to a diameter of 0.626 inch at its exit. The angle of taper is 2.26° . The constant-area section is approximately 7 inches in length and has an

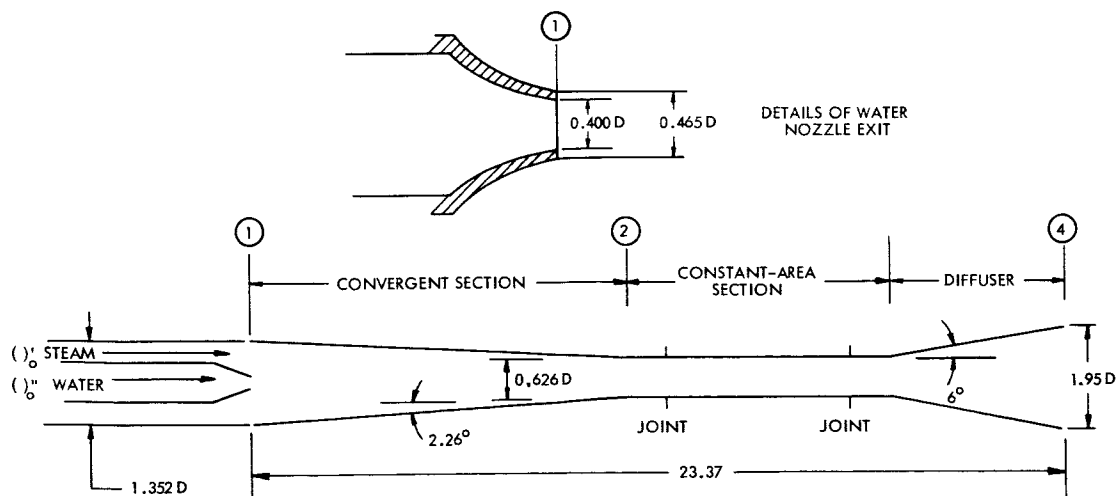


Fig. 1. Details of mixing section M-1.

*This work is supported by the U.S. Air Force (Research and Technology Division) under Contract AF33(615)-3489 with the Air Force Aero Propulsion Laboratory, Wright-Patterson Air Force Base, Ohio.

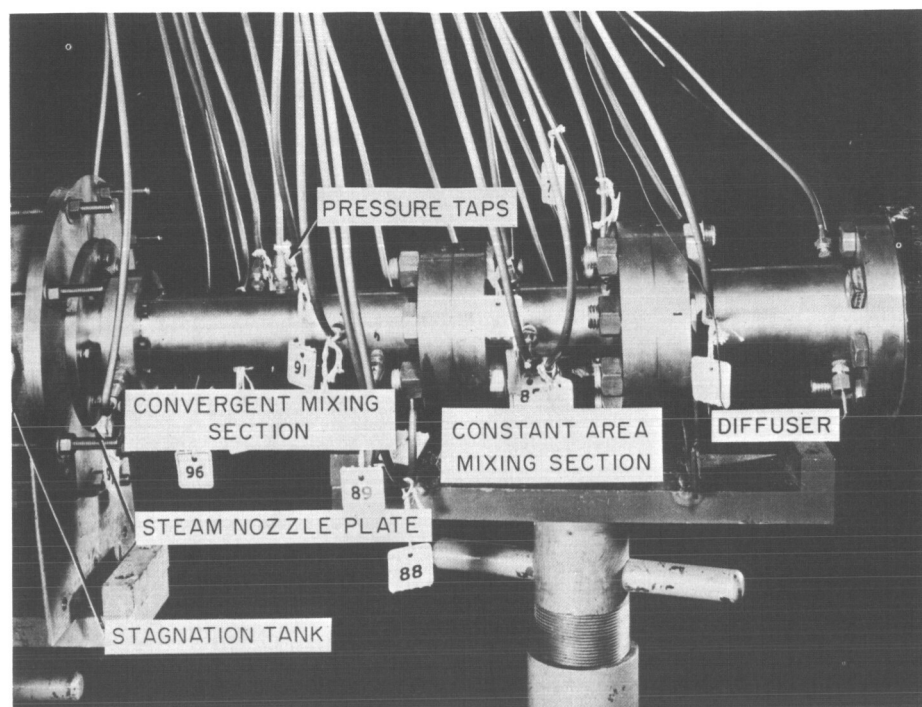


Fig. XI-2. Mixing section M-1 installation.

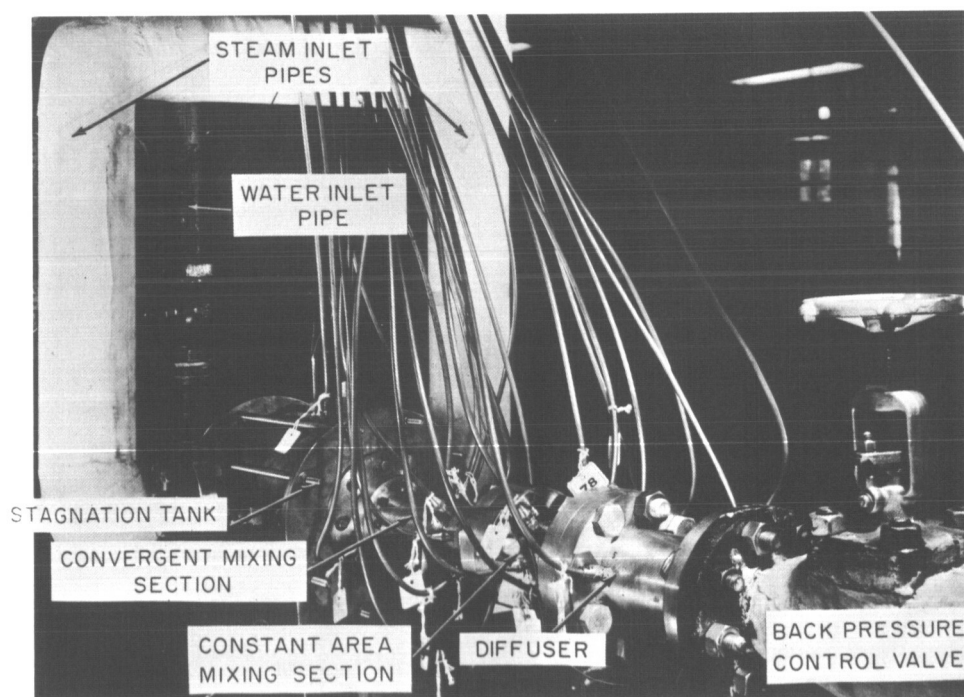


Fig. XI-3. Over-all view of mixing section M-1 installation.

inside diameter of 0.626 inch. The diffuser has a 6° angle of divergence with inlet and exit diameters of 0.626 and 1.95 inches, respectively. The water nozzle at the inlet of the convergent section has an inside diameter of 0.400 inch. The outside diameter is approximately 0.465 inch. The contours of the convergent section and diffuser are blended smoothly to the contour of the constant-area section. Pressure taps are located at numerous points along the condensing ejector.

The ratio of water-flow area to steam-flow area at section 1 (A_1''/A_1') is 0.1. The contraction ratio for the mixing section (A_1/A_2) is 5.

Figure XI-2 shows the installation of the mixing section in the condensing ejector test facility. Figure XI-3 shows additional details of the installation. Detailed pictures of the stagnation tanks were given in Quarterly Progress Report No. 78 (pages 150, 151).

Mixing section M-1 has been tested for inlet steam pressures at 20-50 psia and for water inlet pressures as shown in Fig. XI-4. The steam velocity at section 1 was approximately sonic velocity. The steam was saturated at the inlet to the condensing ejector while the water inlet temperature was approximately 40°F . For the test results

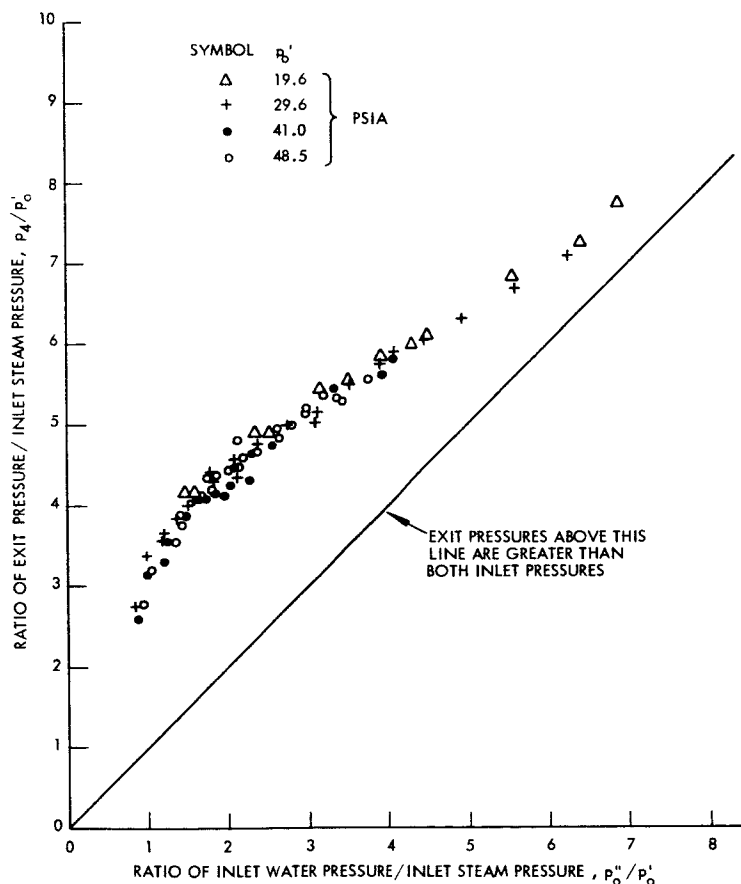


Fig. 4. Performance for mixing section M-1.

(XI. ENERGY CONVERSION RESEARCH)

in Fig. XI-4 the pressure discontinuity was moved as far upstream as possible in the constant-area section and the diffuser exit pressure (p_4) was measured. This location of the discontinuity is such that any farther upstream movement would cause the discontinuity to move rapidly through the convergent section and change the conditions at section 1. For these test conditions no major effects of the inlet steam pressure (p'_0) are observable. All test conditions correspond to exit pressures greater than the inlet pressures. The exit pressure varies linearly with the inlet water pressure above values of $p''_0/p'_0 \approx 1.5$. This behavior is expected theoretically. Theoretical values of the exit pressure, although not shown, are in good agreement with predicted values. For values of p''_0/p'_0 less than 1.5, the exit pressures are lower than expected. In this range the details of the mixing process must be known. This information is being obtained with the new plastic sections.

G. A. Brown, E. K. Levy

XI. ENERGY CONVERSION RESEARCH*

B. Alkali-Metal Magnetohydrodynamic Generators

Academic and Research Staff

Prof. J. L. Kerrebrock
Prof. M. A. Hoffman
Prof. G. C. Oates

Graduate Students

R. Decher
R. Dethlefsen

M. L. Hougen

D. J. Vasicek
G. W. Zeiders, Jr.

1. PERFORMANCE POTENTIAL OF SUPERHEATED RANKINE CYCLE SPACE POWER SYSTEMS EMPLOYING MAGNETOHYDRODYNAMIC GENERATORS

The Rankine cycle space power system is generally considered to have a higher specific power potential than the Brayton cycle system, particularly in the megawatt range.

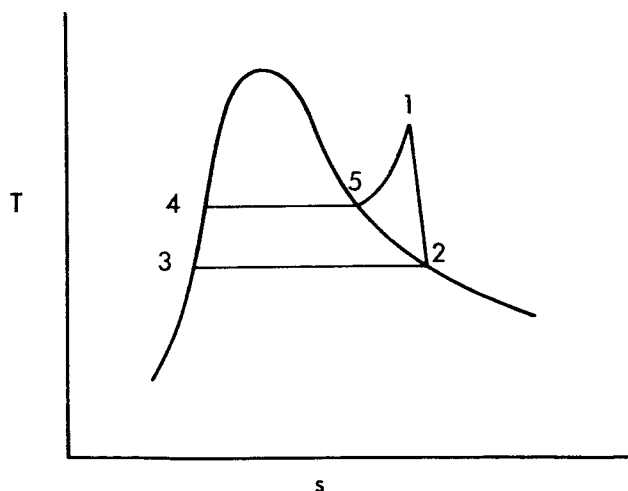


Fig. XI-5. Superheated Rankine cycle employing dry vapor in the MHD generator.

This conclusion is predicated on the assumption that even with the use of condensable metal vapors in the Rankine cycle, the maximum cycle temperature and component specific weights are not substantially different from those for the Brayton cycles.

When high-temperature reactors capable of surface temperatures over 2000°K are developed, the use of magnetohydrodynamic generators becomes attractive for large space power systems in the megawatt range. Even at these high surface temperatures, however, thermal ionization is inadequate for providing the necessary electrical

conductivity of the metal vapor, and nonequilibrium ionization must be employed.

It has been verified experimentally that dry potassium vapor can yield nonequilibrium electrical conductivities above 1 mho/cm at pressures of approximately .01 atm.¹ This

* This work is supported by the U. S. Air Force (Research and Technology Division) under Contract AF33(615)-3489 with the Air Force Aero Propulsion Laboratory, Wright-Patterson Air Force Base, Ohio.

(XI. ENERGY CONVERSION RESEARCH)

is adequate for an efficient MHD generator. Thus alkali metals could be employed in a superheated Rankine cycle of the type shown in Fig. XI-5.

The optimum radiator temperature, T_2 , for maximum specific power for this cycle, under the assumption of a fixed T_1 , can be shown to be given implicitly by

$$\gamma_c \triangleq \frac{a\epsilon\sigma T_1^4}{b} = \left(\frac{T_1}{T_2}\right)_{\text{opt}}^5 \left[4 - 5 \left(\frac{T_2}{T_1}\right)_{\text{opt}} \right],$$

where

a = radiator specific area, A_r/m_r (m^2/kg)

b = reactor heat source specific power, P_s/m_s (kw/kg)

ϵ = emissivity of the radiation

σ = Stefan-Boltzmann constant

T_1 = maximum cycle temperature.

The corresponding optimum cycle efficiency is given by

$$\eta_{R(\text{opt})} = \frac{1}{H} \frac{\left[1 - \left(\frac{T_2}{T_1}\right)_{\text{opt}} \right]}{1 + \frac{1}{H} \left[1 - \left(\frac{T_2}{T_1}\right)_{\text{opt}} \right]},$$

where

$$H \triangleq \frac{\gamma - 1}{\gamma} \frac{h_{fg}}{RT_1}.$$

Here it is assumed that the vapor is a perfect gas and that the liquid phase has a constant heat of vaporization, h_{fg} .

The maximum specific power can be calculated from

$$a_{\text{max}} \triangleq \frac{P_e}{M_e} = b\eta_{R(\text{opt})} \frac{1}{\left[1 + \frac{\left(1 - \eta_{R(\text{opt})}\right)}{\gamma_c \left(\frac{T_2}{T_1}\right)_{\text{opt}}^4} \right]}.$$

For a radiator-dominated system, γ_c approaches zero and $(T_2/T_1)_{\text{opt}} \Rightarrow 0.8$. The

optimum cycle efficiency and maximum specific power have the simple approximate forms

$$\eta_{R(\text{dry})} \approx \left(\frac{0.2}{H} \right)$$

$$a_{\text{dry}} \approx 0.41 \left(a_{\epsilon\sigma} T_1^4 \right) \left(\frac{\eta_{R(\text{dry})}}{1 - \eta_{R(\text{dry})}} \right).$$

If we are able to operate the MHD generator into the wet region, as illustrated by the cycle in Fig. XI-6, substantial gains in specific power are possible.

An estimate of the gains to be made by operating into the wet regime can be obtained

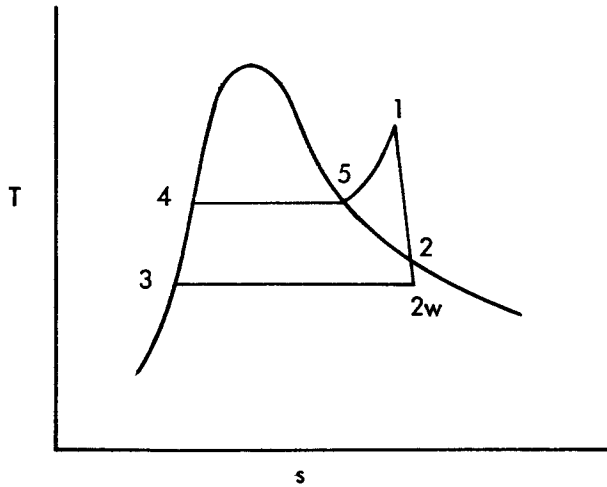


Fig. 6. Superheated Rankine cycle utilizing an MHD generator that operates into the wet region.

by assuming the same radiator temperature, T_{2W} , as for the dry cycle. For a radiator-dominated system with $T_{2W}/T_1 = 0.8$ we obtain

$$\eta_{R(\text{wet})} \approx \eta_{R(\text{dry})}^{[1+5H\mu]}$$

$$a_{(\text{wet})} \approx a_{(\text{dry})} \frac{\left(\frac{\eta_{R(\text{wet})}}{1 - \eta_{R(\text{wet})}} \right)}{\left(\frac{\eta_{R(\text{dry})}}{1 - \eta_{R(\text{dry})}} \right)}.$$

Consider lithium with $H \approx 2.3$ for $T_1 = 2000^\circ\text{K}$. Then for 5 per cent moisture, the cycle efficiency and specific power are both increased more than 50 per cent over the dry-cycle values.

(XI. ENERGY CONVERSION RESEARCH)

It should be noted that the cycle just discussed requires the boiler temperature, T_5 , to increase as μ is increased. If the maximum permissible boiler temperature of the reactor is limited, a more conservative cycle for comparison purposes might be one in which T_1 , T_2 , and T_5 are all maintained at the same values as for the optimum dry-vapor Rankine cycle. The MHD generator would then be assumed to be made somewhat longer to allow operation into the wet regime of point 2W.

For this cycle the fractional wetness, μ , is a function of both (T_{2W}/T_1) and the generator efficiency. For lithium, under the perfect gas assumptions, we obtain approximately 5 per cent moisture for $T_{2W}/T_1 = 0.7$ and $\eta_{\text{gen}} \approx 75$ per cent. This results in a cycle efficiency and specific power for a radiator-dominated system given by

$$\eta_{R(\text{wet})} \approx 2\eta_{R(\text{dry})}$$

$$a_{(\text{wet})} \approx 1.25a_{(\text{dry})}$$

Therefore, even for this very conservative case, the cycle efficiency is approximately double, and the specific power is increased about 25 per cent over the dry vapor values.

These potential increases in specific power to be obtained by operating into the wet region are predicated under the assumption that the generator efficiency remains near the dry-vapor value. If the generator efficiency decreases appreciably in the wet regime, King² has shown that the best specific power is obtained by operating only with dry vapor to the saturated vapor line as in Fig. XI-5.

A recent theoretical study by Solbes³ indicates that under certain conditions with drop radius large compared with the Debye length, nonequilibrium ionization can be sustained in a wet vapor. His initial experimental results tend to support this conclusion.

If nonequilibrium ionization can be obtained and sustained in a wet vapor, high generator efficiency in the wet regime should be attainable. The substantial increases in specific power which would then be possible provide strong motivation for the present study of the electrical conductivity of wet potassium vapor.

M. A. Hoffman, G. W. Zeiders

References

1. A. Rowe and J. L. Kerrebrock, "Nonequilibrium Electric Conductivity of Wet and Dry Potassium Vapor," A.P.L. Technical Documentary Report No. APL-TDR-64-106, Air Force Systems Command, United States Air Force, November 2, 1964.
2. R. King, "Performance Analyses of MHD Generators with Alkali Metal Working Fluids," S.M. Thesis, Massachusetts Institute of Technology, Cambridge, Mass., June 1965.
3. J. L. Kerrebrock, M. A. Hoffman, and A. Solbes, "Characteristics of a Pure Alkali-Metal Vapor Plasma," Quarterly Progress Report No. 79, Research Laboratory of Electronics, M.I.T., October 15, 1965, pp. 167-174.

XII. SPONTANEOUS RADIOFREQUENCY EMISSION FROM HOT-ELECTRON PLASMAS*

Academic and Research Staff

Prof. A. Bers

Graduate Students

C. E. Speck

A. INSTABILITIES IN THE EXTRAORDINARY WAVES ACROSS THE MAGNETIC FIELD

We have completed the stability analysis for propagation across the magnetic field in a plasma with energetic electrons having an unperturbed distribution function

$$f_0(\vec{v}) = \frac{1}{2\pi v_{0\perp}} \delta(v_{\perp} - v_{0\perp}) \delta(v_{\parallel}), \quad (1)$$

where the subscripts \perp and \parallel refer to directions across and along the applied magnetic field B_0 .

The dispersion relation for small-amplitude perturbations with dependence

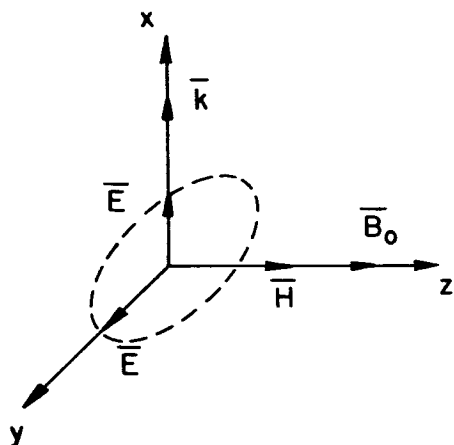


Fig. XII-1. Extraordinary wave propagation across the applied magnetic field B_0 .

$\exp(j\omega t - jkx)$ (see Fig. XII-1) was obtained from the relativistic, collisionless, Vlasov equation and Maxwell's equations.^{1, 2} The dispersion relation for the extraordinary wave (Fig. XII-1) and the electron distribution function of Eq. 1 is

$$\frac{c^2 k^2}{\omega^2} = \frac{K_{xy}^2}{K_{xx}} + K_{yy}, \quad (2)$$

*This work was supported by the U.S. Atomic Energy Commission (Contract AT (30-1)-3581).

(XII. SPONTANEOUS RF EMISSION FROM HOT-ELECTRON PLASMAS)

where

$$K_{xx} = 1 - \frac{a^2}{\gamma^2} \sum_{n=-\infty}^{\infty} \left[\frac{\gamma n^2 (J_n^2)' }{\nu(\nu-n)} - \frac{\beta^2 n^2 J_n^2}{(\nu-n)^2} \right] \quad (3)$$

$$K_{yy} = 1 - a^2 \sum_{n=-\infty}^{\infty} \left\{ \frac{[\gamma^2 (J_n')^2]' }{\gamma \nu(\nu-n)} - \frac{\beta^2 (J_n')^2}{(\nu-n)^2} \right\} \quad (4)$$

$$K_{xy} = j \frac{a^2}{\gamma} \sum_{n=-\infty}^{\infty} \left[\frac{n(\gamma J_n J_n')' }{\nu(\nu-n)} - \frac{\beta^2 n J_n J_n'}{(\nu-n)^2} \right], \quad (5)$$

and we have used the following abbreviations: $\nu = \omega/\omega_b$, with ω_b the relativistic cyclotron frequency; $a = \omega_p/\omega_b$, with ω_p the relativistic plasma frequency; $\gamma = kv_{0\perp}/\omega_b$, $J_n = J_n(\gamma)$ is the ordinary Bessel function of order n and argument γ ; the prime indicates a derivative with respect to γ ; and $\beta = v_{0\perp}/c$, with c the velocity of light in free space.

With the aid of the CTSS of Project MAC, and of the Newton-Raphson technique for finding roots of a transcendental equation, Eq. 2 was programmed to give the complex ω solutions for real wave numbers k . The results are summarized in Figs. XII-2 and XII-3. Three distinct types of instabilities can be identified: (i) fast-wave, relativistic, (ii) slow-wave, relativistic; and (iii) electrostatic. The terms "fast-wave" and "slow-wave" refer to the phase velocity regimes of the instability, being faster or slower than the velocity of light in free space. The term "relativistic" indicates that in the interaction the change in electron mass is crucially important. The term "electrostatic" refers to the approximation in which $\bar{k} \parallel \bar{E}$ is valid.

The fast-wave, relativistic instability is illustrated in Fig. XII-2. It can be seen to arise from the interaction between the fast-wave extraordinary mode that would exist in a cold plasma and the cyclotron harmonic wave branches that exist for finite $v_{0\perp}/c$. The instabilities occur near the velocity-of-light line where the extraordinary wave is essentially linearly polarized and the wavelength is large compared with the electron's Larmor radius. The physical description of these instabilities and their relativistic nature can be understood from the simple model shown in Fig. XII-4 for $\omega \gtrsim \omega_b$. Electrons that are in phase with respect to the electric field so as to give up energy (Fig. XII-4a) have their mass reduced and therefore their cyclotron frequency increased. But since the frequency of the field is slightly greater than the cyclotron frequency, these electrons remain in the same phase (Fig XII-4b) with respect to the electric field and continue to give up energy. Electrons of opposite phase (Fig. XII-4c), which initially

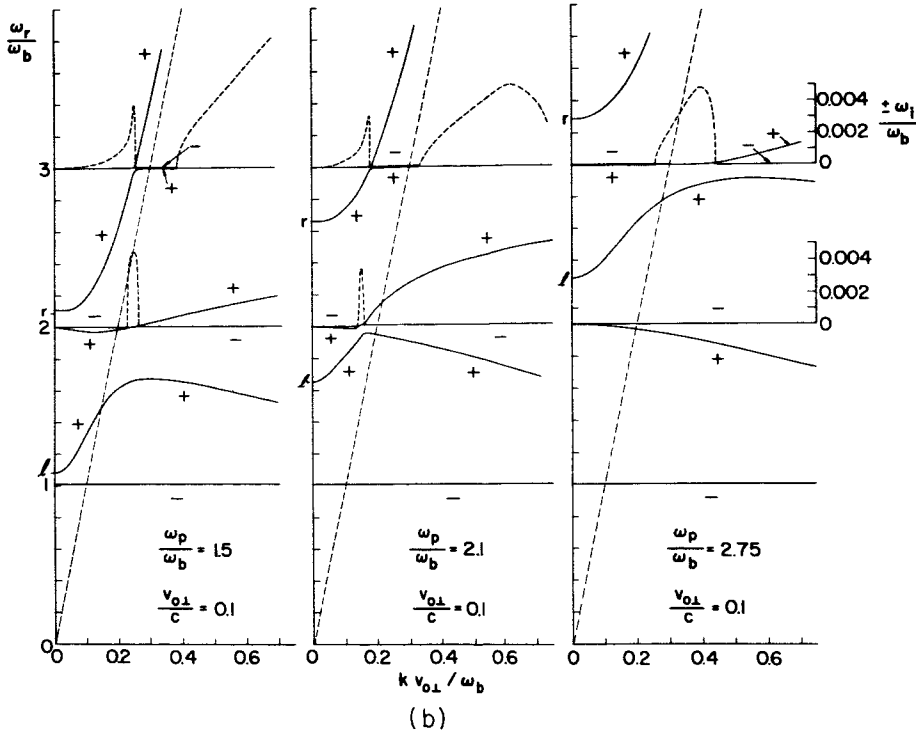
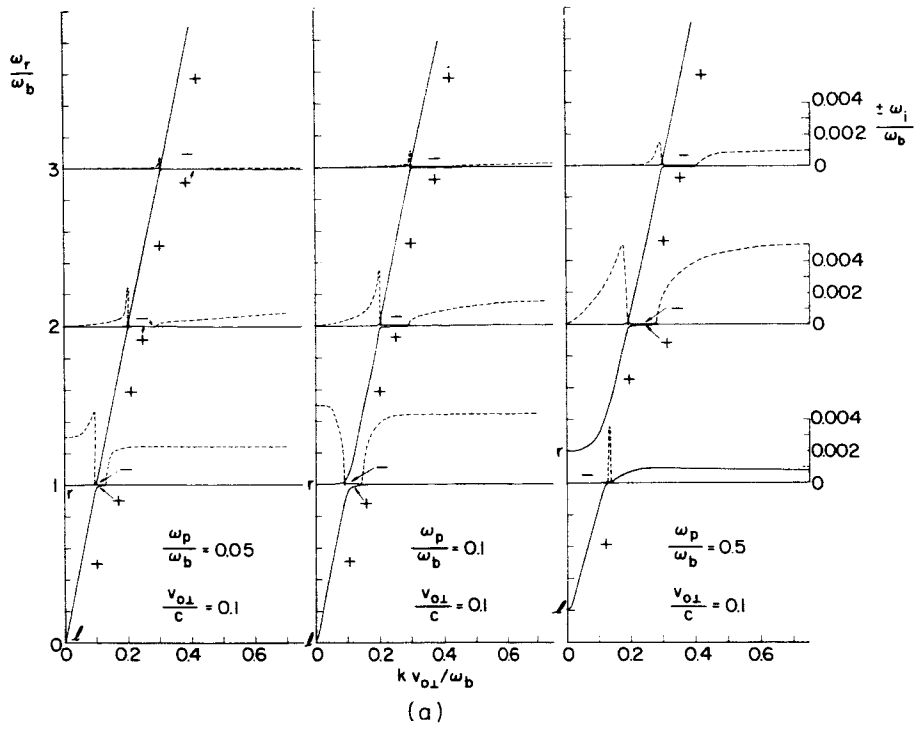


Fig. XII-2. Dispersion diagrams showing the fast-wave relativistic instabilities as a function of (ω_p/ω_b) for fixed $(v_{0\perp}/c) = 0.1$. The frequencies marked "l" and "r" are the cold-plasma cutoff frequencies of the extraordinary wave which are left- and right-circularly polarized.

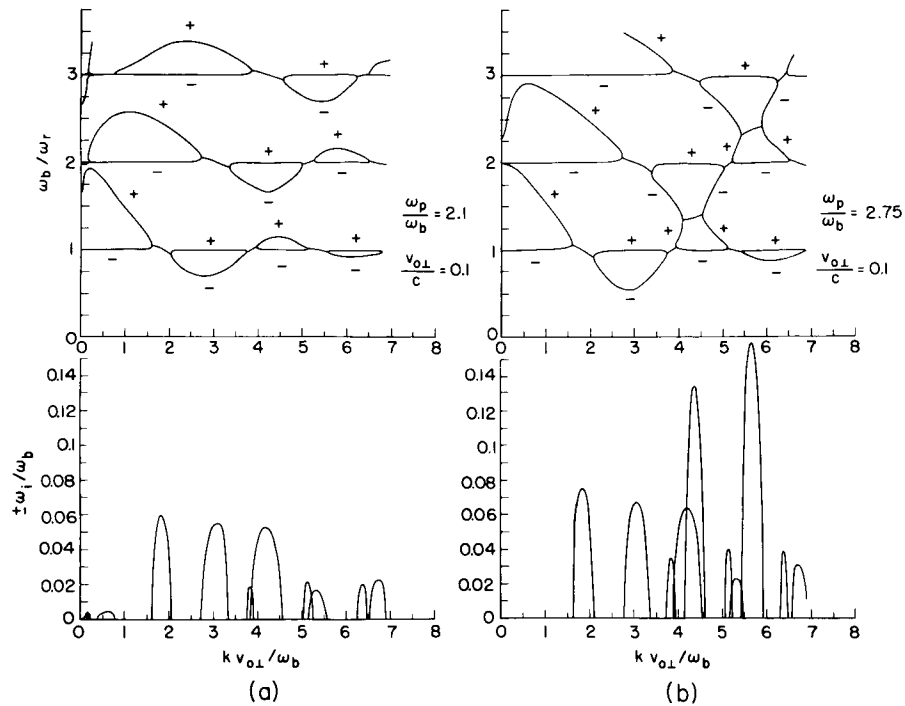


Fig. XII-3. Dispersion diagrams showing the slow-wave, relativistic instabilities (at cyclotron harmonics) and electrostatic instabilities (in between cyclotron harmonics). (a) (ω_p/ω_b) is below the threshold for the electrostatic instabilities. (b) Both types of instability are present. (For detail of the fast-wave region see Fig. XII-2b.)

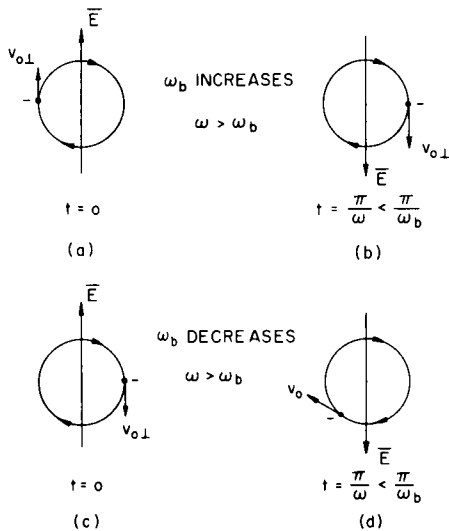


Fig. XII-4.

Model for the fast-wave, relativistic instability. The magnetic field B_0 is into the paper. The wavelength is assumed large compared with the electron-cyclotron orbit, and ω is slightly greater than ω_b .

(XII. SPONTANEOUS RF EMISSION FROM (HOT-ELECTRON PLASMAS)

take energy from the field, become heavier and come into phase with respect to the electric field so as to take less energy from the field (Fig. XII-4d). Thus phase conditions for a net loss of transverse energy from the electrons, and a consequent build-up of the fields, is established. As we have remarked previously,³ these instabilities are seen to vanish as (ω_p/ω_b) is increased to a value that makes the (cold-plasma) cutoff frequency exceed the (hot-plasma) cyclotron mode frequency. Figure XII-2a illustrates this for the unstable mode at $\omega \gtrsim \omega_b$, and Fig. XII-2b for the unstable modes at $\omega \gtrsim 2\omega_b$ and $\omega \gtrsim 3\omega_b$.

The slow-wave, relativistic, and the electrostatic instabilities are illustrated in Fig. XII-3. We have discussed certain aspects of these instabilities in previous reports.⁴⁻⁶ These can be understood in terms of wave-wave coupling in the presence of negative-energy modes that are due to finite $v_{0\perp}$. The slow-wave, relativistic instability (Fig. XII-3) occurs at the cyclotron harmonic frequencies; it depends upon $(v_{0\perp}/c)^2$ and occurs for arbitrarily low (ω_p/ω_b) . As (ω_p/ω_b) increases, the range of wave numbers over which this instability exists shrinks. The electrostatic instabilities, on the other hand, occur at frequencies in between cyclotron harmonics, and only if $(\omega_p/\omega_b) \gtrsim 2.5$. These instabilities occur even in the absence of relativistic mass effects.^{5,7} Relativistic effects produce a reduction of this instability.⁴

A. Bers, C. E. Speck

References

1. A. Bers, "Relativistic Formulation of the Conductivity Tensor for a Collisionless Plasma in a Magnetic Field," Internal Memorandum, Research Laboratory of Electronics, M.I.T., July 20, 1964 (unpublished).
2. A. Bers, "Relativistic Formulation of the Dispersion Relations for Waves in a Collisionless Plasma, Parts II and III," Internal Memorandum, Research Laboratory of Electronics, M.I.T., August 1, 1964 (unpublished).
3. A. Bers, "Instabilities in Plasmas with Beam-Type Distributions," Bull. Am. Phys. Soc. 10, 221 (1965).
4. A. Bers and C. E. Speck, "Instabilities of Longitudinal Waves Across the Magnetic Field," Quarterly Progress Report No. 78, Research Laboratory of Electronics, M.I.T., July 15, 1965, pp. 110-114.
5. C. E. Speck and A. Bers, "Instabilities in Quasi-Static Waves Across B_0 ," Quarterly Progress Report No. 79, Research Laboratory of Electronics, M.I.T., October 15, 1965, pp. 113-117.
6. C. E. Speck and A. Bers, "Electrostatic Plasma Instabilities at Cyclotron Harmonics," Quarterly Progress Report No. 80, Research Laboratory of Electronics, M.I.T., January 15, 1966, pp. 159-161.
7. F. W. Crawford and J. A. Tataronis, "Absolute Instabilities of Perpendicularly Propagating Cyclotron Harmonic Plasma Waves," J. Appl. Phys. 36, 2930-2934 (1965).

XIII. INTERACTION OF LASER RADIATION WITH PLASMAS AND NONADIABATIC MOTION OF PARTICLES IN MAGNETIC FIELDS*

Academic and Research Staff

Prof. D. J. Rose
Prof. T. H. Dupree
Prof. L. M. Lidsky

Graduate Students

T. S. Brown
J. D. Callen
M. V. Cesarski
J. F. Clarke

D. E. Crane
J. N. Hamawi
W. T. Hebel

M. D. Lubin
R. W. Moir
A. A. Offenberger
M. A. Samis

A. INCOHERENT SCATTERING OF LIGHT FROM A PLASMA III

The adoption of an infrared laser, optics, and detector, for observation of cooperative scattering effects from a plasma, was previously reported.¹ Provided the signal-to-noise is not seriously degraded for detection of small signals in the infrared versus visible light, a great benefit in the form of enhanced spectral width is available, thereby enabling a more detailed experimental view of plasma cooperative effects. The attendant difficulties are mainly two: one being the considerable black-body radiation at a wavelength of 10 microns, the other arising because thermal wavelength detectors are not as sensitive as photomultipliers in visible light.

The H_2 , CO_2 laser² was operated at an internal power level of several hundred watts, the measurement being achieved by coupling a fraction of the power out through a small hole in one mirror. A direct current discharge of ≈ 50 ma, at a field of 4 kv/meter in a gas mixture of 0.7 torr CO_2 , 1.5 torr N_2 , 2.8 torr He in a glass tube of 25 mm I.D. and 3 meters length yielded 1-watt cw coupled out through a 1-mm diameter hole in one mirror. Since the laser produces its power at a nominal 10.6 microns, NaCl windows and gold-coated mirrors (aligned in a hemispherical mode) formed the optical arrangement. Measurements were made with a calorimeter designed to measure power directly in the steady state. The power absorbed at one end of a copper rod gives a thermal conduction along the rod, which in a few heat-diffusion times relaxes to a constant energy conducted per unit time. The temperature difference between two points is linear with the input power, for nominal temperature rises; moreover, convective and radiative losses can be corrected for. It is anticipated that through a larger hole, a significant increase in power could be coupled out, and future work will explore this possibility.

With regard to the scattering experiment; the equivalent noise power, in the thermal fluctuations of dry-ice temperature black-body radiation, previously reported was

*This work was supported by the United States Atomic Energy Commission (Contract AT(30-1)-3285).

(XIII. INTERACTION OF LASER RADIATION WITH PLASMAS)

$P_N \approx 10^{-13}$ watt/(cps) $^{1/2}$. This calculation was based on an effective field of view of 6° for the mercury-doped germanium detector. In fact, to observe a larger scattering volume, a re-design has led to an F.O.V. $\approx 20^\circ$, thereby increasing noise. Furthermore, since it would be desirable to leave the optics at room temperature rather than to cool to dry-ice temperature, the more obvious way to proceed would be to use a cooled optical filter in front of the sensitive area of the detector. With the filter inside the cold shield of the detector (4°K), the filter would be essentially noise-free, the limiting noise being the background fluctuation level within the filter bandpass.

A comparison of the merits of cooling the background (temperature T_b) and reducing the bandwidth at the detector (nominal bandwidth ≈ 12 microns) is made in tabular form below. The detector has an area $= 10^{-3}$ cm 2 , and sees a solid angle $\Delta\Omega = 0.094$ ster.

$T_b(^{\circ}\text{K})$	$\Delta\lambda(\mu)$	$P_N(\text{watts}/(\text{cps})^{1/2})$
300	12	4.3×10^{-13}
300	0.12	4.3×10^{-14}
195	12	1.3×10^{-13}
195	0.12	1.3×10^{-14}

Equally important with keeping noise power down to tolerable levels (since signal watts will be $\lesssim 10^{-14}$ watt) is the problem of achieving high enough detector responsivity = signal volts per unit power detected. The responsivity goes up proportional to the decrease in DC background radiation. Typically, a detector with full-wavelength bandwidth looking at a 300°K background has a responsivity of 4×10^5 volt watt $^{-1}$, whereas a reduction of 100 in DC background would give 4×10^7 volt watt $^{-1}$. At the former responsivity a signal voltage of only 2 nanovolts would have to be measured (from a source impedance of many hundred kilohms) which is considerably below the noise figure for any available preamplifier. Thus amplifier noise would intrude along with photon noise. Also, the photoconductive detector is quiescent current biased, and a load resistor couples out the signal. The Johnson noise of a 1-M Ω resistor is ≈ 130 nanovolts/(cps) $^{1/2}$ at room temperature, and ≈ 15 nanovolts/(cps) $^{1/2}$ at 4°K . Thus a high responsivity is mandatory, and the use of, or combination of, cooled optical filter and reduced background is required. The one disadvantage to reducing the background lies in the fact that the detector impedance goes up, typical values being ≈ 4 M Ω for a background noise power $\approx 10^{-13}$ watt/(cps) $^{1/2}$.

Noise measurements of several low-noise preamplifiers have been conducted, with noise source input impedances from a few hundred kilohms to 10 megohms. A preamplifier utilizing field-effect transistors with an input impedance of 1000 M Ω was tested, and

(XIII. INTERACTION OF LASER RADIATION WITH PLASMAS)

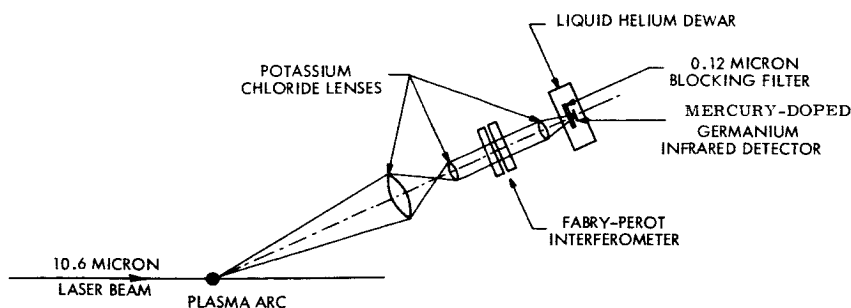


Fig. XIII-1. Experiment for observation of cooperative scattering effects from a plasma.

a high-Q bandpass filter for the output was designed and tested. The nominal noise voltage referred to the preamplifier input is $70 \text{ nanovolts}/(\text{cps})^{1/2}$ near 1 kc, with a source impedance of up to $10 \text{ M}\Omega$. With the larger responsivity, then, the signal level will be equal to or greater than the amplifier noise.

The detector has provision for installing a narrow bandpass filter, and this will be done. The filter achieves two ends – namely, reducing the background fluctuation level, and blocking all of the lower and higher modes of the Fabry-Perot interference filter. An over-all schematic diagram of the experiment is shown in Fig. XIII-1. The question of whether the plasma will be intracavity to the laser, or whether a focused external beam will be used, will depend on the final ratio of internal to external watts.

A. A. Offenberger

References

1. A. A. Offenberger, Quarterly Progress Report No. 79, Research Laboratory of Electronics, M.I.T., October 15, 1965, p. 145.
2. C. K. N. Patel, Phys. Rev. Letters 13, 617 (1964).

B. NONADIABATIC TRAPPING IN TOROIDAL GEOMETRY

The construction of a toroidal nonadiabatic electron trap¹ is now complete, and a cw circulating electron beam has been achieved. This report describes measured and calculated characteristics of the injected and trapped electron beam.

The device consists of a racetrack-shaped torus, 6.15 meters long with an 11.1-cm I.D. The straight sections are 1.45 m long, $B = 70$ gauss, injection energy $E = 2.0 \text{ kV}$, base pressure in the 10^{-6} torr range, Larmor radius (if all 2.0 kV are in the perpendicular direction) $r_{b0} = 2.1 \text{ cm}$. The U-bend drifts are cancelled by vertical magnetic fields. Rotational transform windings have been installed, but are not being used at present. The electron beam (a few microamperes) is injected at an angle of 63.3° with respect

(XIII. INTERACTION OF LASER RADIATION WITH PLASMAS)

to the magnetic field. This results in a Larmor radius $r_b = 1.9$ cm with 80% of the beam energy perpendicular to B .

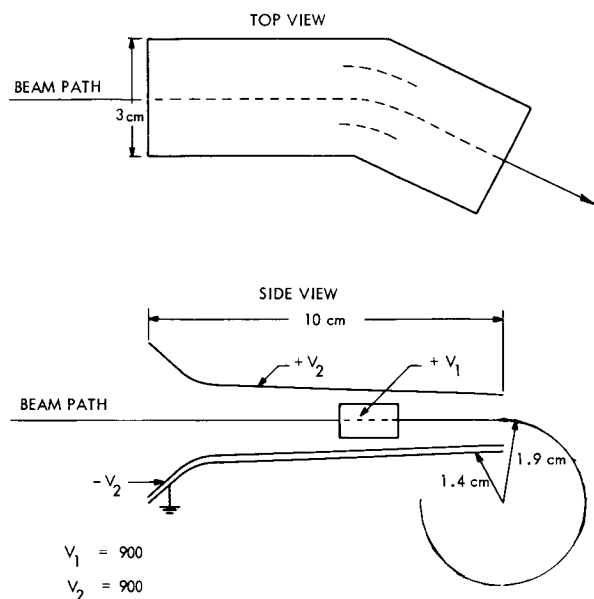


Fig. XIII-2. Electron-beam injector.

Figure XIII-2 shows the injector configuration. The injection point is one Larmor radius off-axis so that the guiding center is on the axis. The vertical electrostatic plates furnish the proper E field to yield a horizontal trajectory to the tip of the injector snout. A horizontal deflector bends the beam through an angle of 26.7° in the horizontal plane. The beam is thus injected as a helix of radius 1.9 cm and pitch 6.0 cm. The beam then encounters the "corkscrew"² which has been designed to transform perpendicular energy to parallel energy by resonant perturbation of the orbit. The corkscrew produces a small magnetic field (3.0 gauss) which is perpendicular to the main field and rotates in space with a pitch that increases with length (see Fig. XIII-3) in synchronism with the pitch of the beam. Thus the beam "sees" a $\vec{v} \times \vec{B}$ force which monotonically increases the parallel energy and straightens or "unwinds" the helical beam.

The performance of the corkscrew in unwinding the beam was checked by analyzing the parallel energy of the beam with a retarding potential screen and Faraday cup appropriately biased to retain secondary electrons. The parallel energy distribution is shown in Fig. XIII-4. Ideally the beam at the input to the corkscrew would be a spike at 400 volts, and the output a spike at 2000 volts. In reality the input beam has a large divergence, and so the output is spread in energy. The fact that such a large fraction of the input beam is unwound is due to the stability of the unwinding orbits.³ The reason for the large spread in parallel energy of the input beam is not yet understood.

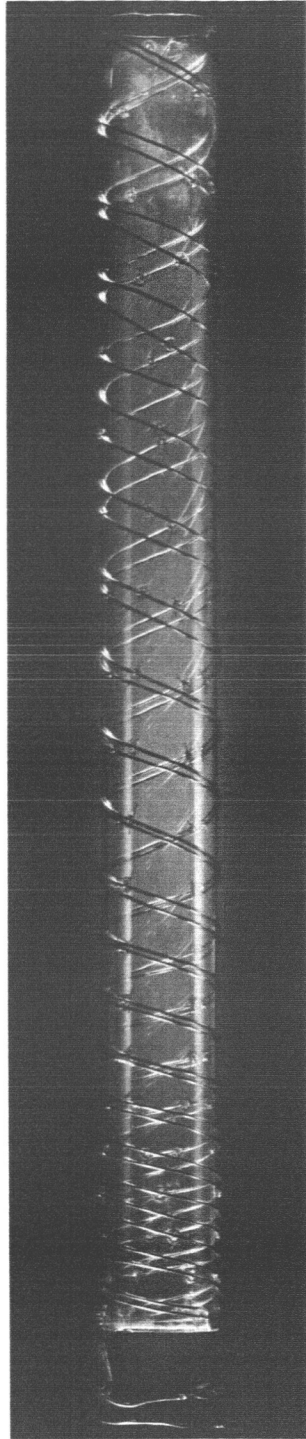


Fig. XIII-3. Perturbation field coil "Corkscrew."

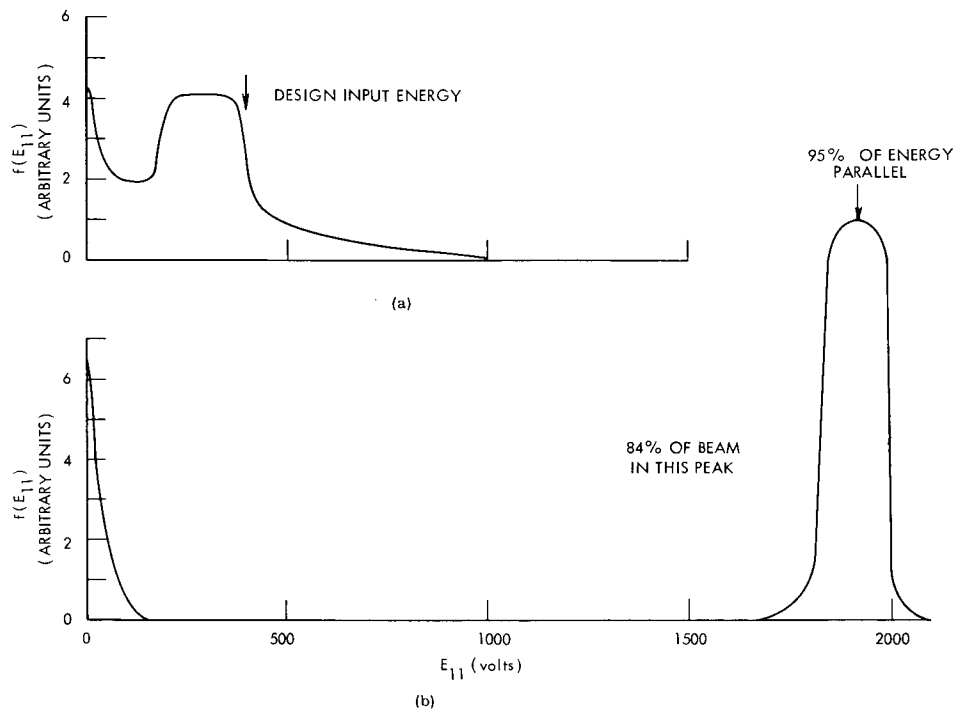


Fig. XIII-4. (a) Parallel energy distribution of the beam at the entrance to the corkscrew.
(b) Parallel energy distribution of the beam at the exit of the corkscrew.

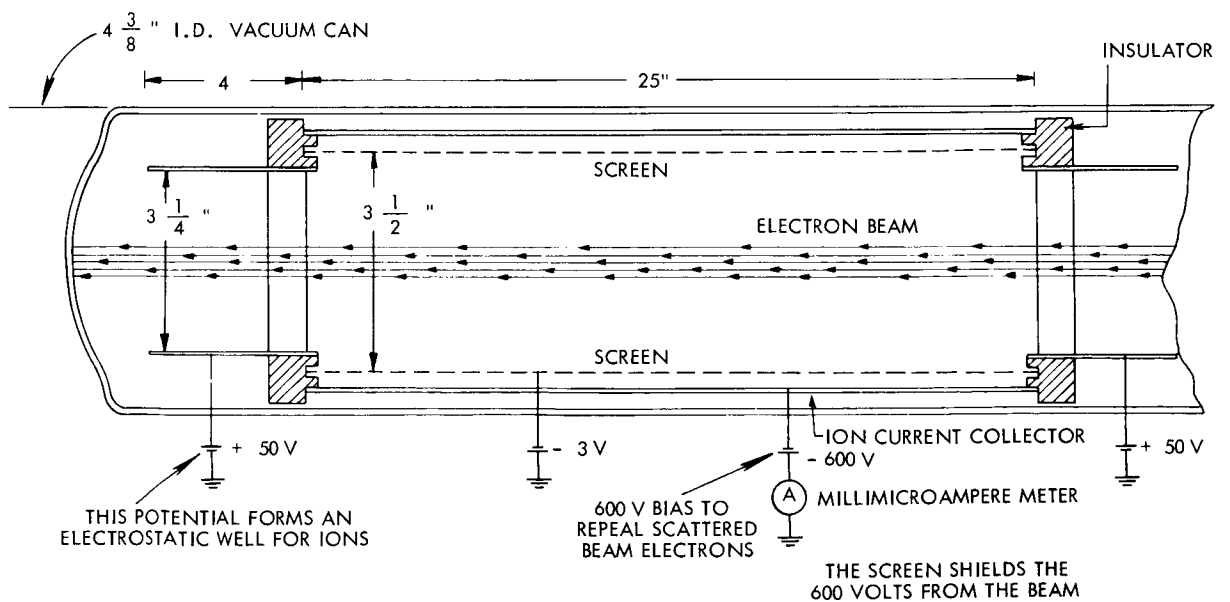


Fig. XIII-5. Ion collector.

(XIII. INTERACTION OF LASER RADIATION WITH PLASMAS)

With the aid of fluorescent screens and grids which could be rotated into the beam path, we ascertained that the beam was, in fact, closing on itself. In order to measure the number of transits around the device, we employed the ion collector⁴ shown in Fig. XIII-5. The ion current collected is proportional to the electron current and the background gas pressure. By bending the beam into the wall after it passes through the collector, we measure I_1 , the ion current for one transit. Then I_N is measured for the closed circulating beam. The average number of transits, N , is the ratio of the measured currents, I_N/I_1 . By varying the vertical field on the U-bends to obtain the "best" beam closure, N was maximized at approximately 15.

If all the loss was due solely to a directed drift, then $N = v_{\perp o} / \langle \Delta v_{\perp} \rangle$, and if the loss was due solely to random steps, then $N = v_{\perp o}^2 / \langle \Delta v_{\perp}^2 \rangle$. In reality we have a combination of both; however, we can take the two extreme cases and place upper bounds on $\langle \Delta v_{\perp} \rangle$ and $\langle \Delta v_{\perp}^2 \rangle^{1/2}$ as follows. $v_{\perp o}$ is proportional to the radius to the gun snout, 1.4 cm (see Fig. XIII-2), and v_o is proportional to $r_{b_o} = 2.1$ cm. Also, we assume that the guiding center stays on the axis.

$$\frac{\langle \Delta v_{\perp} \rangle}{v_o} < \frac{v_{\perp o}}{N v_o} = \frac{1.4}{15 \times 2.13} = .04$$

$$\frac{\langle \Delta v_{\perp}^2 \rangle^{1/2}}{v_o} < \frac{v_{\perp o}}{N^{1/2} v_o} = \frac{1.4}{15^{1/2} \times 2.13} = .17$$

A theoretical description is being worked out simultaneously with the experimental work and runs as follows. Let f be a vector whose components f_i equal the number of electrons with normalized magnetic moment $s = v_{\perp}^2 / v_o^2$ between $s_i \leq s < s_{i+1}$. Then

$$\frac{df(s, t)}{dt} = Of(s, t-t') - Lf(s, t-t') + S(s, t),$$

where t' is the transit time,

$$f = \begin{bmatrix} f_1 \\ f_2 \\ \vdots \\ f_n \end{bmatrix} = \text{distribution function} \quad S = \begin{bmatrix} S_1 \\ S_2 \\ \vdots \\ S_n \end{bmatrix} = \text{source}$$

(XIII. INTERACTION OF LASER RADIATION WITH PLASMAS)

$$O = \begin{bmatrix} O_{11} & O_{12} & \cdots & O_{1N} \\ O_{21} & & & \\ \vdots & & & \\ O_{N1} & & & O_{NN} \end{bmatrix} = \text{scattering in matrix}$$

$$L = \begin{bmatrix} L_1 & & & & 0 \\ & L_2 & & & \\ & & L_3 & & \\ & & & \ddots & \\ 0 & & & & L_N \end{bmatrix} = \text{scattering out matrix}$$

where

O_{ij} = probability that an electron in the j^{th} , s interval when it enters the "corkscrew" perturbation field will make a transition to the i^{th} , s interval divided by the time that the electron took to make one transit of the torus.

O_{ii} is set to zero, since this transition does not contribute to df/dt .

L_i = probability that an electron in the i^{th} , s interval will make a transition out of the i^{th} , s interval divided by its transit time.

For the steady state,

$$df/dt = 0$$

$$f = -(O-L)^{-1}S.$$

The elements of the O and L matrix are obtained by numerically integrating the equation of motion for a given input s and many phase angles θ , which gives an s at the output for each θ at the input. From these computations the probabilities can be constructed, the O - L matrix can be formed, and the inverse obtained on the computer. This gives the steady-state distribution.

We have divided s space into 9 intervals plus the "loss cone" where $s(\text{loss}) = 0.44$ (see Fig. XIII-6) and where the guiding center has been assumed to remain on the axis. The results are

$$N = \frac{\sum_{i=1}^9 f_i \Delta s_i}{\sum_{i=1}^9 s_i \Delta s_i} = 6.4 \text{ transits.}$$

(XIII. INTERACTION OF LASER RADIATION WITH PLASMAS)

It is quite likely that the discrepancy between measured and computed values results from a slow downward drift of the beam when the circulating current is experimentally maximized. This would move the particle guiding centers away from the injection snout even as they scattered in s and so reduce the effective size of the velocity-space loss cone.

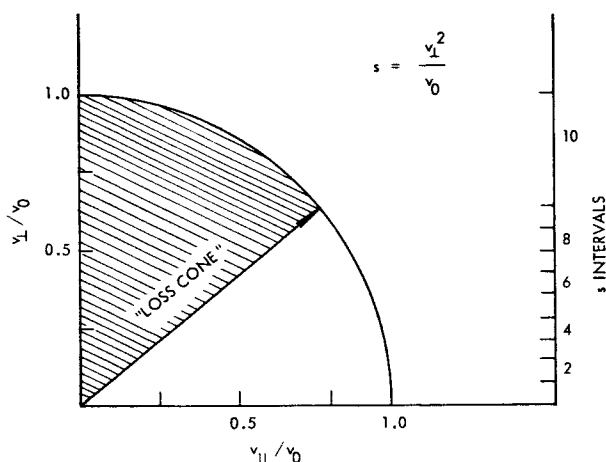


Fig. XIII-6. Loss cone in velocity.

The number of transits obtained experimentally and computationally are preliminary, and work is in progress to improve the techniques; however, the number of transits is large enough to be used for measurements of diffusion produced by added perturbing fields as originally planned.

R. W. Moir, L. M. Lidsky

References

1. Quarterly Progress Report No. 77, Research Laboratory of Electronics, M.I.T., April 15, 1965, pp. 164-167; Quarterly Progress Report No. 78, July 15, 1965, pp. 126-127; Quarterly Progress Report No. 79, October 15, 1965, pp. 131-132.
2. R. C. Wingerson, T. H. Dupree, and D. J. Rose, *Phys. Fluids* 7, 1475 (1964).
3. L. M. Lidsky, *Phys. Fluids* 7, 1484 (1964).
4. A. P. Slabospitskii and V. D. Fedorchenko, International Atomic Energy Conference on Plasma Physics and Controlled Nuclear Fusion Research, Culham, United Kingdom, 6-10 September 1965, Paper CTO/105.

C. NONADIABATIC SCATTERING IN MAGNETIC FIELDS

1. Measurements of Particle Escape from a Corkscrew Magnetic Trap

Figure XIII-7 shows the experimental apparatus that is being used to investigate the trapping and loss of particles in a "corkscrew"¹ nonadiabatic magnetic field. A 1600-volt

(XIII. INTERACTION OF LASER RADIATION WITH PLASMAS)

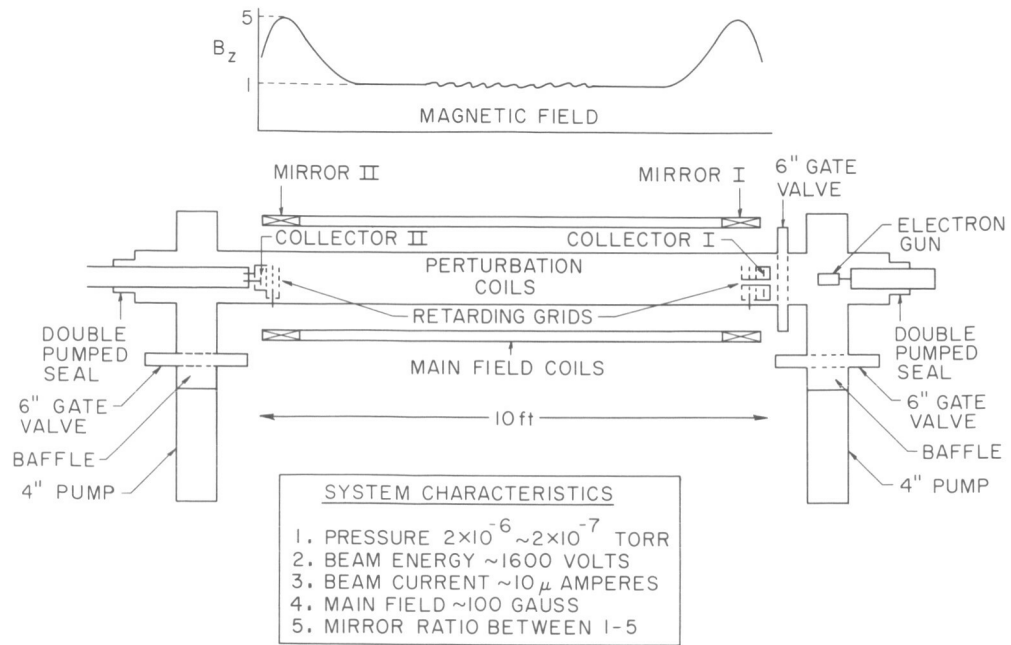


Fig. XIII-7. Nonadiabatic trapping experiment.

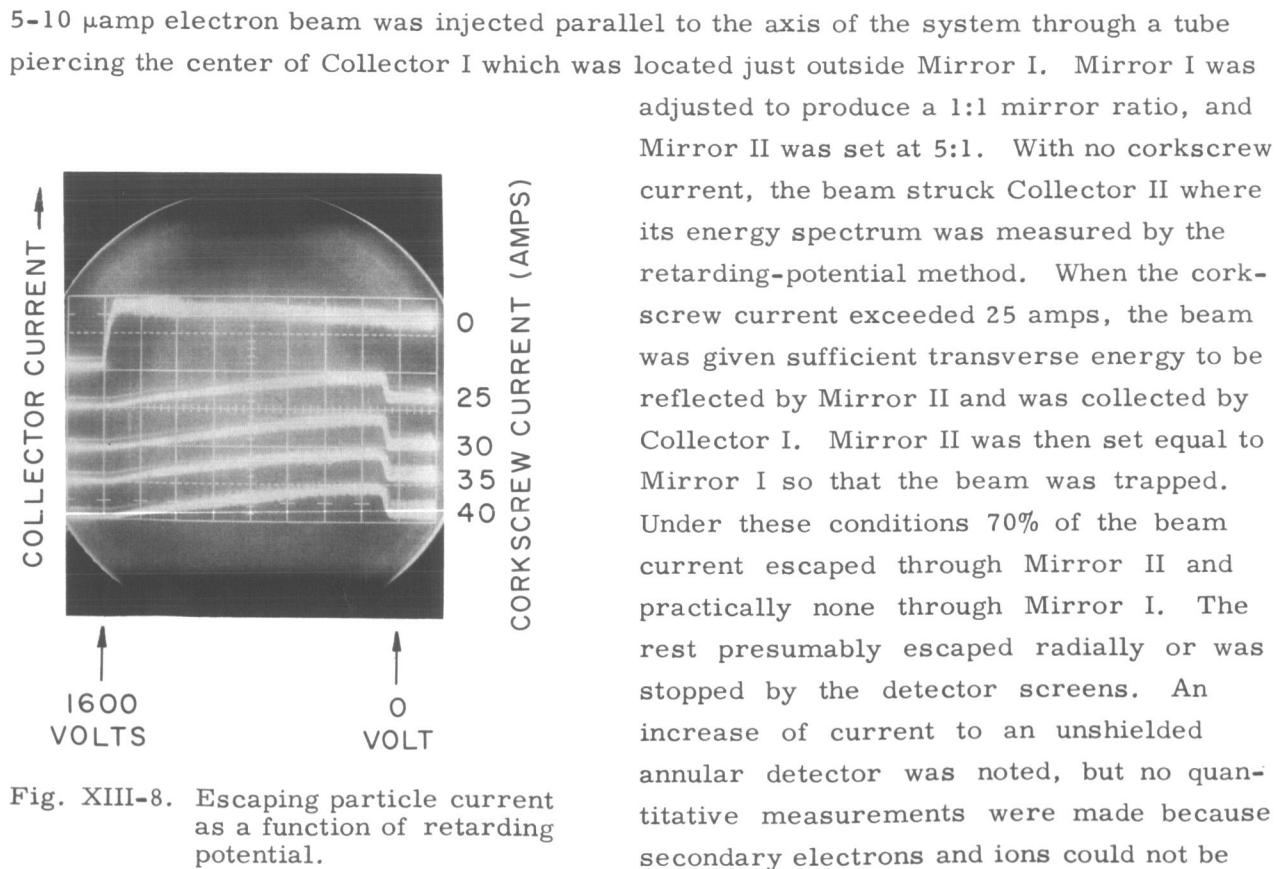


Fig. XIII-8. Escaping particle current as a function of retarding potential.

separated from the injected particles.

Figure XIII-8 shows the energy analysis made at Collector II for 5 values of the corkscrew current. In this figure the particles are distributed from 1600 volts (the total beam energy) to nearly zero. This is due to the position of Collector I in the mirror's throat. Particles that are scattered into the loss cone in the uniform central region have parallel energies ranging from 1600 volts to 1280 volts, the minimum parallel energy necessary to penetrate the mirror. As the 1280-volt particles move farther into the mirror from the central field region, conservation of magnetic moment converts parallel into perpendicular energy. Just at the mirror neck these particles have zero parallel energy, while the 1600-volt particles, which have zero magnetic moment, still possess all of their parallel energy.

The dip on the right in Fig. XIII-8 is due to the analyzing screen swinging positive and collecting the beam. This point locates the zero retarding voltage. The first trace, which is for the unperturbed beam, indicates the 1600-volt point. A similar energy analysis taken with the detector retracted to a 100-gauss region outside the mirror accurately reproduces the distribution of particles in the loss cone within the trap at any instant. A derivative of this curve, which is proportional to the parallel energy distribution of the particles, is shown in Fig. XIII-9 superimposed on an energy-space diagram. It is apparent that the peak of this distribution lies well inside the edge of the loss cone. This indicates the existence of a strong preferential scattering as opposed to a diffusive loss mechanism.

The decay of the trapped particles was observed for pulsed injected beams. Fig-

ure XIII-10 shows a typical result. The lower trace is for zero corkscrew current and shows that the rise time of the detection circuit is less than $0.5 \mu\text{sec}$. The upper curve is for a corkscrew current of 38.5 amps. The signal is constant at its equilibrium level for approximately 3 transit times after the beam is cut off. This indicates that the dominant loss of particles is associated with the second and subsequent forward transits of the perturbation. The decay is exponential to the limiting detector sensitivity and has a time constant of $1.49 \mu\text{sec}$.

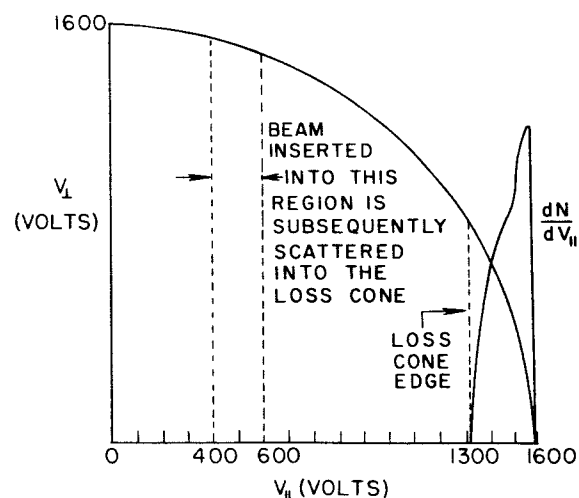


Fig. XIII-9. Loss-cone particle distribution as a function of their parallel energy.

A series of decay curves for varying corkscrew currents were obtained, and the decay time as a function of this

(XIII. INTERACTION OF LASER RADIATION WITH PLASMAS)

current is shown in Fig. XIII-11. In each case the decay was exponential to the limit of detector sensitivity. Because of this limit on sensitivity ($\sim 5\%$ of the equilibrium signal),

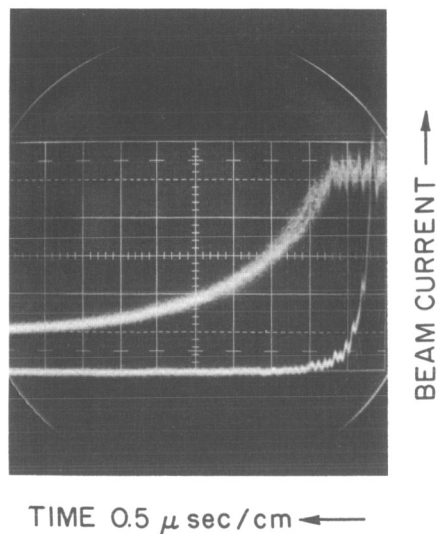


Fig. XIII-10. Upper trace: Trapped particle decay.
Lower trace: Untrapped beam.

the existence of a group of long-lived particles is not ruled out. For example, a group of particles trapped in a region of velocity space where their lifetime against scattering was $15 \mu\text{sec}$ would be undetected unless their density exceeded 50% that of the fast-decaying group. We are now at work on this problem. Figure XIII-11 does indicate that the maximum lifetime occurs at the design current of the corkscrew.

For helical resonant trapping, the product of the current and the cosine of the design phase angle is a constant. At lower currents the particle must follow closer to the position of maximum radial field to follow the resonant orbit. Such orbits have been shown to be less stable,² and the particle will experience less windup. On the third pass these

particles having more v_{\parallel} will be locally resonant nearer to the center of the corkscrew where the perturbation is strongest and will be lost rapidly. For currents higher than the design current, the particle sees a higher perturbation field and is lost rapidly because the scattering is stronger.

The rapid initial loss of particles and the preferential forward scattering reported above were not predicted by the previously existing theories of nonadiabatic scattering.^{3,4} These experiments have motivated a new approach to

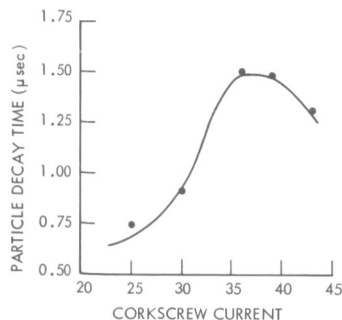


Fig. XIII-11. Lifetime as a function of corkscrew current.

(XIII. INTERACTION OF LASER RADIATION WITH PLASMAS)

the description of this scattering which is outlined below.

The experiments described here were performed with a seven-turn corkscrew. In order to obtain a better test of existing theoretical analyses, a highly tuned fifteen-turn corkscrew was built and is being tested. This "Mark II corkscrew" has a screened radial particle detector which should yield more accurate particle accountability. Also, a scintillator-photomultiplier electron detection system was tested. Preliminary results show that we might be able to increase the sensitivity of the lifetime measurements enough to allow a conclusive check on the existence of a substantial long-lived group.

2. Validity of Stochastic Descriptions of Nonadiabatic Motion

The system under consideration can be idealized as in Fig. XIII-12. In a particular case the fields in the magnetic-moment nonconserving region might be due either to a

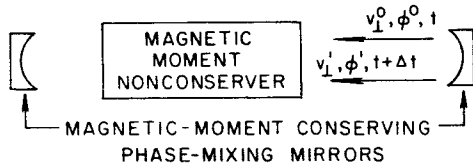


Fig. XIII-12. Idealization of a non-adiabatic trap.

plasma wave or to external current windings and, in any case, they will be assumed to be known functions of space and time. Thus, we shall consider purely deterministic systems. The conditional probability per unit v_{\perp} and ϕ that for given v_{\perp}^0 and ϕ^0 one will observe v_{\perp}^1 and ϕ^1 between v_{\perp}^1 and $v_{\perp}^1 + \Delta v_{\perp}^1$ and ϕ^1 and $\phi^1 + d\phi^1$ after a transit time Δt is

$$P_2(v_{\perp}^0 \phi^0 / v_{\perp}^1 \phi^1 \Delta t) = \delta(v_{\perp}^1 - v_{\perp}^S) \delta(\phi^1 - \phi^S) \quad (1)$$

where

$$v_{\perp}^S = v^S(v_{\perp}^0, \phi^0)$$

$$\phi^S = \phi^S(v_{\perp}^0, \phi^0)$$

are solutions of the equations of motion. But ϕ varies between zero and 2π many times during the particle's orbit, so that ϕ^1 and ϕ^0 appear to be uncorrelated. Symbolically, we can write the conditional probability as

$$P_2(\phi^0 / \phi^1 \Delta t) \approx \frac{1}{2\pi}. \quad (2)$$

In a magnetic trap we are mainly interested in describing the statistical behavior of a particle's magnetic moment and so concern ourselves with v_{\perp} . To simplify the problem

(XIII. INTERACTION OF LASER RADIATION WITH PLASMAS)

of solving N orbit equations for N particles, it is tempting to employ the pseudorandom character of the phase ϕ .

If we allow some uncertainty in ϕ^0 , the delta function in Eq. 1 is broadened to the extent of this uncertainty. Furthermore, one might hope that in the weak-field limit the change in v_{\perp} per transit would be small. If we make this assumption, we can state that the conditional probability (1) is a sharply peaked function around

$$v'_{\perp} = v_{\perp}^0 + \Delta v_{\perp}^0(\phi^0, v_{\perp}^0), \quad (3)$$

where

$$\Delta v_{\perp}^0 \ll v_{\perp}^0.$$

Then, if we ignore the initial phase dependence of the small quantity Δv_{\perp}^0 , the conditional probability (1) becomes

$$P_2(v_{\perp}^0 \phi^0 / v'_{\perp} \phi' \Delta t) = P_2(v_{\perp}^0 / v'_{\perp} \Delta t) P_2(\phi^0 / \phi' \Delta t), \quad (4)$$

where the velocity conditional probability is peaked around v_{\perp}^0 . If the initial phase dependence of Δv_{\perp} is not ignored, the separation in (4) is not valid. We shall show that the results of the existing stochastic theories depend on this assumption and consequently will fail if the assumption proves untenable.

The conditional probability in (4) can be used to generate a Fokker-Planck equation in the usual way with the exception that higher order terms are not dropped because they are proportional to high powers of the elemental time steps. They are dropped solely because the small-field assumption ensures that they are small. The result is

$$\Delta f = 2 \frac{\partial}{\partial s} \left\{ -\sqrt{s} \frac{\overline{\Delta v_{\perp}}}{v} + \frac{\sqrt{s}}{2} \frac{\partial}{\partial s} \left(\frac{\overline{\Delta v_{\perp}^2}}{v^2} \right) \right\} f + 2 \frac{\partial}{\partial s} \left(s \frac{\overline{\Delta v_{\perp}^2}}{v^2} \right) \frac{\partial}{\partial s} f, \quad (5)$$

where

$$s = v_{\perp}^2 / v^2$$

$$\overline{\Delta v_{\perp}^n} = \int_0^{2\pi} d\phi' \int_0^v dv'_{\perp} \Delta v_{\perp}^n P_2(v_{\perp}^0 \phi^0 / v'_{\perp} \phi' \Delta t). \quad (6)$$

If we make the pseudorandom approximation, we may replace the integration over ϕ' by integration over ϕ^0 and, by using Eq. 4, find

$$\overline{\Delta v_{\perp}^n} = \int_0^{2\pi} d\phi^0 \Delta v_{\perp}^n \bigg|_{v_{\perp}^0} P_2(\phi^0 / \phi' \Delta t) \quad (7)$$

and by using (2) get

$$\overline{\Delta v_{\perp}^n} = \int_0^{2\pi} \frac{d\phi^0}{2\pi} \Delta v_{\perp}^n \bigg|_{v_{\perp}^0} \quad (8)$$

This is the starting point of the previous stochastic theories.⁴ We have shown that it is based on the assumption that the probability of the transition $v_{\perp}^0 \rightarrow v_{\perp}'$ is independent of ϕ^0 . This assumption is only true in the limit of zero perturbation. Numerical analysis will show that it does not apply in the case of the corkscrew magnetic trap.

The consequence of the usual assumption (Eq. 8) is that the dynamical friction term in Eq. 5 is of second order and is in fact cancelled by the second term in braces. We are left with

$$\Delta f = \frac{\partial}{\partial s} 2s \left(\frac{\overline{\Delta v_{\perp}^2}}{v^2} \right) \frac{\partial f}{\partial s} \quad (9)$$

which predicts only currents proportional to the second power of the small field quantities. In other words, Eq. 9 predicts a current resulting from the dependence of the diffusion coefficient on s , but it cannot account for a current caused by a preferred direction of scattering.

If $P_2(v_{\perp}^0 \phi^0 / v_{\perp} \phi \Delta t)$ is not split up as indicated above, we might still assume that it is peaked around v_{\perp}^0 on the basis of perturbation theory. In this case, however, Eq. 8 should be written

$$\overline{\Delta v_{\perp}^n} = \int_0^{2\pi} \frac{d\phi^0}{2\pi} \Delta v_{\perp}^n \bigg|_{v_{\perp}^0} F(\phi^0), \quad (10)$$

where $F(\phi^0)$ is an unknown function containing the previously neglected phase dependence of the conditional probability. Now the dynamical friction term in the Fokker-Planck equation is of first order in the small-field quantities. This could lead to a much larger directional scattering than was previously suspected. Such rapid loss has been observed experimentally and is consistent with numerical analysis of particle motions.

3. Digital-Statistical Description of Nonadiabatic Scattering

The equations describing the motion of a particle in a nonadiabatic magnetic field are¹

$$\frac{dv_{\perp}}{dz} = \omega_{\perp}(r, z) \cos \chi \quad (11)$$

(XIII. INTERACTION OF LASER RADIATION WITH PLASMAS)

$$\frac{dx}{dz} = \frac{\omega_o}{v} - \frac{2\pi}{p(z)}, \quad (12)$$

where ω_{\perp} and ω_o are qB_{\perp}/m and qB_o/m , respectively, and p is the pitch of the perturbation field B_{\perp} . Most of the interaction between a particle beam and the nonadiabatic field in a magnetic trap take place near the axis. Then Eqs. 11 and 12 can be simplified by neglecting the radial dependence of ω_{\perp} . Employing this assumption and the normalizations of Lidsky,² we obtain a simplified set of equations which closely describes the motion of a particle in a corkscrew

$$\frac{dv}{dx} = \alpha \sin 2x \frac{\cos \chi}{\cos \chi_o} \quad (13)$$

$$\frac{d\chi}{dx} = \Lambda \left(\frac{1}{\sqrt{1-v^2}} - \frac{1}{p(x)} \right). \quad (14)$$

The parameters are defined as follows:

α^2 = final magnetic moment after one transit in the equilibrium orbit

p = corkscrew pitch normalized to its initial value p_o

χ = a phase angle between the particle's position and the field maximum

χ_o = phase angle in equilibrium orbit

$\Lambda = 4L/p_o$ normalized corkscrew length

$x = \pi z/2L$.

These equations were solved numerically to determine the change in a particle's magnetic moment as a function of the initial phase. Typical results are shown in Fig. XIII-13. This is a plot of the relative field-particle phase χ as a function of position along the corkscrew for a particle of initial magnetic moment 0.40 and various initial phases. The insert shows the final magnetic moment as a function of initial phase. The insert also shows that particles increase their magnetic moments over only 17% of the possible initial phases. In other words, a particle with random initial phase has an 83% probability of decreasing its magnetic moment. This is a startling conclusion that clearly invalidates the stochastic theory already referred to. The physical reason for this preferential downward scattering can be seen by examining the phase curves above the insert in Fig. XIII-13. Upon entrance to the corkscrew, a particle with 40% initial windup is rotating faster than the field in the frame moving with the particle's axial velocity. Thus the phase is initially increasing as shown. Since the perturbing field pitch is decreasing along the axis, there is some point where the field and particle will rotate with the same angular velocity. This resonance condition is expressed analytically by

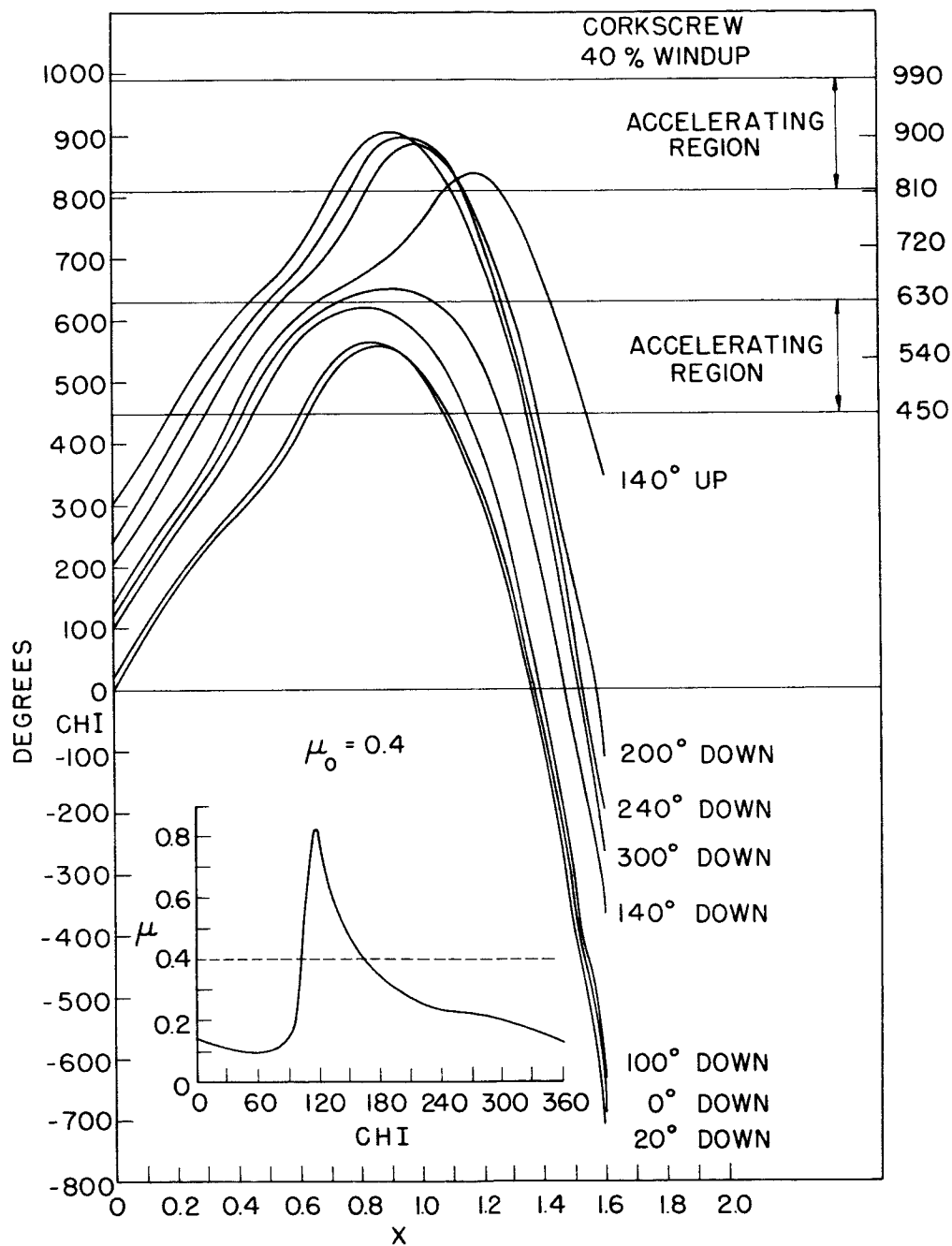


Fig. XIII-13. Computer analysis of trapped-particle motion.

$$\frac{d\chi}{dx} = 0 \quad (15)$$

These zero slope points are shown in Fig. XIII-13, and we shall refer to them as turnover points.

Referring to Eq. 13 one notes that the direction of the change in the perpendicular velocity (and consequently in the magnetic moment) is determined by the relative field-particle phase χ . In Fig. XIII-13 we have indicated two phase quadrants in which the particle loses magnetic moment as "acceleration regions" since a particle losing magnetic moment is accelerated along the field. If a particle has a turnover point in such a region, it experiences a resonant accelerating interaction. Figure XIII-13 shows that most of the curves have turnovers in the accelerating region. The curve for 140° initial phase which starts to turn over in the middle of the deceleration region is pushed upward into the next accelerating quadrant.

The physical basis for preferential acceleration can be seen by examination of the necessary condition for turnaround. From (12) we get the turnaround condition

$$\frac{d^2\chi}{dz^2} = \frac{2\pi}{p^2} \frac{dp}{dz} + \frac{\omega_o}{(v^2 - v_\perp^2)^{3/2}} v_\perp \frac{dv_\perp}{dz} < 0 \quad (16)$$

Employing the resonance condition, we obtain

$$\frac{2\pi}{p} = \frac{\omega_z}{(v^2 - v_\perp^2)^{1/2}}, \quad (17)$$

and by using Eq. 11 this reduces to

$$\frac{d^2\chi}{dz^2} = \left[\frac{2\pi}{p} \right]^2 \left[\frac{v_\perp \omega_\perp}{\omega_o^2} \right] [\cos \chi - \cos \chi_o]. \quad (18)$$

This shows that for the corkscrew there is a forbidden region in phase where turnaround is impossible. This forbidden region covers the range of phase where the particle sees the maximum decelerating force. Thus, since the particle cannot come into resonance in the most effective part of the decelerating region, its average step will be an acceleration.

When we look at the physics of this effect, we see that it is more general than the derivation above might indicate. Consider Eq. 11 which has general validity. Given a particle that is rotating faster than the field, this equation tells us that v_\perp fluctuates as χ increases; however, it is the particle's z velocity which causes χ to change. The

(XIII. INTERACTION OF LASER RADIATION WITH PLASMAS)

faster v_z , the slower χ fluctuates. Alternatively, the slower v_\perp , the slower χ fluctuates. Thus decelerating regions which decrease v_z have, on the average, more fluctuations than equivalent accelerating regions. The net result is a preferential downward scattering in resonant systems with pitch-length decrease in the direction of particle motion. Another way of stating this is that χ tries to become stationary by decreasing v_\perp . If it finds itself in a decelerating quadrant, it tends to move onward into the next favorable quadrant. This effect is shown in the 140° initial phase case in Fig. XIII-13.

We have also performed calculations on a Whistler model field. This is a helical field with a linear phase variation along its axis. Although this calculation was not scaled to any physical system supporting real waves, the effect noted above did appear. We feel that with proper scaling Eqs. 11 and 12 should apply to the ionosphere. The necessary calculations to check this scaling are being performed.

We have tried to indicate just how perturbation theory fails in the presence of preferential scattering. Figures XIII-14 and XIII-15 show the mean step and mean-square step in v_\perp^2/v^2 obtained from our orbit calculations and from perturbation theory.³ We have indicated that preferential scattering will generate a current term proportional to the first power of the field variable and also modify the second-order diffusion coefficients. The magnitude of the discrepancy depends upon the relative width of the forbidden zone, and is a complicated function of the details of the resonant-field perturbation. The discrepancy becomes more important as the size of the normalized velocity steps decreases because the confinement time is proportional to N^{-1} for currentlike and to N^{-2} for diffusivelike losses, where N is approximately $v^0/\Delta v^0$.

The peak at $v_\perp^2/v^2 = 0.35$ in Fig. XIII-13 is a case in point. This initial magnetic moment displays the same behavior as that shown in the insert in Fig. XIII-13 which is for $v_\perp^2/v^2 = 0.40$. The difference is that the 0.35 case has a narrow range of initial phases that place the particle in the design orbit somewhere in the corkscrew. The particles with their initial phases make very large steps upward in magnetic moment and bias the mean-step upward. A particle with random initial phase will probably still make a step downward. Thus, in this case, the Fokker-Planck equation with its average coefficient $\overline{\Delta s}$ is not truly descriptive of the situation. Thus, the results of Section I call into question the utility of the Fokker-Planck equation in describing the solution of the distribution function in systems of physical interest even if asymmetric scattering is correctly taken into account. Particles may fall into near-resonant orbits and suffer selectively large perturbations. This behavior violates the essential assumption that the distribution function changes slowly in the time scale describing individual particle motion.

To describe the evolution of a particle distribution in a nonadiabatic trap, we have developed a numerical-statistical analysis which we hope combines the economy of a statistical approach with the accuracy of digital computation. Our basic postulate is that

(XIII. INTERACTION OF LASER RADIATION WITH PLASMAS)

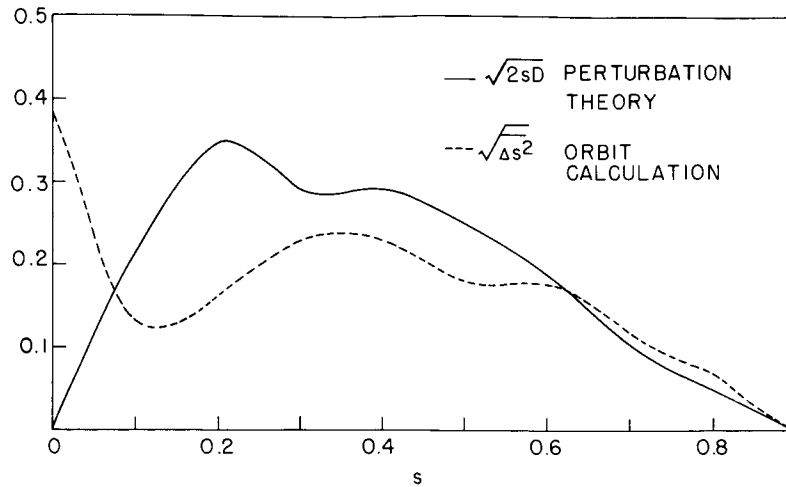


Fig. XIII-14. Mean change in magnetic moment per transit.

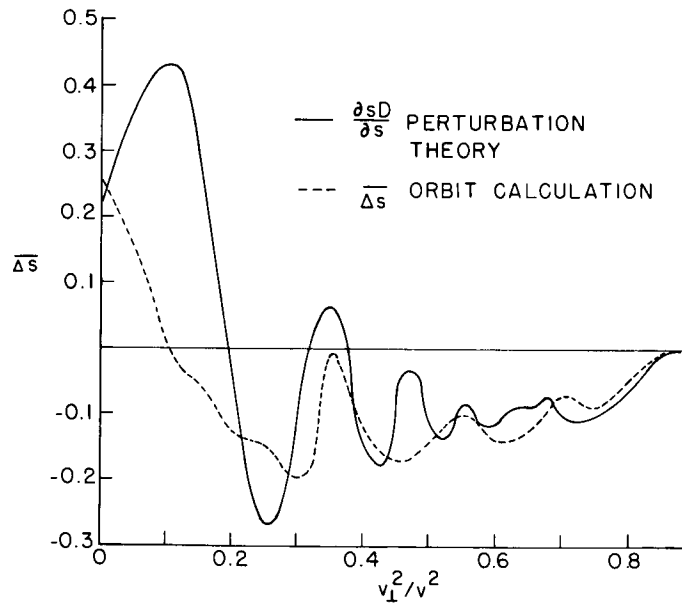


Fig. XIII-15. RMS change in magnetic moment per transit.

our system can be described by a scattering matrix, each term of which gives the probability of a particle's transition from a "state" of magnetic moment s_1 to a "state" s_2 . Each term in this matrix is obtained from numerical orbit calculations and is given by

$$P_{ij} = \frac{\Delta\phi_{ij}}{2\pi},$$

(XIII. INTERACTION OF LASER RADIATION WITH PLASMAS)

where $\Delta\phi_{ij}$ is the range of initial phases for which a particle with a magnetic moment within a small range of s_j will scatter into a small range of s_i in a suitably normalized time interval. The time evolution of the distribution is given by

$$\Delta s_i = S_i + P_{ij} D s_j - s_i,$$

where Δs_i is the change in density of forward-streaming particles in magnetic moment interval i , S_i is the external source of such particles, P_{ij} is the matrix representing scatter from group j to group i , and D_j is the operator describing the mirror losses and variable transit time delays. Thus we are able to compute both the transient and steady-state behavior of the system and, in particular, to compute the particle currents through either mirror. These results will be directly comparable with the experimental measurements described in Section I.

J. F. Clarke, L. M. Lidsky

References

1. R. C. Wingerson, Phys. Rev. Letters 6, 446 (1961).
2. L. M. Lidsky, Phys. Fluids 7, 1484 (1964).
3. R. C. Wingerson and T. H. Dupree, Phys. Fluids 7, 1475 (1964).
4. J. F. Clarke, S.M. Thesis, Department of Physics, M.I.T., 1964.

COMMUNICATION SCIENCES
AND
ENGINEERING

XIV. STATISTICAL COMMUNICATION THEORY*

Academic and Research Staff

Prof. Y. W. Lee
Prof. A. G. Bose

Prof. H. L. Van Trees†

Prof. J. D. Bruce
Prof. A. V. Oppenheim

Graduate Students

M. E. Austin†
A. B. Baggeroer†
R. F. Bauer
L. D. Collins†
D. A. Feldman
T. Huang

R. W. Koralek
J. F. Kososki
D. E. Nelson
L. R. Poulou
R. W. Schafer
J. E. Schindall

D. L. Snyder†
J. C. Stafford
J. J. Wawzonek
C. J. Weinstein
D. H. Wolaver
P. D. Wolfe

A. WORK COMPLETED

1. A CLASS OF NONLINEAR FILTERS

This study has been completed by E. Jeenicke. It was submitted as a thesis in partial fulfillment of the requirements for the Degree of Master of Science, Department of Electrical Engineering, M. I. T., January, 1966.

A. V. Oppenheim

B. AN EFFICIENT TRANSVERSAL EQUALIZER FOR TWO-PATH CHANNELS

The intersymbol interference arising in digital communication over time-variant dispersive channels imposes practical limitations on the data rates that one can attain by using fixed modem structures. Using an adaptive modem – that is, one capable of measuring the channel dispersion and attempting to compensate for it by altering its own structure – it is possible, however, to achieve marked improvement in data rates, as demonstrated by Lucky in his recent work with dispersive telephone lines.¹

In this report we shall consider reduction of the multipath distortion for a discrete two-path channel, in which the signals received via the two paths may vary arbitrarily in amplitude with respect to each other. Such a situation might occur, for example, in communication over the HF ionospheric channel if one is operating sufficiently below the MUF. The discussion here will be limited to modem structures that one might employ for dispersion correction for this channel, under the assumption that its characteristics are known, although in practice an adaptive modem would have to obtain estimates of these characteristics through channel measurement.

*This work was supported by the Joint Services Electronics Programs (U. S. Army, U. S. Navy, and U. S. Air Force) under Contract DA 36-039-AMC-03200(E), the National Aeronautics and Space Administration (Grant NsG-496), and the National Science Foundation (Grant GP-2495).

†This work was supported by the National Aeronautics and Space Administration Grant (NsG-334).

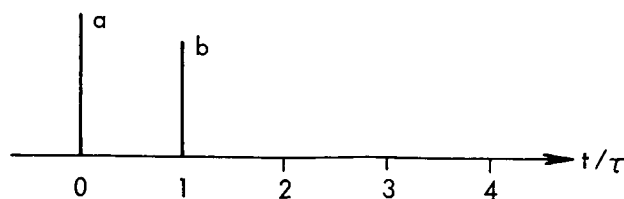


Fig. XIV-1. Impulse response of a two-path channel.

The channel of interest has the impulse response shown in Fig. XIV-1, where the first pulse position has been taken as time reference, and the time axis normalized to the separation, τ , between the pulses. One may represent this output, using z-transform notation, as

$$H(z) = az^0 + bz^{-1}.$$

As discussed by Hulst for the HF ionospheric channel,² one would like to construct the "equalization" or "inverse" filter defined by the z-transform

$$F(z) = \frac{1}{H(z)},$$

for then cascading this filter with the channel would give the desired over-all output z-transform

$$H(z) F(z) = 1$$

and the multipath would have been eliminated.

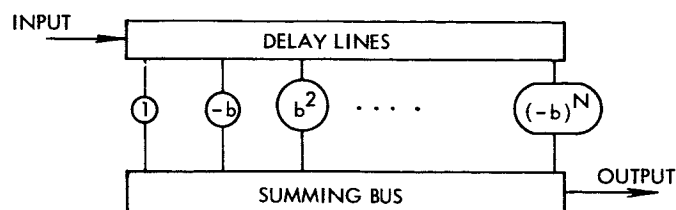
Before proceeding to the general case, we consider first the special case in which the longer path is always weaker than the shorter path — that is, $|b| < |a|$. Since there is no loss in generality in normalizing the input, we shall take $a = 1$, and require that $|b| < 1$. Defining the distortion to be the magnitude of the weaker path strength to that of the stronger path, we have at the input to the equalization filter a distortion

$$D_{\text{input}} = \frac{|b|}{|a|} = |b|.$$

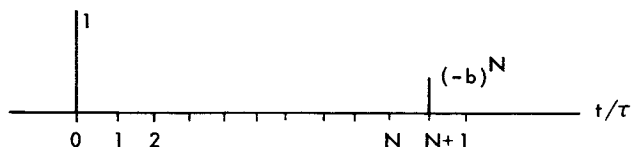
Now the desired equalization filter is described by its z-transform

$$F(z) = \frac{1}{H(z)} = \frac{1}{1 + bz^{-1}} = \sum_{n=0}^{\infty} (-bz^{-1})^n.$$

While the numbers of terms in this series expansion is infinite, in practice one



(a)



(b)

Fig. XIV-2. (a) Conventional transversal equalizer for the channel in Fig. XIV-1, where $a = 1$, $|b| < 1$.

(b) Result of passing channel impulse response through this equalizer.

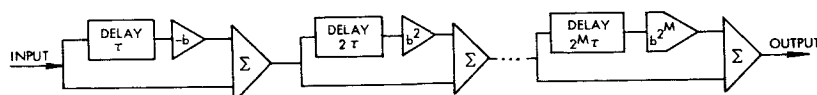
truncates the series after $n = N$, and the result is the well-known transversal equalizer structure shown in Fig. XIV-2a. This equalizer has a z -transform

$$F_N(z) = \frac{1 - (-bz^{-1})^{N+1}}{1 + bz^{-1}},$$

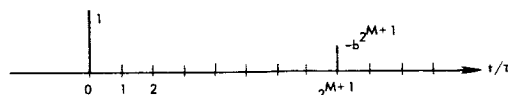
and so cascading it with the channel renders an over-all output having a z -transform

$$H(z) F_N(z) = 1 - (-bz^{-1})^{N+1}$$

which is shown in Fig. XIV-2b. This transform corresponds to an output distortion



(a)



(b)

Fig. XIV-3. (a) Cascade transversal equalizer for the channel of Fig. XIV-1, where $a = 1$, $|b| < 1$.

(b) Result of passing channel impulse response through this equalizer.

(XIV. STATISTICAL COMMUNICATION THEORY)

$$D_{\text{output}} = |b|^{N+1}$$

which has reduced the effective multipath under our assumption $|b| < 1$.

We next derive an alternative equalizer structure for the case considered above, using an alternative expansion of the filter z -transform:

$$F(z) = \frac{1}{H(z)} = \frac{1}{1 + bz^{-1}} = \prod_{m=0}^{\infty} \left[1 + (-bz^{-1})^{2^m} \right].$$

By truncating this product after $m = M$, the resulting filter becomes the cascade of transversal filters shown in Fig. XIV-3a. This transversal equalizer has a z -transform

$$F_M(z) = \frac{1 - b^{2^{M+1}} z^{-2^{M+1}}}{1 + bz^{-1}},$$

and so cascading it with the channel renders an over-all output having a z -transform

$$H(z) F_M(z) = 1 - b^{2^{M+1}} z^{-2^{M+1}}$$

which is shown in Fig. XIV-3b. This transform corresponds to an output distortion

$$D_{\text{output}} = b^{2^{M+1}}$$

which again is less than the input distortion $|b|$, since $|b| < 1$ was assumed.

The performance of the equalizers of Figs. XIV-2a and XIV-3a will be identical if one takes

$$N + 1 = 2^{M+1},$$

for then both filters render an output distortion of $b^{2^{M+1}}$. Note, however, that the number of cascaded transversal filters required with the second approach, $M+1$, will in general be considerably smaller than the number of taps on a single transversal filter, $N+1$. The actual values required, of course, depend upon the maximum input distortion and the desired maximum output distortion. For example, with a maximum input distortion of .9 and a maximum output distortion of .01, $M+1 = 6$, while $N+1 = 44$. Thus while the delay requirements and distortion reductions of the equalizers of Figs. XIV-2a and XIV-3a are equivalent, it is seen that the second equalizer is more efficient in terms of the number of variable-gain amplifiers required. Moreover, it has the additional practical advantage of requiring (except for the first cascade stage) only amplifiers to provide positive gains, while in the conventional approach nearly half of the amplifiers must be capable of providing both positive and negative gains.

(XIV. STATISTICAL COMMUNICATION THEORY)

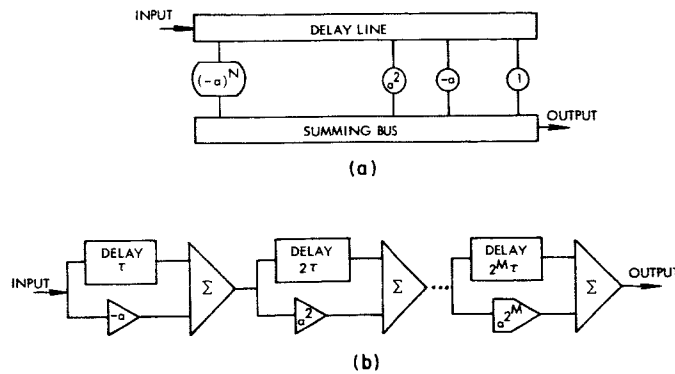


Fig. XIV-4. (a) Conventional transversal equalizer. (b) Cascade transversal equalizer. (Both for the channel of Fig. XIV-1, where $b = 1$, $|a| < 1$.)

Thus far, we have restricted the discussion to channels for which the longer path was always weaker than the shorter. Similarly, if the shorter path were always the weaker, one would normalize the input so that $b = 1$, and proceed as described above with bz^{-1} replaced by az , and so forth, to derive the structures shown in Fig. XIV-4, where the cascade approach is again seen to be more efficient than the conventional

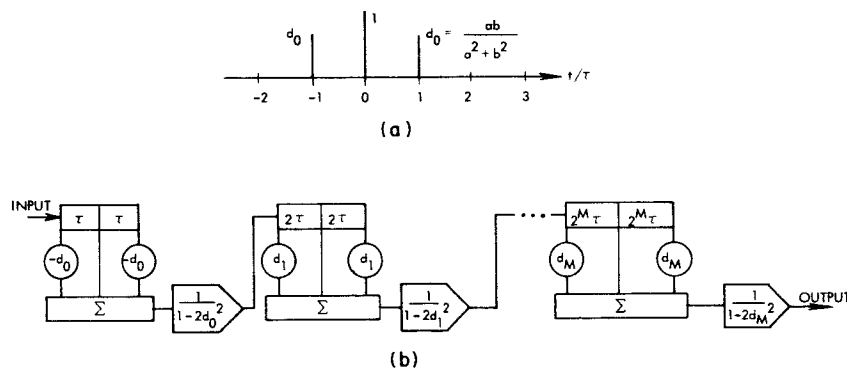


Fig. XIV-5. (a) Normalized matched-filter output for the channel of Fig. XIV-1. (b) Cascade transversal equalizer for this output.

approach. We next consider equalization for the general case, that is, where a and b may vary arbitrarily with respect to each other. By matched filtering to the channel output and again normalizing, one has the matched filter output shown in Fig. XIV-5a, in which now the input distortion is

(XIV. STATISTICAL COMMUNICATION THEORY)

$$D_{\text{input}} = 2 |d_o| = \frac{2 |ab|}{a^2 + b^2},$$

and the input z -transform is the matched filter output

$$H_{\text{MF}}(z) = d_o z + 1 + d_o z^{-1},$$

and now the center pulse has been taken as time reference. The desired equalization filter is

$$F(z) = \frac{1}{H_{\text{MF}}(z)} = \frac{1}{d_o z + 1 + d_o z^{-1}}.$$

One could divide this out, expanding $F(z)$ as the sum of a sufficient number of terms, and realize the inverse filter approximately with a single transversal equalizer. Instead we shall follow the more efficient cascade approach introduced above, by first expanding $F(z)$ in the product

$$F(z) = \prod_{i=0}^{\infty} \left[\frac{d_i (-z)^{2^i} + 1 + d_i (-z)^{-2^i}}{1 - 2d_i^2} \right],$$

where

$$d_i = \frac{d_{i-1}^2}{1 - 2d_{i-1}^2},$$

and the distortion after the i^{th} filter is

$$D_{\text{output}}(i) = 2d_i.$$

The structure for this general case is shown in Fig. XIV-5b. The normalization gains after each stage could be combined into a single gain. It is straightforward to show that

$$|d_i| < |d_{i-1}|$$

whenever

$$|d_{i-1}| < 1/2$$

which is satisfied for every stage whenever $|d_o| < 1/2$. Since d_o can have magnitude $1/2$ only in the event that the path strengths $|a|$ and $|b|$ are identical, an event of probability zero, it is clear that this cascading of filters renders a transversal equalizer which reduces the multipath distortion with probability one. It is also clear that this

(XIV. STATISTICAL COMMUNICATION THEORY)

cascaded transversal equalizer structure enjoys the same efficiency, in terms of implementation requirements, relative to the conventional transversal equalizer as that found for our earlier example.

M. E. Austin

References

1. R. W. Lucky, "Automatic Equalization for Digital Communication," Bell System Tech. J. 44, 547-588 (April 1965).
2. G. D. Hulst, "Inverse Ionosphere," IRE Trans., Vol. CS-8, No. 1, pp. 3-9, March 1960.

XV. PROCESSING AND TRANSMISSION OF INFORMATION*

Academic and Research Staff

Prof. R. M. Gallager
Prof. E. V. Hoversten

Prof. I. M. Jacobs

Prof. R. E. Kahn
Prof. R. S. Kennedy

Graduate Students

D. S. Arnstein
J. D. Bridwell
E. A. Bucher
D. Chase
D. D. Falconer
R. L. Greenspan
D. Haccoun
H. M. Heggstad

J. A. Heller
M. Khanna
J. Max
J. H. Meyn
J. C. Molden
G. Q. McDowell
G. C. O'Leary

R. Pilc
J. T. Pinkston III
E. M. Portner, Jr.
J. S. Richters
J. E. Roberson
M. G. Taylor
D. A. Wright
R. Yusek

A. CODING FOR SOURCE-CHANNEL PAIRS

In many communication problems the source output is not simply one of M equally likely messages and the user is not merely interested in the probability that the received

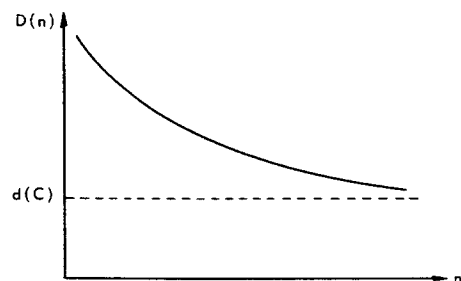


Fig. XV-1. Performance curve for source \mathcal{S} transmitted over channel \mathcal{C} .

information is right or wrong. More generally, a source may have any probability distribution $P(w)$ defined over its possible outputs, and the system performance may be measured by the average value of a distortion function $d(w_i, w_j)$ which gives the distortion to the user when w_i is transmitted but decoded as w_j . The problem of communicating the output of such a source over a given channel with minimum distortion is being studied in this research.

Unlike previous work, which separated the coding operation into two parts, a source representation problem^{1,2} and a channel coding problem, we shall consider the coding operation as one process.

The performance curve is defined for a given source-channel pair as the minimum obtainable distortion, using a direct source to channel encoder which operates on a block of source outputs of length n . A typical curve is shown in Fig. XV-1. If the capacity of the channel \mathcal{C} is C , it is known from Shannon's earlier results¹ that $d(C)$, the value of distortion at the rate C on the rate-distortion curve for the source \mathcal{S} , provides a lower bound to the performance curve. It is also shown by Shannon to be obtainable, therefore it must be the limit of the performance curve as n becomes large.

A stronger lower bound has been derived which, unlike Shannon's, is a function of n

*This work was supported by the National Aeronautics and Space Administration (Grant NsG-334).

PRECEDING PAGE BLANK NOT FILMED

(XV. PROCESSING AND TRANSMISSION OF INFORMATION)

and therefore provides information about the rate of approach of the performance curve to its limiting value as n increases. The derivation is summarized below.

1. Lower Bound to $D(n)$

The first step in the derivation is an application of sphere-packing ideas used many times before in Information Theory. If a source word \underline{w} is transmitted, using a channel input word \underline{x} , and two lists are made – one a list of possible decoded words \underline{w}' ordered in decreasing distortion $d(\underline{w}, \underline{w}')$ from \underline{w} , and the other a list of channel output words \underline{y} ordered in decreasing conditional probability $p(\underline{y}/\underline{x})$ – a lower bound to any obtainable distortion can be found by evaluating the completely ideal, and unrealizable, situation wherein channel output words that have higher conditional probabilities are always in decoding regions that result in lower transmission distortions.

It has been shown by Fano³ that an improvement in this bound can be made if a probability function $f(\underline{y})$, defined over the channel output space Y , is included in the ordering of channel output words and subsequently varied to obtain the tightest possible bound. We shall use this idea and order the channel output words according to increasing values of information difference

$$I(\underline{x}, \underline{y}) = \ln \frac{f(\underline{y})}{p(\underline{y}|\underline{x})},$$

where

$$f(\underline{y}) = \prod_{i=1}^n f(y_i).$$

To obtain a lower bound, it is necessary to relate members on the list of all possible decoded words with members on the list of all possible received words (now ordered in distortion and information difference respectively). This is the "idealized decoder function" and is defined as that function which maps y_j into the $w_i^!$ for which

$$\sum_{\underline{w}' \in W_i^!} g(\underline{w}') \leq \sum_{\underline{y} \in Y_j} f(\underline{y}) < \sum_{\underline{w}' \in W_{i+}^!} g(\underline{w}'), \quad (1)$$

where

$$Y_j = \{\underline{y} : I(\underline{x}, \underline{y}) \leq I(\underline{x}, y_j)\}, \quad (2)$$

$$W_i^! = \{\underline{w}' : d(\underline{w}, \underline{w}') \leq d(\underline{w}, w_i^!)\}, \quad (3)$$

$$W_{i+}^! = W_i^! \cup (\text{the next } \underline{w}' \text{ on the list}), \quad (4)$$

and where $g(w')$ is a probability function, defined over the decoding space W' , that will be determined later. The function value $g(\underline{w}'_1)$ can be interpreted as the total "size", as measured by $f(\underline{y})$, of the subset of Y^n that is decoded into \underline{w}'_1 . That is,

$$g(\underline{w}'_1) = \sum_{\underline{y} \in Y(\underline{w}'_1)} f(\underline{y}),$$

where

$$Y(\underline{w}'_1) = \{\underline{y}: \text{decoded into } \underline{w}'_1\}.$$

The lower bound to the distortion that results when the source word \underline{w} is transmitted using a channel input word \underline{x} can now be shown to be

$$D(\underline{w}) \geq \int d(I) dF_2(I) \quad (5)$$

in which $F_2(I)$ is the cumulative distribution function of the information difference $I(\underline{x}, \underline{y})$ when the probability distribution $p(\underline{y}/\underline{x})$ is in effect, and $d(I)$ is the distortion function implicitly defined by the first inequality of Equation 1 which essentially equates two distribution functions; one $G(d)$ where

$$G(d) = \frac{\Pr(d(\underline{w}, \underline{w}') \leq d)}{g(\underline{w}')}.$$

and the other $F_1(I)$ where

$$F_1(I) = \frac{\Pr(I(\underline{x}, \underline{y}) \leq I)}{f(\underline{y})}.$$

Since $G(d)$ and $F_1(I)$ can only be approximated,⁴ an upper bound to $G(d)$ is equated to a lower bound to $F_1(I)$ to define a function $d_L(I)$ satisfying $d_L(I) \leq d(I)$. This is consistent with the inequality in Equation 5. Finally expanding $d_L(I)$ in a Taylor series about $E(I)$ with respect to the cumulative distribution $F_2(I)$ yields

$$D(\underline{w}) \geq \int d_L(I) dF_2(I) = \sum_{i=0} \frac{d_L^{(i)}(I)}{i!} \int (I - \bar{I}) dF_2(I).$$

After successive derivatives and central moments are evaluated we obtain the result

$$D(\underline{w}) \geq \mu'(s_o) - \frac{1}{2ns_o} \left[\frac{\gamma^n(-1)}{s_o^2 \mu^n(s_o)} - 1 \right] + o\left(\frac{1}{n}\right) \quad (6)$$

(XV. PROCESSING AND TRANSMISSION OF INFORMATION)

where s_0 satisfies

$$\mu(s_0) - s_0 \mu'(s_0) = \gamma'(-1) - \frac{1}{2n} \ln \frac{\gamma''(-1)}{s_0^2 \mu''(s_0)} + o\left(\frac{1}{n}\right), \quad (7)$$

and in which

$$\mu(s) = \sum_i q_i \mu_i(s), \quad \text{comp } (\underline{w}) = \bar{q}, \quad (8)$$

$$\gamma(t) = \sum_i c_i \gamma_i(t), \quad \text{comp } (\underline{x}) = \bar{c}. \quad (9)$$

In Eqs. 8 and 9, $\mu_i(s)$ and $\gamma_i(t)$ are, respectively, the semi-invariant moment-generating functions of the random variables d_i and I_i , which have the distribution functions

$$\Pr_{d_i}(d_{ij}) = g(w_j')$$

and

$$\Pr_{I_i}(I_{ij}) = f(y_j).$$

The transmission distortion for the source can be obtained by averaging $D(\underline{w})$ over the entire source space W^n . If the code is restricted to be a "fixed-composition" code, that is, all channel input words have composition \bar{c} , the averaging can be completed, and it results in the lower bound

$$D \geq \mu'(s_0) - \frac{1}{2ns_0} \left[\frac{\gamma''(-1)}{s_0^2 \mu''(s_0)} - 1 + \frac{\sigma^2(s_0)}{s_0^2 \mu''(s_0)} \right] + o\left(\frac{1}{n}\right) \quad (10)$$

with

$$\sigma^2(s_0) = \text{Variance}_{p(w_i)} [\mu_i(s_0) - s_0 \mu'(s_0)],$$

$$\bar{q} = \bar{p} = (p(w_1), p(w_2), \dots, p(w_J))$$

and with s_0 satisfying Eq. 7.

The lower bound in Eq. 10 is in terms of the vectors \bar{g} , \bar{c} , and \bar{f} which have not yet been specified. The vectors \bar{g} and \bar{c} must be picked to minimize the right side of Eq. 10, abbreviated $D(g, \bar{c}, \bar{f}, s_0)$, in order to choose the optimum set of decoding set sizes and the best channel-input composition. The vector \bar{f} can be freely chosen, but

the tightest lower bound results when $D(\bar{g}, \bar{c}, \bar{f}, s_0)$ is maximized with respect to \bar{f} . Therefore

$$D \geq \min_{\bar{g}} \min_{\bar{c}} \max_{\bar{f}} D(\bar{g}, \bar{c}, \bar{f}, s_0). \quad (11)$$

As n becomes large, the vectors \bar{c} and \bar{f} which provide the bound in Eq. 11 approach the channel input and output probabilities associated with the channel \mathcal{C} when it is used to capacity, and the vector \bar{g} approaches the output probability distribution of the test channel associated with the point $(d(c), c)$ on the rate-distortion curve for δ . For finite, but large n , these vectors could be used in Eqs. 7 and 10 to obtain an approximation to the correct lower bound. The limit, as n increases, of the lower bound is

$$D(n=\infty) \geq \mu'(s_0),$$

where

$$\mu(s_0) - s_0 \mu'(s_0) = -C$$

which is the correct parametric expression for the distortion at the point $(d(c), c)$ on the rate-distortion curve for δ .²

The previous results can be applied, with obvious modifications, to a communication system with vector sources and channels and with amplitude continuous sources and channels. If, in particular, for Gaussian sources and channels the channel-input fixed-composition requirement is replaced by an input energy constraint, the lower bound to distortion is the same as that given in Eq. 10, except the term involving $\sigma^2(s_0)$ is not present. The channel-input composition problem, which is believed to affect only this term, remains one of the problems under present investigation.

At this point it is not known how well the dependence upon n given in the lower bound agrees with that of the actual performance curve. To get this information, an upper bound to the performance curve is also required. Such a bound is now being developed.

R. Pilec

References

1. C. E. Shannon, "Coding Theorems for Discrete Sources with a Fidelity Criterion," *Information and Decision Processes*, 1960.
2. T. J. Goblick, "Coding for a Discrete Information Source with a Distortion Measure," Ph.D. Thesis, Department of Electrical Engineering, M.I.T., October 1962.
3. R. M. Fano, *Transmission of Information* (The M.I.T. Press, Cambridge, Mass, 1961).
4. R. G. Gallager, "Lower Bounds on the Tails of Probability Distribution," Quarterly Progress Report, No. 65, Research Laboratory of Electronics, M.I.T., April 15, 1962.

(XV. PROCESSING AND TRANSMISSION OF INFORMATION)

B. AN UPPER BOUND ON THE DISTRIBUTION OF COMPUTATION FOR
SEQUENTIAL DECODING WITH RATE ABOVE R_{comp}

A previous report¹ has described the simulation of a sequential decoder operating at a rate just above R_{comp} , the computational cutoff rate of a discrete memoryless channel. The tail of the cumulative distribution of the number of computations per search was observed to be Pareto; that is,

$$\text{pr}(C \geq X) = AX^{-\alpha} \quad (X \gg 1), \quad (1)$$

where A is a constant. The measured Pareto exponent, α , was less than one, and satisfied the relation

$$\frac{E_0(\alpha)}{\alpha} = R \quad (2)$$

to a good approximation. In (2), R is the code information rate in nats per channel use, and $E_0(\alpha)$ is a well-known function of α and of the channel input and transition probabilities.² In fact it turns out that $R_{\text{comp}} = E_0(1)$.

We have obtained by random coding arguments an upper bound on $\text{pr}(C \geq X)$ for rates in the range $R_{\text{comp}} \leq R < C$, where C is the channel capacity. Previously Savage³ and Yudkin⁴ have established similar upper bounds for $0 \leq R < R_{\text{comp}}$. Jacobs and Berlekamp⁵ have obtained a lower bound agreeing asymptotically with (1) and (2) for $0 \leq R < C$. Thus the asymptotic behavior of the distribution of computation for any rate less than capacity is now known to be Pareto with exponent given by (2).

1. Outline of the Derivation

In what follows, we will provide a rough outline of the derivation of the bound. A complete description of tree codes and sequential decoding will not be given here. An up-to-date description has been given by Wozencraft and Jacobs.² Suffice it to say that the decoding procedure is a sequential search through a tree in an attempt to find the correct path representing the intended information sequence. Decisions are made by comparing a path metric, which is a function of the received and hypothesized channel symbol sequences, to a running threshold. The path metric along the correct path tends to increase, while incorrect path metrics tend to decrease with increasing penetration into the code tree.

We assume that the decoder employs the Fano algorithm and that the k^{th} path metric increment is

$$Z_k = \ln \frac{p(y_k | x_k)}{f(y_k)} - R.$$

The spacing between adjacent thresholds is Δ .

We are concerned with the total number of computations ever done in the incorrect subset of a reference node on the correct path. The incorrect subset consists of the reference node plus all nodes on incorrect paths stemming from the reference node. One computation is said to be done on a node whenever the decoding algorithm visits that node to examine branches diverging from it or leading to it. This is the usual measure of computation for purposes of establishing upper bounds.³ Other definitions are more convenient for experimental measurements, but the same asymptotic Pareto distribution is always observed.^{1, 7}

Each node in the incorrect subset will be labelled by indices (ℓ, n) , where $\ell = 0, 1, 2, \dots$ is its depth in the tree measured from the reference node, and n denotes which node it is at depth ℓ . $[n = 1, 2, \dots, (u-1)u^{\ell-1}]$.

The expression overbounding the number of computations in the incorrect subset of a reference node depends on three properties of the Fano algorithm which we state here without further elucidation. A fuller exposition is found in Savage,³ and in Wozencraft and Jacobs.⁶

- (1). With a given running threshold in effect, no more than $(u+1)$ computations are done on any node.
- (2). For at least one computation to be done on some node (ℓ, n) when a given running threshold is in effect, a necessary condition is that the path metric along the path connecting node (ℓ, n) to the reference node be everywhere greater than the running threshold.
- (3). The running threshold is not eventually reduced by Δ from its current value unless the path metric at some node along the entire correct path stemming from the reference node is less than the current running threshold.

Properties (1), (2), and (3) may be combined to enable us to write a mathematical expression overbounding C , the total number of computations that must eventually be done on all nodes in the incorrect subset:

$$C \leq (u+1) \sum_{m=-1}^{\infty} \sum_{\ell=0}^{\infty} \sum_{n=1}^{M(\ell)} S \left[\left(\sum_{k=1}^{\ell v} Z_k^i(n) - \min_{0 \leq h < \infty} \sum_{k=1}^{h v} Z_k^o \right) - m\Delta \right], \quad (3)$$

where $M(\ell) = (u-1)u^{\ell-1}$, and $S[\cdot]$ is the unit step function which is one when its argument is zero or positive, and zero otherwise. Z_k^o and $Z_k^i(n)$ are the k^{th} path metric increments on the correct path and on the n^{th} incorrect path, respectively.

The minimum over h in (3) may be removed by the use of a simple union bound:

$$C < (u+1) \sum_{m=-1}^{\infty} \sum_{\ell=0}^{\infty} \sum_{h=0}^{\infty} \sum_{n=1}^{M(\ell)} S \left[\sum_{k=1}^{\ell v} Z_k^i(n) - \sum_{k=1}^{h v} Z_k^o - m\Delta \right]. \quad (4)$$

For the upper bound, following Savage, we use a form of the Chebysheff inequality:

If C is a positive random variable,

$$\text{pr}(C \geq L) \leq \frac{\overline{C^a}}{L^a} \quad \text{for } a > 0. \quad (5)$$

Thus finding a Pareto upper bound on the cumulative distribution of computation is equivalent to showing that moments of C lower than the a^{th} are bounded for a satisfying (2).

The upper bound on $\overline{C^a}$ is established by a random-coding argument. It is assumed that the channel is discrete and memoryless, has an input alphabet of P symbols and an output alphabet of Q symbols and that it is characterized by the set of transition probabilities $\{q_{ij}, i=1, 2, \dots, P; j=1, 2, \dots, Q\}$. The tree characterizing the code is assumed to be infinite, implying a convolution code with infinite constraint length. There are u branches diverging from every node and v symbols of the channel input alphabet for each branch (the code rate, R , is then $\frac{1}{v} \ln u$ nats per channel use). Each symbol is picked statistically independently from a probability distribution $\{p_i, i=1, 2, \dots, P\}$. Thus the joint probability is $p(\mathbf{x}_k^o) p(y_k | \mathbf{x}_k^o) p(\mathbf{x}_k^i(n))$ that during the k^{th} use of the channel a symbol \mathbf{x}_k^o is transmitted, a symbol y_k is received and that the k^{th} symbol on the n^{th} incorrect path up to depth k is $\mathbf{x}_k^i(n)$. Similarly, for the first L uses of the channel, the sequences of symbols may be written as L -component vectors, and the joint probability measure is

$$p(\bar{\mathbf{x}}_L^o) p(\bar{y}_L | \bar{\mathbf{x}}_L^o) p(\bar{\mathbf{x}}_L^i(n)) = \prod_{k=1}^L p(\mathbf{x}_k^o) \prod_{k=1}^L p(y_k | \mathbf{x}_k^o) \prod_{k=1}^L p(\mathbf{x}_k^i(n)), \quad (6)$$

where, for example, $\bar{\mathbf{x}}_L^o$ represents the first L input symbols to the channel. There is also a probability distribution defined on the channel output symbols $f_j = \sum_{i=1}^P p_i q_{ij}$ $j=1, 2, \dots, Q$.

Now since successive uses of the channel are assumed to be statistically independent, we have from the definitions of $Z_k^i(n)$ and Z_k^o and our joint probability measure that

$$\sum_{k=1}^{\ell v} Z_k^i(n) - \sum_{k=1}^{h v} Z_k^o = \ln \left[\frac{p(\bar{y}_{\ell v} | \bar{\mathbf{x}}_{\ell v}^i(n)) f(\bar{y}_{h v})}{f(\bar{y}_{\ell v}) p(\bar{y}_{h v} | \bar{\mathbf{x}}_{h v}^o)} \right] - (\ell - h)R \quad (7)$$

for the n^{th} incorrect path at depth ℓ , ($n=1, 2, \dots, M(\ell)$).

In bounding $\overline{C^a}$ we exploit the Chernoff bounding technique, in which the unit step function $S[t]$ is overbounded by $e^{\frac{t}{1+a}}$ before averaging. The second principal mathematical artifice is the use (on all but the innermost sum on n in (4)) of the following standard inequality⁸:

For a sequence of positive random variables $\{x_i\}$,

$$\overline{\left(\sum_i x_i\right)^a} \leq \sum_i \overline{x_i^a}, \quad \text{provided } 0 \leq a \leq 1. \quad (8)$$

Then after some algebraic manipulations, we obtain

$$\overline{C^a} < A_1 \sum_{\ell=0}^{\infty} e^{-\frac{a\ell v R}{a+1}} \sum_{h=0}^{\infty} e^{-\frac{ahvR}{a+1}} F(h, \ell), \quad (9)$$

where

$$A_1 = \frac{(u+1)^a e^{\frac{\Delta a}{a+1}}}{\left(1 - e^{-\frac{\Delta}{a+1}}\right)^a}$$

which is a constant, and

$$F(h, \ell) = \left[\sum_{n=1}^{M(\ell)} \left(\frac{p(\bar{y}_{\ell v} | \bar{x}'_{\ell v}(n)) f(\bar{y}_{hv})}{p(\bar{y}_{hv} | \bar{x}^o_{hv}) f(\bar{y}_{\ell v})} \right)^{\frac{1}{1+a}} \right]^a.$$

It is straightforward to obtain a simple overbound on $F(h, \ell)$ by using the basic probability measure (6) and the inequality⁸ $\bar{x}^0 < \bar{x}^p$ if $0 < p < 1$ and x is a positive random variable. The bound on $F(h, \ell)$ was originally derived by Yudkin.⁴ Substitution of this bound in (9), leads to an infinite sum which converges if

$$R < \frac{1}{a} E_0(a)$$

where $E_0(a) = -\ln \sum_{j=1}^Q \left(\sum_{i=1}^P p_i q_{ij}^{\frac{1}{1+a}} \right)^{1+a}$. Thus $\overline{C^a}$, for $0 < a < 1$, is bounded if

$$R < \frac{1}{a} E_0(a). \quad (10)$$

Condition (10) agrees with the lower-bound condition found by Jacobs and Berlekamp.⁵ Thus we have obtained the (asymptotically) tightest possible result. Condition (10) is also identical to Savage's upper bound for integer values of a .³ Recently, Yudkin has extended this result to all $a \geq 1$.⁴

2. Remarks

We may now employ (5) to obtain an upper bound on the distribution of computation. Over the ensemble of infinite tree codes, $\text{pr}(C > L) < \overline{C}^{\overline{\rho}} \overline{L}^{\overline{\rho}}$, provided $R < \frac{1}{\overline{\rho}} E_O(\overline{\rho})$ and $\overline{\rho} > 0$. If $R = \frac{E_O(a)}{a}$, the tightest asymptotic result follows from letting $\overline{\rho}$ approach a .

$$\text{Thus for } R = \frac{E_O(a)}{a}, \text{ pr}(C \geq L) < \overline{C}^{a-\epsilon} \overline{L}^{-(a-\epsilon)}, \quad (11)$$

where ϵ is positive but arbitrarily small. Comparison of our result with the lower bound of Jacobs and Berlekamp shows that (neglecting ϵ);

$$\text{pr}(C \geq L) = AL^{-a} \quad (L \gg 1).$$

For any R and a such that $R = \frac{E_O(a)}{a}$, where A is a finite constant, it can be shown that $\frac{E_O(a)}{a}$ approaches C , the channel capacity as a approaches zero.

Figure XV-2 shows the Pareto exponent a , as a function of R for the communication system described in the previous report,¹ consisting of binary antipodal signalling, white

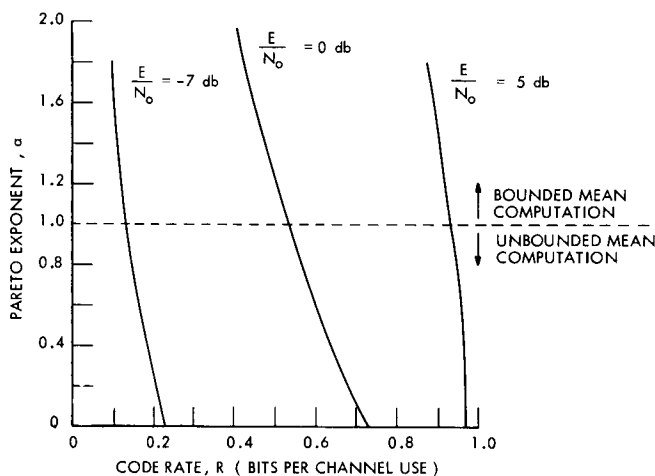


Fig. XV-2. Variation of a with R for a white Gaussian noise channel.

above R_{comp} would still be possible (and perhaps feasible). For example, the average number of computations per digit could be made finite simply by imposing an upper limit on the allowable number of computations per digit or group of digits, and passing on as erasures any group of digits for which this limit is exceeded. In such a scheme, periodic resynchronization or a feedback channel would be necessary to allow the decoder to continue past a group of "erased" digits. If no gaps in the incoming data stream can be

Gaussian noise channel, matched filter and 8-level output quantizer. The only difference is that the outer quantization levels have been changed from $\pm 2T$ to $\pm 1.7T$.⁹ We are indebted to Professor I. Jacobs for providing these curves. Note the high sensitivity of the Pareto exponent to small changes in rate, both above and below R_{comp} .

We observe that if $R_{\text{comp}} < R < C$, then $0 < a < 1$, and the average computation is unbounded; however, an asymptotically Pareto cumulative distribution still exists. For some applications, operation at a rate

tolerated, the erasures may be corrected by an outer level of block encoding and decoding. As a further feature, the upper limit on computation could be variable, being made just large enough to enable the number of erasures in a block of the outer code to be correctable by that code.

Concatenation schemes of this type are being investigated analytically and by simulation.

D. D. Falconer

References

1. D. Falconer and C. Niessen, "Simulation of Sequential Decoding for a Telemetry Channel," Quarterly Progress Report No. 80, Research Laboratory of Electronics, M. I. T., January 15, 1966, pp. 180-193.
2. R. G. Gallager, "A Simple Derivation of the Coding Theorem and Some Applications," IEEE Trans., Vol. IT-11, No. 1, pp. 3-18, January 1965.
3. J. E. Savage, "The Computation Problem with Sequential Decoding," Ph. D. Thesis, Department of Electrical Engineering, M. I. T., February, 1965.
4. H. L. Yudkin (paper submitted for publication).
5. I. M. Jacobs and E. Berlekamp, "A Lower Bound to the Distribution of Computation for Sequential Decoding," JPL SPS 37-34, Vol. 4 (to appear also in IEEE Trans. on Information Theory).
6. J. M. Wozencraft and I. M. Jacobs, Principles of Communication Engineering (John Wiley and Sons, Inc., New York, 1965).
7. G. Blustein and K. L. Jordan, Jr., "An Investigation of the Fano Sequential Decoding Algorithm by Computer Simulation," Group Report 62G-5, Lincoln Laboratory, M. I. T., 1963.
8. G. H. Hardy, J. E. Littlewood, and G. Polya, Inequalities (Cambridge University Press, London, 1959).
9. See Fig. XXII-1, Quarterly Progress Report No. 80, op. cit., p. 184.

XVI. LINGUISTICS

Academic and Research Staff

Prof. R. Jakobson	Prof. J. Kurylowicz	Dr. S-Y. Kuroda
Prof. A. N. Chomsky	Prof. G. H. Matthews	Dr. A. Schwartz
Prof. J. A. Fodor	Prof. Krystyna Pomorska	Dr. D. E. Walker
Prof. J. J. Katz	Dr. S. Bromberger	G. B. Gragg
Prof. R. P. V. Kiparsky	Dr. M. F. Garrett	P. L. Peterson
Prof. E. S. Klima	Dr. J. S. Gruber	J. J. Viertel

Graduate Students

G. D. Bedell IV	J. L. Fidelholtz	R. L. Mendelsohn
T. G. Bever	M. L. Geis	Amy E. Myers
R. J. Carter	R. Goldfield	D. M. Perlmutter
S. W-C. Chan	J. W. Harris	P. S. Peters, Jr.
P. G. Chapin	T. R. Hofmann	C. B. Qualls
R. J. Carter	T. A. Huntington	J. R. Ross
Janet P. Dean	R. S. Jackendoff	M. S. Snow
R. P. G. DeRijk	L. Jenkins	Carol A. Spielman
R. C. Dougherty	R. S. Kayne	R. J. Stanley
J. E. Emonds	J. P. Kimball	Nancy H. Woo

A. PLAYING WITH DISTINCTIVE FEATURES IN THE BABBLING OF INFANTS

In this report I shall describe the data obtained all on one day, consisting of the utterances of an infant, aged 403 days.¹ We shall discuss the utterances in an attempt to discover what if any patterns exist among them. It will be seen that significant patterns do exist when distinctive features are referred to,² and further theoretical implications of these patterns will be touched upon.

The following sequences of more than one syllable were found in the babbling of Mackie at the age of 403 days. This corresponds to an advanced stage of babbling. Approximately six weeks later the babbling has greatly decreased, and the child makes much simpler and much less frequent sequences of sound. It appears that the child at this later stage is speaking language, as opposed to babbling which is intentional, but not meant to be intelligible, sequences of sound. Utterances at this later stage, if and when produced, for the most part correspond to morphemes of English.

The largest number of sequences of more than one syllable consisted of any number of syllables beginning with a nonGrave segment, followed by any number of syllables beginning with a Grave segment. Here, a syllable is defined rather loosely, because

*This work was supported principally by the U.S. Air Force Electronics Systems Division) under Contract AF 19(628)-2487; and in part by the Joint Services Electronics Programs (U.S. Army, U.S. Navy, and U.S. Air Force) under Contract DA 36-039-AMC-03200(E), the National Science Foundation (Grant GP-2495), the National Institutes of Health (Grant MH-04737-05), and the National Aeronautics and Space Administration (Grant NsG-496).

(XVI. LINGUISTICS)

of possible great complexity in the initial nonVocalic segment, and because of the difficulty in ascertaining the presence of a vowel between nonVocalic segments at times. In general, however, a syllable is a sequence consisting of a nonVocalic segment followed by a Vocalic segment, possibly augmented by one or more glides. When a particular segment is colored, either at the onset or the offset, by the features of some other type of segment, the symbol indicating the coloring segment is raised from the line.

Such sequences of nonGrave syllables followed by Grave ones are exhaustively listed below:

1.		nonGrave	Grave						
	ye	dew	tæ	gə	w ^V ə				
		dey	dæ	gə	w ^V ə				
			dæ	gi	v ^W əy				
			yi	p					
			ye	mp					
			ye	ge	v ^W i				
	yeh	yo	wey						
		də	we	gi	we	gi	we	gi	
		yə	gə	m:					
	ye	ye	gi	v ^W ih					
		də	we	gi	gi	wi	wi	ge	
	de	yə	wa						
		nə	m ^V						
	də ^r	tə	m	v ^g ə ^r					

Next we see that there were sequences consisting only of nonGrave syllables, which are listed below:

2.		nonGrave		
	yə ^l	do	dəh	
		do:	yo:	
	ə ^r	dey	day	ti
	də	do		

In addition there are sequences of syllables beginning with only Grave segments:

3.

Grave

	ge	v ^w iy
	ge	v ^w i
	ge	v
m	ngi	v ^w eh
m	ngo	
	bə	w ^v ə
m	ba	wə
way	be	b
way	w:	
mə	mə	wə

No sequences of syllables beginning with a Grave segment followed by a sequence of syllables beginning with a nonGrave segment occur. (There are two exceptional cases: e wi na and go we də. These two cases are exceptional in that they have the segments /n/ and /d/, the voiced fricative, both of which occur very seldom in sequence. After our analysis we shall be able to handle these two cases.)

Consequently we see that we have the generality up to this point that every babbling sequence consists in any number of nonGrave syllables followed by any number of Grave syllables, including zero as a possible number of syllables. We also get sequences of all sorts consisting of only one syllable, which will also follow from the generalization above.

We have also on this day, sequences consisting of syllables beginning with /h/, followed by any number of syllables beginning with a nonGrave segment, as below:

4.

/h/ nonGrave

hə	yə
hə	yə
he ^w hə	yo
he	dyo dyəy
he	y ^a a ^w

There is a couple of sequences consisting of an /h/ followed by a nonGrave syllable, followed by a Grave syllable:

5.

/h/ nonGrave Grave

ha	ye	gə
hə	y:	w:

(XVI. LINGUISTICS)

Although there were no sequences consisting of /h/ followed by a Grave syllable, we shall have evidence to include that as a possibility later. Consequently we can elaborate our generalization to say that a babbling sequence consists of any number of /h/-initial syllables, followed by any number of nonGrave-initial syllables, followed by any number of Grave-initial syllables. In other words, we have a set of sequences corresponding to a finite-state language, expressed by the formula:

$$f-1. \quad [h]^* [\text{nonGrave}]^* [\text{Grave}]^*$$

There were only four sequences in the data which appeared to be real exceptions to f-1. These are

6. Exceptions

wə	heh
næ	hæ
da:	ho:
ga	he f ^{lw} o

Apparent exceptions only, however, are the very long sequences:

7. Apparent Exceptions

hey	də	b ^v ə	də	b ^v ə		
hə		b ^w i	de	wi	de	wə
h	wi	b ^w e	də	bi	de	bi we
ha	yə	go	ha	yə	wə	
	yə	v ^w ə	yə	v ^w ə	yə	
	de	wa	də	gə	ge	

It seems that these sequences may be treated as repetitions of the formula f-1. In favor of this is the length of these sequences and some very apparent iterative characteristics about them.

If we allow f-1., to be repeated, however, and since single syllables do occur, we in fact allow anything at all to occur. What will save this from being vacuous would be some evidence, such as intonation or pause, which would necessitate the postulation of a sequence boundary. This will be investigated. Even without this, however, we could predict that the utterances that follow the rule given above are far more numerous than those that do not.

Note in the repetitions of 7., we have two instances of an /h/ followed by a Grave sequence, so that we are corroborated in including this possibility in the generalization above.

If rule f-1. represents a reality of the infants babbling, it is reasonable to ask what in fact the infant is doing on a more explanatory level. What we can say is that the initial segments of syllables increase in markedness from beginning to end in the sequence. A segment unmarked (u) for some feature is said to take the simplest or least effort value for that feature; a segment marked (m) for some feature takes the more complex value for that feature. Which is the marked and which is the unmarked value of a given feature is a question of universal grammar.

It has been postulated that /h/ represents a segment marked only for the feature Vocalic, being unmarked in all others. /y/ is marked for Sonorant and /d/ is marked for Consonantal, both being marked for Vocalic. Hence /y/ and /d/ have two marks, Vocalic and Consonantal or Sonorant. In a parallel fashion, /w/, /g/, and /b/ have three marks, differing from the others in being marked for the feature Grave. Thus /h/ is less marked than /y/ or /d/; and /y/ or /d/ is less marked than any of /w/, /g/, or /b/.³

The universal rules for interpreting markedness (m's and u's) in terms of feature values (+s and -s) for the features indicated here are:

r-1	[m Vocalic]	→	[- Vocalic]
	[u Vocalic]	→	[+ Vocalic]
	[m Sonorant]	→	[+ Sonorant]
	[u Sonorant]	→	[- Sonorant]
	[m Consonantal]	→	[+ Consonantal]
	[u Consonantal]	→	[- Consonantal]
	[m Grave]	→	[+ Grave]
	[u Grave]	→	[- Grave]

In particular, we have the following:

r-2	<u>1 Mark</u>		
	$\begin{bmatrix} \text{m Vocalic} \\ \text{u Sonorant} \\ \text{u Consonantal} \end{bmatrix}$	→	$\begin{bmatrix} \text{-Vocalic} \\ \text{-Sonorant} \\ \text{-Consonantal} \end{bmatrix} = /h/$
	<u>2 Marks</u>		
	$\begin{bmatrix} \text{m Vocalic} \\ \text{m Sonorant} \\ \text{u Consonantal} \\ \text{u Grave} \end{bmatrix}$	→	$\begin{bmatrix} \text{-Vocalic} \\ \text{+Sonorant} \\ \text{-Consonantal} \\ \text{-Grave} \end{bmatrix} = /y/$
	$\begin{bmatrix} \text{m Vocalic} \\ \text{u Sonorant} \\ \text{m Consonantal} \\ \text{u Grave} \end{bmatrix}$	→	$\begin{bmatrix} \text{-Vocalic} \\ \text{-Sonorant} \\ \text{+Consonantal} \\ \text{-Grave} \end{bmatrix} = /d/$

3 Marks

$$\begin{array}{l}
 \left[\begin{array}{l} m \text{ Vocalic} \\ m \text{ Sonorant} \\ u \text{ Consonantal} \\ m \text{ Grave} \end{array} \right] \rightarrow \left[\begin{array}{l} -\text{Vocalic} \\ +\text{Sonorant} \\ -\text{Consonantal} \\ +\text{Grave} \end{array} \right] = /w/ \\
 \\
 \left[\begin{array}{l} m \text{ Vocalic} \\ u \text{ Sonorant} \\ m \text{ Consonantal} \\ m \text{ Grave} \end{array} \right] \rightarrow \left[\begin{array}{l} -\text{Vocalic} \\ -\text{Sonorant} \\ +\text{Consonantal} \\ -\text{Grave} \end{array} \right] = /g, b/
 \end{array}$$

Intuitively, then, what this seems to mean is that the child begins an utterance with a certain degree of markedness, which he may increase in subsequent syllables of the sequence. The child may be thought of as playing a game, which consists of adding more commands to the syllable, producing more complex initial segments, for syllables toward the end of the sequence.

Several of the exceptions, such as e wi na and go we dæ, can now be seen not to be exceptions at all, since nasality, when it appears, must be marked, as must continuency. Thus markedness still increases from left to right.

J. S. Gruber

References

1. Material for this study comes from the longitudinal investigations headed by Margaret Bullowa, M.D., entitled "Development from Vocal to Verbal Behavior in Children," NIH Grant MH 04300-01-04.
2. These are the distinctive features postulated in R. Jakobson, M. Halle, and C. G. M. Fant, "Preliminaries to Speech Analysis," Technical Report No. 13, Acoustics Laboratory, M. I. T., 1952.
3. I am indebted to Richard Carter for having pointed this out to me. The revitalization and reinterpretation of the Prague School notion of markedness is due to Morris Halle.

B. SYLLABLE FINALS IN CHINESE PHONOLOGY¹

The crucial fact to be captured concerning the Chinese monosyllable is the unity of its structure and function. The Chinese tradition will be followed here in assuming the underlying form of the monosyllable to consist of two 'segments', an initial and a final. For the purposes of this discussion, the feature analysis of initials given by Hashimoto¹ will be adopted, unless otherwise stated. We shall return briefly to the initials after a consideration in detail of the content of the finals.

The final will contain features specifying the tone of the monosyllable. Gruber³ has suggested a set of features to handle such phenomena, and his formulation will be assumed here. The final will also contain the feature + or - compact, which will result in two classes of finals, with e (a mid central vowel) and with a (a low central vowel).

The final will contain the features + or - flat and + or - sharp, and the grammar will contain a phonological rule of the following sort:

$$a. \begin{bmatrix} \alpha \text{ compact} \\ \beta \text{ flat} \\ \gamma \text{ sharp} \end{bmatrix}_1 \rightarrow \begin{bmatrix} \beta \text{ flat} \\ \gamma \text{ sharp} \end{bmatrix}_1 \left[\quad \right]_1 / \text{---} +^4$$

Rule a. then creates a new 'segment' between the initial and the final which agrees in flatness and sharpness with the final. An additional rule will be needed, since only three such medials actually appear:

$$b. \begin{bmatrix} -\text{flat} \\ -\text{sharp} \end{bmatrix} \rightarrow \phi$$

The final may also contain the features + or - grave and + or - nasal, and analogously the phonology will contain:

$$c. \begin{bmatrix} \alpha \text{ compact} \\ \beta \text{ grave} \\ \gamma \text{ nasal} \end{bmatrix}_1 \rightarrow \left[\quad \right]_1 \begin{bmatrix} \beta \text{ grave} \\ \gamma \text{ nasal} \end{bmatrix}_1 / \text{---} +$$

Rule c., like Rule a., results in the creation of a new 'segment', this time following the final, agreeing in gravity and nasality. Rules a. b. and c. will produce a set of finals as in Table XVI-1.

Table XVI-1 contains 40 distinct finals; since there exist but 33 in fact,⁵ some further rules will be required. They fall into the morpheme structure category, and must apply before Rules a. b. and c.

Table XVI-1. Set of finals produced by rules a, b, and c.

e	a	ei	ai	eu	au	en	an	eng	ang
ie	ia	iei	<u>iai</u> ₂	ieu	iau	ien	ian	ieng	iang
ue	ua	uei	uai	ueu	<u>uau</u> ₂	uen	uan	ueng	uang
üe	üa	<u>üei</u> ₁	<u>üai</u>	<u>üeu</u>	<u>üau</u> ₁	üen	üan	üeng	<u>üang</u> ₃

where

i-	is	$\begin{bmatrix} -\text{flat} \\ +\text{sharp} \end{bmatrix}$	-i	is	$\begin{bmatrix} -\text{grave} \\ -\text{nasal} \end{bmatrix}$
u-	is	$\begin{bmatrix} +\text{flat} \\ -\text{sharp} \end{bmatrix}$	-u	is	$\begin{bmatrix} +\text{grave} \\ -\text{nasal} \end{bmatrix}$
ü-	is	$\begin{bmatrix} +\text{flat} \\ +\text{sharp} \end{bmatrix}$	-n	is	$\begin{bmatrix} -\text{grave} \\ +\text{nasal} \end{bmatrix}$
			-y	is	$\begin{bmatrix} +\text{grave} \\ +\text{nasal} \end{bmatrix}$

(XVI. LINGUISTICS)

- d. $\begin{bmatrix} -\text{nasal} \\ +\text{flat} \end{bmatrix} \rightarrow [-\text{sharp}]$
- e. $\begin{bmatrix} -\text{nasal} \\ \alpha \text{ flat} \\ -\alpha \text{ sharp} \\ \beta \text{ compact} \end{bmatrix} \rightarrow [\beta \text{ grave}]$
- f. $\begin{bmatrix} +\text{grave} \\ +\text{nasal} \\ +\text{sharp} \\ +\text{compact} \end{bmatrix} \rightarrow [-\text{flat}]$

Rule d. will exclude box 1 in Table XVI-1; Rule e., boxes 2; and Rule f., box 3.

Additional rules will be needed to approximate more closely the phonetic reality of various finals. The following are suggested.

- g. $\begin{bmatrix} \alpha \text{ flat} \\ \beta \text{ sharp} \end{bmatrix} \rightarrow [+vocalic] / \text{---} [-\text{compact}] \begin{cases} [+nasal] \\ [\alpha \text{ grave}] \end{cases}$
- g'. $\begin{bmatrix} +\text{flat} \\ +\text{sharp} \end{bmatrix} \rightarrow [+vocalic] / \text{---} [\text{compact}]$
- h. $[+\text{compact}] \rightarrow [-\text{compact}] / \begin{cases} [+sharp] \\ [+flat \\ +sharp] \end{cases} \begin{bmatrix} +nasal \\ -grave \end{bmatrix}$
- i. $\begin{bmatrix} -\text{compact} \\ -\text{vocalic} \end{bmatrix} \rightarrow \phi$

Rules g. and g'. affect the assignment of the feature vocalic, which operates through a simple marking convention: 1) the segment specified for compactness is + vocalic if there are no other segments so marked in the syllable; 2) all segments not + vocalic are - vocalic. This could of course be stated in the form of rules (which would come between g'. and h.) but the conventional interpretation seems quite natural here. Table XVI-2 shows the results of Rules g. through i.

Table XVI-2. Finals produced by rules g, h, and i.

e	a	ei	ai	eu	au	en	an	eng	ang
ie	ia	i		ieu	iau	in	ien	ing	iang
ue	ua	uei	uai	u		un	uan	ung	uang
<u>ü</u>	üe					ün	üen	üng	

Though more rules will be required to fill in and adjust the exact qualities of the various segments, in particular the non-compact vowels,⁶ familiar ground has been achieved. The rules will, among other things, replace the features on the main vowels 'left over' from rules a. and c. These features do not embarrass any of the later rules written above, but care will clearly be needed in their adjustment.

The general implications of the proposed analysis will now be evident. The part most in need of justification is the 'segment-creating' Rules a. and c. Of course there is nothing unprecedented in the elements that compose these rules: segment creation is an unavoidable aspect of any epenthetic phenomenon, and assimilation of epenthetic elements is familiar enough. So it would perhaps be difficult to exclude Rules a. and c. on any principled basis from present assumptions on the nature of phonology.

On the other hand, it is clear that unusual effects are obtained by the application of Rules a. and c. which ought to require a real evaluational gain to justify. Rule d., for example, plainly owes its simplicity to a. and c. Rule e. is a less clear case: if one accepts Table XVI-1 as an underlying stage, it too shows a simpler statement than could be arranged over three segments; but the value of Table XVI-1 as a real stage might be undermined in the absence of a. or c. Rule f. would presumably be equally costly in any case, and one might choose to consider the nonoccurrence of box 2 in Table XVI-1 merely an accidental gap in the Chinese lexicon.

Rules d. e. and f. provide only minimal justification, however. A more significant test will be a good solution to the complex restrictions which apply between initials and finals, a question not gone into in detail here. In particular, it has been promisingly suggested by T. R. Hoffman that the medial feature sharp is predictable under a proper analysis of the initials, and can therefore be eliminated from the final.

Under the assumption that Rules a. and c. are legitimate, there remain some difficulties in the analysis which must be pointed out. The primary one is the handling of those finals in which Rule c. does not apply (the two leftmost columns of Tables XVI-1 and XVI-2). The solution adopted has the effect of making the nonspecification of certain features distinctive. This has been judged preferable to the introduction of an ad hoc feature. The fact remains that the treatment of 5 distinct elements with binary features is troublesome. This may affect the analysis further in the apparent inability to incorporate Rule g'. into Rule g., where by all rights it should be. Rule g'. applies significantly to a single final, that boxed in Table XVI-2, which is one of the cases in question. It is not, however, clear that any ad hoc feature to allow a better statement of Rule c.

G. D. Bedell IV

Footnotes and References

1. This paper is a preliminary and abbreviated version of one chapter of a longer paper, tentatively entitled "An Essay on Chinese Phonology." The other chapters discuss the Chinese phonological tradition, 'phonemic' analyses, and some typological implications of the problem.
These remarks have profited from the criticisms of G. H. Matthews, T. R. Hoffman, B. K. T'sou, and other participants in the Chinese seminar at Massachusetts Institute of Technology in 1964-1965 and 1965-1966.
2. M. J. Hashimoto, Phonological Rules in Mandarin - Synopsis, 1964, p. 5.
3. J. S. Gruber, The Distinctive Features of Tone (Cambridge, 1964).
4. The symbol + in rules is used to denote a syllable boundary. It is quite likely redundant, and will not need to appear in the underlying representation.
5. Left out of account is the final r as clearly outside the system discussed.
6. The final -y is considered an instance of -i.

C. TRANSITIVE SOFTENING IN RUSSIAN

The fundamental role in Russian morphology of a truncation rule (Rule C' below) which elides vowels before vowels was discovered by Jakobson.¹ Halle then showed² that the occurrence of so-called transitive softening in the conjugation in cases such as (1-4) below is determined by a simple rule (Rule A below) on the basis of the sequence of vowels in the underlying representation of verb forms. He proposed that (A) and (C'), in that order, applied in a transformational cycle to verb forms, for which he assumed the following constituent structure:

((ROOT + VERB SUFFIX + TENSE) + DESINENCE)

A further result was obtained by Lightner.³ He demonstrated that forms such as (5-8) are also regular because a rule of glide formation (B), which replaces prevocalic short u, i with their corresponding glides w, j, intervenes between (A) and (C'). In Lightner's formulation, the three cyclical rules are essentially as follows:

(A) $V \rightarrow j \quad / \quad ______ + V$

(B) $i, u \rightarrow [-\text{vocalic}] \quad / \quad ______ V$

(C)) $V \rightarrow \phi \quad / \quad ______ + V$

Derivations:

		(1) <u>pi<u>se</u>t</u> ((pis+o+e)+t)	(2) <u>pi<u>s</u>u</u> ((pis+o+e)+U)	(3) <u>si<u>d</u>it</u> ((sid+e+i)+t)	(4) <u>si<u>z</u>u</u> ((sid+e+i)+U)
I	A	(pis+j+e)	(pis+j+e)	(")	(")
	B	(")	(")	(")	(")
	C'	(")	(")	(sid +i)	(sid +i)
II	A	(pis +j+e+t)	(pis+j+e +U)	(sid +i +t)	(sid +j +U)
	B	(")	(")	(")	(")
	C'	(")	(pis+j +U)	(")	(")
		(5) <u>ku<u>j</u>ot</u> ((kou+o+e)+t)	(6) <u>ku<u>u</u></u> ((kou+o+e)+U)	(7) <u>lo<u>v</u>it</u> ((lou+i+i)+t)	(8) <u>lo<u>v</u>lju</u> ((lou+i+i)+U)
I	A	(kou+j+e)	(kou+j+e)	(")	(")
	B	(")	(")	(low+i+i)	(low+i+i)
	C'	(")	(")	(low +i)	(low +i)
II	A	(kou+j+e +t)	(kou+j+e +U)	(low +i +t)	(low +j +U)
	B	(")	(")	(")	(")
	C'	(")	(kou+j +U)	(")	(")

Now note first that rule (C') can be generalized by allowing vowels to elide before all nonconsonantal segments, that is, before glides as well as vowels, provided that the elided vowel is flanked by morpheme boundaries:

$$(C) \quad V \longrightarrow \phi \quad / \quad + \text{---} + [-\text{consonantal}]$$

It will be seen that all verb forms dealt with by Halle and Lightner can still be derived as above if (C) is substituted for (C').

More important, however, is the fact that this simpler version (C) of the truncation rule, unlike (C'), does not require the constituent structure for the verb forms which has been described here. Indeed, with this change rules (A-C) no longer critically depend on the correctness of any particular syntactic analysis at all. This is because the correct phonetic forms are obtained if rules (A-C) apply postcyclically to a string whose internal constituent structure has been erased. Thus, consider examples (1-8) anew. Derivative nouns like lovlja are derived in the same way: e.g., $\text{lou+i+o} \longrightarrow (\text{B}) \text{low+j+o}$.

The proposed generalization of the truncation rule, if correct, strengthens the case for Halle's rule for transitive softening by making its validity immune to the outcome of still unsolved problems concerning the correct assignment

(XVI. LINGUISTICS)

	(1) <u>pi</u> set pis+o+e+t	(2) <u>pi</u> su pis+o+e+U	(3) <u>si</u> dit sid+e+i+t	(4) <u>si</u> zu sid+e+i+U
A	pis+j+e+t	pis+j+e+U	"	sid+e+j+U
B	"	"	"	"
C	"	pis+j +U	sid +i+t	sid +j+U
	(5) <u>ku</u> jot kou+o+e+t	(6) <u>ku</u> ju kou+o+e+U	(7) <u>lo</u> vit lou+i+i+t	(8) <u>lo</u> vlju lou+i+i+U
A	kou+j+e+t	kou+j+e+U	"	lou+i+j+U
B	"	"	low+i+i+t	low+i+j+U
C	"	kou+j +U	low +i+t	low +j+U

of derived constituent structure in morphology.

R. P. V. Kiparsky

References

1. R. Jakobson, "Russian Conjugation," Word 4, 155-67 (1948).
2. M. Halle, "Note on Cyclically Ordered Rules in the Russian Conjugation," Quarterly Progress Report No. 63, Research Laboratory of Electronics, M.I.T., October 15, 1961, p. 149; "O pravilakh russkogo sprjazhenija," American Contributions to the Fifth International Congress of Slavists, I (1963).
3. T. M. Lightner, "O tsiklicheskih pravilakh v russkom sprjazhenii," Voprosy Jazykoznanija 2, 45-54 (1965); "Segmental Phonology of Modern Standard Russian," Ph. D. Thesis, Department of Modern Languages and Linguistics, M.I.T., 1965.

XVII. COGNITIVE INFORMATION PROCESSING*

Academic and Research Staff

Prof. S. J. Mason	Prof. B. Prasada	Dr. P. A. Kolers
Prof. W. L. Black	Prof. O. J. Tretiak	Dr. N. Sezaki
Prof. M. Eden	Prof. D. E. Troxel	K. R. Ingham
Prof. T. S. Huang	Prof. D. Cohen	G. L. Wickelgren
	Dr. M. P. Beddoes	

Graduate Students

A. K. Bhushan	P. H. Hartmann	J. A. Newell
J. D. Bigham, Jr.	M. Kawanami	L. C. Ng
D. Caldwell	E. E. Landsman	D. H. Pruslin
A. L. Citron	M. B. Lazarus	C. L. Seitz
R. W. Cornew	F. F. Lee	S. D. Shoap
A. Gabrielian	J-H. Liu	A. Spiridon
B. P. Golden		J. A. Williams

A. COGNITIVE PROCESSES

1. CONFUSION ERRORS FOR SPATIALLY TRANSFORMED LETTERS

We have shown before that various geometric transformations of connected discourse impose different burdens on the reader who is trying to decode the text.¹ One way of accounting for these differences is in terms of the difficulty of recognizing individual letters that have been transformed, and so it becomes of interest to learn whether the order of difficulty of various transformations of individual letters is the same as the order of difficulty for decoding connected text.

The first 800 letters of a page of connected discourse used previously were transformed by a computer into eight different random arrangements. Each arrangement was then prepared in one of eight possible geometrical transformations.¹ Ten students at M.I.T. named all of the characters on a page in a counterbalanced order for the various transformations. The transformations may be described with respect to the plane of the paper as rotation in the plane, top-to-bottom inversion, and mirror reflection. Furthermore, one half of the sample was named from left to right, the other half from right to left. Direction of scanning may be represented as D (left to right) or -D (right to left); the orientation of a character as X (normally faced) or -X (facing to the left); and whether it is upright or upside down as Y and -Y, respectively. The average time (in minutes) that the 10 subjects required to name the characters is shown in Table XVII-1.

*This work was supported in part by the Joint Services Electronics Programs (U.S. Army, U.S. Navy, and U.S. Air Force) under Contract DA 36-039-AMC-03200(E), and in part by the National Science Foundation (Grant GP-2495), the National Institutes of Health (Grant MH-04737-05), and the National Aeronautics and Space Administration (Grant NsG-496).

(XVII. COGNITIVE INFORMATION PROCESSING)

Table XVII-1. Time taken to name characters in different geometric configurations.

(Minutes)							
D, X, Y	-D, X, Y	D, -X, -Y	-D, -X, -Y	D, -X, Y	-D, -X, Y	D, X, -Y	-D, X, -Y
4.65	5.66	7.16	6.72	7.06	7.20	7.96	8.55

In comparing these results with those obtained from subjects reading continuous text,¹ we see that the order of difficulty of the transformations is not maintained, although there are similarities in the two orders. Furthermore, it is clear that characters otherwise identical except for the direction in which they are scanned require different amounts of time to be named correctly; the same is true for characters varying only in X, only in Y or in combinations. Thus, character naming is clearly not the same task as reading, and variations in the x, y coordinate values of characters affect human detectors differentially. One might also conclude that these results indicate that humans do not detect characters by tracing their contours, since identical contours yield different results (Table XVII-1).

P. A. Kolars, Kathryn F. Rosenthal

References

1. P. A. Kolars, M. Eden, and Ann Boyer, "Reading as a Perceptual Skill," Quarterly Progress Report No. 74, Research Laboratory of Electronics, M.I.T., July 15, 1964, pp. 214-217.

B. PICTURE PROCESSING

1. REDUCTION OF THE OUTPUT NOISE POWER ON A VERY NOISY PCM CHANNEL

When PCM is transmitted over a white Gaussian noise channel it is generally assumed that the signal-to-noise ratio per pulse is at least 10 db. Bedrosian¹ has shown that with the same energy per pulse group it is possible to reduce the output noise power approximately 8 db by using weighted PCM. He indicates an approximate formula for the pulse energies which, however, does not give good results when the signal-to-noise ratio per pulse falls below 10 db.

For such small signal-to-noise ratios a graphical solution can be obtained which will be derived here. We make the following assumptions: (i) the quantization steps are uniform and equal to unity, and (ii) the probability distribution of the input levels is flat.

Under these assumptions, the output noise power N_e is

$$N_e = \sum_{i=1}^n p_i \cdot 4^{i-1},$$

where

$$p_i = \int_{\sqrt{\frac{2E_i}{N_o}}}^{\infty} \frac{1}{\sqrt{2\pi}} \cdot e^{-a^2/2} \cdot da = Q\left(\sqrt{\frac{2E_i}{N_o}}\right),$$

n is the number of pulses per code group, and $2E_i/N_o$ is the signal-to-noise ratio for the i^{th} pulse.²

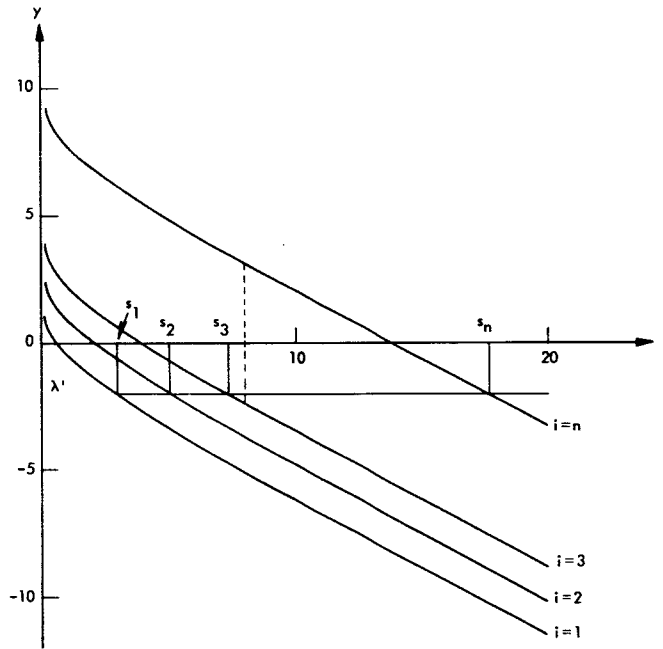


Fig. XVII-1. Family of curves $y = -\frac{1}{2} S - \frac{1}{2} \ln S + (i-1) \cdot \ln 4$.

We want to minimize N_e under the constraint

$$\sum_{i=1}^n \frac{2E_i}{N_o} = n \cdot \frac{2 \cdot \bar{E}}{N_o} = n \cdot S$$

Defining the quantities

$$S_i \triangleq \frac{2E_i}{N_o}, \quad S \triangleq \frac{2\bar{E}}{N_o}$$

S_{db}	N_e not w.	N_e weigh.	$\frac{N_e \text{ weigh.}}{N_e \text{ not w.}} \text{ db}$
7.3	13.65	2.2	-7.9
8.2	6.83	1.0	-8.3
9.8	1.37	0.19	-8.6

Fig. XVII-2. Comparison between unweighted and weighted PCM systems.

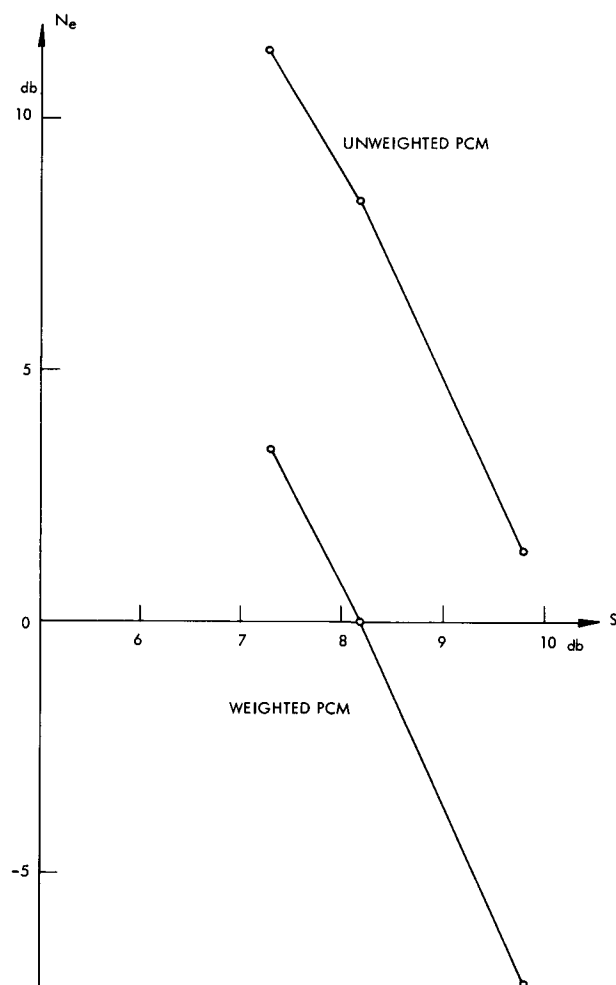


Fig. XVII-3. Comparison between unweighted and weighted PCM systems.

UNWEIGHTED

WEIGHTED



(a) $S = 9.8$ db



(b) $S = 8.2$ db



(c) $S = 7.3$ db

Fig. XVII-4. Effect of using weighted PCM on the test picture.

(XVII. COGNITIVE INFORMATION PROCESSING)

and introducing the Lagrange multiplier λ , we arrive at the following function which is to be minimized:

$$\phi(S_1, \dots, S_n, \lambda) = \sum_{i=1}^n \left[\int_{\sqrt{S_i}}^{\infty} \frac{1}{\sqrt{2\pi}} \cdot e^{-a^2/2} \cdot da \right] \cdot 4^{i-1} + \lambda \cdot \sum_{i=1}^n S_i.$$

Setting the partial derivatives equal to zero, we have

$$\frac{\partial \phi}{\partial S_i} = -\frac{1}{\sqrt{2\pi}} \cdot e^{-S_i/2} \cdot \frac{1}{2\sqrt{S_i}} \cdot 4^{i-1} + \lambda = 0.$$

Simplifying and taking the logarithm on both sides, we get

$$-\frac{1}{2} \cdot S_i - \frac{1}{2} \cdot \ln S_i + (i-1) \cdot \ln 4 = \lambda' \quad i=1, \dots, n$$

Here, $\lambda' = \ln(2\sqrt{2\pi}\lambda)$.

The equations

$$y = -\frac{1}{2} \cdot S - \frac{1}{2} \cdot \ln S + (i-1) \cdot \ln 4 \quad i=1, \dots, n$$

represent a family of congruent curves separated from each other by a vertical distance of $\ln 4$. (cf. Fig. XVII-1). Now the problem is to find a parallel to the S axis which intersects the n curves in such a way that the abscissas S_i of the intersections add up to $n \cdot S$. Once the curves are plotted this is not very difficult. From the S_i the corresponding error probabilities p_i can be determined by using a table or a plot.³

By using this method, results were obtained for a 6-bit PCM system (Fig. XVII-2). The last column represents the reduction of the error noise power in decibels. Figure XVII-3 shows the same results in graphical form.

These results were obtained in the context of an investigation of how the quality of television pictures could be improved when they are transmitted over a very noisy PCM channel. Both the unweighted and the weighted PCM system were simulated on the IBM 7094 computer, and the improvement of the picture quality is remarkable (cf. Fig. XVII-4).

We shall investigate the problem of whether a different weighting function will yield still better pictures. It is seen that the graphical method discussed here can be extended to any weighting function: the curves preserve their shape, but the vertical distance between them will be changed according to the weighting function.

H. P. Hartmann

References

1. E. Bedrosian, "Weighted PCM," IRE Trans., Vol. IT-4, pp. 45-50, March 1958.

2. J. M. Wozencraft and I. M. Jacobs, Principles of Communication Engineering (John Wiley and Sons, Inc., New York, 1965), p. 250.
3. For example, ibid., p. 252.

2. CONSIDERATIONS ON THE GENERATION AND PROCESSING OF HOLOGRAMS BY DIGITAL COMPUTERS

a. Introduction

Holography and other coherent optical processing schemes¹ have aroused considerable interest among those working in the field of television bandwidth compression and image processing. These new techniques have made possible relatively simple ways of obtaining the Fourier transforms of two-dimensional functions and operating on them in the frequency domain.

Holography provides an alternative description of pictures, which might be more amenable to bandwidth compression. To investigate this possibility, it is desirable to measure various statistics of the hologram, and to try various operations on it to see what their effects would be on the reconstructed pictures.

The types of processing that one can do by using coherent optics are rather limited. If one can get the hologram into a digital computer, however, or generate the hologram in the computer in the first place, then the number of possible operations one can do on the hologram is almost unlimited. The reconstruction of the picture from the processed hologram can be done either on the computer or by coherent optics (after having first obtained a transparency of the hologram from the computer).

The advantages in using a digital computer for the generation and processing of holograms are the following.

(i) The computer is flexible. It can be used to do various linear and nonlinear operations such as amplitude generalization which are either not easily done or impossible to do by coherent optics.

(ii) The problem of dirt and fingerprints on lenses is a very real one in an optical processing system. These produce rather prominent spurious patterns on the hologram which are irrelevant for the reproduction of the picture, and will distort the statistics of the hologram. This problem is completely eliminated by using computers.

(iii) The imperfection of lenses and the nonlinearities of films introduce limitations in an optical system. They can be avoided by using computers.

In this report we discuss the problems involved in the generation and processing of holograms on digital computers and, in particular, the limitations of such an approach.

b. Generation of Holograms

Theory of Fourier Transform Holograms

There are various types of holograms. We plan, as a first step, to consider the Fourier-transform holograms of two-dimensional images. Let the amplitude transmission of the original two-dimensional image (on a transparency) be $f(x, y)$, where x and y are the spatial coordinates, and let $F(u, v)$ be the Fourier transform of $f(x, y)$, where u and v are the spatial (angular) frequencies. Then the amplitude transmission of the hologram transparency (except for some scale factors) is

$$\begin{aligned} H(u, v) &= |F(u, v) + A e^{jau}|^2 \\ &= |F(u, v)|^2 + A^2 + AF(u, v) e^{-jau} + AF^*(u, v) e^{jau} \\ &= |F(u, v)|^2 + A^2 + 2A |F(u, v)| \cos (au - \phi(u, v)), \end{aligned} \quad (1)$$

where $\phi(u, v)$ is the phase angle of $F(u, v)$, and A and a are real constants, and $*$ denotes complex conjugation.

In reconstruction, the inverse Fourier transform of $H(u, v)$ is obtained:

$$\begin{aligned} h(x, y) &= R_f(x, y) + A^2 \delta(x, y) \\ &\quad + Af(x-a, y) \\ &\quad + Af(-x-a, -y), \end{aligned} \quad (2)$$

where $R_f(x, y)$ is the autocorrelation function of $f(x, y)$, and $\delta(x, y)$ is the unit impulse function. Let the size of $f(x, y)$ be $L \times L$ (that is, assume $f(x, y) = 0$, for $-\frac{L}{2} \leq x \leq \frac{L}{2}$ and $-\frac{L}{2} \leq y \leq \frac{L}{2}$). Then the size of $R_f(x, y)$ is $2L \times 2L$. Therefore, if we choose

$$a \geq \frac{3}{2} L, \quad (3)$$

the desired reconstruction (the third term of Eq. 3) will be shifted far enough away from $R_f(x, y)$ so that there is no overlap between the two (Fig. XVII-5).

In practice, we have to truncate $H(u, v)$ in reconstruction, and thereby introduce overlap between the first and third terms of Eq. 2. Assume that, instead of $H(u, v)$, a truncated hologram $\hat{H}(u, v) = H(u, v) Q(u, v)$ is used, where

$$Q(u, v) = \begin{cases} 1, & \text{for } -\frac{W}{2} \leq u \leq \frac{W}{2} \text{ and } -\frac{W}{2} \leq v \leq \frac{W}{2} \\ 0, & \text{elsewhere} \end{cases} \quad (4)$$

Then the reconstruction is

$$\begin{aligned}
\hat{h}(x, y) &= h(x, y) \otimes q(x, y) \\
&= R_f(x, y) \otimes q(x, y) + A^2 q(x, y) \\
&\quad + Af(x-a, y) \otimes q(x, y) + Af(-x-a, y) \otimes q(x, y),
\end{aligned} \tag{5}$$

where \otimes denotes convolution, and $q(x, y)$ is the inverse Fourier transform of $Q(u, v)$.

$$q(x, y) = \frac{W^2}{\pi} \left(\frac{\sin Wu}{Wu} \right) \left(\frac{\sin Wv}{Wv} \right). \tag{6}$$

In addition to introducing overlap between the terms of Eq. 5, the truncation also distorts the desired third term. To make the distortion negligible, we want

$$W \gg \frac{2\pi}{L}. \tag{7}$$

To ensure that the desired third term is not obscured by the first term, we can either use a large value for a to reduce the amount of overlapping or a large value for A to make

$$Af(x-a, y) \gg R_f(x, y) \tag{8}$$

in the overlapping region.

The hologram of Eq. 1 can be made by using coherent optics. It can also be made by using a digital computer: A picture $f(x, y)$ is first recorded on magnetic tape by the CIPG digital scanner.² This tape is read into the computer which generates the function $H(u, v)$ and writes it on an output tape. The CIPG digital scanner plays back this output tape and

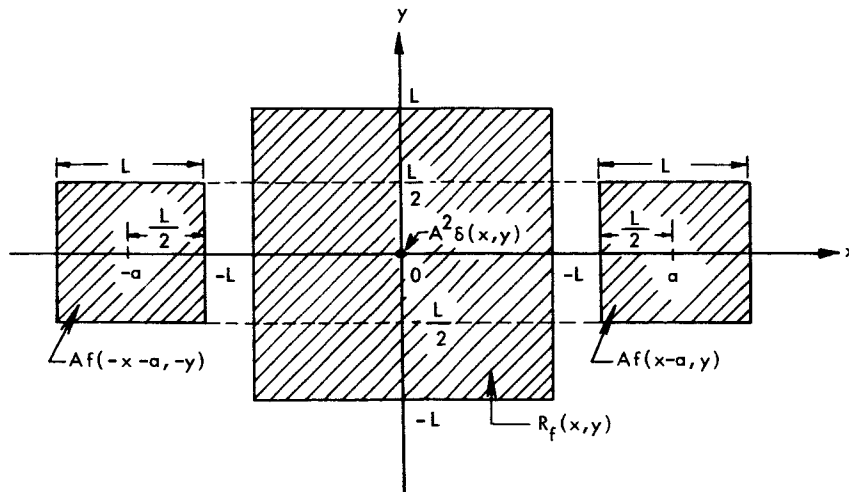


Fig. XVII-5. Reconstruction from hologram. The functions are nonzero only in their respective shaded regions.

displays the hologram on a cathode-ray tube, from which a photograph (transparency) can be taken. The reconstruction can again be done either by using coherent optics or the computer.

Resolution Requirements

To generate a hologram on the digital computer, the original image must be sampled. Assume that the original image can be adequately represented by $N \times N$ (complex) samples. From Fig. XVII-5, it is clear that if we choose $a = \frac{3}{2} L$, then the hologram can be adequately represented by $4N \times N$ samples. Notice that no matter how big a value we use for a , the number of samples required in the vertical direction of the hologram is always N .

Two-Dimensional Fourier Transform

To generate a hologram according to Eq. 1, one has first to calculate the two-dimensional Fourier transform $F(u, v)$ of $f(x, y)$. To do this on a digital computer using a straightforward method requires an amount of time proportional to M^2 , where $M = N \times N$ is the number of samples in the input. For large M , this time could be considerable. Recently, however, Cooley and Tukey³ have developed an efficient algorithm for calculating Fourier transforms which only requires an amount of time proportional to $M \log_2 M$. For large M , the saving in time is great.

Different "Biasing" Schemes

The hologram of Eq. 1 is a way of representing the complex Fourier transform of some function in a positive real form so that it can be realized on a photographic transparency. The term of interest in Eq. 1 is

$$K(u, v) = 2A |F(u, v)| \cos (au - \phi(u, v)) \quad (9)$$

which is real but can be negative. The other two terms $|F(u, v)|^2 + A^2$ can be thought of as a bias which is added to $K(u, v)$ to make the total sum always positive. This particular biasing scheme happens to be easily realizable by using coherent optics.

If a digital computer is used to generate the hologram, then other biasing schemes are feasible. For example, one can use $2A |F(u, v)|$ as a bias to get

$$H_1(u, v) = 2A |F(u, v)| + 2A |F(u, v)| \cos (au - \phi(u, v)) \quad (10)$$

with inverse Fourier transform

$$h_1(x, y) = 2Ag(x, y) + Af(x-a, y) + Af(-x-a, -y), \quad (11)$$

where $g(x, y)$ is the inverse Fourier transform of $|F(u, v)|$.

If $g(x, y)$ is essentially zero outside $-\frac{J}{2} \leq x \leq \frac{J}{2}$ and $-\frac{J}{2} \leq y \leq \frac{J}{2}$, then to avoid overlapping of the terms in Eq. 11, we have to choose

$$a \geq J \quad (12)$$

instead of the inequality (3). Notice that the dynamic range required of the film which records the hologram is the same for $H(u, v)$ and $H_1(u, v)$.

Windows

As we have mentioned, in practice the hologram has to be truncated in reconstruction. A square "window" $Q(u, v)$ was used to truncate $H(u, v)$, which resulted in a reconstructed desired image $f(x, y) \otimes q(x, y)$. Since $q(x, y)$ has large positive and negative side lobes, ringing will occur at the edges in the picture $f(x, y)$. To avoid ringing, we can use a different window $Q_1(u, v)$ whose inverse transform $q_1(x, y)$ has small side lobes. One such window is the so-called "hanning" window⁴:

$$Q_1(u, v) = \begin{cases} \frac{1}{4} \left(1 + \cos \frac{2\pi u}{W}\right) \left(1 + \cos \frac{2\pi v}{W}\right), & \text{for } |u| \leq \frac{W}{2} \\ & \text{and } |v| \leq \frac{W}{2} \\ 0, & \text{elsewhere} \end{cases} \quad (13)$$

For this window, the side lobes of $q_1(x, y)$ are smaller than 1 per cent of $q_1(0, 0)$.

Hologram of Complex Pictures

To make a hologram using coherent optics, one starts with a picture $f(x, y)$ which is real and positive (at least one does not care about its phase). On a digital computer, one can easily compose a complex picture

$$f(x, y) = f_1(x, y) + j f_2(x, y), \quad (14)$$

where f_1 and f_2 are two positive-real pictures, and then generate a hologram of $f(x, y)$. The reconstruction of f_1 and f_2 from such a hologram is clearly feasible by using the computer, although optical reconstruction seems difficult.

Our discussions are valid whether $f(x, y)$ is complex or real. In particular, if each of f_1 and f_2 consists of $N \times N$ samples, and if we use $a = \frac{3}{2}L$, then the hologram of f requires $4N \times N$ samples.

Limitations of the Digital Computer Approach

There are three limitations: (a) the speed of the computer; (b) the memory capacity of the computer; and (c) the resolution of the digital scanner raster.

The CIPG digital scanner has a resolution of approximately 512×512 points.

Therefore, it is capable of displaying the hologram of a picture with 128×128 samples. The state of the art is such that a 3000×3000 point digital scanner seems feasible. Using such a scanner, one can display holograms of 750×750 sample pictures, which are better than broadcasting television pictures in resolution.

To calculate the Fourier transform of a 64×64 point picture, using the Cooley-Tukey algorithm, takes approximately 0.1 minute³ on the IBM 7094 computer, which has a cycle time of 2 μ sec. To do this for a picture with resolution comparable to that of broadcasting television pictures (500×500 points), would take approximately 10 minutes, which is long but still tolerable.

Each point of the Fourier transform depends on all the input samples. Therefore, it is almost mandatory to store the entire input picture in the computer memory. The size of the computer memory, then, limits the size of the input pictures that one can handle. For the IBM 7094 computer, which has a memory of 2^{15} words, one can handle input pictures of up to 64×64 points.

None of the limitations mentioned here are fundamental. They will be removed with the progress of computer technology.

c. Discussion

The hologram can be considered as an alternative description of the picture and hence most of the picture-processing schemes that have been proposed for the picture can be tried on the hologram. Also with the use of computer, the requirement that the description be positive and real so that it can be recorded on film is no longer valid. Therefore, instead of the hologram, one can study the two-dimensional Fourier transform itself.

Specifically, sampling and quantization are two operations that are inherent in any processing on the digital computer. It will be interesting to observe the subjective effects of coarse quantization of the hologram and the Fourier transform.

We can study the amplitude probability distributions, as well as the adjacent sample difference distributions of the hologram and the Fourier transform. These will indicate whether the hologram is more amenable to some of the statistical encoding schemes than the picture itself.

It will be interesting to study the effect on the reconstructed picture of additive Gaussian noise, as well as digital noise added to the hologram or the Fourier transform. Another problem is to study the effect of slope-limiting coding schemes such as delta modulation.

Our future plan is to carry out some of the computer processing suggested in this report and to consider the generation and processing of holograms of three-dimensional objects and of holograms other than the Fourier-transform type.

T. S. Huang, B. Prasada

(XVII. COGNITIVE INFORMATION PROCESSING)

References

1. E. N. Leith and J. Upatnieks, "Wavefront Reconstruction with Continuous-tone Objects," J. Opt. Soc. Am. 63, 1377-1381 (April 1963).
2. T. S. Huang and O. J. Tretiak, "Research in Picture Processing," Chapter 3 in Optical and Electro-Optical Information Processing (The M.I.T. Press, Cambridge, Mass., 1965), pp. 45-49.
3. J. W. Cooley and J. W. Tukey, "An Algorithm for the Machine Calculation of Complex Fourier Series," Mathematics of Computation 19, 297 (April 1965).
4. D. Blackman and J. Tukey, The Measurement of Power Spectra (Dover Publications, New York, 1958).

XVIII. COMMUNICATIONS BIOPHYSICS*

Academic and Research Staff

Prof. D. B. Geselowitz†	Prof. H. Yilmaz††	Dr. N. Y. S. Kiang‡
Prof. P. R. Gray	Dr. J. S. Barlow‡‡	Dr. R. R. Pfeiffer‡
Prof. H. B. Lee	Dr. A. W. B. Cunningham	Dr. R. Rojas-Corona
Prof. W. T. Peake‡	Dr. G. F. Dormont***	Dr. G. F. Songster
Prof. W. A. Rosenblith	N. I. Durlach	R. M. Brown‡
Prof. W. M. Siebert	Dr. H. Fischler†††	A. H. Crist‡
Prof. R. Suzuki**	Dr. P. Gogan‡‡‡	F. N. Jordan
Prof. T. F. Weiss‡	Dr. R. D. Hall	D. P. Langbein‡

Graduate Students

J. A. Anderson	A. J. M. Houtsma	M. Nahvi
G. von Bismarck	L. K. Krakauer	P. H. O'Lague
L. D. Braida	R. G. Mark	D. J.-M. Poussart
S. K. Burns	E. G. Merrill	M. B. Sachs
H. S. Colburn	P. J. Metz III	M. M. Scholl
J. A. Freeman	D. C. Milne	J. J. Singer
J. J. Guinan, Jr.	E. C. Moxon	I. H. Thomae
D. K. Hartline		M. L. Wiederhold

A. WAVEFORMS RECORDED EXTRACELLULARLY FROM NEURONS IN THE ANTEROVENTRAL COCHLEAR NUCLEUS OF THE CAT

In continuing studies of properties of single units in the cochlear nucleus, emphasis has been placed on the "oral pole" of the anteroventral cochlear nucleus. The anatomy of this region suggests that it may be the simplest to study from the standpoint of trying

*This work is supported by the National Institutes of Health (Grants MH-04737-05 and NB-05462-02), the Joint Services Electronics Programs (U.S. Army, U.S. Navy, and U.S. Air Force) under Contract DA 36-039-AMC-03200(E), the National Science Foundation (Grant GP-2495), and the National Aeronautics and Space Administration (Grant NsG-496).

†Visiting Associate Professor from the Moore School, University of Pennsylvania, NIH Fellow.

‡Also at Eaton-Peabody Laboratory, Massachusetts Eye and Ear Infirmary, Boston, Massachusetts.

**Visiting Assistant Professor from the Research Institute of Dental Materials, Tokyo Medical and Dental University, Tokyo, Japan.

††Visiting Professor from Arthur D. Little, Inc., Cambridge, Massachusetts.

‡‡Research Affiliate in Communication Sciences from the Neurophysiological Laboratory of the Neurology Service of the Massachusetts General Hospital, Boston, Massachusetts.

***Visiting Scientist from Centre d'Études de Physiologie Nerveuse, Paris, France.

†††From the Department of Electronics, Weizmann Institute of Science, Rehovoth, Israel.

‡‡‡Visiting Scientist from Université de Paris, Laboratoire de Neurophysiologie Comparée, Paris, France (IBRO Traveling Fellow).

PRECEDING PAGE BLANK NOT FILMED.

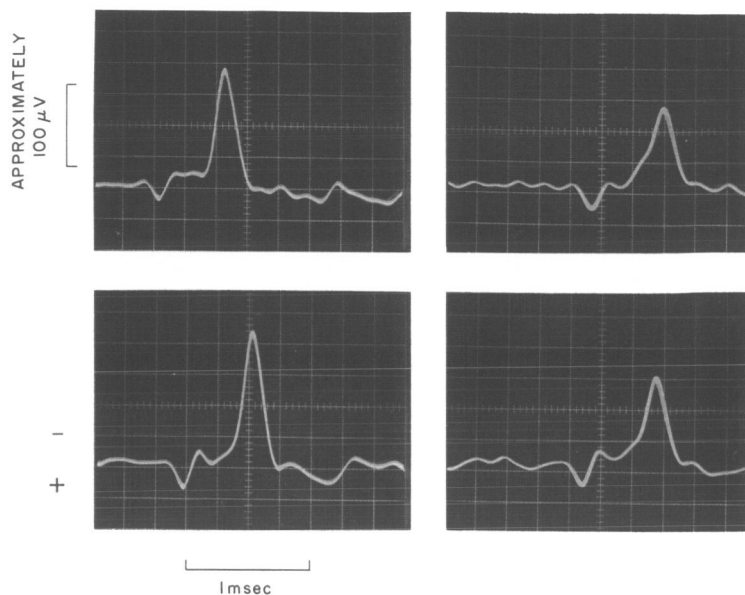


Fig. XVIII-1. Typical waveforms from neurons in the "oral pole" of the anteroventral cochlear nucleus. Although it is not shown here, relative amplitudes of the positive and negative components varies from unit to unit, presumably because of the electrode position relative to the cell body. Occasionally the positive component is quite small; however, it has not been difficult to detect its presence.

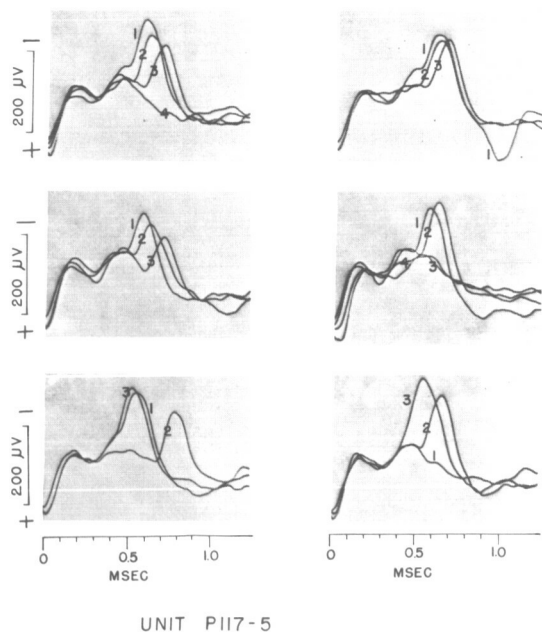


Fig. XVIII-2.

Superposed traces of series of 3 or 4 spikes. The numbers on each trace, in each set, indicate their temporal order. The times between spikes are not given (cf. Fig. XVIII-6). Each trace is synchronized to the positive component. The negative wave is composed of two components, the second of which occasionally fails to develop. Generally, as the time between spikes decreases, the delay of the second negative component as well as its probability of failure increases (cf. Fig. XVIII-6). These waveforms are in response to stimulation by continuous tone. The waveforms for spontaneous discharges are similar, but the probabilities of failure of the second negative component are much less. The failure of the second spike does not occur for all units; this failure may be a result of pressure applied to the cell body on account of the electrode's presence.

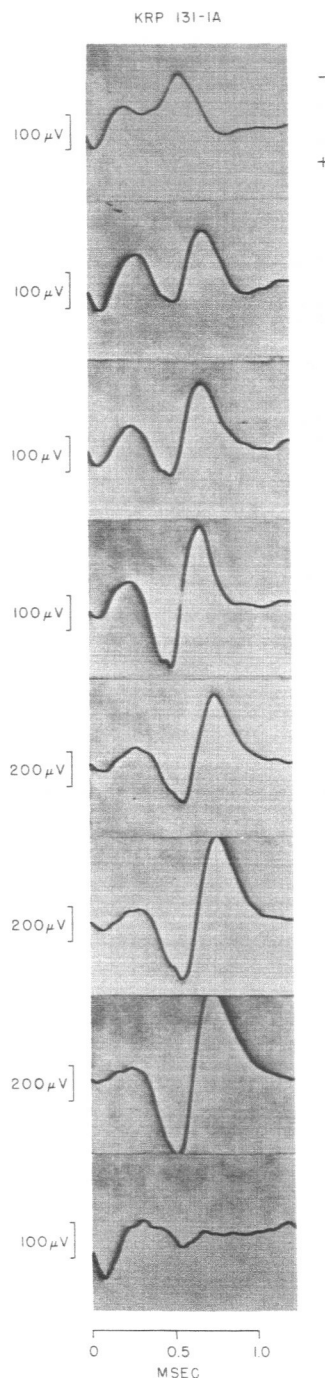


Fig. XVIII-3.

"Injury" sequences of spike discharge as the electrode is advanced (top to bottom). Each trace is synchronized to the positive component. Only the negative wave undergoes "injury." The positive wave is still present after the negative wave can no longer be developed.

to determine the functions of individual neurons. Two main features are: the relative homogeneity of this region with respect to anatomical description of the cells located there; and the fact that each of these cells receives single terminations from only a few – perhaps one to four – auditory nerve fibers.¹

This report is limited to a brief description and interpretation of the extracellular wave shape recorded from neurons in this region. These single-neuron recordings were obtained by using metal-filled microelectrodes. We have found, however, that the wave shapes considered here can also be recorded extracellularly by using large fluid-filled (Ringer's solution) microelectrodes.

Figure XVIII-1 shows four spike potentials recorded from this region. The salient feature of these potentials – and that which makes them unique for cells in the cochlear nucleus – is the positive component preceding the more commonly encountered, extracellularly recorded negative component. That this waveform is actually composed of three separate components can be concluded from the data shown in Figs. XVIII-2 through XVIII-4. While the majority of recordings exhibit waveforms as shown in Fig. XVIII-1, often conditions are such that the negative wave separates into two components (Fig. XVIII-2). Also, when neurons in this region are subjected to injury, by advancement of an electrode, only the negative component is affected; the positive component is not (Fig. XVIII-3). Finally, in rare cases,

(XVIII. COMMUNICATIONS BIOPHYSICS)

when these neurons discharge with pairs of spikes, the second spike does not have a positive component (Fig. XVIII-4).

We shall call the positive, the first negative, and the second negative components the P, A, and B components, respectively. Thus, we see P, A, B (Figs. XVIII-1 and

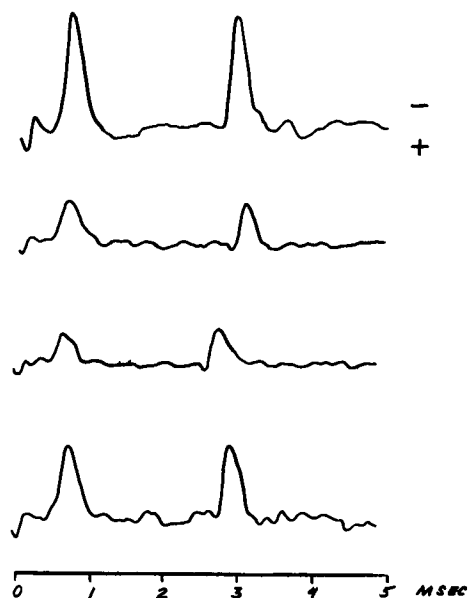


Fig. XVIII-4.

Tracings of waveforms of paired discharges. These pairs are infrequently encountered and relate, perhaps, to a pathology that will be handled elsewhere. Nevertheless, each of the second discharges in the pair does not have a positive component.

XVIII-2); P, A (Fig. XVIII-2); P (Fig. XVIII-3); and A, B (Fig. XVIII-4) combinations of components. Whether or not an A or a B component can occur in isolation has not yet been determined from our data.

Our present interpretation of the various components may be outlined as follows:

a. The P component is interpreted as a presynaptic event, detectable by the electrodes because of the large size of the synaptic endings; furthermore, the P components signify individual incoming spikes of all of the auditory-nerve fibers terminating on the neuron under study.

This interpretation is based, in part, on the following factors.

- (i) The fact that the P component is not affected when the neuron undergoes "injury."
- (ii) The delay (0.4-0.6 msec) between the P and the A component, which is reasonable for a synaptic delay between incoming spike and initiation of cell discharge.
- (iii) The similarity between these positive potentials and those observed extracellularly from large synaptic endings in other preparations.^{2,3,4a}
- (iv) The consistency with the interpretation that the A and B components are postsynaptic – one that can be arrived at independently of this interpretation of the P spike.

(v) The fact that we have also recorded this type of waveform in the nucleus of the

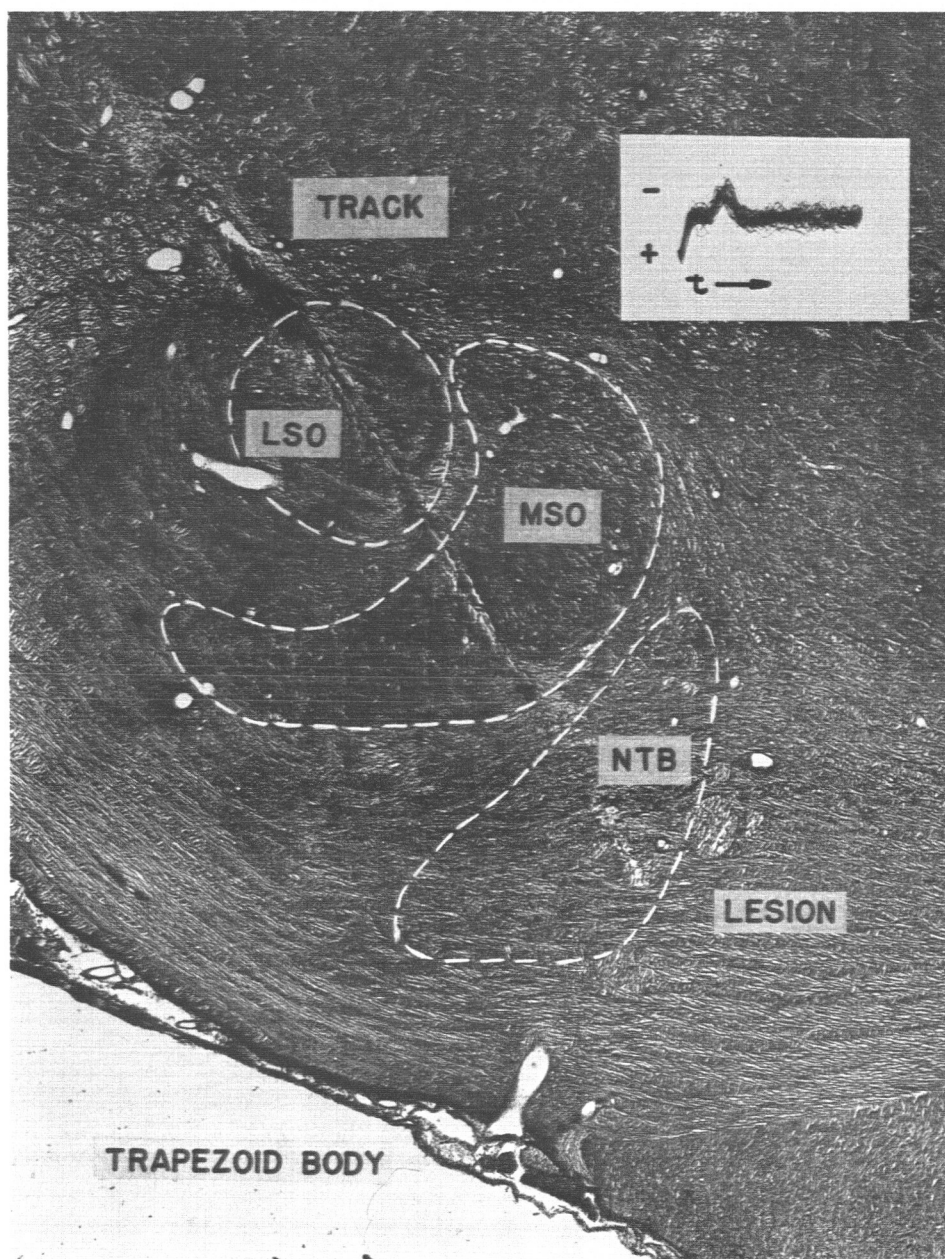


Fig. XVIII-5. Micrograph of electrode track leading to the nucleus of the trapezoid body. The neurons in this region have endings similar to those of neurons in the AVCN. Insert is a photograph of multiple tracings of waveforms recorded from the cell whose location was at the site of the lesion. The P component is obvious. LSO, lateral superior olivary nucleus; MSO, medial superior olivary nucleus; NTB, nucleus of the trapezoid body. Transverse section of left superior olivary complex.

trapezoid body in which there are neurons with similar large synaptic endings (Fig. XVIII-5).

b. The A and B components are interpreted as being postsynaptic events.

This interpretation is based, in part, on the following observations.

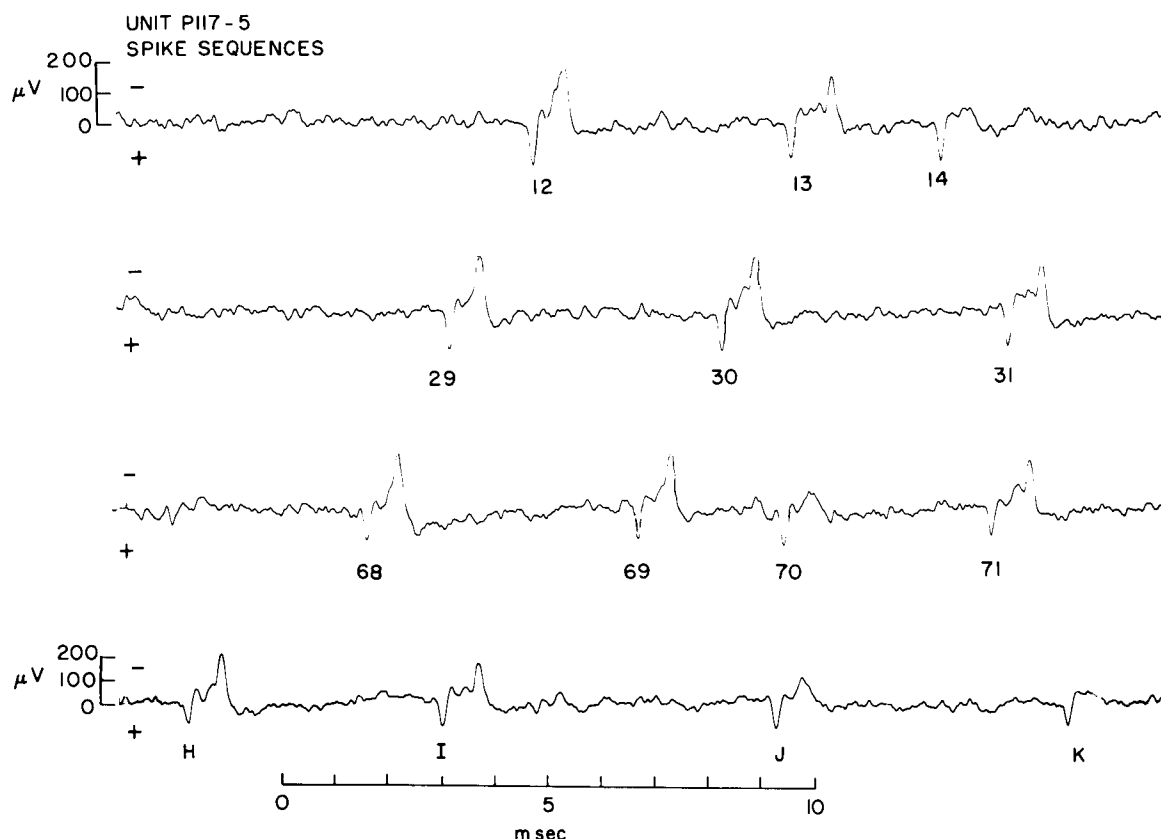


Fig. XVIII-6. Sequences of spikes illustrating the change in delay between the P and B (or A and B) components and the failure of the B component (cf. Fig. XVIII-2). These phenomena have been seen elsewhere (Fuortes et al.,² Li⁶). Perhaps the last spike shown consists only of a P component, which would indicate that the A component also failed to develop.

(i) The injury sequences demonstrated in Fig. XVIII-3 which are associated with injury of cell bodies.

(ii) The remarkable similarity to extracellular wave shapes recorded elsewhere, which exhibit this same A,B relation, and have been demonstrated to be postsynaptic events.^{4b,5}

(iii) The similarity between the failure of the B component, in cases of spikes occurring close to each other in time, for these cochlear nucleus neurons (Figs. XVIII-2

and XVIII-6) and the postsynaptic component failure observed in cortical⁶ and motoneurons.⁷

(iv) The consistency with the interpretation that the P component is presynaptic.

The interpretation of the origin of the A and B components can be identical to that of Terzuolo and Araki (as well as others) for cases of spinal motoneurons. There appears to be no conflict with their interpretation – that the A component is the discharge of the initial segment (IS) of the cell structure and that the B component is the discharge of the soma-dendrite (SD) complex. It is possible, however, that the A component is not an IS discharge but rather an excitatory postsynaptic potential (EPSP).

Our present explanation of the polarities of the various components as monitored by extracellular electrodes is essentially that of Takeuchi and Takeuchi² for the P component, and of Terzuolo and Araki⁵ for the A and B components. Further details of these waveforms, as well as other properties of these neurons, will be considered elsewhere.

R. R. Pfeiffer, W. B. Warr

[Dr. W. B. Warr is a Research Associate in Otolaryngology at the Massachusetts Eye and Ear Infirmary, Boston, Massachusetts.]

References

1. S. Ramón y Cajal, *Histologie du système nerveux de l'homme et des vertebres*, Vol. 1 (Maloine, Paris, 1909), pp. 781-787.
2. A. Takeuchi and N. Takeuchi, "Electrical Changes in Pre- and Postsynaptic Axons of the Giant Synapse of *Loligo*," *J. Gen. Physiol.* **45**, 1181-1193 (1962).
3. J. I. Hubbard and R. F. Schmidt, "An Electrophysiological Investigation of Mammalian Motor Nerve Terminals," *J. Physiol. (Lond.)* **166**, 145-167 (1963).
4. J. C. Eccles, "The Physiology of Synapses" (Springer-Verlag, Berlin, 1964), (a) pp. 122-127; (b) Chapters VII and X.
5. C. A. Terzuolo and T. Araki, "An Analysis of Intra- versus Extracellular Potential Changes Associated with Activity of Single Spinal Motoneurons," *Ann. N. Y. Acad. Sci.* **94**, 547-558 (1961).
6. C. L. Li, "Cortical Intracellular Synaptic Potentials," *J. Cell. Comp. Physiol.* **58**, 153-167 (1961).
7. M. G. F. Fuortes, K. Frank, and M. C. Becker, "Steps in the Production of Motoneuron Spikes," *J. Gen. Physiol.* **40**, 735-752 (1957).

B. THE FLUCTUATION OF EXCITABILITY OF A NODE OF RANVIER

1. Introduction

Fluctuations of the excitability of a node of Ranvier from a peripheral nerve fiber were first reported by Blair and Erlanger,¹ studied by Pecher,² and more recently by Verveen^{3,4} and Derksen.⁵ Following is a brief account of some experiments dealing with this phenomenon which we have recently performed.⁶

(XVIII. COMMUNICATIONS BIOPHYSICS)

The workers cited above observed that a node of Ranvier, when excited by identical rectangular depolarizing current pulses (of duration τ and intensity i) exhibits fluctuations of two types:

- (i) In the vicinity of the threshold, a response is obtained in only a fraction of the trials.
- (ii) The latency of the response fluctuates from trial to trial.

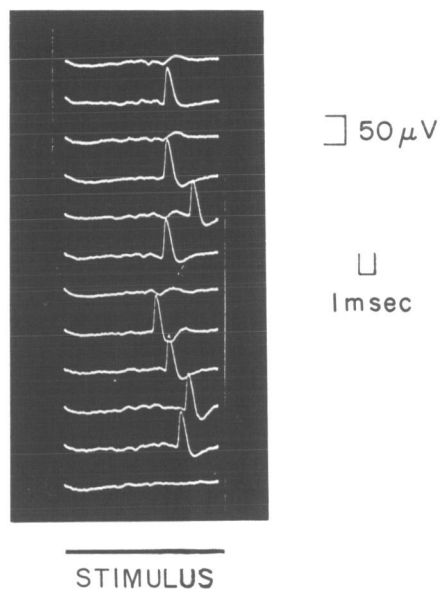


Fig. XVIII-7.

Samples of repetitive trials. A fiber is stimulated at a rate of 0.5 sec^{-1} with identical current stimuli of near-threshold intensity. Each record starts with the onset of the stimulus, which is represented by a heavy bar. The observed delay of the response consists of two terms: first, a delay produced by the "excitation process" at the locus of stimulation, second, a delay caused by the finite conduction velocity of the fiber (in this case over a distance of 7 cm). The second delay can be considered as a constant for our purpose. In the sequel, "latency" is to be equated with the first delay.

These two types of fluctuation are illustrated by the data presented in Fig. XVIII-7. It appears that for rates of stimulation lower than 0.5 sec^{-1} , the firings can be described as a set of Bernoulli trials, that is, the responses to successive trials appear to be mutually independent and to occur with a fixed probability.

Excised sciatic-peroneal nerve preparations from Rana pipiens were used in these experiments. Action potentials were recorded from fibers in the phalangeal branches of the nerve by means of gross electrodes. The signal-to-noise ratio of the recorded signals and the amplitude of the artifact were such that the latency could be measured with a standard error of $20 \text{ } \mu\text{sec}$ by means of a level-crossing device. The preparation was stimulated proximally with tri-polar tungsten or silver silver-chloride electrodes. Throughout a sequence of successive trials, the stimuli could be maintained constant within 0.1% of a prescribed value, both in intensity and in duration. The temperature of the preparation was between 18°C and 22°C and was kept within 0.1°C of a fixed value during the course of an experiment. The responses of 63 single fibers were obtained.

2. Intensity Function

For a given stimulus duration τ , it has been found that a Gaussian distribution, with mean \bar{i}_τ and standard deviation σ_τ , could be fitted to the experimental curve relating the average number of firings to the intensity i of the stimulus^{2,3} (the intensity function). The threshold is defined as \bar{i}_τ .

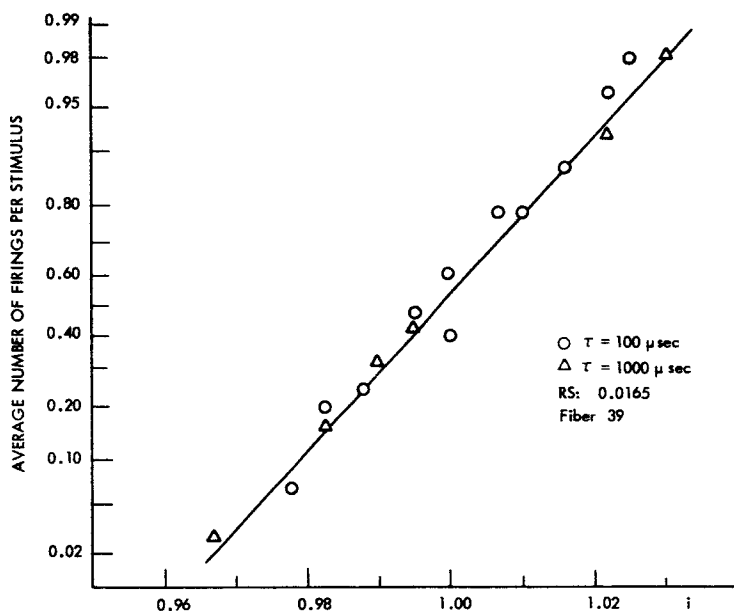


Fig. XVIII-8. Intensity Function, plotted on a normal scale for two durations of the stimulus. The corresponding threshold is normalized to 1.0 in both cases.

Figure XVIII-8 shows a measurement of the intensity function obtained in the present study. The vertical scale is such as to map a Gaussian distribution into a straight line whose slope is inversely related to the standard deviation. The figure presents data obtained for $\tau = 100 \mu\text{sec}$ and $\tau = 1000 \mu\text{sec}$. Each point corresponds to the relative frequency of response to 100 successive, identical stimuli presented at the rate of 0.5 sec^{-1} . For both values of τ , \bar{i}_{100} and \bar{i}_{1000} have been normalized to 1.0 and i correspondingly transformed. These data support the hypothesis that the intensity function can be described as a Gaussian distribution function. The superposition of the experimental points for both values of τ illustrates the invariance of the quantity $(\sigma_\tau / \bar{i}_\tau)$, called "Relative Spread" (RS). This is in agreement with Verveen,³ who has reported such invariances over the 200-2000 μsec range of τ , but at variance with the results of DeBecker⁷ (for $\tau = 200$ and $4000 \mu\text{sec}$) which were obtained, however, on a different preparation.

3. Latency Distribution

The necessity of using low rates of stimulation, coupled with the limited time over which a preparation yields reproducible observations (typically a few hours), has restricted the number of samples from which the distribution of the latency could be estimated. For this reason, only the mean and standard deviations were considered quantitatively.

Qualitatively, as the intensity of the stimulus is increased, the mean, M , and the standard deviation, S , of the distribution of latency decrease, while the distribution changes from highly unsymmetrical, with a positive third central moment, to more symmetrical.

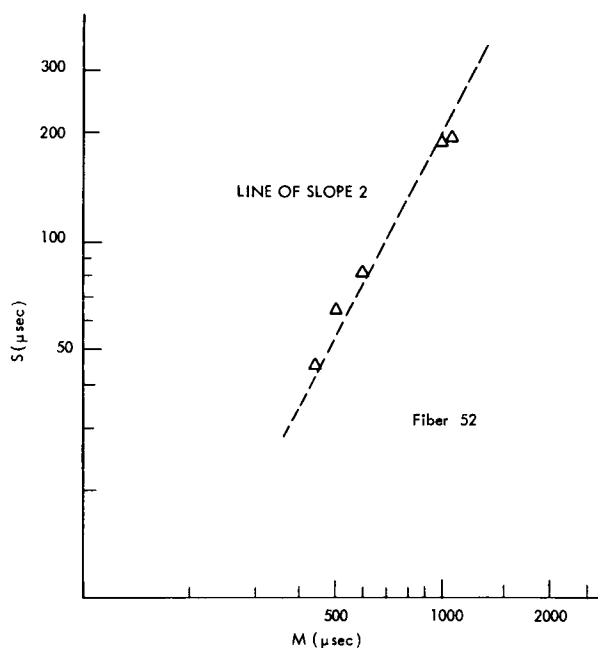


Fig. XVIII-9.

Standard deviation of the latency, S , as a function of the mean, M , of the latency in log-log coordinates.

Quantitatively, one observes an interesting relation between S and M , illustrated in Fig. XVIII-9. S appears to be linearly related to M^2 over a range of stimulus intensity of $0.5\bar{i}_T < i < 2\bar{i}_T$. Unfortunately, the type of preparation that was used is not suited to the estimation of latency distributions outside of the above-mentioned range of intensity.

A similar dependence of S on M has recently been reported by Verveen. A Monte-Carlo simulation^{4,8} of a mathematical model of the fluctuation of excitability has also produced a similar functional relationship between S and M for the range of i given above. [The reader is referred to the original paper of Ten Hoopen and his co-workers⁸ and to the author's thesis⁶ for a description of that model.] Data such as those presented

in Fig. XVIII-9 were compared with the results of the simulation. From this comparison, an estimate of the upper cutoff frequency of the power spectrum of the "membrane noise" was obtained.⁶

4. Remarks

Slow fluctuations (e. g., with time courses of 1 minute or more) in the measured values of both the threshold and the RS of a node of Ranvier were frequently observed in this investigation. It has not yet been possible to ascertain whether or not these fluctuations were intrinsic properties of the membrane. In spite of the care in the control of those factors of known influence on the stability of the preparation, experimental artifacts are not ruled out as a source of such slow fluctuations. For this reason, two of our experimental techniques are currently being re-examined. Liquid-stimulating electrodes are being investigated in order to eliminate possible changes in the coupling between the epineurium and the metal electrodes imbedded in mineral oil. The possible effect of coupling between a given fiber whose responses are observed and its neighbors at the locus of stimulation will be examined soon. An optically coupled stimulator has been designed in order to be able to both stimulate and record on a phalangeal branch with a negligible artifact. It will thus be possible to monitor the responses of all excited fibers of a branch, and investigate the effect of interfiber coupling.

If it can be shown that such slow fluctuations are properties of the membrane, the current form of mathematical models for the excitability of a node in terms of a stationary random process may have to be revised.

D. J-M. Poussart

References

1. E. A. Blair and J. Erlanger, "A Comparison of the Characteristics of Axons through Their Individual Electrical Responses," *Am. J. Physiol.* 106, 524-564 (1933).
2. C. Pecher, "La fluctuation d'excitabilité de la fibre nerveuse," *Arch. Int. Physiol.* 49, 129-152 (1939).
3. A. A. Verveen, "Fluctuations in Excitability," Netherlands Central Institute for Brain Research, Drukkerij Holland N. V., Amsterdam, 1961.
4. A. A. Verveen and H. E. Derksen, "Fluctuations in Membrane Potentials of Axons and the Problem of Coding," *Kybernetik* 2, 4 ht (1965).
5. H. E. Derksen, "Axon Membrane Voltage Fluctuations," *Acta Physiol. Pharmacol. Neerl.* 13, 373-466 (1965).
6. D. J-M. Poussart, "Measurements of Latency Distributions in Peripheral Nerve Fibers," S. M. Thesis, Department of Electrical Engineering, Massachusetts Institute of Technology, 1965.
7. J. C. DeBecker, "Fluctuations in Excitability of Single Myelinated Nerve Fibers," *Separatum Experientia* 20, 553 (1964).
8. M. Ten Hoopen, A. Den Hertog, and H. A. Reuver, "Fluctuations in Excitability - A Model Study," *Kybernetik* 2, 1 ht, 1-8 (1963).

C. BIOELECTRIC POTENTIALS IN AN INHOMOGENEOUS VOLUME CONDUCTOR

Electric potentials of cardiac origin can readily be recorded at the surface of the body. A fundamental problem in electrocardiography is to relate these potential differences to their sources in the heart muscle. In this report an attempt is made to provide a formal analysis of this problem. While the emphasis is on the electrocardiographic problem, the basic problem is one of the distribution of action currents in an inhomogeneous volume conductor, and the results should be applicable to potentials arising from nerve, as well as from muscle.

The solution to the problem depends, of course, on the electrical properties of body tissues. These properties have been studied quite extensively^{1,2} and several important conclusions can be drawn. First, electromagnetic wave effects can be neglected³ and the problem is thus a quasi-static one. Hence if \vec{E} is the electric field intensity at a point in the body, and V is the electric scalar potential, at each instant

$$\vec{E} = -\nabla V. \quad (1)$$

A second conclusion is that for the current densities present as a result of action potentials, body tissues are linear,¹ and the current density, \vec{J} , is linearly related to the field \vec{E} . Furthermore, the capacitive component of tissue impedance is negligible at frequencies of interest to electrocardiography² (below 1 kHz), and there is also evidence that pulses with rise times of approximately 1 μ sec suffer negligible distortion.⁴ If tissue conductivity is designated g , then

$$\vec{J} = g\vec{E} \quad (2)$$

for regions where there are no bioelectric sources.

In Eq. 2 it is assumed that tissues are isotropic, at least if g is to be a scalar quantity. Evidence on this point is incomplete. Clearly, individual muscle fibres are not isotropic, but apparently to a good approximation, for the present purposes, a region of tissue is effectively isotropic because of randomness in the orientation of cells,¹ and can be assigned a bulk conductivity that is isotropic.

As a consequence of these properties of body tissues, the currents at any instant depend only on the values of the sources at that instant. Formally, we can represent the sources by a distribution of impressed current densities, \vec{J}^i . Later we shall attempt to relate \vec{J}^i to electrical activity associated with the plasma membranes of the active cells. Equation 2 can be modified to include active regions as follows:

$$\vec{J} = g\vec{E} + \vec{J}^i. \quad (3)$$

If the accumulation of charge in any region is to be zero, we have the additional relation

$$\nabla \cdot \bar{J} = 0 \quad (4)$$

which can be combined with Eqs. 1 and 3 to give

$$\nabla \cdot g \nabla V = \nabla \cdot \bar{J}^i. \quad (5)$$

Conductivities of the various tissue masses in the thorax are quite similar. Major exceptions are blood, which has a much higher conductivity than the average, and lung, whose conductivity may vary considerably over the respiratory cycle. It is reasonable, then, to divide the body into homogeneous regions, in each of which the conductivity is constant.

Let the surface S_j separate regions of conductivity g' and g'' , and let $d\bar{S}_j$ be a differential element of the area of this surface. Adopt the convention that $d\bar{S}_j$ is directed from the primed region to the double primed one. Since the current must be continuous across each boundary,

$$g' \nabla V' \cdot d\bar{S}_j = g'' \nabla V'' \cdot d\bar{S}_j. \quad (6)$$

Furthermore, the potential is also continuous at each boundary. Hence

$$V'(S_j) = V''(S_j). \quad (7)$$

Our problem, then, is to determine V from a knowledge of \bar{J}^i , using Eqs. 5, 6, and 7. More particularly in electrocardiography, our problem is to determine \bar{J}^i , given V on the body surface. Similarly, in studying action potentials from nerve or cardiac muscle with microelectrodes, the problem is often to determine J^i from a knowledge of the potential difference between the microelectrode and a reference electrode. This "inverse" problem will be discussed further.

Let dv be an element of volume of a homogeneous region, and ψ and ϕ be two functions that are well behaved in each region. Green's theorem⁵ then states that

$$\sum_j \int_{S_j} [g'(\psi' \nabla \phi' - \phi' \nabla \psi') - g''(\psi'' \nabla \phi'' - \phi'' \nabla \psi'')] \cdot d\bar{S}_j = \sum_v \int_v [\psi \nabla \cdot g \nabla \phi - \phi \nabla \cdot g \nabla \psi] dv. \quad (8)$$

Three cases are of interest and they will be discussed separately.

Case I

Let

$$\phi = V \quad (9)$$

$$\nabla^2 \psi = 0 \quad (10a)$$

$$\psi'(S_j) = \psi''(S_j). \quad (10b)$$

Then from Eqs. 5, 6, and 7,

$$-\sum_j \int_{S_j} V(g'-g'') \nabla \psi \cdot d\vec{S}_j - \int_{S_0} g V \nabla \psi \cdot d\vec{S}_0 = \sum_v \int_v (\psi \nabla \cdot \vec{J}^i - V \nabla g \cdot \nabla \psi) dv, \quad (11)$$

where S_0 is the external surface of the body, and the summation j is over internal surfaces of discontinuity. Our assumption is that ∇g is zero in each region, that is, each region is homogeneous. Hence the last term vanishes. The first term on the right can be transformed as follows:

$$\int \nabla \cdot (\vec{J}^i \psi) dv = \int \psi \vec{J}^i \cdot d\vec{S} = \int (\vec{J}^i \cdot \nabla \psi + \psi \nabla \cdot \vec{J}^i) dv.$$

If \vec{J}^i vanishes on S , then

$$\int \psi \nabla \cdot \vec{J}^i dv = - \int \vec{J}^i \cdot \nabla \psi dv \quad (12)$$

and Eq. 11 becomes

$$\int_{S_0} g V \nabla \psi \cdot d\vec{S}_0 + \sum_j \int_{S_j} (g'-g'') V \nabla \psi \cdot d\vec{S}_j = \int \vec{J}^i \cdot \nabla \psi dv. \quad (13)$$

Let \vec{P} be a fictitious volume distribution of sources in a homogeneous conductor, g_0 , chosen so that V on S_0 remains the same. Then

$$\int_{S_0} g_0 V \nabla \psi \cdot d\vec{S}_0 = \int \vec{P} \cdot \nabla \psi dv. \quad (14)$$

Now consider that the conductivity at the body surface is constant and let its value be g_0 . From Eqs. 13 and 14,

$$g_0 \int_{S_0} V \nabla \psi \cdot d\vec{S}_0 = \int \vec{P} \cdot \nabla \psi dv = \int \vec{J}^i \cdot \nabla \psi dv - \sum_j \int_{S_j} (g'-g'') V \nabla \psi \cdot d\vec{S}_j. \quad (15)$$

Equation 15 is the basic result of Case I. It is valid for each choice of ψ satisfying Eqs. 10a and 10b. Note that to evaluate the integral on the left, only a knowledge of the surface potential distribution is required. The fictitious, or equivalent, source distribution, \vec{P} , is not uniquely determined. Indeed there is an infinite number of choices of \vec{P} that will satisfy Eq. 14. The multipole expansion⁶ provides a canonical description of \vec{P} . In this representation \vec{P} consists of singularities at a single point.

The various terms of the multipole expansion can be obtained by letting

$$\psi_{nm} = \left(2 - \delta_m^0\right) \frac{(n-m)!}{(n+m)!} r^n P_n^m(\cos \theta) e^{im\phi}, \quad (16)$$

where (r, θ, ϕ) are the coordinates of a point in space relative to the origin at the location

of the multipoles, P_n^m is an associated Legendre polynomial, and δ_m^0 is the Kronecker delta which is unity for $m = 0$ and zero for other values of m . Both n and m are non-negative integers, and m is less than or equal to n . Note that ψ_{nm} satisfies Eqs. 10a and 10b.

In particular, the multipole components a_{nm} and b_{nm} are given by

$$a_{nm} + ib_{nm} \equiv \int \vec{P} \cdot \nabla \psi_{nm} dv. \quad (17)$$

Therefore

$$a_{nm} + ib_{nm} = \int g_o V \nabla \psi_{nm} \cdot d\vec{S}_o = \int \vec{J}^i \cdot \nabla \psi_{nm} dv - \sum_j \int_{S_i} (g' - g'') V \nabla \psi_{nm} \cdot d\vec{S}_j. \quad (18)$$

Thus the multipole components can be evaluated from a knowledge of the surface potential distribution and can be related to the actual source distribution, if known. The monopole term a_{00} vanishes. When n is 1, we have the dipole term for which

$$\psi_{10} = r \cos \theta = z$$

$$\psi_{11} = r \sin \theta e^{im\phi} = x + iy.$$

If the dipole moment, \vec{p} , is defined as

$$p \equiv ia_{11} + jb_{11} + ka_{10}, \quad (19)$$

then

$$\vec{p} = \int g_o V d\vec{S}_o = \int \vec{J}^i dv - \sum_j \int_{S_i} (g' - g'') V d\vec{S}_j = \int \vec{P} dv. \quad (20)$$

The five components of the quadrupole are obtained by letting $n = 2$, and can be evaluated in similar fashion. Note that it is impossible to distinguish two equivalent distributions whose multipole expansions are identical.

Case II

Let us retain Eqs. 9 and 10b, but change Eq. 10a so that

$$\psi = \frac{1}{r}, \quad (21)$$

where r is the distance from an arbitrary point to the element of volume or area. The derivation then proceeds in a very similar manner except that in Eq. 11 we must retain the term involving $\nabla^2 \psi$. Thus

$$-\sum_j \int_{S_j} V(g' - g'') \nabla \left(\frac{1}{r} \right) \cdot d\vec{S}_j - \int_{S_o} g V \nabla \left(\frac{1}{r} \right) \cdot d\vec{S}_o = \int_v \left[\frac{1}{r} \nabla \cdot \vec{J}^i - V g \nabla^2 \left(\frac{1}{r} \right) \right] dv. \quad (22)$$

(XVIII. COMMUNICATIONS BIOPHYSICS)

The first term on the right can be transformed by using Eq. 12. The second term can be evaluated to give

$$\int_V g V \nabla^2 \left(\frac{1}{r} \right) dv = -4\pi g V, \quad (23)$$

where g and V are evaluated at $r = 0$, that is, the arbitrary point. Therefore

$$\psi \pi g V = \int_V \vec{J}^i \cdot \nabla \left(\frac{1}{r} \right) dv - \sum_j \int_{S_j} V (g' - g'') \nabla \left(\frac{1}{r} \right) \cdot d\vec{S}_j - \int_{S_0} g V \nabla \left(\frac{1}{r} \right) \cdot d\vec{S}_0. \quad (24)$$

This equation is the basis of an iterative technique⁷ for the solution of Eq. 5, subject to the boundary conditions (6) and (7). If each side of the equation is divided by $4\pi g$, then the first term on the right can be interpreted as the potential that would exist at a point in an unbounded homogeneous conductor of conductivity g resulting from a current source distribution \vec{J}^i . The next two terms can be similarly interpreted in terms of double layers at the discontinuities.

Case III

Return to Eq. 8 and let

$$g\phi = V \quad (25)$$

$$\psi = \frac{1}{r}.$$

Then, with the use of Eqs. 5 and 7,

$$-\sum_j \int_{S_j} \frac{1}{r} (\vec{E}' - \vec{E}'') \cdot d\vec{S}_j - \int_{S_0} \frac{1}{r} \vec{E}'' \cdot d\vec{S}_0 = \sum_V \int_V \left[\frac{1}{rg} \nabla \cdot \vec{J}^i - V \nabla^2 \left(\frac{1}{r} \right) \right] dv. \quad (26)$$

The two terms of the right-hand integral can be transformed by using Eqs. 12 and 23. The terms on the left of the equality sign can be rearranged as follows. From Eq. 6,

$$g' E'_n = g'' E''_n. \quad (27)$$

Here the subscript n indicates the normal component, that is, in the direction of $d\vec{S}_j$. Define

$$E_j \equiv \frac{1}{2} (E'_n + E''_n) = \frac{1}{2} E'_n (1 + g'/g''). \quad (28)$$

Then

$$E'_n - E''_n = E'_n (1 - g'/g'') = 2E_j \frac{g'' - g'}{g'' + g'} \quad (29)$$

and Eq. 26 becomes

$$-\sum_j \int_{S_j} \frac{2E_j}{r} \frac{g'' - g'}{g'' + g'} dS_j + \int_{S_0} \frac{2E_j}{r} dS_0 = -\int \frac{1}{g} \vec{J}^i \nabla \left(\frac{1}{r} \right) dv + 4\pi V$$

or

$$V = \int \frac{1}{4\pi g} \vec{J}^i \nabla \left(\frac{1}{r} \right) dv + \sum_j \int_{S_j} \frac{2\epsilon E_j}{4\pi \epsilon r} \frac{g' - g''}{g' + g''} dS_j + \int_{S_0} \frac{2\epsilon E_j}{4\pi \epsilon r} dS_0. \quad (30)$$

Equation 30 can be interpreted in a manner analogous to that used for Eq. 24. The first term on the right again gives the potential that would exist at an arbitrary point in an unbounded medium of conductivity g resulting from current sources \vec{J}^i . The second and last terms represent the potential in an unbounded medium of permittivity ϵ arising from a surface charge distribution, ω_j , given by

$$\omega_j = 2\epsilon E_j \frac{g' - g''}{g' + g''}. \quad (31)$$

Note that the last term is a special case in which $g'' = 0$, and the potential is independent of the value chosen for ϵ .

E_j can be looked upon as the normal component of the electric field that would exist at the point in question if the surface charge, ω_j , at the point were not present. This interpretation follows from the fact that if E_0 is the normal component of the field attributable to all other sources, then

$$E'_n = E_0 - \delta E$$

$$E''_n = E_0 + \delta E,$$

where

$$\delta E = \frac{\omega_j}{2\epsilon},$$

in order to satisfy the boundary condition

$$E''_n - E'_n = \omega_j / \epsilon. \quad (32)$$

Note that Eq. 32 is consistent with Eqs. 29 and 31.

Equation 30 can also be used as the basis of an iterative technique to solve the boundary value problem.⁸ The potential, and hence E_j , can be determined from the first integral on the right by taking ω_j initially equal to zero. Next, ω_j can be evaluated from Eq. 31, and E_j recalculated from Eq. 30. The process can be repeated until the values of ω_j stabilize.

Relation to Membrane Activity

Thus far, the myocardium has been represented by a distribution of current sources, \bar{J}^i , in a uniform conductor. It is of interest to relate \bar{J}^i to electrical activity associated with cell membranes. We shall assume that the interior of each cell is a passive conductor of conductivity g_i , while the intracellular fluid is a passive conductor of conductivity g_e . The membranes are sites of complex electrical activity; they will be excluded when applying Green's theorem.

Return to Case II. Equation 22 must now be modified to exclude membranes in the myocardial region. Since all remaining regions are passive, the term involving J^i disappears. Conversely on the left-hand side of Eq. 22 new terms appear involving integrations over the internal surface, S_{mi} , and external surfaces, S_{me} , of each plasma membrane. The net result in Eq. 25 is thus to replace the volume integral involving J^i with surface integrals over membranes as follows:

$$\int \bar{J}^i \cdot \nabla \left(\frac{1}{r} \right) dv = \int_{S_{mi}} g_i \left[\frac{1}{r_i} \nabla V_i - V_i \nabla \left(\frac{1}{r_i} \right) \right] \cdot d\bar{S}_{mi} - \int_{S_{me}} g_e \left[\frac{1}{r_e} \nabla V_e - V_e \nabla \left(\frac{1}{r_e} \right) \right] \cdot d\bar{S}_{me}, \quad (33)$$

where r_i and r_e are distances from an arbitrary point outside the heart region to the elements dS_{mi} and dS_{me} , respectively, and V_i and V_e are the corresponding potentials.

Following Plonsey⁹ we shall assume that the transverse membrane current, J_m , taken positive outward, is

$$-J_m = g_i (\nabla V_i)_n = g_e (\nabla V_e)_n. \quad (34)$$

Furthermore, if the membrane thickness, m , is small compared with r , then

$$\frac{dS_{mi}}{r_e} - \frac{dS_{me}}{r_i} \approx dS_m \left(\frac{1}{r_e} - \frac{1}{r_i} \right) \approx d\bar{S}_m \cdot m \nabla \left(\frac{1}{r} \right). \quad (35)$$

To the same order of approximation,

$$\nabla \left(\frac{1}{r_i} \right) \cdot d\bar{S}_{mi} = \nabla \left(\frac{1}{r_e} \right) \cdot d\bar{S}_m = \nabla \left(\frac{1}{r} \right) \cdot d\bar{S}_m. \quad (36)$$

Hence

$$\int \bar{J}^i \cdot \nabla \left(\frac{1}{r} \right) dv = \int_{S_m} [J_m m - g_i V_i + g_e V_e] \nabla \left(\frac{1}{r} \right) \cdot d\bar{S}_m = \int (J_m m - g_i V_i + g_e V_e) d\Omega, \quad (37)$$

where $d\Omega$ is the solid angle subtended by dS_m . Plonsey has pointed out that generally

$$g_e |V_e - V_i| \gg m J_m. \quad (38)$$

For example, let $g_e = g_i = 10^{-3}$ mho/cm, $|V_i - V_e| = 10$ mv, and $m = 1000 \text{ \AA}$. Then

$g_e(V_i - V_e)/m$ is approximately 1000 ma/cm^2 , which is much larger than observed values of J_m . With this approximation, then, for $g_e = g_i$,

$$\bar{J}^i dv = (g_e V_e - g_i V_i) d\bar{S}_m, \quad (39)$$

and each element of membrane area acts as a current dipole source whose moment is related to the transmembrane potential.

Note that when the cell is in its resting state V_e and V_i are constant over S_m . In this circumstance, the integral in Eq. 37 taken over the entire cell boundary becomes

$$(g_e V_e - g_i V_i) \oint d\Omega = 0. \quad (40)$$

Thus a uniform potential along both sides of the membrane produces no external fields. Consequently, calculations involving Eqs. 24 and 37 can be done equivalently by considering departures of $\left(V_e - \frac{g_i}{g_e} V_i\right)$ from its resting value. As a corollary, if a region of membrane is uniformly depolarized, it is sometimes convenient to use Eq. 40 and replace the active region by complementary regions that complete a closed surface and have an opposite dipole moment.

When Eq. 37 is substituted in Eq. 24, the result is

$$4\pi gV = \int_{S_m} (J_m - g_i V_i + g_e V_e) d\Omega - \sum_j \int_{S_j} V(g' - g'') \nabla\left(\frac{1}{r}\right) dS_j - \int_{S_o} gV \nabla\left(\frac{1}{r}\right) dS_o. \quad (41)$$

The first integral is the source term, the second integral accounts for inhomogeneities in the volume conductor, and the third integral accounts for the external boundary. While the equation cannot be directly integrated to obtain solutions, since the last two integrals require a knowledge of the potentials we are seeking, it does provide insight into the nature of the solution. As indicated above, iterative techniques can be used to obtain solutions with the aid of digital computers.

Equation 41 was obtained from Case II by excluding the membrane from the region of integration. Case III can be treated in an identical manner. The result is

$$4\pi V = \int \left[\left(\frac{1}{g_e} - \frac{1}{g_i} \right) \frac{\bar{J}_m}{r} + (V_e - V_i) \nabla\left(\frac{1}{r}\right) \right] \cdot dS_m + \sum_j \int_{S_j} \frac{2E_j}{r} \frac{g' - g''}{g' + g''} dS_j + \int_{S_o} \frac{2E_j}{r} dS_o. \quad (42)$$

If $g_i = g_e$, then the first integral in Eq. 41 is just g times the first integral in Eq. 42.

In electrocardiography the major discontinuities are those at the inner and outer surfaces of the heart, for example, at the interface with the intracavitary blood mass and with the lungs. The changing impedance of the lungs during respiration is probably responsible for the respiratory variations observed in the electrocardiogram.

(XVIII. COMMUNICATIONS BIOPHYSICS)

Note that the first integrals in Eqs. 41 and 42 involve the potential and its normal derivative over a surface bounding a region containing no sources. These two functions are not independent. In practice, only a portion of a cell membrane is actively depolarized at any instant. Strictly speaking, the presence of transverse current, J_m , at nonactive membrane sites must also be taken into account in evaluating the fields everywhere in the present formulations. To a first approximation, only potentials and currents at active membrane sites need be considered.

Equation 41 or 42 should also be applicable for determining the potential at an extracellular microelectrode. In this case effects of inhomogeneities can be neglected to a first approximation if they are sufficiently far removed from the recording electrodes and the active areas.

Either equation, then, provides an implicit expression for the potentials throughout an inhomogeneous volume conductor, given a knowledge of membrane potentials and currents at all active sites at any instant of time. In practice, the transverse currents at adjacent membrane sites will result in the spread of depolarization. A knowledge of the voltage current relation at the membrane should enable one to calculate the spread of excitation. This topic is beyond the scope of the present treatment.

D. B. Geselowitz

References

1. H. P. Schwan and C. F. Kay, "Specific Resistance of Body Tissues," *Circulation Research* 4, 664-670 (1956).
2. H. P. Schwan and C. F. Kay, "Capacitive Properties of Body Tissues," *Circulation Research* 5, 439-443 (1957).
3. D. B. Geselowitz, "The Concept of an Equivalent Cardiac Generator," *Biomedical Sciences Instrumentation*, Vol. I (Plenum Press, New York, 1963).
4. S. A. Briller, D. B. Geselowitz, G. K. Danielson, C. R. Joyner, and S. D. Arlinger, "Use of a Current Probe in the Evaluation of Failure of Artificial Pacemakers," *Proceedings of 17th Annual Conference on Engineering in Medicine and Biology*, Cleveland, Ohio, November, 1964, Vol. 6, p. 120.
5. W. P. Smythe, *Static and Dynamic Electricity* (McGraw-Hill Book Company, New York, 1950), pp. 48-58; 129-138.
6. D. B. Geselowitz, "Multipole Representation for an Equivalent Cardiac Generator," *Proc. IRE*, 48, 75-79 (1960).
7. R. Barr, T. C. Pilkington, J. P. Boineau, and M. S. Spach, "Correlation between Body Surface Potential Distribution and Ventricular Excitation," *Proc. 18th ACEMB*, Philadelphia, November 1965, Vol. 7, p. 98.
8. H. Gelernter and J. C. Swihart, "A Mathematical-Physical Model of the Genesis of the Electrocardiogram," *Biophys. J.* 4, 285-301 (July 1964).
9. R. Plonsey, "An Extension of the Solid Angle Potential Formulation for an Active Cell," *Biophys. J.* 5, 663-667 (September 1965).

XIX. NEUROPHYSIOLOGY*

Academic and Research Staff

Dr. W. S. McCulloch	Dr. K. Kornacher	Dr. Barbara C. G. Pickard
Dr. J. Y. Lettvin	Dr. R. Moreno-Diaz	Dr. W. F. Pickard
Prof. P. D. Wall	Dr. T. McLardy	Dr. T. G. Smith, Jr.
Prof. M. Blum	Dr. A. Natapoff	Dr. A. Taub
Prof. J. E. Brown	Dr. S. A. Papert	B. Howland
Dr. H. Hartman		W. H. Pitts

Graduate Students

E. E. Fetz	J. I. Simpson	Barbara G. Wickelgren
L. M. Mendell		W. A. Wright

A. MODELLING THE GROUP 2 GANGLION CELL OF THE FROG'S RETINA†

1. Introduction

Since Lettvin, Maturana, McCulloch, and Pitts^{1,2} published their measurements of signals in the optic fibers of the frog, considerable effort^{3,4} has been given to developing models that could account for the properties they found. Such models are of importance to engineers and neurophysiologists for two reasons. First, models provide clues on which to base advanced and versatile engineering systems. Second, models provide a basis of thought consistent with reported neurophysiological findings. Such a basis could be useful to neurophysiologists in interrelating experimental results.

Lettvin, Maturana, and co-workers have distinguished four major groups of retinal ganglion cell which report to the tectum. These have been designated as follows: Group 1, edge-detector; Group 2, bug-detector; Group 3, dimming-detector; and Group 4, event-detector ganglion cells. Of these, relatively simple explanations can be given^{5,6} to the operations of the Group 1, 3, and 4 ganglion cells. The Group 2, or bug-detector ganglion cell, however, is a more intricate and the most exciting cell to model because it is sensitive to small dark convex objects that move centripetally with respect to the responsive retinal field (RRF) of this cell. In essence, it is the most specialized pattern recognition cell of the frog's retina. Gaze and Jacobson⁷ suggest that the Group 2 operation may be due to the existence of an excitatory area surrounded by an inhibitory ring, such that large objects will cause inhibition, whereas small objects will be detected by the cell.

*This work was supported by the National Institutes of Health (Grants 5 RO1 NB-04985-03, 5 RO1 NB-4897-03, and NB-06251-01), the U.S. Air Force (Office of Scientific Research) under Grant AF-AFOSR-880-65, U.S. Air Force (Research and Technology Division) under Contract AF33(615)-1747, and by grants from The Teagle Foundation, Inc. and Bell Telephone Laboratories, Inc.

†This report was prepared at the Instrumentation Laboratory under the auspices of DSR Project 55-257, sponsored by the Bioscience Division of National Aeronautics and Space Administration.

Grusser and co-workers⁸ reported that in their experiments no special construction of the receptive field, with respect to inhibitory or excitatory areas, was found. Grusser⁹ pointed out that patterns moved outside the RRF can have an inhibitory effect on the response elicited by a small moving object inside the RRF, i. e., the inhibitory effect of the supposed ring appears only if the object moves. Evidence⁸ has been given suggesting that these cells are directionally sensitive, although the argument is not definitive.

We present an analytical model that is consistent with the findings of the aforementioned authors. In structuring our model, we follow the anatomy of the Group 2 ganglion cell as understood by Lettvin and his co-workers. They identified¹⁰ the Group 2 ganglion cell as multilevel E-shaped neuron from Ramon y Cajal's drawings. Accordingly, we distribute cell computations in three layers. Those computations are, in general, compatible with commonly accepted neural processes. It has not been necessary to postulate an exclusively inhibitory ring, although the model cell receives information from an area wider than the responsive retinal field. Some cellular properties appear as consequences of the model structure. As a consequence, it is not necessary to make ad hoc hypotheses to explain each of them.

The operation of the model can be summarized as follows. First, a convex function Φ , depending upon the penetration of an object into the responsive retinal field (RRF), is defined. It is only significant when the object moves centripetally. Second, a similar function, Ψ , is defined, which is dependent on the size of the object, being a maximum for one particular size. The coincidence of both is computed by the product $\Phi\Psi$. Third, an inhibitory effect, X , is defined which acts upon the function $\Phi\Psi$. The inhibition is large for bright objects and small for dark objects. As a result, an activity function, Ω , is obtained. The pulse repetition frequency of the cell is assumed to be proportional to Ω .

2. The Model

We assume that, for the purpose of the Group 2 ganglion cell operation, the photoreceptors are connected to two different types of bipolar cells, the outputs of which are pulses of width δt and amplitude r . Each bipolar cell performs a different operation on the retinal image. Let us call $n_I(t)$ and $n_{II}(t)$ the number of bipolar cells (belonging to Types I or II) that fire at time t as a response to a changing image on the retina.

We postulate:

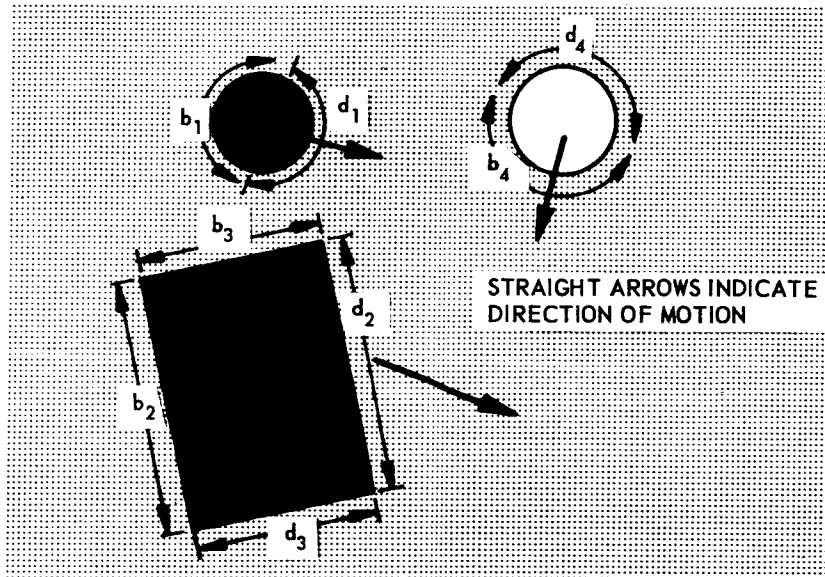
- a. $n_I(t)$ is proportional to the total length of the edges in the retinal image which are coincident with a local dimming.
- b. $n_{II}(t)$ is proportional to the total length of the edges in the retinal image which are coincident with local brightening.

The author has previously described¹¹ a model in which photoreceptors and bipolar

cells perform in a manner similar to that postulated here.

Type I bipolar cells we term contrast-dimming detectors, whereas Type II bipolar cells we term contrast-brightening detectors. In both cases, spatiotemporal changes of the illumination on the photoreceptors feeding each bipolar cell are necessary to fire the latter.

Figure XIX-1 illustrates $n_I(t)$ and $n_{II}(t)$ for several bright and dark moving objects.



$$n_I(t) \propto d_1 + d_2 + d_3 + d_4$$

$$n_{II}(t) \propto b_1 + b_2 + b_3 + b_4$$

Fig. XIX-1. Equivalences of $n_I(t)$ and $n_{II}(t)$ for several moving objects.

Consider one Group 2 ganglion cell. It receives signals from Types I and II bipolar cells, and processes these signals in three computation layers (Fig. XIX-2).

In layer 1, pulses emanating from Type I bipolar cells are collected over a circular area equal to the RRF of the ganglion cell. Each pulse originates a signal level that is maintained for a time Δt . (Δt is made equal to the transit time across the RRF of the slowest object to be detected by the cell.) We may regard this as a short-term memory. Let $n_1(t)$ be the number of pulses impinging on layer 1 at time t . $N_1(t)$, the number of existing signals levels at time t , will be equal to the total number of pulses that have reached layer 1 in the previous time interval $(t-\Delta t, t)$. Note that $N_1(t)$ is proportional to the area that has been scanned by dimming, within the RRF, because of a moving object. Furthermore, each existing signal level at time t is affected by divisional inhibition,¹³ by the ensemble of incoming pulses at time t . Thus, $N_1(t)$ new signal

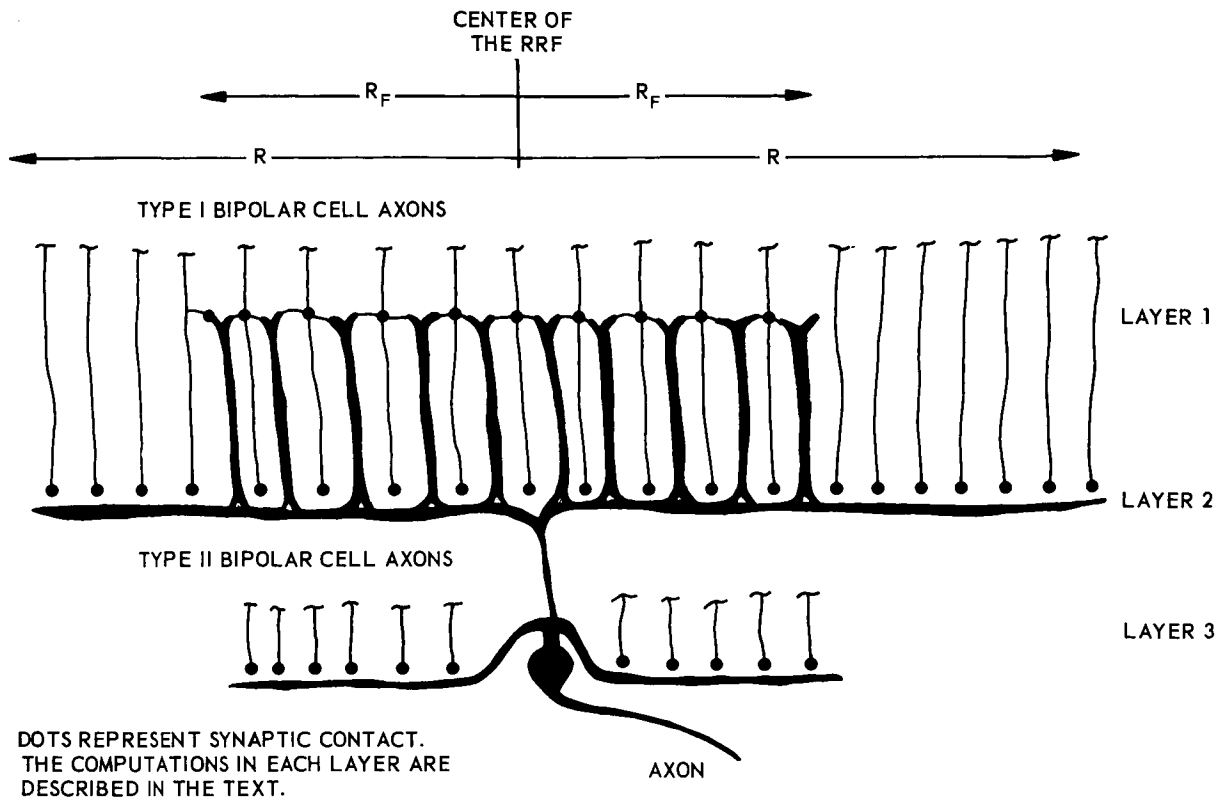


Fig. XIX-2. A section of Group 2 ganglion cell model.

levels are originated, each of them having an identical value, α , defined by

$$\alpha = a/[2+bn_1(t)], \quad (1)$$

where a and b are constants. For $bn_1(t) \gg 1$, Eq. 1 becomes

$$\alpha = K/[n_1(t)], \quad (2)$$

where $K = a/b$.

In layer 2, three operations are distinguished. First, the $N_1(t)$ signal levels from layer 1, each of them having a value $K/n_1(t)$, interact in a manner such that a signal, $\Phi[N_1(t)/n_1(t)]$, is obtained, which has the convex shape shown in Fig. XIX-3. $\Phi[N_1(t)/n_1(t)]$ is maximum for particular value $[N_1(t)/n_1(t)]_{opt}$, and is zero for $N_1(t) = 0$ and for $[N_1(t)/n_1(t)] \geq [N_1(t)/n_1(t)]_{lim}$. The ratio

$$[N_1(t)/n_1(t)] = \frac{\text{area scanned by contrast-dimming in the RRF}}{\text{length of contrast-dimming in the RRF}}$$

provides a measure of the penetration of a round-shaped dark object moving into the RRF.

By appropriately choosing the value of constants in the function Φ , we can make Φ significant only when the image moves centripetally across the RRF.

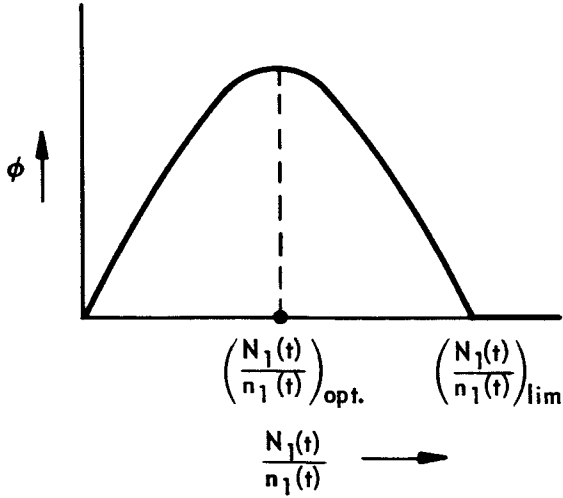


Fig. XIX-3. Shape of the curve $\phi\left(\frac{N_1(t)}{n_1(t)}\right)$.

A particular function, Φ , containing the previously mentioned characteristics can be obtained by assuming that the active-level signals interact by processes commonly accepted in neurophysiology; namely, lateral divisional inhibition, adaptation, and spatial summation. To demonstrate, let us assume that each afferent active line is laterally inhibited by all the others. If the signal level of each line is $K/n_1(t)$, the total inhibition upon each line is

$$\Psi = k[N_1(t) - 1] \cdot K/n_1(t), \quad (3)$$

where $N_1(t)$ is the total number of active lines, and k is a constant.

If $N_1(t) \gg 1$, Eq. 3 becomes

$$\Phi = K_1[K_1(t)/n_1(t)], \quad (4)$$

where $K_1 = kK$.

As a result of divisional inhibition, the signal in each active line becomes

$$A_C = [K/n_1(t)]/[1 + K_1[N_1(t)/n_1(t)]]. \quad (5)$$

If we assume that each active line is adaptive, i. e., its threshold, θ , increases proportionally to the incoming signal,

$$\theta = A[K/n_1(t)], \quad (6)$$

where A is a constant. This is a form of linear adaptation.

From Eqs. 5 and 6, the net signal in each line is

$$A_C - \theta = \frac{K/n_1(t)}{1 + K_1[N_1(t)/n_1(t)]} - A[K/n_1(t)]. \quad (7)$$

By spatial summation over all the $N_1(t)$ active lines at time t , we have

$$\Phi \left[\frac{N_1(t)}{n_1(t)} \right] = \sum_{\text{all active lines}} A_C - \theta = K \left[\frac{N_1(t)/n_1(t)}{1 + K_1[N_1(t)/n_1(t)]} - A[N_1(t)/n_1(t)] \right]. \quad (8)$$

Equation 8 is plotted in Fig. XIX-4 for $K_1 = 1/0.22 R_F$ and $A = 0.25$. R_F is the number of contrast-dimming bipolars contained in one radius of the RRF. K_1 and A have

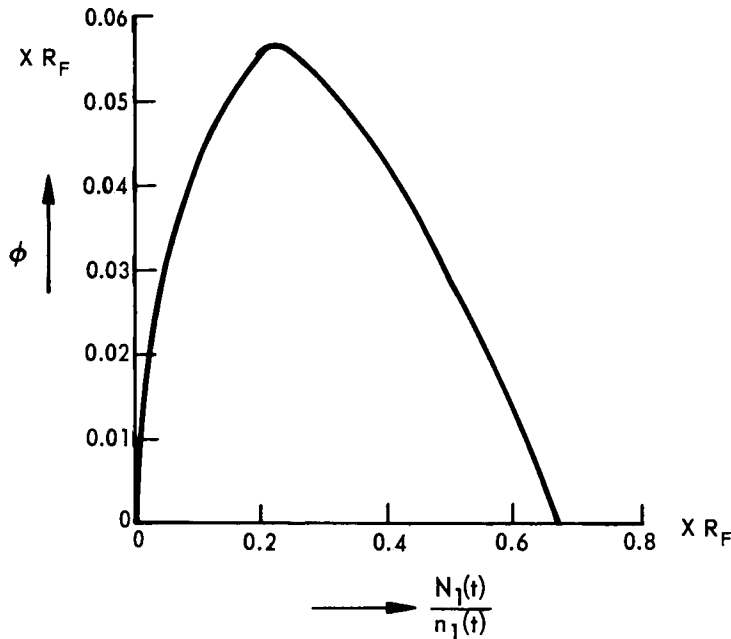


Fig. XIX-4.
Example of function $\Phi \left(\frac{N_1(t)}{n_1(t)} \right)$.

been chosen in a manner such that Φ is significant only for a round-shaped dark object when it moves centripetally across the RRF. Again, note that the essential feature of $\Phi[N_1(t)/n_1(t)]$ is its convex shape as shown in Fig. XIX-3. There exists an infinite number of functions with these characteristics. Among them, Eq. 8 is an example, which is compatible with neurophysiological facts. (The author¹¹ has previously obtained a similarly shaped curve by assuming nonlinear divisional inhibition of the type E/e^I , where E is the excitation and I the inhibition.)

The second operation in layer 2 is performed on afferent pulses from Type I bipolar cells over a circular area of radius R , which is wider than the RRF. Let $n_2(t)$ be the number of incoming pulses collected at time t over this area. $n_2(t)$ is proportional to the total length of contrast-dimming within the circular area of radius R .

The $n_2(t)$ pulses interact in a manner such that a function, $\Psi[n_2(t)]$, is obtained which is similar to Φ . Thus, $\Psi[n_2(t)]$ is maximum for $n_2(t)_{\text{opt}}$, and it is zero for $n_2(t) = 0$ and for $n_2(t) \geq n_2(t)_{\text{lim}}$. Again, constants in $\Psi[n_2(t)]$ can be computed to adjust $n_2(t)_{\text{opt}}$ and $n_2(t)_{\text{lim}}$ to the experimental results.

As an example, we assume again that the $n_2(t)$ pulses interact by lateral divisional inhibition and that adaptation and spatial summation exists. Ψ can be expressed as

$$\Psi[n_2(t)] = K' \left[\frac{n_2(t)}{1 + K'_1 n_2(t)} - B n_2(t) \right], \quad (9)$$

where K' , K'_1 , and B are constants.

Experimental results^{1,2,9} have shown that when experimenting with dark discs, the ganglion cell output is maximum for a disc of radius $\approx R_F/2$, and is zero for discs of radii larger than R_F . Using these findings, we then compute $K'_1 = 3/\pi R_F$ and $B = 0.25$. The radius, R , of wider circular area is estimated to be $R = 3.2 R_F$ by using the criterion^{1,2} that a straight band wider than R_F does not produce a response. The results of Gaze and Jacobson⁶ appear then as a consequence of this restriction.

The third layer 2 operation is a multiplication of the functions Φ and Ψ . We do not have enough neurophysiological evidence to support this assumption, although we still tacitly assume its validity. Thus the activity function

$$\Phi[N_1(t)/n_1(t)] \Psi[n_2(t)]$$

is generated, and we consider this as the output of layer 2. (An explanation of this hypothesis and the shapes of the curves Φ and Ψ may be given in terms of probability. We shall discuss this point of view in a later report, since it could be applied to the description of any nerve cell.)

In layer 3, the outputs from the Type II bipolar cells are of concern. These afferent pulses are collected over the RRF, and they generate signal levels that are maintained for a time Δt . Let $N_3(t)$ be the number of these levels at time t . $N_3(t)$ is then proportional to the area that has been scanned by contrast-brightening within the RRF in the time interval $(t-\Delta t, t)$.

The $N_3(t)$ signal levels are spatially summed and generate a signal

$$X[N_3(t)] = C N_3(t), \quad (10)$$

where C is a constant. This signal affects, by divisional inhibition, the output from layer 2. Therefore, we have

$$\Omega = \frac{\Phi \Psi}{1 + X}. \quad (11)$$

We assume that the pulse frequency, f , of the ganglion cell is proportional to Ω . Thus,

$$f = f_0 \Omega = f_0 (\Phi \Psi / 1 + X), \quad (12)$$

where f_0 is a constant.

(XIX. NEUROPHYSIOLOGY)

The value of constant C in Eq. 10 can be chosen to achieve a cell output for bright objects suitably less than that for dark objects.

3. Discussion

The performance of the model can be derived from Eq. 12. For purposes of illustration, we shall assume that Φ and Ψ are given by Eqs. 8 and 9, respectively. Constant C is fixed by the arbitrary condition that the maximum response for a bright disc

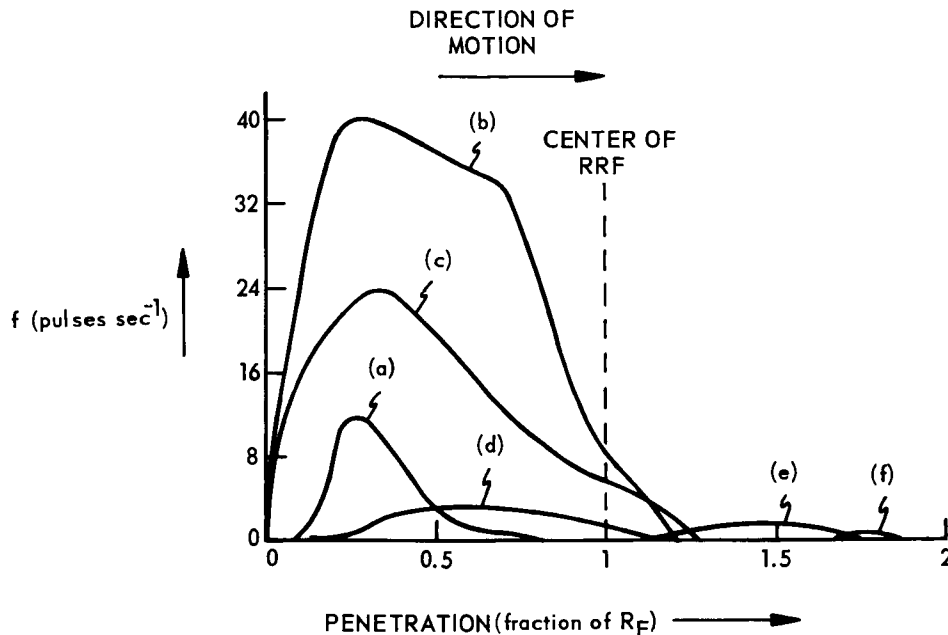


Fig. XIX-5. Output of the model versus penetration of different objects into the RRF.

RRF/8 wide is $1/10$ of that which would have resulted without the inhibition produced by X . This condition gives $C = 60 R_F^{-2}$. The maximum pulse frequency⁸ is approximately $40 \text{ pulses} \cdot \text{sec}^{-1}$, which fixes $K = K' = 1$ and $f_0 = 300/R_F^2 \text{ sec}$. The pulse frequency of the ganglion-cell model is plotted against the penetration of the leading edge of the object crossing the RRF in Fig. XIX-5. Curves (a), (b), and (c) are for dark discs of radii $0.125 R_F$, $0.5 R_F$, and $0.75 R_F$, respectively. Curves (d), (e), and (f) are for bright discs of radii $0.125 R_F$, $0.5 R_F$, and $0.75 R_F$, respectively.

Following are some of the consequences that may be derived from the characteristics of the model.

a. No response occurs to a general change in illumination. (In agreement with Lettvin, Maturana, and co-workers.^{1, 2, 10})

b. A corner may produce a response. (In agreement with Maturana.²)

c. Several small object images moving simultaneously in the RRF may produce either very small or null responses. This is in accord with Lettvin's observation.^{1, 2}

d. No evidence of the annulus surrounding the RRF can be detected by fixed dark or light spots with a simultaneous moving testing spot. This is in agreement with Grusser-Cornehls and co-workers.⁸

e. If the spots in the surrounding ring move, however, the response to the testing spot may be either increased or decreased, the amount depending on the size of the spots. This is in agreement with Grusser and co-workers.⁹

The Group 2 ganglion cells respond for approximately one second after an object has entered and stops in the RRF. This response is erased by a corresponding step to darkness.^{1, 2, 10} In the model, however, the response disappears when the object is stopped within the RRF. The persistence of the response might be explained by feedback from the tectum, as suggested by Lettvin.¹⁰ If we assume that tectal feedback acts on the Type I of the bipolar cells, and that the feedback has the same effect as that of dimming, the ganglion cell will provide an output as long as feedback exists. This can be formulated in the following manner. Boolean magnitudes $C(t)$, $D(t)$, $F(t)$, and $B_I(t)$ are defined as follows:

$C(t)$ is 1 if contrast exists, at time t , in the field of a Type I bipolar cell
0 if there is no contrast

$D(t)$ is 1 if dimming occurs, at time t , in the field of a Type I bipolar cell
0 if there is no dimming

$F(t)$ is 1 if there is feedback from tectum, at time t , on a Type I bipolar cell
0 if there is no feedback

$B_I(t)$ is 1 if the Type I bipolar cell fires at time t .
0 if it does not fire.

The condition for Type I bipolar cell firing is then the Boolean expression

$$B_I(t) = C(t) \cdot [D(t) + F(t)]. \quad (14)$$

Feedback from the tectum must be maintained for approximately 1 sec after local dimming has disappeared. This feedback might be provided by the newness cells of the tectum.¹⁰

R. Moreno-Diaz

References

1. J. Y. Lettvin, H. R. Maturana, W. S. McCulloch, and W. H. Pitts, "What the Frog's Eye Tells the Frog's Brain," Proc. IRE 47, 1940-1951 (1959).

(XIX. NEUROPHYSIOLOGY)

2. H. R. Maturana, J. Y. Lettvin, W. S. McCulloch, and W. H. Pitts, "Anatomy and Physiology of Vision in the Frog (Rana pipiens)," *J. Gen. Physiol.* **43**, 129-175 (July 1960).
3. M. B. Herscher and T. P. Kelley, "Functional Electronic Model of the Frog's Retina," Bionics Symposium, Wright-Patterson Air Force Base, Ohio, March 1963.
4. L. L. Sutro (ed.), "1964 to September 1965 Advanced Sensor and Control Systems Studies," R-519, Instrumentation Laboratory, Massachusetts Institute of Technology, Cambridge, Massachusetts, January 1966.
5. L. L. Sutro, D. B. Moulton, R. E. Warren, C. L. Whitman, and F. F. Zelse, "1963 Advanced Sensor Investigations," R-470, Instrumentation Laboratory, Massachusetts Institute of Technology, Cambridge, Massachusetts, September 1964.
6. J. J. Shypperheyn, "Contrast Detection in Frog's Retina," *Acta Physiol. Pharmacol. Neerl.* **13**, 231-277 (1965).
7. R. M. Gaze and M. Jacobson, "Convexity Detectors in the Frog's Visual System," *Proc. Physiological Society, Edinburgh Meeting*, July 1963.
8. U. Grusser-Cornehls, O. J. Grusser, and T. H. Bullock, "Unit Responses in the Frog's Tectum to Moving and Nonmoving Visual Stimuli," *Science* **141**, 820-822 (August 1963).
9. O. J. Grusser, U. Grusser-Cornehls, and T. H. Bullock, "Functional Organization of Receptive Fields of Movement Detecting Neurons in the Frog's Retina," *Pflugers Arch. ges. Physiol.*, **279** Bd., 1 ht, s. 88-93, 1964.
10. J. Y. Lettvin, H. R. Maturana, W. H. Pitts, and W. S. McCulloch, "Two Remarks on the Visual System of the Frog," in *Sensory Communication*, W. A. Rosenblith (ed.) (The M.I.T. Press, Cambridge, Mass., and John Wiley and Sons, Inc., New York and London, 1961), pp. 757-776.
11. R. Moreno-Diaz, "An Analytical Model of the Bug Detector Ganglion Cell in the Frog's Retina," E-1858, Instrumentation Laboratory, Massachusetts Institute of Technology, Cambridge, Massachusetts, November 1965.
12. J. Y. Lettvin, "Form-Function Relations in Neurons," Quarterly Progress Report No. 66, Research Laboratory of Electronics, M.I.T., July 15, 1962, pp. 333-335.
13. "Divisional Inhibition," proposed by Lettvin in Quarterly Progress Report No. 66 (pages 333-335), can be formulated as follows: Let E and I be the excitory and inhibitory signals, respectively, expressed as dimensionless numbers. After inhibition, the resulting signal is $E/(1+I)$; if $I \gg 1$, $E/(1+I) \simeq E/I$.

B. EXPERIMENT DEALING WITH THE DEVELOPMENT OF LOGICAL AND ABSTRACT THOUGHT IN YOUNG CHILDREN

1. A Concept Formation Experiment

The purpose of this research was to study the development of logical and abstract thought in young children. To determine the thought processes used by the child in the solution of such problems.

2. Method

Our method was a modified version of Dr. Jean Piaget's techniques. The child was placed in a typical experimental testing situation. He was presented with familiar

objects such as rubber animals, and questioned as to color, form, size, and number. The child was then led, by the use of clinical techniques, explain and defend his solution. I wanted to know: Did the child understand the question; Was he answering the whole question or only a part of it; Was he answering the question asked or something he thought was being asked; Was he just verbalizing or did he have some degree of insight? Correct and incorrect responses were analyzed.

3. The Subjects

Fifty-one children were tested on three separate occasions. The sample consisted of 36 "average" children from the Newton Public Schools and 15 children from the M.I.T. Day Camp. The age range was from 5 to 11 years. Grades: 1, 2, 3, 5, 6.

4. Results

The thought processes involved were clearly demonstrated in the test asking, "Are there more lions or more animals on the table in front of you?" Seventy-three per cent of our children said that "There were more lions than animals." Only 27% realized that lions were animals as well as being lions. The percentages of lion choice and of animal choice are listed below according to grade.

<u>Grade</u>	<u>Lion</u>	<u>Animal</u>
I	87%	17%
II	57%	43%
III	100%	0%
IV	63%	27%
VI	57%	43%

The children tended to separate lions and animals into distinct groups. There was a juxtapositioning of the two groups. The lions were seen as group A, while the animals were thought to belong to group B. Lions were seen as a different kind of an animal. When answering "Lions" the child felt that his answer was perfectly logical and correct. The child was actually answering only one part of the question, or had changed the meaning of the question into one which he could understand and answer. This appears to follow Piaget's schemata of classification – the application of familiar schemata to a new situation and of application of one different solution at one time.

The children in grades 5 and 6 could realize that a lion was an animal when they were asked. The children in the lower grades remained firm in their conviction that a lion could not be an animal. The younger children, also could not

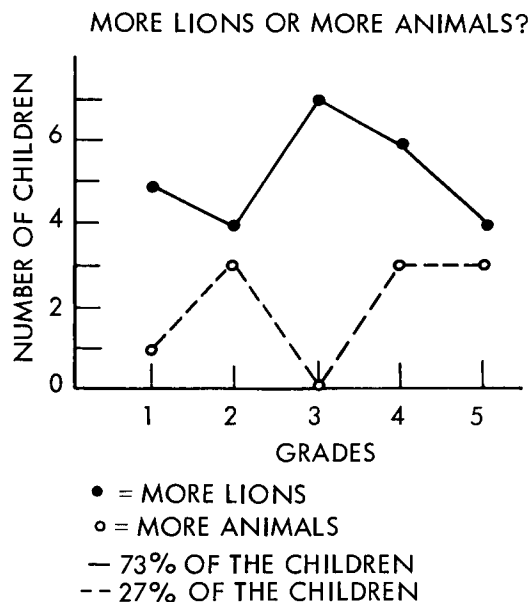


Fig. XIX-6. Results from 36 Newton (Massachusetts) school children.

accept mixed sizes of the same animal as belonging to one group. Color presented no problem.

Figure XIX-6 indicates no real pattern of development of logical thought at a pre-adolescent age. The child just has it or he does not. The children tend to parrot "proper" answers long before they truly understand what they are talking about.

Sylvia G. Rabin

C. STEREOMICROSCOPY WITH ONE OBJECTIVE

It can be very difficult to make out spatial relations in thick histological sections. The obvious answer is to use a stereomicroscope, but most commercial stereomicroscopes do not give useful magnification above approximately 50X, and provide only rudimentary staging and lighting facilities.

Faced with such a problem, we re-invented an old method for obtaining stereo images from a single objective. Our solution takes the form of a simple and inexpensive modification which can be made to most microscopes equipped with a binocular body. It gives a true stereo image, and does not interfere with normal use of the microscope.

Because of the wide aperture of microscope objectives, the left- and right-hand parts of the objective "look at" the subject from significantly different angles. Therefore, if the rays from each half of the objective are sent to the corresponding eye, a stereo image

results. (Actually, because the image is inverted the rays from the left half of the objective should go to the right eye, and vice versa, if an orthoscopic image is desired.)

We use Polaroids to sort out the rays from the two halves of the objective. At the objective, we place a disc made from two pieces of Polaroid filter cemented together; one half of the disc is polarized "vertically" (i. e., in the observer's plane of symmetry) and the other half "horizontally." Corresponding Polaroid filters in the oculars sort out the rays.

The split filter can be obtained from the Polaroid Corporation (split field disc $0^\circ - 90^\circ$). This split filter is placed just below the diaphragm at the top of the objective. This placement works well with objectives up to 40X. With oil immersion objectives, however, there is a vignetting effect – each eye sees only half the field illuminated – and the method is not usable.

The image quality is acceptable for most purposes; there is, however, a noticeable loss of resolution at high powers. Some of the loss may be due to the loss in numerical aperture (N. A.), since each eye sees an image made with only half of the objective. We suspect that some of it is a psychological result of the fact that the "circles" of confusion are no longer round, and are differently shaped for each eye. If viewed through oculars without Polaroids, a nonstereo view is obtained. In this view, there is still some loss of resolution, perhaps owing to the extra optical path length introduced by the filter at a critical point in the system. There is also some loss of contrast, because of scattering at the cemented filter junction, and diffusion in the Polaroid material itself.

Needless to say, the filter at the objective should be of good quality. It also helps to begin with a good image, by using objectives of large N. A. and avoiding high-power eyepieces. The quality of the eyepiece filters is comparatively unimportant.

The axes of the halves of the split filter should be as described – parallel to and normal to the observer's plane of symmetry. It is not sufficient for them merely to be perpendicular to each other, or there will be loss of polarization in the prisms of the binocular body. When they are as described, there is no serious loss of polarization in any style of microscope that we have tried.

One last note is in order. At low powers, say, below 200X, it is possible to obtain a stereo view without any extra equipment at all! All that is necessary is to adjust the oculars so that they are slightly closer together than the observer's interpupillary distance. When this is done, the pupils of the observer's eye each mask off a part of the exit pupil of each ocular. Since the exit pupils are optical images of the objective, this has the same effect as masking the objective itself. This is a trick worth knowing, although it only works at low powers and produces eyestrain if used for prolonged periods.

The use of Polaroids for splitting the objective may be novel; but the fundamental idea is far from new^{1, 2, 4-9} and pupillary masking is mentioned by Ives.³ For some reason,

binocular microscopes on this principle have almost completely disappeared from the scene. Perhaps it is time for a revival.

D. P. Smith

References

1. C. D. Ahrens, "On a New Form of Binocular Eyepiece and Microscope for High Powers," *Monthly Microscopical Journal* 5, 113 (1871).
2. S. Holmes, "The New Binocular Microscope," *Monthly Microscopical Journal* 3, 273 (1870).
3. F. C. Ives, "A New Binocular Microscope," *J. Franklin Inst.* 154, 441 (1902).
4. M. Nachet, "On Some Modifications of the Binocular Microscope," *Monthly Microscopical Journal* 1, 31 (1869).
5. J. L. Riddell, "Notice of a Binocular Microscope," *Am. J. Sci.* 15, 25 (1953).
6. "Professor Riddell's Binocular Microscope," *Quart. J. Microscopical Science* 1, 304 (1853).
7. J. W. Stephenson, "On an Erecting Binocular Microscope," *Monthly Microscopical Journal* 4, 61 (1870).
8. E. H. Wenham, "On the Application of Binocular Vision to the Microscope," *Trans. Microscopical Society of London (New Series)* 2, 1 (1854).
9. C. Wheatstone, "On the Binocular Microscope, and on Stereoscopic Pictures of Microscopic Objects," *Trans. Microscopical Society of London (New series)* 1, 99, (1853).

D. SPECIAL FUNCTION THEORY

Properties of the polylogarithm function $\text{Li}_\nu(z) = \sum_{n=1}^{\infty} z^n/n^\nu$ have been examined for complex order and argument. The results of this investigation have been submitted for publication to *Annali di Matematica*. The chief findings are summarized below.

Section 1 dealt with defining relations and integral representations. The principal new result was

$$\frac{d^p \text{Li}_\nu(z)}{dz^p} = \frac{1}{z^p} \sum_{m=1}^p S_p^{(m)} \text{Li}_{\nu-m}(z),$$

where the $S_p^{(m)}$ are Stirling numbers of the first kind.

Section 2 presented a generalized proof of the well-known factorization theorem and a derivation of the new expansion

$$\text{Li}_\nu(z^\lambda) = \sum_{m=0}^{\infty} \frac{(\lambda - \lambda_0)^m}{m!} \ln^m z \text{Li}_{\nu-m}(z^{\lambda_0}).$$

Section 3 discussed various expansions in z , the most novel of which was

$$\text{Li}_\nu(z) \sim -\frac{\gamma^\nu}{\Gamma(\nu+1)} - \frac{\gamma^{\nu-1}}{\Gamma(\nu)} \sum_{m=0}^M (1-\nu)_m \gamma^{-m} \cdot \left[\text{Li}_{m+1}(e^{-i\theta}) + (-1)^{m+1} \text{Li}_{m+1}(e^{i\theta}) \right],$$

where $0 < \theta = \arg z < 2\pi$, $\ln |z| = \gamma \gg 1$, and $\text{RE } \nu > 0$.

Section 4 discussed various expansions in ν , the most novel of which was

$$\text{Li}_\nu(z) = \sum_{n=1}^N \frac{z^n}{n^\nu} + \mathcal{O} \left\{ \frac{|z|^{N+1}}{N^{\nu'}} \frac{\Gamma(\nu')}{|\Gamma(\nu)|} \right\},$$

where $\nu' = \text{RE } \nu > 0$ and $0 < \arg z < 2\pi$.

In Section 5 were placed results on the expansion of functions in terms of polylogarithms; the most novel of these was

$$\text{Li}_\nu(z) = z + z \sum_{p=0}^{\infty} a_p(\nu) \text{Li}_{\nu+p}(z),$$

where $\text{RE } \nu < 0$ and

$$a_p(\nu) = \frac{\Gamma(1-\nu)}{\Gamma(1-\nu-p) \Gamma(1+p)}.$$

Section 6 concluded the paper and contained a brief discussion of unsolved problems relating to the polylogarithm.

W. F. Pickard

E. RECEPTOR POTENTIALS IN RETINULAR CELLS IN LIMULUS

The photoreceptor unit of the compound lateral eye of the horseshoe crab, *Limulus polyphemus*, is the ommatidium. Each ommatidium has two kinds of cells involved in the transduction and transmission of photic information to brain: the reticular cells, numbering 8 to 20, which are the photoreceptor cells, and the (usually) single eccentric cell, which is the first-order neuron in the visual pathway. Light incident on the ommatidium is absorbed by the visual pigment rhodopsin.¹ By some still unknown means this leads to a depolarization of the reticular cells. This depolarization is transmitted to the eccentric cell via an electrotonic synapse.² When the eccentric cell is depolarized to a threshold value, all-or-none action potentials are generated, which propagate along its axon to the optic lobe of the brain.^{3,4} Also, some integration of the photic information occurs via lateral inhibition in the plexus just central to the ommatidia.⁴

Thus, while a good deal is known about the means by which photically evoked electrical signals, once produced, are transmitted from cell to cell and conducted to the brain, little is known of the mechanisms by which the absorption of light by rhodopsin leads to a potential change (the receptor potential) across the reticular cell membrane. The nature of this energy transduction from light to electricity remains an important unknown in visual physiology.

In order to gain some insight into the nature of the coupling between the visual pigment and the photoreceptor membrane, the light-evoked potential changes in reticular cells have been investigated with intracellularly placed double-barrel microelectrodes. With such an arrangement, extrinsic current may be passed through the cell membrane via one barrel and the membrane potential measured with the other. The changes in

membrane potential produced by light and by the interactions of light and injected current may also be observed.

The dark-adapted reticular cell has resting membrane potential of 40-50 millivolts, the inside of the cell negative with respect to an extracellularly placed reference electrode. The receptor potential evoked by a long pulse of light is a complicated waveform which may be divided into four components (Fig. XIX-7). Several milliseconds after the onset of the light pulse, the response begins with a depolarizing transient (T in Figs. XIX-7 and XIX-8).

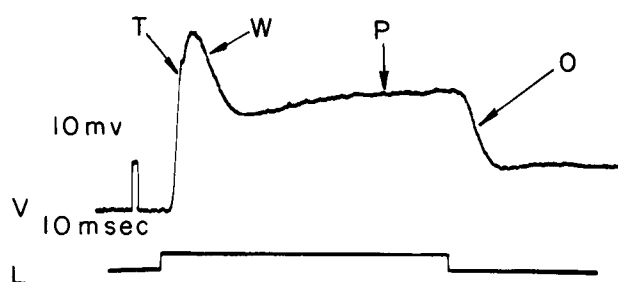


Fig. XIX-7

Receptor potential (upper trace) evoked by long pulse of light (lower trace) of moderate intensity. Pulse on voltage trace is 10 mv and 10 msec. T, W, P and O indicate transient, wave, plateau, and "off" responses, respectively.

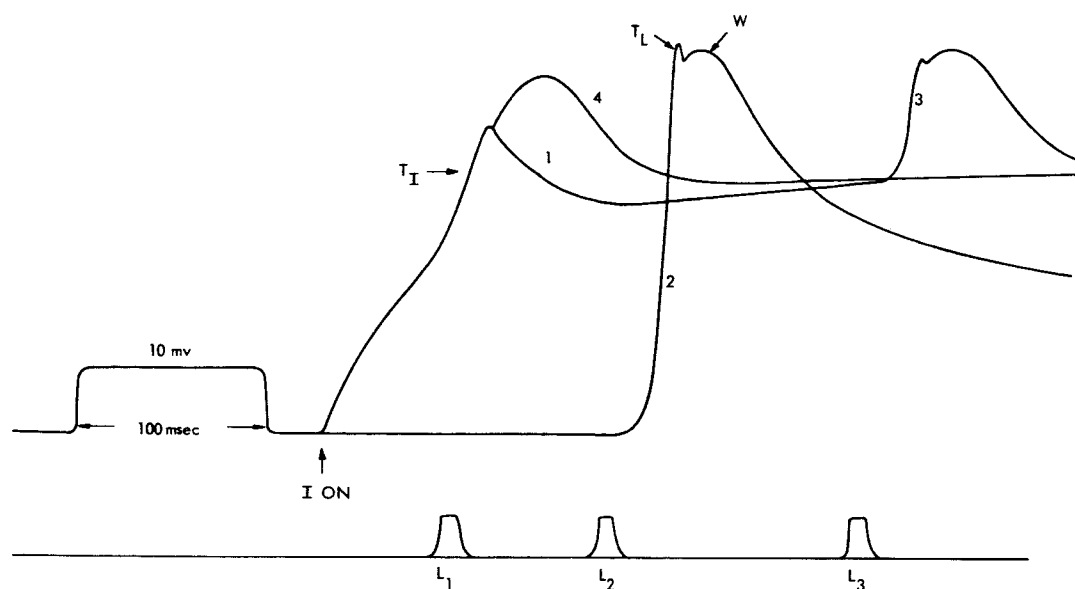


Fig. XIX-8. Occlusion of current and light-evoked transients. Superimposed line drawings from separate single traces. Upper trace is voltage-time recording with intracellular microelectrode from a reticular cell. Lower trace indicates short light pulses. Voltage-time calibration is 10 mv, 100 msec. Trace 1 is response of cell to a step of polarizing current beginning at I ON. Current-evoked transient is T_I . Trace 2 shows transient (T_L) and wave (W) evoked by a short pulse of light (L_2). Trace 3 is interaction of the same light pulse (applied during L_3) and the same current step with a long delay between their onsets. Trace 4 is the same as Trace 3 with a short delay between onset of current and light. Note in 4 the occlusion of T_L .

This is followed by a slow wave, (W), of depolarization. Subsequently, the potential repolarizes to a plateau, P, whose steady-state level, however, is more depolarized than the membrane potential in the dark. Following cessation of the light, the potential returns to its resting level in one of two ways. After long or intense lights, the membrane potential first repolarizes to a potential level greater (more hyperpolarized) than its resting value and then decays to that value. After short or dim lights, the potential shows no hyperpolarizing undershoot, but returns to its resting level (O in Fig. XIX-7). These various components will be examined seriatim.

Extrinsic depolarizing current applied through the microelectrode evokes a transient which has a threshold, T_I (see Fig. XIX-8). Interaction of this current-evoked transient with that generated by light shows that they occlude (see Fig. XIX-8). These data suggest that both transients arise via the same mechanism and are an inherent property of the reticular cell membrane. The transient appears to be regenerative but not propagated. It is not, however, a true all-or-none action potential or spike for several reasons: (i) its peak amplitude is inconstant and varies with the degree of depolarization;

(ii) its duration is an inverse function of its amplitude; (iii) it has a variable refractory period; and (iv) its threshold is a function of the membrane potential (i. e., the greater the resting membrane potential, the larger the membrane potential level of the apparent threshold).

Short light pulses evoke only the transient and wave components (Figs. XIX-7 and XIX-8). Increasing (hyperpolarizing) the membrane potential with current via the micro-electrode increases the amplitude of both components (Figs. XIX-9 and XIX-10). Conversely, depolarization decreases both and when the membrane potential is reversed (i. e., the inside made positive) the wave reverses its polarity (i. e., becomes negative-going) (D_1 and D_2 , Fig. XIX-9). Since at small values of membrane potential the transient often becomes obscure, its reversal potential is not easy to specify with certainty. It appears (Fig. XIX-9, D_1 and D_2), however, to be at some positive potential value. Time-varying impedance measurements indicate that the wave is associated with a large increase in conductance. Thus the wave appears to be a consequence of a virtual short-circuiting of the membrane impedance.

If, during the plateau phase of the response, a short pulse of current is injected, the steady-state potential evoked is a measure of the slope resistance of the membrane. If, in the dark, the membrane is depolarized with extrinsic current to the same absolute membrane potential reached during the light-evoked plateau and if the same short current pulse is then injected, the identical steady-state potential is recorded. This indicates that a steady-state potential level, whether generated by light or current, is associated with the same membrane conductance and suggests that the plateau response is produced via a light-activated constant-current source.

The plateau response can also be studied by examining the current-voltage characteristics of the reticular cell membrane in the dark and under the condition of continuous illumination (Fig. XIX-10). In the dark (curve D), the membrane shows double rectification. Near resting potential, the resistance is greater to hyperpolarizing than to depolarizing currents. When, however, the membrane potential is reversed (inside positive) the resistance again increases with further depolarization. With intense, continuous light (curve L_2), the increased resistance with hyperpolarization persists, but requires more current to demonstrate. The increased resistance to large depolarizing currents, however, is no longer demonstrable. If from the I-V curve obtained in the light, the $\log \frac{I - I_{s1}}{I_{s1}}$ is plotted against V (where I_{s1} is the saturation current obtained from the "dark" I-V curves and is defined as the asymptotic current measured from resting potential required to produce a graphically projected infinite voltage), a straight line results. If the I-V curve obtained in the light is subtracted from the I-V curve obtained in the dark and, from the resultant curve, the $\log \frac{I - I_{s2}}{I_{s2}}$ versus V is plotted

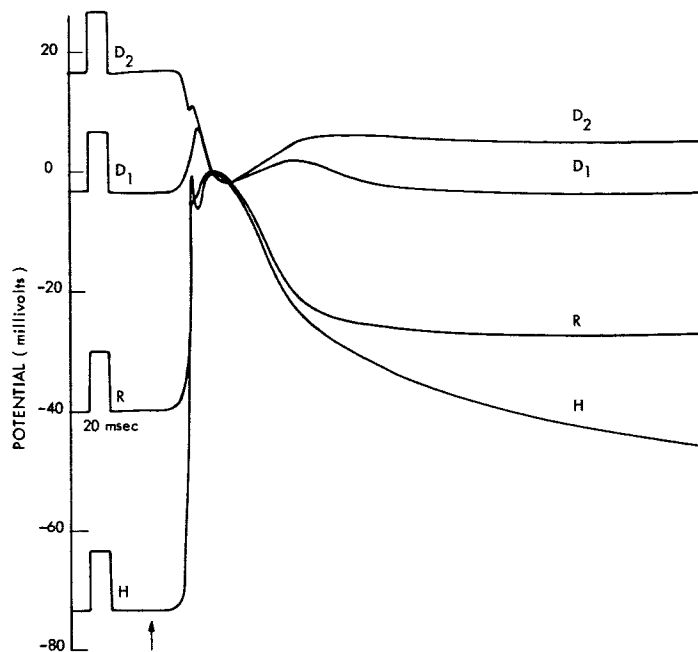


Fig. XIX-9. Effects of changing membrane potential on light-evoked transient and wave. Superimposed line drawings from separate single traces. Calibration is 10 mv and 20 msec. Onset of short light pulse indicated by arrow under Trace H. Potential in millivolts with respect to extracellular reference electrode. Trace R is response to light pulse in the absence of extrinsic current. Trace H is response to identical light pulse after the membrane potential was hyperpolarized with extrinsic current. Traces D_1 and D_2 show response after membrane potential was depolarized to successively higher levels. Note that the peak of the wave reverses near $V = 0$ while the transient reverses at a positive potential.

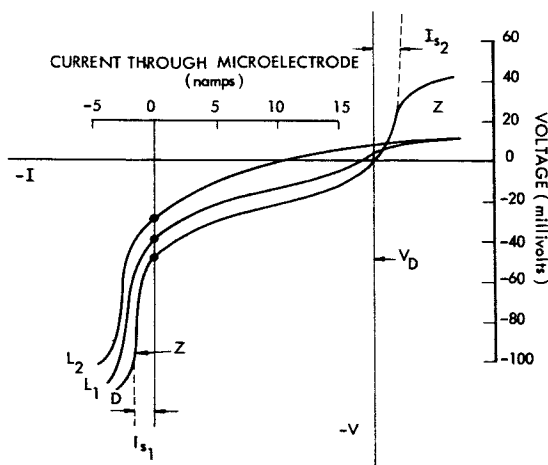


Fig. XIX-10.

Current-voltage characteristics measured with double-barrel microelectrode in reticular cell. Current in namps passed through microelectrode; voltage in millivolts with respect to extracellular reference electrode. V_D is resting potential in the dark. Three curves show characteristic in the dark (D) and at moderate (L_1) and high (L_2) light intensities. Vertical line through closed circles on each curve joins steady-state membrane potentials. I_{s1} and I_{s2} are reversed saturation currents for diodes D_1 and D_2 of Fig. XIX-11.

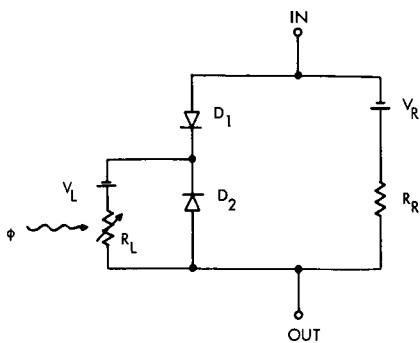


Fig. XIX-11.

Equivalent electrical circuit for reticular cell membrane under steady-state conditions. IN is intracellular; OUT is extracellular. D_1 and D_2 are semiconductor-like diodes. V_R is resting membrane voltage. R_R is a resistance whose value is high with respect to the reverse resistance of diodes D_1 and D_2 . R_L is the resistance whose value is greater than the reverse resistance of D_2 in the dark and is reduced by light (ϕ). V_L is a battery whose current output is increased by light.

Also, detectable current is now drawn from V_L , a battery in series with R_L and in parallel with D_2 . Furthermore, it would appear that the other diode (D_1 , revealed by the increased resistance with hyperpolarization) is not altered by light. This is further suggested by the observation that translation of the "light" I-V curve onto the "dark" I-V curve reveals virtual superposition of the two curves over the range -15 to -100 mv ("dark" values).

If these observations are substantially correct, three conclusions may be allowed. First, the mechanism of the apparent constant-current source is a short-circuiting of one diode (D_2) and the attendant activation of a previously occult battery. The potential changes which result are a consequence of the currents so generated flowing across the other, unaltered diode (D_1). Second, the over-all slope conductance of the membrane changes, but this is mainly due to forward-biasing the passive diode (D_1), which is the major determinant of slope resistance in the physiological range of steady-state membrane potentials, and not to a short-circuiting of the entire membrane, as in the wave response.

The third conclusion is that the Weber-Fechner relationship may be a consequence of the membrane characteristics of the photoreceptor cell. Previous experiments have

(with the appropriate adjustments in sign of I and V), another straight line is obtained. (Here, I_{s2} is also obtained from the "dark" curve and is defined as the asymptotic current, measured from $V = 0$, required to produce a graphically projected infinite voltage.) These results suggest that the equivalent circuit for the resting reticular cell membrane is two semiconductorlike diodes placed back to back (Fig. XIX-11). At resting potential one diode (D_2) (revealed only by membrane potential reversal in the dark) is partially forward-biased. Moreover, these results suggest that the action of intense light is to short-circuit completely this diode D_2 , and that there is a marked increase in conductance of a resistor (R_L) in parallel with D_2 . (The conductance of R_L in the dark is much less than D_2 ; however, its value in intense lights is much greater than D_2 .)

shown (i) that the steady-state firing frequency of eccentric cells is a logarithmic function of light intensity³; (ii) the firing frequency of eccentric cells is a linear function of their membrane potential³; (iii) steady-state membrane potential changes in eccentric and reticular cells are a logarithmic function of light intensity⁵; and (iv) "physiological-range" depolarizations of reticular cells by extrinsic current are linearly transmitted to eccentric cells.⁶ We have shown here that light and current can evoke indistinguishable steady-state changes in reticular cells and thus, presumably, light generates a current linearly related to its intensity. This presumption is supported by the previous conclusions and observations, viz., given a logarithmic I-V curve and a logarithmic relationship between light intensity and membrane potential change, light intensity and current must be linearly related over the ranges studied.

Two ancillary observations of the above studies are worthy of note. First, the I-V curves show a hysteresis effect, i. e., the removal of extrinsic current produces an increased conductance of the reticular cell membrane which may last hundreds of milliseconds and is associated with depolarizing oscillations, often of sufficient magnitude to fire the eccentric cell.² The second is that large hyperpolarizing and depolarizing currents produce reversible "punch-through" or "breakdown" effects in the two diodes in a manner similar to actual semiconductor diodes (the Z's, in Fig. XIX-10).

The "off" response, produced by the removal of light, has been little studied, even in the experiments reported here. By analyzing the time-varying impedance changes, however, we have found that this phase of the response is associated with an impedance greater than the resting, "dark" impedance. This is the case even in those responses that do not show a hyperpolarizing undershoot.

These various experiments define in an operational way the mechanisms by which light evokes potential changes in Limulus photoreceptors. As in most cells, the recorded potentials are a consequence of a complex electrochemical system involving a membrane and both intracellular and extracellular spaces composed of ionic solutions. It might be expected, therefore, that one might produce alterations, perhaps specific, by manipulation of the ionic composition of the extracellular medium.

Previous experiments have shown that, again as in most cells, the resting potential is essentially a function of the ratio of the concentration of potassium between the inside and outside of the membrane in a manner predicted by the Nernst equation.⁶ We have found that alteration of the extracellular concentration of chloride (replacement with sulfate) produces little or no effect on any measured characteristics of reticular cells. Replacement of extracellular sodium with TrisH^+ (keeping osmolarity and pH constant), however, completely and reversibly abolishes the responsiveness of reticular cells to light without altering the I-V curves for values near resting potential. Such cells cease to act as photoreceptors. Thus, as far as the receptor potential is concerned, the action of light on photoreceptors appears to be involved with the mechanisms by which the

permeability of the membrane to sodium ions is regulated.

In summary, we have defined the area of interest to be the means by which the chemical alterations in rhodopsin produced by its absorption of light energy are transduced or coupled to the receptor cell membrane. In pursuing this question we have analyzed the mechanisms by which the resultant potential changes are produced. The initial, transient portion of the response appears to be an inherent property of the membrane to any depolarization of sufficient magnitude. The wave seems to involve a virtual but brief short-circuiting of the membrane impedance. The plateau or steady-state response to light appears to involve constant-current type of generator and we have suggested the way in which this unusual and unexpected mechanism operates, viz., the short-circuiting of a diode and the activation of a battery. We have mentioned, in passing, how the receptor membrane characteristic might account for the Weber-Fechner relationship in Limulus photoreceptors. Moreover, we have suggested that the "off" response is an active process involving an increase in over-all membrane impedance. Finally, we have indicated that the alterations in membrane potential by light appear to involve the means by which the absorption of photic energy by rhodopsin leads to an increase in the permeability of the photoreceptor membrane to sodium ions.

A good deal of the credit for any experimental successes and valid interpretations reported here must go to Dr. Fritz Bauman, Institut de Physiologie, École de Médecine, Geneva, Switzerland, and Dr. M. G. F. Fuortes, Ophthalmology Branch, NINDB, NIH, Bethesda, Maryland, who collaborated in various phases of these researches. The author alone, however, assumes responsibility for the present report.

T. G. Smith, Jr.

References

1. R. Hubbard and G. Wald, "Visual Pigment of the Horseshoe Crab, Limulus Polyphemus," Nature **186**, 212-215 (1960).
2. T. G. Smith, F. Bauman, and M. G. F. Fuortes, "Electrical Connections between Visual Cells in the Ommatidium of Limulus," Science **147**, 1446-1448 (1965).
3. M. G. F. Fuortes, "Electrical Activity of the Cells in the Eye of Limulus," Am. J. Ophthalmol. **46**, 210-213 (1958).
4. H. K. Hartline et al., "Inhibitory Interaction in the Retina and Its Significance in Vision," in Nervous Inhibition (E. Florez, ed.) (Pergamon Press, London, 1961), pp. 241-284.
5. M. G. F. Fuortes and G. F. Poggio, "Transient Responses to Sudden Illumination in Cells of the Eye of Limulus," J. Gen. Physiol. **46**, 435-452 (1963).
6. S. Yeandle, "Studies on the Slow Potential and the Effects of Cations on the Electrical Responses of the Limulus Ommatidium," Doctoral Dissertation, Johns Hopkins University, 1957.

F. DIRECT PHOTOELECTRIC EFFECT IN PHOTORECEPTOR CELL MEMBRANES

When an eye is illuminated, the energy in the incident photons is absorbed by a visual pigment (e.g., rhodopsin), which is a constituent of the photoreceptor cells (rods, cones, reticular cells). This process then leads to a change in the membrane potential of the photoreceptor cell, the so-called receptor potential. In the lateral eye of the horseshoe crab, Limulus polyphemus, this potential change appears to be primarily a consequence of an increase in the permeability of the reticular cell membrane to sodium ions (see Sec. XVIII-E).

When the eye is stimulated with a pulse of light of moderate intensity there is a latency of several milliseconds between the onset of the light and the beginning of the receptor potential. This delay may indicate that there are one or more steps intervening between the absorption of light by the visual pigment and the onset of the receptor potential. Considerable interest has been generated, therefore, by the recent discovery of the so-called early receptor potential (ERP).^{1,2} The ERP, which has been observed only with extracellular recordings in vertebrate eyes, has the following characteristics: (i) its latency of onset is of a few microseconds; (ii) it persists when the cells of the eye are depolarized with potassium ions; (iii) it persists at temperatures as low as -35°C ; (iv) it has, in the albino rat, the action spectrum of rhodopsin; and (v) its amplitude is linearly related to the number of rhodopsin molecules bleached.¹⁻³ For these reasons, the ERP has been interpreted as a direct manifestation of the absorption of light by the visual pigment and perhaps represents a change in the dipole configuration of the pigment molecule.

Efforts to record an ERP in invertebrate eyes have previously been unsuccessful. In an attempt to elicit the response in the lateral eye of the horseshoe crab, a 100-watt mercury-arc lamp and an optical system were employed which would focus several milliwatts of radiant power per square centimeter onto a spot 100 μ in diameter (the diameter of one ommatidium). With a shutter arrangement, light pulses as short as 3 msec could be produced. With such intense lights, considerable care must be taken to shield those components of the recording system (e.g., Ag-AgCl wires) which might generate photoelectric effects. Since the tip of the KCl-filled micropipette, however, must be in the light beam when located inside a reticular cell, it was necessary to investigate the effects of intense lights on microelectrode tips. Lights of the intensity employed during the biological experiments produce a photoconductive effect in KCl microelectrodes. In our recording system (peak-to-peak noise 50 μV , input impedance 10^{12} ohms, grid current less than 10^{-12} amp) this increased conductance is detectable only with currents greater than 10^{-10} amp flowing through the microelectrode. Thus KCl microelectrodes show no detectable photovoltaic effect. Moreover, no effects could be produced by filling the microelectrode with KCl saturated with methylene blue or after plugging the tips of

the microelectrode with tissue fragments from the crab's eye. Thus all observations reported here were recorded in a system with the appropriate light shielding and with grid current of the order of 10^{-12} amp.

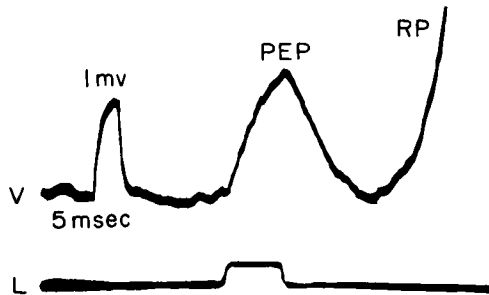


Fig. XIX-12.

Photoelectric potential (PEP) from retinular cell. Upper trace is voltage-time recording via intracellular microelectrode. RP is receptor potential. Calibration pulse is 1 mV and 5 msec. Lower trace shows the application of a brief, intense pulse of light.

When a short pulse of our most intense light stimulates a retinular cell whose trans-membrane potential is recorded with an intracellular microelectrode, a depolarizing potential of 0.5-1.2 mV amplitude is evoked (Fig. XIX-12). The latency of the potential is less than a millisecond and the potential lasts for the duration of the light pulse. Since the mechanism underlying this response has yet to be completely elucidated, we shall call it a photoelectric potential (PEP) rather than an ERP, whereby a specific mechanism is implied.

When a micropipette is extracellularly located, but pressed against the retinular cell membrane, the polarity of the PEP and the receptor potential are both reversed in sign (i. e., now negative-going). Withdrawal of the pipette, only a few microns results in simultaneous loss of both the PEP and the receptor potential. This suggests that both arise from the retinular cell. Like the ERP, the PEP persists when the cell is depolarized with extracellular potassium ions and when the tissue is frozen (to -10°C , the temperature below which recording from a KCl pipette is no longer practicable). Moreover, the amplitude of the PEP is linearly related to light intensity. The PEP shows, however, little evidence of light adaptation. If repetitive light pulses are delivered to a dark-adapted eye, the second and subsequent PEP's are only slightly smaller than the first. This observation does not so readily distinguish the PEP from the ERP as it might first appear. In the first place, the ERP does not completely light-adapt in vertebrate eyes, where the visual pigment is bleached.⁴ This unadaptable ERP is presumably due to light-regenerated rhodopsin. Second, most invertebrate rhodopsins do not bleach at physiological temperatures and are readily regenerated by light.⁵

When two separate single-barrel microelectrodes are placed within the same retinular cell, current may be passed through one electrode across the cell membrane and the resultant potential changes observed with the other. The effects of changing membrane potential on the PEP can then be studied without having a photoconductive effect

in the recording electrode. Hyperpolarization of the reticular cell membrane increases the amplitude of the PEP. Conversely, depolarization decreases its amplitude. Moreover, when the membrane potential is forced to values more positive than a level somewhere near zero membrane potential, the polarity of the PEP is reversed. These observations suggest that the PEP arises from some structure electrically in series with the recording system between the inside and outside of the cell. Presumably this is the membrane itself. An alternative mechanism would appear to be excluded, viz. the injection of a positive charge into the intracellular space of the cell from some exclusively intracellularly located compartment or molecule. If such a mechanism were operative, it would not be possible to reverse the sign of the PEP by passing current across the membrane.

Thus the PEP appears to be a response evoked by light from some component of the reticular cell membrane and has some of the characteristics of the ERP. It remains to be shown, however, that the PEP has anything to do with vision. The evidence that we have on this important point is inconclusive. The PEP can be recorded from the eccentric cell of the *Limulus* eye and from other cells that do not otherwise respond to light. The latter may be the pigment cells known to envelop the ommatidium. In an experiment performed in collaboration with Mr. James Anderson of the Communications Biophysics Group a PEP was recorded from pigmented cells in the cerebral and abdominal ganglion of the sea-slug, *Aplysia californica*. These experiments would suggest that the PEP is a general property of pigmented cells, which is consistent with the recent observations that ERP-like responses can be recorded from isolated pigment epithelium of the frog and rat eye.^{6, 7}

Our light source is insufficiently intense to allow a detailed examination of the action spectrum of the PEP with interference filters. Employing broadband and highpass and lowpass interference filters, however, we have found that the response is most sensitive to lights in the visual spectrum and less so to the deep-blue, the near ultraviolet, the far red, and the near infrared. We cannot, at present, specify the wave length of maximum sensitivity. If the PEP were mainly or exclusively due to rhodopsin, a peak in the action spectrum should occur near 520 mμ.⁸

In an effort to define the action spectrum in some detail, we have recently begun a series of experiments employing argon and krypton lasers. Such light sources have sufficient energy at a number of monochromatic lines to evoke the PEP. The results are still not definitive.

While there is insufficient evidence at present to suggest that the PEP, like the ERP, is a direct manifestation of the absorption of light by visual pigments, should that turn out to be the case the experiments reported in this communication bear importantly on the question of the physical location of such pigments in photoreceptors. They indicate that the pigment molecules are so intimately associated with the cell membrane as to be

a component of the electrical circuit between the inside and outside of the cell and may actually be a molecular constituent of that membrane. The location of the photopigment within the photoreceptor membrane has important implications for the possible mechanisms by which its absorption of light leads to the production of the generator potential. Certain kinds of mechanisms would appear to be excluded. For example, the release by an intracellularly located structure of a transmitter-like substance which acts on the inner surface of the receptor membrane would seem not to be involved. Instead some means by which the alteration of the pigment molecule by light can affect those (presumably) nearby membrane components which control the membranes' permeability to sodium ions would appear to be a more probable mechanism.

T. G. Smith, Jr., J. E. Brown

References

1. K. T. Brown and M. Murakami, "A New Receptor Potential of the Monkey Retina with No Detectable Latency," *Nature* 201, 626-628 (1964).
2. R. A. Cone, "Early Receptor Potential of the Vertebrate Retina," *Nature* 204, 736-739 (1964).
3. W. L. Pak and T. G. Ebrey, "Visual Receptor Potential Observed at Sub-Zero Temperature," *Nature* 205, 484-205 (1965).
4. G. B. Arden and H. Ikeda, "A New Property of the Early Receptor Potential of Rat," *Nature* 208, 1100-1101 (1965).
5. R. Hubbard and R. C. C. St. George, "The Rhodopsin System of the Squid," *J. Gen. Physiol.* 41, 501-528 (1958).
6. K. T. Brown, "An Early Potential Evoked by Light from the Pigment Epithelium-Choroid Complex of the Eye of the Toad," *Nature* 207, 1249-1253 (1965).
7. R. A. Cone, personal communication, 1966.
8. R. Hubbard and G. Wald, "Visual Pigment of the Horseshoe Crab, Limulus polyphemus," *Nature* 186, 212-215 (1960).

XX. COMPUTATION RESEARCH

Research Staff

Martha M. Pennell
T. H. Brooks

Gail M. Fratar

Veronica E. McLoud
R. M. Nacamuli

A. FURTHER COMPUTATIONS USING NEWTON'S METHOD FOR FINDING COMPLEX ROOTS OF A TRANSCENDENTAL EQUATION*

Because of our prior success¹ with Newton's method, we used the same technique on the following, more complicated equation. Given real values for α and β , solve for ν as a function of γ ($0 \leq \gamma \leq 10$):

$$\frac{\gamma^2}{\beta^2 \nu^2} = \frac{K_{xy}^2}{K_{xx}} + K_{yy},$$

where

$$K_{xy} = j \frac{\alpha^2}{\gamma} \sum_{N=-\infty}^{\infty} \left[\frac{N \{ \gamma J_N J_N' \}'}{\nu(\nu-N)} - \frac{\beta^2 N J_N J_N'}{(\nu-N)^2} \right]$$

$$K_{xx} = 1 - \frac{\alpha^2}{\gamma^2} \sum_{N=-\infty}^{\infty} \left[\frac{\gamma N^2 (J_N^2)'}{\nu(\nu-N)} - \frac{\beta^2 N^2 J_N^2}{(\nu-N)^2} \right]$$

$$K_{yy} = 1 - \alpha^2 \sum_{N=-\infty}^{\infty} \left[\frac{\{ \gamma^2 (J_N^2) \}'}{\gamma \nu(\nu-N)} - \frac{\beta^2 (J_N^2)^2}{(\nu-N)^2} \right].$$

$J_N = J_N(\gamma)$, is the n^{th} -order Bessel function of the first kind. All derivatives are taken with respect to γ .

Because we expected roots near integer values of ν , we chose the same method¹ as before to estimate their value. The resulting sixth-degree polynomial yielded roots which, when used as initial guesses in Newton's method, approximated the roots in most cases to two significant figures. Once a root had been determined to the desired accuracy, γ was varied by a small amount (usually 0.1 or 0.05) and the root used as the new initial guess. This eliminated solving the sixth-degree polynomial at each step.

This procedure broke down in the region where γ changed from a pure real to a complex root (but not in the reverse situation). If the initial guess were pure real, the

*This work was supported by the National Science Foundation (Grant GK-614).

(XX. COMPUTATION RESEARCH)

computer program² could only generate real computations because none of the arithmetic operations led to complex numbers. In the reverse situation, however, starting with a complex initial guess and performing several iterations of Newton's method, the program would make the imaginary part of the root disappear.

A second difficulty with this procedure was keeping on the same branch of the root. In this particular problem we were more interested in seeing the change in the root as we varied γ than in finding all roots for a given γ . In the regions where Newton's method could not converge or in the transition regions described above, the program jumped branches to find roots outside our range of interest. We had to keep a constant watch on the calculations. These difficulties might possibly have been solved by judicious programming, but the computer time and human effort involved would outweigh the advantages. Here the availability of a time-sharing computer solved a problem which otherwise might not have been attempted.

Martha M. Pennell

References

1. Quarterly Progress Report No. 80, Research Laboratory of Electronics, M. I. T., pp. 263-266.
2. All computations were performed on the Project MAC time-sharing system.

Author Index

- Allen, R. J., 13
- Andrews, J. M., Jr., 1
- Athans, D. P., 27
- Austin, M. E., 161
- Barrett, A. H., 13, 21
- Bartsch, R. R., 69
- Bedell, G. D., IV, 186
- Bernard, G. D., 102
- Bers, A., 75, 81, 85, 94, 102, 106, 133
- Bolz, G., 104
- Brown, G. A., 125
- Brown, J. E., 249
- Brueck, S. R. J., 106
- Clarke, J. F., 147
- Davis, J. A., 101
- Falconer, D. D., 174
- Fiocco, G., 36
- Fukumoto, A., 8
- Gaut, N. E., 11, 12
- Gentle, K. W., 44
- Geselowitz, D. B., 218
- Grams, G., 36
- Gruber, J. S., 181
- Hartmann, H. P., 194
- Haus, H. A., 49
- Hoffman, M. A., 129
- Huang, T. S., 199
- Ingraham, J. C., 63
- Katyl, R. H., 41
- Kiparsky, R. P. V., 190
- Kolers, P. A., 193
- Lampis, G., 58
- Levy, E. K., 125
- Lidsky, L. M., 141, 147
- Lieberman, M. A., 75, 81, 85, 94
- Moir, R. W., 141
- Moran, J. M., 21
- Moreno-Diaz, R., 235
- Mozzi, R. L., 39
- Offenberger, A. A., 139
- Oppenheim, A. V., 161
- Parker, R. R., 72
- Penfield, P., Jr., 49
- Pennell, Martha M., 253
- Perry, C. H., 27
- Pfeiffer, R. R., 207
- Pickard, W. F., 240
- Pilc, R., 173
- Poussart, D. J-M., 213
- Prasada, B., 199
- Rabin, Sylvia, G., 236
- Rosenthal, Kathryn F., 193
- Ross, J. A., 46
- Schulz, H. M., III, 43, 44
- Smith, D. P., 238
- Smith, T. G., Jr., 242, 249
- Speck, C. E., 137
- Staelin, D. H., 12, 21
- Tse, F. Y-F., 55
- Warr, W. B., 207
- Warren, B. E., 39
- Waymouth, J. F., 35
- Woo, J. C., 115, 121
- Woodson, N. D., 113
- Young, E. F., 27
- Zeiders, G. W., 129
- Zimmerman, R., 33